

First-Principles Modeling of Molecular Switches at Surfaces

im Fachbereich Physik
der Freien Universität Berlin eingereichte
Dissertation zur Erlangung des Akademischen Grades
DOKTOR RERUM NATURALIUM

von
M. Sc.
Erik R. McNellis

Berlin 2009



MAX-PLANCK-GESELLSCHAFT

Erster Gutachter (Betreuer): Prof. Dr. Karsten Reuter

Zweiter Gutachter: Prof. Dr. Martin Weinelt

Disputationstermin: 03. Februar 2010

Du ville, men fick inte se detta
men Du var med mig, hela vägen
för Dig, Morfar

Abstract

The scientific vision of nanotechnology is the atomically precise fabrication and manipulation of mechanical and electronic components. A promising route to such control on the molecular scale, is to construct components from controllable molecules. Of these, molecules with properties bi-stably and reversibly modifiable by external stimuli, so-called *molecular switches*, are the simplest case with obvious applications.

The *azobenzene* molecule qualifies in this class by undergoing reversible photo-isomerization between its *cis* and *trans* conformers with particularly high yield and stability, rendering it an archetype of molecular switches research. Ostensibly, direct interaction with single or few switch units requires localization and ordering of switches, e.g. adsorbed at a solid surface. However, so far, surface adsorption of azobenzene without substantial to total loss of switching function has not been achieved. The use of ligands decoupling switch moieties from the substrate, while a promising possible solution to this problem, has a comparably detrimental influence in a number of cases.

This thesis investigates azobenzene adsorption in the two model cases of complete and no switch - substrate decoupling, using theoretical surface science techniques. Aiming at quantitatively predictive modeling, a wide range of first-principles and *ab initio* simulation methods is employed. Since in particular interactions of organic molecules with metal surfaces pose a tremendous challenge to such methods, the second main theme is methodological in nature, notably addressing the problem of simultaneous treatment of a metallic substrate bandstructure, and weak *van der Waals* (vdW) substrate - adsorbate interactions.

In combination with various experimental X-ray and UV/Vis spectroscopy techniques, azobenzene-functionalized self-assembled monolayers (SAMs) are studied as an example of complete switch - surface decoupling. The results identify excitonic coupling between switch units as a main cause of switch yield loss in this system. Implying that such loss is intrinsic to azobenzene above a critical component density, this finding – in addition to previously discussed steric limitations on switch motion – is crucial to future design of surface-decoupled switch arrays.

Direct switch adsorption at close-packed coinage metal (Cu, Ag, Au) surfaces is modeled explicitly accounting for the substrate electronic structure. The current work-horse simulation method for such a problem – density-functional theory (DFT) with (semi-) local exchange-correlation functionals – is shown to yield qualitatively incorrect results, primarily due to its deficient description of vdW interactions.

Currently beyond the capabilities of accurate *ab initio* techniques, the problem is revisited using DFT with semi-empirical correction potentials (DFT-D), resulting in a more plausible and consistent bonding picture at all three substrates. State-of-the-art X-ray spectroscopy experiments find the geometry prediction of the most sophisticated correc-

tion scheme remarkably accurate. The lower accuracy of the energetic predictions within this approach is explained in terms of its inherent neglect of screening at the metal surface. In addition to identifying a route to further improvements of the DFT-D method, this suggests that already existing schemes are capable of currently otherwise unattainable geometry predictions, from which particularly chemically relevant structures can be selected for a focused higher-level treatment. Finally, a route to arbitrarily accurate such energetic predictions is presented and summarily illustrated with proof-of-concept calculations.

Contents

1. Introduction	1
2. Status of Current Research	5
I. Methodology	11
3. The Many-Body Problem	13
3.1. Hartree Theory	15
3.2. Hartree-Fock Theory	16
3.3. Post Hartree-Fock: MP2	17
4. Density-Functional Theory	19
4.1. Density Functional Approximations	20
4.2. Time-Dependent DFT	22
5. Basis Sets	25
5.1. Gaussian Basis Sets	25
5.2. Plane-waves and Pseudopotentials	26
II. Surface-Decoupled Switches	29
6. Azobenzene-Functionalized SAMs	31
6.1. Modeling of Pure Azobenzene	32
6.2. Electronic Structure	36
6.3. Geometric Structure	42
6.4. Optical Properties	45
6.5. The Extended Dipole Model	46
6.6. Summary	49
III. Surface Adsorbed Switches	51
7. The DFT-GGA Adsorption Picture	53
7.1. Theory	55
7.2. Results and Discussion	58
7.2.1. Gas-phase Azobenzene	58

CONTENTS

7.2.2. Adsorption Geometry and Energetics	59
7.2.3. Electronic Structure	62
7.3. Summary	66
8. The Role of vdW Interactions	69
8.1. Theory	72
8.1.1. Semi-Empirical Dispersion Correction Schemes	72
8.1.2. Density-Functional Theory Calculations	75
8.2. Results	77
8.2.1. Azobenzene Gas-Phase Properties and Adsorbate Geometry	77
8.2.2. Electronic Structure and Energetics of Adsorbed Azobenzene	80
8.3. Discussion	82
8.4. Summary	85
9. An Experimental Benchmark	87
9.1. Results and Discussion	88
9.2. Summary	92
IV. Outlook	93
10. The XC-Correction Method	95
10.1. Theory	96
10.2. Results	96
10.3. Summary	100
11. Future Steps	101
Acknowledgments	105
V. Appendices	107
A. Surface-Decoupled Switches	109
A.1. Basis Set Tests	109
A.2. TDDFT: ALDA / Basis Set Tests	110
B. Surface Adsorbed Switches	113
B.1. Bulk Metal Properties	114
B.2. Surface Properties	116
B.3. Adsorbed Azobenzene Convergence Tests	120
B.4. Work Functions	123
B.5. (P)DOS Convergence Tests	125
B.6. Dispersion Corrected (P)DOS	127

C. The XC-Correction Method	131
C.1. Cluster Geometries and Basis Sets	131
C.2. The MP2 XC-Correction	135
Publications	141
Bibliography	143

List of Figures

1.1. Sketch of the azobenzene molecule	2
1.2. Light-polarization dependent bending of an azobenzene-coated film	3
2.1. The frontier orbitals of azobenzene	7
6.1. Structural formula of the TF-Az n molecule	31
6.2. Characteristic geometry parameters of azobenzene	33
6.3. Measured C 1s XPS spectra of C6, Az6 and TF-Az6	37
6.4. The π, n, π^* , LUMO+1, and LUMO+2 π^* orbitals of TF-Az6	39
6.5. Comparison of theoretical and experimental core level shifts	40
6.6. The TF-Az6 geometry and relevant tilt angle definitions	43
6.7. Structural model of the TF-Az6 SAM	44
6.8. DFT linker bond- and azimuthal angle PES of Az3	44
6.9. UV/Vis absorption spectra of TF-Az6 and Az6	46
6.10. Definition and results of the Extended Dipole Model	47
7.1. Azobenzene in super-cells of a Au(111) slab	54
7.2. Considered high-symmetry geometries of azobenzene at the (111) surface	56
7.3. GGA-PBE frontier orbital isodensity contours	58
7.4. The azobenzene adsorption geometry	59
7.5. DOS and molecular PDOS of azobenzene at coinage metals	65
8.1. Illustration of the Ag-C dispersion correction potential	73
8.2. Dispersion corr. induced changes in the azobenzene adsorbate geometry	78
8.3. Illustration of the effect of dispersion corrections on ΔE_{C-T}	80
8.4. Benzene binding energy curves	83
9.1. Theoretical trans@Ag(111) binding curves compared to experiment	89
9.2. Structural formula of the PTCDA molecule	90
9.3. PBE+TS BE curves of PTCDA @ Ag(111) compared to EXX+RPA	91
10.1. Hybrid functional xc-correction calculations	97
10.2. BE curves of benzene at Cu(111) xc-corrected at PBE0 and B3LYP level	98
10.3. The calculated MP2-PBE xc-correction as a function of cluster size	99
11.1. The TS-corrected geometry of TBA at Ag(111)	103
A.1. Basis set test study of the properties of pure azobenzene	109

LIST OF FIGURES

B.1. Bulk Cu properties	115
B.2. Convergence of clean Cu $\sigma_{(111)}$ and F_Z with \mathbf{k} -points and E_{kin} cutoff . . .	117
B.3. Clean Cu $\sigma_{(111)}$ and F_Z convergence w. r. t. slab and vacuum thickness .	118
B.4. GGA-PBE convergence tests on azobenzene adsorbed at Ag	121
B.5. Surface work functions of the cis isomer at Au	124
B.6. DOS and PDOS convergence tests on the trans isomer at Au	126
B.7. G06-corrected DOS and PDOS	127
B.8. TS-corrected DOS and PDOS	129
C.1. The Cu cluster geometries used in the xc-correction calculation	132
C.2. Basis set test of the MP2 and B3LYP xc-corrections	134

List of Tables

6.1. Azobenzene geometry: Comparison between theory and experiment	34
6.2. Azobenzene excitation energies: Comp. between theory and experiment .	35
6.3. Select optimized geometry parameters of TF-Az6	42
7.1. GGA geometry parameters of azobenzene at coinage metals	60
7.2. GGA adsorption energies of azobenzene at coinage metals	61
7.3. GGA EA,IP,EN and work functions for azobenzene at coinage metals . .	63
8.1. Calculated effective C_6 and R^0 coefficients	74
8.2. Dispersion corrected geometry parameters of azobenzene	77
8.3. Dispersion corrected E_{ads} , Φ and $\Delta E_{\text{C-T}}$ of adsorbed azobenzene	81
8.4. Dispersion corrected benzene adsorption geometry and energetics	84
A.1. TDDFT basis set / potential correction test	110
B.1. Comp. of calculated LDA / GGA bulk / surface properties to literature .	118
B.2. Relaxed top inter-layer spacings of clean Cu (111)	120
B.3. Work functions of clean (111) surfaces	123

1. Introduction

The discovery of quantum theory revolutionized science. Fundamental questions posed by earlier scientific advances, such as the nature of the spectrum of light, the principles behind the structure of the periodic table of elements, and what causes atoms to repel or bond to each other, all were answered in a single, comprehensive theory.

In a perhaps quintessentially human fashion, this new-found insight soon evolved into the desire to control and exploit properties of matter in technological applications on the molecular or *nano*-scale. Of the several post-war scientific visions of the potential of nanotechnology, Richard Feynman's 1959 lecture "*There's Plenty of Room at the Bottom*"* is considered seminal. In his characteristic no-nonsense manner, Feynman argued that it should be possible to store information at a density limited only by the size of single atoms, and manipulate "tiny hands" to create mechanical and electronic components out of molecular-sized chunks of matter.

As of this writing, mere weeks before the 50th anniversary of Feynman's lecture, the pursuit of nanotechnology – or more precisely, the effort to fabricate and control *atomically precise* mechanical and electronic components – has brought a host of groundbreaking technological advances, including everything from the mind-boggling development of computers and the Internet, to first successes with nano-particle assisted cancer drug delivery in lab animals. In science, this process has brought forth and relied upon related fields such as *surface science* – the study of the physics and chemistry of solid interfaces – to which this thesis contributes.

A possible answer to the question of *how* control over molecular-scale components can be achieved, is to simply construct components out of *controllable molecules*. The simplest such component with obvious applications is a molecule bi-stably and reversibly modifiable by external stimuli – a so-called *molecular switch*. The class of molecular switches contains a number of variations on the theme, including e.g. conformational switches via reversible molecular chirality, and switching of spin-states, and therefore visible color, of certain ferrous compounds in solution. Molecular switching is also a common biological process, exemplified by the conformational switching of *retinal*¹ transforming light detected by the eye into neural impulses.

However, an ideal candidate molecule for a technical implementation should be chemically simple, easily modifiable, and switch at particularly high efficiency. The *azobenzene* molecule ($C_6H_5-N_2-C_6H_5$, sketched in Fig. 1.1), fulfills all of these criteria – in gas-phase, it bi-stably photo-isomerizes between its *trans* and *cis* isomers under illumination with light of two well-separated wavelengths. Essentially a microscopic light-to-mechanical energy converter, or light-driven motor, this molecule is even robust enough to switch

*See transcript at www.its.caltech.edu/~feynman/plenty.html

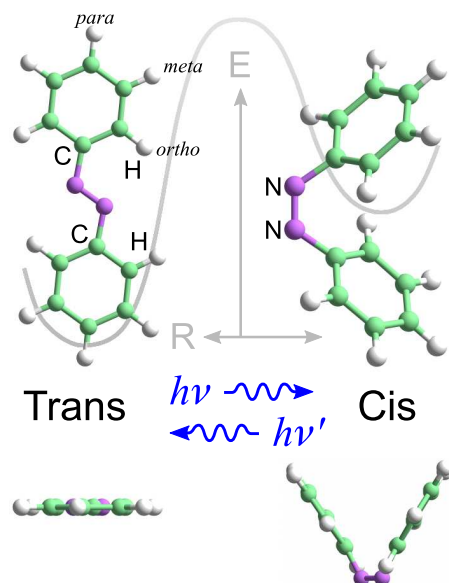


Figure 1.1.: Sketch of the azobenzene molecule, superimposed on a symbolic reaction path. Left: The trans isomer. Right: The cis isomer. Top: View perpendicular to the molecular axis. Bottom: View parallel to the molecular axis.

macroscopic objects in large ensembles – for example, in Fig. 1.2, a plastic film coated with an azobenzene derivative is shown reversibly bending in a direction dependent on the polarization of incident photons.

Consequently, azobenzene has particularly in the last two decades come under intense scrutiny, to the point of rendering it a candidate *Drosophila* of the molecular switches class. Its suggested potential applications now include everything from high-density storage media^{2,3} and conductors⁴ in logical gate circuits, to the simple light-driven actuator⁵ shown in Fig. 1.2.

Nevertheless, switching of molecular ensembles is not technically nanotechnology – in order to fully exploit the properties of azobenzene, control over individual or few molecular units must be attained. The perhaps most obvious route to this goal, is by localization and ordering of switches in a fixating medium, e.g. in a molecular crystal, or adsorbed at a solid surface. For microelectronics, in particular the latter option is of interest.

However, such localization, implying modification and / or influencing of the switch on the scale of the switch itself, generally has subtle and detrimental consequences for the switch function. In fact, as will be further elaborated upon in the next chapter, switching by light of pure azobenzene directly adsorbed at a solid surface has never been attained, despite ample attempts.

The obvious solution to this problem, namely decoupling the switch unit from the surface by functionalizing it with a ligand which in turn attaches to the surface, also by necessity implies a modification of the switch electronic and geometric structure, with equally subtle – and in several cases comparably negative – consequences for the

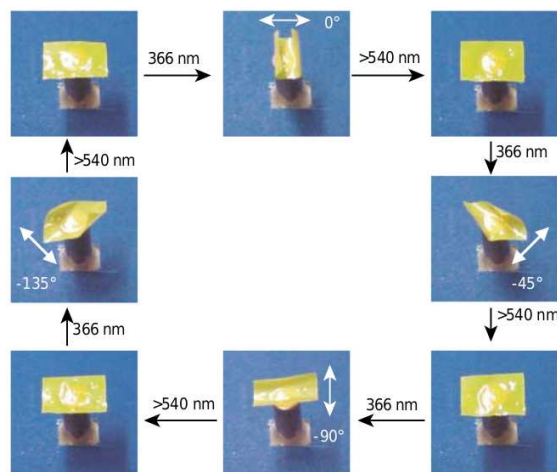


Figure 1.2.: From Yu et al.⁵: A plastic film coated with an azobenzene-based compound bends reversibly in the polarization direction upon illumination with ultraviolet and visible light.

switch function. The realization of azobenzene-based nanotechnological components is evidently entirely contingent on a detailed understanding of not only the molecule itself, but also of its interaction with various environments and changes of function with small variations of the switch structure.

In this context, theoretical first-principles and *ab initio* modeling – or the search for and study of practical approximate solutions to the equations of quantum mechanics – stands to offer a unique perspective. Modeling the microscopic properties of matter from the mathematical laws of physics alone allows for explanations and predictions of the material-specific mechanisms behind observed phenomena of unprecedented detail. Ideally, given models of sufficient rigor, first-principles theory could predict precisely how those mechanisms work, in the case of adsorbed azobenzene e.g. under variations of substrate or ligand type and structure.

This defines the main theme of this thesis, namely the investigation of azobenzene adsorption at solid surfaces, in the two model cases of maximal (here represented by azobenzene-functionalized self-assembled monolayers) and minimal (corresponding to direct surface adsorption) surface decoupling of the switch moiety, by means of first-principles and *ab initio* techniques in the context of theoretical surface science.

However, the dramatic, sensitive and in significant parts unexplained behavior of azobenzene imposes severe restrictions on acceptable assumptions: Every concession of simplifying approximations to the complexity of a problem falling squarely between traditional divisions of – and inheriting the methodological challenges of both – theoretical physics and -chemistry, risks smoothing over significant detail. As we shall see, the aim of quantitative predictions under such conditions quickly reaches the current limits of standard methodology. Specifically, the combination of explicitly treated metal surface physics with light molecule chemistry implied by the second adsorption case above, is a daunting task for current first-principles theory. Therefore, the secondary theme of

CHAPTER 1. INTRODUCTION

this thesis is methodological in nature, focusing on exploring the limits and furthering the development of available simulation methods.

This thesis is organized as follows: Previous research and the details of the consensus view on the properties of azobenzene are summarized in chapter 2. Next, the textbook theoretical techniques used in this work are summarily described in Part I (all non-standard methodology is described and discussed in context in the main chapters). Part II details the work on surface-decoupled switches. For greater clarity and brevity of the main text, much of the routine (albeit important) technical detail in this and the following two parts has been relegated to appendices in Part V. The second case of minimal switch - surface decoupling is the topic of Part III. Finally, a few purely methodological aspects of, and potential future developments made possible by this work, are discussed in Part IV. Unless explicitly otherwise stated and duly cited, all results, figures, numbers and conclusions presented constitute original research. Most of this work has been published in various scientific journals; the publications are for convenience listed separately on page 141.

2. Status of Current Research

One of the first accounts of the interesting properties of azobenzene was given by Teitel in 1957⁶. It reports, that a viscous solution of the the azobenzene derivative Congo Red under illumination with polarized light becomes dichroic, an effect which remains stable for on the order of a week. Later confirmed by Neporent et al.^{7,8}, this phenomenon was initially attributed to simple rotation of photon-absorbing molecules upon illumination. Studies on derivatives in a solid form preventing reorientation of the molecules were performed in the following years, and in 1971 Makushenko et al.^{9,10} could confirm that the azobenzene moiety indeed reversibly isomerizes under illumination with light in the visible and ultraviolet spectrum. Perhaps the first prototypical technical implementation appeared in 1984, when Todorov et al.¹¹ reported an optical application in holography, exploiting photo-induced dichroism and birefringence in the azobenzene derivative Methyl Orange. Proposed applications of azobenzene continued to emerge with steadily increasing frequency until the early nineties when, following the budding nanotechnological research, the interest in azobenzene sharply increased. Ever since, hundreds of scientific publications on properties and applications of azobenzene and -derivatives have been produced per year.

Consequentially, the crystal structure of azobenzene is by now well characterized^{12,13}. The molecule has two conformers, a C_{2h} symmetric, planar *trans* and some 0.6 electron-volt (eV) less stable¹⁴, C_2 symmetric, torsioned-twisted *cis* isomer (see Fig. 1.1). The photo-isomerization reaction is induced by resonant excitations involving the frontier π^* , n , and π molecular orbitals (MOs), corresponding to the lowest unoccupied MO (LUMO), the highest occupied MO (HOMO) and HOMO-1, respectively (see Fig. 2.1). In the *cis* isomer, the *cis-trans* reaction is triggered by excitation of the $n - \pi^*$ resonance centered at 430 nanometers (nm) wavelength¹⁵, corresponding to the first singlet excited state or S_1 . This resonance is dipole forbidden in the higher symmetry of the *trans* isomer, in which the *trans-cis* isomerization is therefore induced chiefly by excitation of the $\pi - \pi^*$ resonance at 320 nm¹⁵, corresponding to the second singlet excited state S_2 . In the *trans* isomer the two lower lying π orbitals, in Fig. 2.1 labeled π_ϕ , are degenerate by symmetry. The corresponding $\pi - \pi^*$ resonances or singlet excitations S_3 and S_4 are naturally also degenerate. Of these, only the latter is optically bright and visible in experiments¹⁶. In solution, the yield of both ways of this reaction is very high – near unity, and isomerization (or switching) can be achieved using a simple photodiode^{17,18}. The activation energy for thermal isomerization is also high¹⁹, approximately 1 eV, leaving both conformers exceptionally stable even at room temperature.

Why and how the photo-isomerization reaction occurs, has long been a controversial issue. Photo-isomerization being an electronic structure phenomenon with geometrical structure consequences, it can be formulated as the question of how the electronic and

geometric structure evolve along the reaction path, and to what degree these evolutions are coupled. In particular, the question of which of the structural *torsion* path, where bending and twisting of the azo (-N=N-) bridge is accompanied by a rotation of a phenyl ring around what in the trans isomer would be the molecular axis (see Fig. 1.1), or the *inversion* path, in which the latter rotation is replaced chiefly by bending around the CNN bond angle, is favored, is almost as old as the field itself^{20–22}.

The first conclusive experimental indication of the latter mechanism appeared in 1982, when Rau et al.²³ observed cis-trans isomerization in azobenzene molecules functionalized in such a way as to specifically block the rotation path. Still, functionalization substantially reduced the yield of the trans-cis reaction, leading the authors to conclude that rotation (inversion) was the main mechanism in the trans-cis (cis-trans) isomerization. This result was followed up and further confirmed in 1984²⁴.

Ab initio theoretical simulations have made substantial contributions to the characterization of the electronic degrees of freedom. Using potentially highly accurate configuration interaction (CI, see chapter 3) calculations to scan the molecular geometry in the S_1 state, Monti et al.²⁵ found a large barrier along the rotation pathway, and no barrier along the inversion path, ostensibly in agreement with Rau et al.’s findings. Unfortunately, the computational cost of CI only allowed for small, Slater type basis sets in these calculations, leaving the accuracy of the overall level of theory relatively modest. Lednev et al.^{26,27} explained transient absorption components in terms of the S_1 and S_2 barriers calculated by Monti et al.

Using time-resolved absorption measurements, Nägele et al.¹⁷ found that the cis-trans isomerization occurs considerably faster (170 fs) than the trans-cis isomerization (320 fs), suggesting a steep, barrier-free reaction path in the former, and a somewhat more gradual reaction path in the latter case, adding further clues for the theoretical investigations. Cattaneo and Persico²⁸ were able to more exhaustively characterize the low-lying excited singlet as well as triplet reaction paths, using multireference perturbation theory and complete active space self-consistent field (CASSCF) methods, justified by the strong multireference character of the wave-function at the transition geometries. While the resulting paths differed substantially from those found by Monti et al., this did not lead to any essentially different conclusions.

Ishikawa et al.²⁹ revisited the problem using similar methodology, finding a so-called conical intersection, or degeneracy in two electronic states “funneling” de-excitations from higher excited states, between the S_1 and ground (i.e. S_0) states near the midpoint of the rotation pathway. Additionally, it was found that the S_2 surface lacked conical intersections with S_0 , leading to the assertion that trans-cis isomerization must follow $\pi - \pi^*$ excitation via de-excitation through S_1 and S_3 , in contrast to the simpler mechanisms discussed by previous theoretical work.

Femtosecond spectroscopy combined with *ab initio* excited state molecular dynamics performed by Schultz et al.¹⁶ underscored the importance of the S_3 and S_4 surfaces in the trans-cis isomerization, with the resonance corresponding to the latter found to be of comparative brightness to the S_2 resonance. Later work by Cembran et al.^{30,31}, using a combination of CASSCF, second-order CAS perturbation theory (CASPT2) and density-functional theory (DFT), in essence confirmed the picture established by

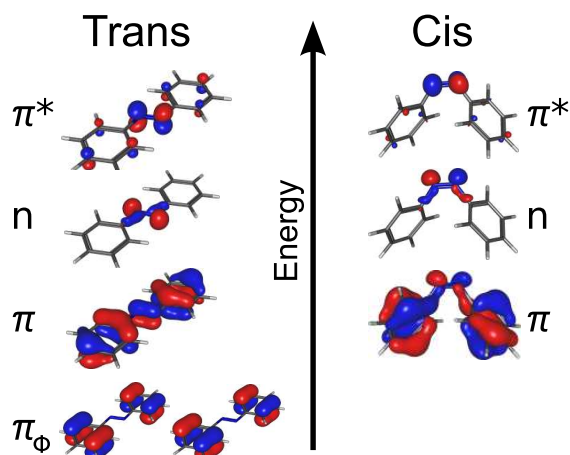


Figure 2.1.: The azobenzene frontier orbitals most important for the photo-isomerization process. Left: The trans isomer. Right: The cis isomer.

Ishikawa et al., with the photo-isomerization on the S_1 surface clearly preferring the torsion path, and the inversion path only open to S_1 isomerization at excitation energies above 1 electronvolt. In addition, this study found a conical intersection between S_2 and S_3 , and identified S_3 as the lowest lying state at large phenyl – phenyl twists.

Later work by Tiago et al.³², using the alternative methods of constrained (CDFT) and time-dependent (TDDFT) DFT also supported the view of the rotation path as the most favorable. Concurrent with the Cembran et al. publications, Diau³³ proposed a *combination* of the torsion and inversion paths, the *concerted* inversion path, as the most favorable.

In summary, one could characterize the results of these endeavors as one of those intriguing, and often frustrating, cases in science where further investigation only seems to add to the dimensionality of the problem. Despite the considerable progress in the understanding of the details of the photo-isomerization of azobenzene the above cited literature represents, no given path or specific mechanism can be attributed to all observed reactions and reaction characteristics. Another evident conclusion is, that whatever the preferred switching reaction path is, it must be highly sensitive to modification of the molecular geometric or electronic structure – in fact, it is not clear whether azobenzene in different ambient conditions isomerizes in ways at all similar to that of the actual gas-phase molecule.

Obviously, a necessary requirement for the use of azobenzene as a nano-scale mechanical component, is that its function is not destroyed by its very integration into the machinery. Furthermore, precise control over the function and state of such a component, is contingent on a corresponding degree of control over the molecular geometry. It is therefore natural, that current literature on azobenzene adsorbed at solid surfaces is characterized by its pursuit of two major goals, namely maintenance or enhancement of the switch reaction yield, and control of the adsorption geometry.

Given these two requirements, the choice of an optimal substrate is difficult. While

bonding of some strength is necessary for localization and ordering of adsorbates, strong electronic coupling between adsorbate and substrate likely disturbs the switching mechanism. Switching may also be sterically hindered by adsorbate ordering incompatible with the free volume requirements of either isomer. Ostensibly, the non-zero but weak interactions^{34–38} of aromatic molecules with close-packed surfaces of the coinage metals (copper, silver and gold) make them prime candidates for such an optimal substrate. However, even at these in the field predominantly adopted substrates, adsorbate excited states are quenched by coupling to the substrate electronic structure³⁹.

This is a problem for photo-chromic molecular switches in general, and strategies aiming at decoupling the switching moiety from the substrate by functionalization with ligands acting as spacers have been developed⁴⁰. Still, such a functionalization may itself affect switching mechanisms, e.g. in the case of azobenzene significantly shifting the energetic positions of the resonant excitations⁴¹, quenching transitions dependent on where the ligand is attached⁴², or modulating solvent effects^{43,44} in addition to changing steric properties.

The optimal decoupling of the azobenzene moiety from the substrate, depending on the intended application, lies between the two limits of none, where the pure molecule is adsorbed directly on the surface, and total, where the spacer ligand is sufficiently large for the surface influence on the switch moiety to be negligible.

Literature on systems around the former extreme is dominated by a multitude of experimental Scanning Tunneling Microscope (STM) studies^{45–65}. Atomic Force Microscopes (AFM) have also been successfully, albeit more rarely, employed^{66,67}. Pure, ligand-free azobenzene adsorbed directly at Au(111) have been found to self-assemble in superstructures commensurate with the substrate⁴⁶, and exhibit strongly substrate-dependent diffusion behavior at Cu(100)⁴⁷.

While nicely adhering to the second above requirement, this approach is less successful by the first, since no experiment to date has been able to photo-isomerize pure azobenzene at coinage metals by illumination with light. This is likely a consequence of the mentioned quenching of the molecular excited states. At Au(111) however, switching can be induced by the STM-tip⁴⁸ by ramping the bias voltage in short pulses, creating a powerful local electric field in the vicinity of the tip. Although the precise mechanism behind this field-induced switching as of yet is not well understood, interest in experimental investigations of the properties of adsorbed pure azobenzene appears to have waned, judging by the relative sparse publication record. Presumably, this is because of the difficulties in maintaining the switching yield.

Instead, the effects of functionalization by ligands of intermediate size have been studied in a host of derivatives^{56–59,68}. Results show, that even relatively modest variations in functional group (ligand) form, substrate element and substrate packing fraction give rise to a plethora of different switching behaviors:

For instance, azobenzene functionalized with methoxycarbonyl groups in one *meta* position (see Fig. 1.1) per phenyl ring, or di-*meta*-methoxycarbonyl-azobenzene (CMA), self-assembles in a rich structure of several distinct structural species at Au(111)⁵⁶. Instead substituting the methoxycarbonyl groups for cyano groups in di-*meta*-cyano-azobenzene (DMC), gives irreversible STM tip-induced switching at Cu(100)⁵⁵, as is also

the case of Methyl Orange (4-dimethylaminoazobenzene-4-sulfonic acid) at Au(111)⁵². In contrast, tip-induced switching of the derivatives amino-nitro-azobenzene and Disperse Orange 3 at Au(111) is reversible between the two conformers^{53,58}, in the former case even selectively between the constituent molecules of the dimeric adsorption geometry.

The perhaps most studied intermediate-sized azobenzene derivative is tetra-*tert*-butyl-azobenzene (TBA), in which groups of three butyl (CH₃) groups are added to both *meta* positions of each phenyl ring, forming 'legs' of an azobenzene 'table' adsorbing standing on the substrate. TBA switches efficiently at Au(111)⁵⁹⁻⁶⁵, also by illumination with light⁶⁰⁻⁶², albeit requiring laser intensity as opposed to a photo-diode. The latter effect appears to be mediated by charge transfer of optically excited hot carriers from the substrate into the TBA π^* (LUMO) orbital⁶². Since substrate carriers are excited at all wavelengths, the possibility of choosing between trans-cis and cis-trans reactions by tuning the photon energy is lost. At Ag(111)⁴⁹, Cu(111) or Au(100)⁶⁴, the very same molecule does not switch by any means at all, in spite of the ostensibly comparable chemical properties of these surfaces. The intricate role played by the substrate in the switching process is emphasized by the for nano-technological applications perhaps most promising result so far:

In experiments performed by Dri et al.⁵¹, TBA functionalized with an additional methoxy group (M-TBA) to add a finite dipole moment, was at Au(111) observed to switch with some two orders of magnitude greater probability at sites in a rectangular super-lattice in the molecular over-layer, commensurate with the herringbone-reconstructed substrate. This hints at another possible substrate role, namely *mediating* or even *enhancing* switching yield in a defined and predictable manner.

To date, the proposed explanations for these phenomena are almost as numerous as the different phenomena themselves. In addition to the traditional idea of the photo-isomerization, mechanisms such as switching by inelastic electron tunneling (IET)⁵⁸, coupling of energetic electrons to the substrate⁴⁸, or simply STM tip-induced changes in the electric field⁵⁹ have been proposed.

The approach of completely decoupled switches to a degree circumvents the complexity of these phenomena, potentially providing a better foothold for technical applications by reducing the problem to a chiefly chemical one. Still, the described sensitivity of azobenzene to environment factors is not diminished by such functionalization, as the importance of aspects of the molecular assembly increases⁶⁹.

For instance, as the size of the spacer grows, the importance of the spacer inducing the desirable switch order increases with the diminishing direct switch-substrate interaction. Self-Assembled Monolayers^{70,71} (SAMs) of aliphatic molecules form a promising⁷² candidate class of such spacers. In particular *n*-alkanethiols (HS - (CH₂)_n - CH₃) form SAMs of exceptional simplicity, stability and high order⁷³⁻⁷⁵. Advanced contemporary synthetic chemistry allows for highly precise functionalization of azobenzene with for instance such a compound, potentially offering a wide range of 'switchable' functional surfaces.

However, the high degree of orientation observed in bi-phenyl-based SAMs⁷⁶⁻⁷⁸ suggests a further possibility, namely that the switch moieties themselves interact and

order. In fact, azobenzene derivatives with smaller spacers adsorbed at Au surfaces are known^{67,79} to form periodic structures with nearest neighbor distances of some 4.9 Ångström (Å), which is smaller than the unit cell of pure aliphatic SAMs⁸⁰⁻⁸². If the switch moiety interaction is sufficiently strong to dominate the structure of the functionalized SAM, the steric hindrance associated with the resulting high packing fraction could have a detrimental influence on the switch function. This has indeed been attributed to the fact, that azobenzene-functionalized alkanethiolate SAMs to date have not been successfully optically switched^{83,84}. This is a general problem for functional self-assembled molecules⁸⁵, and has been addressed by further functionalizing the compound such that lateral molecular interactions become more repulsive, with some success⁸⁶. Nevertheless, such an add-on may be undesirable, as it naturally restricts the freedom of design of the SAM-switch compound.

For a theorist, the study of properties of surface-adsorbed azobenzene switches is a daunting task: Experimental results indicate as presented, that the properties of the pure or functionalized metal-surface adsorbed molecule, its ground- and excited state electronic structure, as well as switch-switch, switch-surface, where applicable switch-spacer, and spacer-surface interactions all play an important part. A predictive theoretical treatment thus ostensibly requires theoretical models numerically feasible for medium to large model systems, yet sophisticated enough to treat light element chemistry, strong as well as weak, non-covalent interactions, excited states, and heavy-element metallic band-structure on an equal and accurate footing. As of this writing, no well-established solutions for such problems exist.

Consequentially, it comes as no surprise that, while the contributions of theory to the understanding of the *gas-phase* molecule are seminal, theoretical work on *adsorbed* azobenzene-based switches have hitherto been comparatively inconsequential, including e.g. simulations aiding the interpretation of STM images⁶¹, attempts at inducing the properties of surface mounted switches from gas-phase properties alone⁸⁷, and explicit treatments of surface interaction effects at low levels of computational accuracy⁵⁵ or using highly simplified surface models⁸⁸.

This obvious deficiency forms the main justification of the scientific relevance of this thesis.

Part I.

Methodology

3. The Many-Body Problem

“The underlying physical laws necessary for the mathematical theory of a large part of physics and the whole of chemistry are thus completely known, and the difficulty is only that the exact application of these laws leads to equations much too complicated to be soluble. It therefore becomes desirable that approximate practical methods of applying quantum mechanics should be developed, which can lead to an explanation of the main features of complex atomic systems without too much computation.”

Thus spoke Dirac⁸⁹, in a famous publication from 1929. While the exuberance of this statement may seem exaggerated from a present-day perspective, it succinctly describes the goal of modern first-principles and *ab initio* modeling. Indeed, the mathematical framework of quantum theory in principle allows for extremely accurate theoretical simulations of the electronic structure of atoms, molecules and solids, and on a *qualitative* level, these equations define the fundamental working principles of modern chemistry. However, solutions for simulations of relevant *quantitative* accuracy have only in recent decades become tractable, even for very simple systems.

The chapters of this Part are intended as a very brief review of the textbook such solutions employed in this thesis. As this review neither could achieve nor aims at achieving the level of detail and rigor found in standard literature on the subject, the reader is for each topic referred to suitable textbooks for greater depth. See e.g. the excellent review by Szabo and Ostlund⁹⁰ for a superior presentation of the theory of the current chapter. All non-textbook techniques employed or developed in this work are described in their respective contexts in the main chapters.

In general, predicting the ground-state electronic structure of matter amounts to solving the time-independent Schrödinger equation

$$E = \langle \Psi | \hat{H} | \Psi \rangle \quad (3.1)$$

where E , \hat{H} and $|\Psi\rangle$ represent the total energy, the Hamiltonian operator and wavefunction of the N constituent electrons and M atomic nuclei in a given arbitrary system, respectively.

In principle, Eq. (3.1) is a partial differential equation of $3(N+M)$ variables. However, due to the large rest mass ratio between electrons and nucleons, the nuclei can be assumed stationary on the scale of electronic motion, over a large range of momentum ratios. The resulting *Born-Oppenheimer*⁹¹ (BO) approximation decouples the nuclear and electronic degrees of freedom, and allows for solving Eq. (3.1) only for the latter ($3N$ variables). This approximation is generally well justified for typical chemical systems, but breaks down in e.g. ultra-fast scattering processes.

The BO Hamiltonian has a simple form in atomic units:

$$\hat{H} = -\frac{1}{2} \sum_{i=1}^N \nabla_i^2 - \sum_{i=1}^N \sum_{k=1}^M \frac{Z_k}{|\mathbf{r}_i - \mathbf{r}_k|} + \sum_{i=1}^N \sum_{j>1}^N \frac{1}{|\mathbf{r}_i - \mathbf{r}_j|} + E_{\text{nuc}} \quad , \quad (3.2)$$

where Z_m and \mathbf{r}_m are nuclear charges and particle position vectors, respectively. Since the kinetic energy of the nuclei is approximated as zero, the Laplacians of Eq. (3.2) specifically represents the electronic kinetic energy. The remaining terms from left to right correspond to the electron - nuclear interaction, the electron - electron interaction, and the constant nuclear - nuclear interaction. The last, constant term is henceforth excluded (implicitly added) for brevity.

Electrons are fundamental *fermionic* particles. The famous Pauli exclusion principle^{92,93} states, that a wave-function of identical fermions must be anti-symmetric. The spectrum of \hat{H} is bounded below by the *exact* BO ground-state total energy E_{BO} . Calculating the ground state total energy of a set of identical fermions thus amounts to finding the energy minimum under arbitrary variations in a set of anti-symmetric functions $\{\Phi\}$ – the ground-state satisfies the *variational principle*. If $\{\Phi\}$ spans the full space of eigensolutions to \hat{H} , the energy minimum corresponds to the exact E_{BO} . The set $\{\Phi\}$ can be written as linear combinations of a set of spatial *orbitals* $\{\varphi_i\}$, which in turn can be formed from a set of orthonormal three-dimensional basis functions. In a collinear spin model, i.e. with two different kinds of identical electrons, these orbitals are doubly degenerate.

Simple linear algebra yields, that the sought linear combinations correspond to *Slater determinants*

$$\Phi = \frac{1}{\sqrt{N!}} \begin{vmatrix} \varphi_1(\mathbf{x}_1) & \cdots & \varphi_N(\mathbf{x}_1) \\ \vdots & \ddots & \vdots \\ \varphi_1(\mathbf{x}_N) & \cdots & \varphi_N(\mathbf{x}_N) \end{vmatrix} \quad (3.3)$$

where $\mathbf{x}_i = (\mathbf{r}_i, \sigma_i)$ is a generalized spatial and spin (σ) coordinate of electron i . The full set $\{\Phi\}$ is defined by all possible row (particle) permutations of Eq. (3.3).

This solution has three properties of particular relevance. First, it is entirely *transferable*: \hat{H} contains no information specific to a given system, and the above sketched approach can be applied to a single atom, a finite molecule or a semi-infinitely extended solid alike. Second, it is highly *accurate*: Apart from the generally well justifiable BO approximation, the finite basis set is the only limitation on the accuracy. Although infinite and orthonormal – and thereby complete – basis sets can be constructed, one is in practice restricted to the choice of a certain finite basis set. Finding an exact finite basis set for a given physical wave-function is technically possible, but generally requires knowledge of that wave-function. However, thanks to the variational principle, the exact E_{BO} is monotonically approached as the ground state total energy is recalculated for basis sets of increasing size. Therefore, the basis set constitutes an approximation, but a systematically and arbitrarily improvable one.

Third and most importantly, it is very poorly *scaling*: The number of necessary Slater

determinants is a binomial coefficient of N . The number of terms to calculate is to leading order proportional to that coefficient, in strict analogy to a general many-body problem. Thus, this solution is in practice only feasible for benchmark calculations of single small molecules – already N_2 is a tremendous challenge with a decent basis set – and the necessary computational effort increases so rapidly with system size, that this method is not likely to become significantly more useful even in the future.

In summary, this nicely illustrates the known but difficult solution discussed by Dirac. One might further define the criteria for a “practical method” for the prediction of a given quantity in a given system, as scaling low enough to make a solution for this and preferably slightly larger systems at all possible, accurate enough to provide a falsifiable prediction of the relevant quantity, and transferable enough to not require detailed information specific to each studied system. In the following, a few standard such solutions are discussed from the perspective of these three criteria.

3.1. Hartree Theory

A simpler *classical mean-field* approach satisfying the variational principle was proposed by D. R. Hartree⁹⁴. In the so-called Hartree approximation (HA), electrons only interact via an effective single-particle potential corresponding to the mean Coulomb field of the other electrons, and the Pauli principle is neglected – the Ansatz wave-function is a simple product of orbitals. With the norm of each orbital φ_i constrained by a Lagrangian multiplier ϵ_i , the Hartree ground state energy E_{HA} is explicitly written as

$$\begin{aligned}
 E_{\text{HA}} = & -\frac{1}{2} \sum_{i=1}^N \int d^3\mathbf{r} \varphi_i^*(\mathbf{r}) \nabla_i^2 \varphi_i(\mathbf{r}) - \sum_{k=1}^M Z_k \int d^3\mathbf{r} \varphi_i^*(\mathbf{r}) |\mathbf{r} - \mathbf{r}_k|^{-1} \varphi_i(\mathbf{r}) \\
 & + \frac{1}{2} \sum_{i,j=1}^N \int d^3\mathbf{r} d^3\mathbf{r}' \varphi_i^*(\mathbf{r}) \varphi_j^*(\mathbf{r}') |\mathbf{r} - \mathbf{r}'|^{-1} \varphi_j(\mathbf{r}') \varphi_i(\mathbf{r}) = T_0 + E_{\text{ext}} + E_{\text{H}} = \sum_{i=1}^N \epsilon_i
 \end{aligned} \tag{3.4}$$

where the kinetic energy of non-interacting electrons T_0 , the interaction energy with an external potential E_{ext} (here equal to that of the ionic nuclei) and the Hartree energy E_{H} have been identified in the second to last step.

The Hartree potential corresponds to that of the *total* electronic density $n(\mathbf{r}) = \int d^3\mathbf{r}' |\varphi|^2$. Specifically, e.g. in the case of a *single* electron ($i = j$), the Hartree term of Eq. (3.4) does not vanish – the single electron has a ‘many-body’ interaction with its *own* density. Thus, this formulation of E_{HA} includes an unphysical *self-interaction* energy. In combination with the unphysical symmetry of the wave-function, this makes the Hartree approximation highly inaccurate. On the other hand, the Hamiltonian is still that of the exact solution, making the Hartree approximation equally transferable, and its formal scaling is a comparatively very modest N^3 .

The Hartree ground state of a given Hamiltonian and basis set via the orbitals corresponds to a certain basis function coefficient matrix. In practice, this is found by

variation of the coefficients under iterative updates of the charge density, effective potential and wave-function, until a stationary point, corresponding to a *self-consistent* charge density, is found.

3.2. Hartree-Fock Theory

Faced with the limited accuracy of the Hartree approximation, V. Fock suggested⁹⁵ an extension of the Hartree approximation to a *non-classical mean-field* approximation of correct wave-function symmetry, but still satisfying the variational principle. This is achieved either by instead choosing a *single* Slater determinant as the Ansatz wave-function, or equivalently introducing the so-called *Fock operator* in Eq. (3.4). Thus, the previously sketched exact solution corresponds to minimizing \hat{H} in the set of all possible permutations of particles, or *configurations* of the Hartree-Fock wave-function, and is consequentially called *configuration interaction* (CI) in contemporary literature.

The ground state total energy E_{HFA} in the Hartree-Fock approximation (HFA) is

$$\begin{aligned} E_{\text{HFA}} &= E_{\text{HA}} - \frac{1}{2} \sum_{i,j=1}^N \int d^3\mathbf{r} d^3\mathbf{r}' \varphi_i^*(\mathbf{r}) \varphi_j^*(\mathbf{r}') |\mathbf{r} - \mathbf{r}'|^{-1} \varphi_i(\mathbf{r}') \varphi_j(\mathbf{r}) \\ &= E_{\text{HA}} + E_x \end{aligned} \quad (3.5)$$

Equation (3.5) illustrates an important point: An anti-symmetric wave-function is inverted in sign under particle permutation or *exchange*, giving rise to an additional *exchange interaction* energy E_x equal to the expectation value of the Fock operator. This interaction effectively repels identical fermions, leaving wave-functions of electrons with like spin strongly correlated. This correlation is a purely quantum mechanical effect, and completely neglected by the classical Hartree approximation. Furthermore, as a comparison of Equations (3.4) and (3.5) shows, E_x exactly cancels E_{H} when $i = j$: E_{HFA} is entirely self-interaction free.

E_{HFA} is typically, analogous to E_{HA} , calculated using an iterative *self-consistent field* (SCF) algorithm. Again, the BO Hamiltonian has not been modified, leaving the transferability of the Hartree-Fock method intact, and because of the additional many-body interactions computed, it scales as N^4 . The reward for this added computational effort is a substantially improved accuracy over Hartree theory – Hartree-Fock total energies typically recover on the order of 99 % of the exact BO ground state energies.

However, electronic wave-functions are also correlated by the instantaneous Coulomb interaction irrespective of spin. This weaker correlation is – given the nature of the exchange interaction somewhat unfortunately labeled the *correlation interaction* – neglected by *any* mean-field approximation. Therefore, just as the difference $E_{\text{HFA}} - E_{\text{HA}}$ defines the exchange energy E_x for a given Hamiltonian and basis set, the difference $E_{\text{BO}} - E_{\text{HFA}}$ defines the corresponding *correlation energy* E_c .

Unfortunately, while the Hartree-Fock method is sufficient for a qualitative discussion of many chemical problems, quantitative predictions of interesting properties typically

require an accuracy up to three orders of magnitude better than 1 % of the total energy. Therefore, current *ab initio* modeling typically uses so-called *post* Hartree-Fock techniques to add approximate correlation energies to E_{HFA} .

3.3. Post Hartree-Fock: MP2

The neglect of electronic correlation in Hartree-Fock can hand-wavily be described as the neglect of possible non ground-state configurations of the Hartree-Fock ground-state. Correspondingly, post Hartree-Fock methods can be classified by the level of such *excitations* at which they approximate electronic correlation. Since the correlation energy is a relatively small contribution to the total ground state energy a wide range of possibilities for approximations exist, e.g. by means of an additional excitation operator in so-called coupled-cluster (CC) theory⁹⁶, or as a low-order many-body perturbation theory (MBPT) expansion of the difference between the CI and HFA solutions.

However, even these by now well understood and refined solutions are still plagued by the immutably mutually exclusive good transferability, accuracy and scalability: While *ab initio* methods as discussed are highly transferable, the formal scaling of accurate low-order methods such as CCSD (CC with single and double excitations) or CCSD(T) (CCSD with triple excitations added perturbatively) is still prohibitively poor; N^6 and N^7 , respectively. Thus, if for example a CCSD(T) total energy of one benzene molecule takes a mere day with a given basis set and computational setup, calculating the corresponding dimer total energy requires more than two months of continuous runtime.

In this context, the second-order Møller-Plesset⁹⁷ (MP2) approximation (i.e. second-order Rayleigh-Schrödinger MBPT) offers a popular alternative: Arguably the oldest of all post Hartree-Fock (HF) models, it is well studied, very simple to implement, and scales as a modest N^5 . The MP2 total energy E_{MP2} is written as

$$E_{\text{MP2}} = E_{\text{HFA}} - \frac{1}{4} \sum_{aibj} \frac{((ai | bj) - (aj | bi))^2}{\varepsilon_a + \varepsilon_b - \varepsilon_i - \varepsilon_j} \quad (3.6)$$

where ε labels a HF orbital eigenvalue, indices a, b and i, j represent occupied and virtual HF orbitals, respectively, and using the integral notation convention

$$(ai | bj) = \int d^3\mathbf{r} d^3\mathbf{r}' \varphi_a^*(\mathbf{r}) \varphi_i^*(\mathbf{r}) |\mathbf{r} - \mathbf{r}'|^{-1} \varphi_b(\mathbf{r}') \varphi_j(\mathbf{r}') \quad (3.7)$$

The MP2 approximation has a few important disadvantages, however: First, its correlation approximation is *strictly* second order, neglecting higher order terms that *could* be expressed in terms of double or lower excitations, as opposed to e.g. CCSD⁹⁶. Such so-called *disconnected* excitations are important low-order correlation contributions in many systems. Second, the MP2 correlation energy is the lowest order in a perturbation expansion. As such, it fails to describe repulsive terms present at higher MP orders – MP2 generally overestimates the correlation energy, e.g. in π -stacked compounds^{98,99}. Third, Eq. 3.6 becomes *singular* in a metallic system (i.e. in which Hartree-Fock orbitals such that $\varepsilon_a = \varepsilon_b = \varepsilon_i = \varepsilon_j$ exist).

4. Density-Functional Theory

As explained, the goal of first-principles and *ab initio* theory can be described as the search for accurate, transferable and scalable approximations for the electronic exchange-correlation (xc) energy $E_{\text{xc}} = E_c + E_x$. While calculating accurate exchange energies is relatively simple, competitive post Hartree-Fock correlation models are generally tremendously costly or of limited accuracy or applicability.

Another approach descendant of Thomas-Fermi theory is *density-functional theory* (DFT). The following is but a rough sketch of the basics of DFT – the reader is referred to e.g. the excellent book by Dreizler and Gross¹⁰⁰ for a more comprehensive introduction. The idea of DFT is to rewrite the Schrödinger equation with the charge density $n(\mathbf{r})$ as the basic variable. Specifically, if there is a bijective correspondence between the Hamiltonian and the charge density, *every* observable of the ground-state quantum system can be calculated from the charge density *alone, regardless of how that charge density is obtained*. Since \hat{H} maps to a given ground-state wave-function $\varphi(\mathbf{r})$, from which the corresponding ground-state charge density $n_0(\mathbf{r})$ follows, the map $\hat{H} \rightarrow n_0(\mathbf{r})$ is trivially injective.

The existence of the inverse map was proved by Hohenberg and Kohn (HK) in 1964¹⁰¹. The proof has since been simplified and generalized by Levy¹⁰², and extended by Vignale and Rasolt¹⁰³. The discussion of the foundations of DFT also includes notable contributions of Langreth¹⁰⁴ and Görling¹⁰⁵. Specifically, the HK theorem states, that $n_0(\mathbf{r})$ uniquely defines \hat{H} and the corresponding (degenerate) ground-state wave-function(s) – the total energy of the system can be written as a *functional* of the wave-functions forming $n_0(\mathbf{r})$. This functional satisfies the variational principle – its minimum under arbitrary wave-function variations corresponds to the exact Born-Oppenheimer ground state total energy E_{BO} . The DFT total energy E_{DFT} is written as

$$E_{\text{DFT}} = T_0[n] + E_{\text{ext}}[n] + E_{\text{H}}[n] + E_{\text{xc}}[n] \quad (4.1)$$

where the terms of Eq. (3.4), here explicitly written as functionals of the density, are added to an xc-functional $E_{\text{xc}}[n]$ describing all exchange- and correlation effects and the difference of the kinetic energy functionals of fully-interacting and non-interacting electrons. If \hat{H} can be described by a unique effective single-particle potential (mean field), i.e. it is *v-representable*, then the exact ground state density can be obtained from a local such single-particle potential corresponding to the external and Hartree potentials added to the *functional derivative*

$$v_{\text{xc}}(\mathbf{r}) = \frac{\delta E_{\text{xc}}[n_0]}{\delta n(\mathbf{r})} \quad (4.2)$$

It has been shown¹⁰⁶, that the condition of v -representability is fulfilled by any physical charge density on a lattice (see also Levy's discussion¹⁰²).

As stated, *how* $n_0(\mathbf{r})$ is obtained is not important. The most commonly – and in this work exclusively – employed approach was suggested by Kohn and Sham¹⁰⁷, and amounts to calculating E_{DFT} analog to E_{H} , as the sum of single-particle eigenvalues via an iterative SCF procedure in which the charge density is expanded in a basis set (cf. Eq. (3.4)). Kohn-Sham DFT is thus well characterized as a form of constrained Hartree theory¹⁰⁸.

DFT has several considerable advantages over wave-function techniques: With standard current functional approximations, it is generally considerably more accurate than Hartree-Fock theory. Since E_{xc} is not directly derived from a wave-function, it is not subject to the limitations of single-determinantal wave-functions in e.g. post Hartree-Fock methods (despite surprisingly pervasive myths to the contrary¹⁰⁹). For the same reason, the DFT E_{c} does not depend on virtual orbitals, making DFT relatively basis-set insensitive, and correspondingly numerically efficient. Like Hartree theory, DFT formally scales as N^3 , which with modern numerical technology often can be lowered considerably, in several current implementations all the way to *linear* (N) scaling.

The greatest disadvantage to DFT is the unknown form of the exact xc-functional: While DFT as stated is exact given the right 'constraints', the xc-functional must in practice always be approximated in some way. Non-empirical such approximations usually correspond to well-known model systems. Thus, by way of v_{xc} , DFT in practice effectively modifies the Hamiltonian with information specific to a given system and as such is only conditionally transferable, in contrast to the *ab initio* methods described above.

Another obvious deficit of DFT is self-interaction (SI), from which it generally suffers in much the same way as Hartree theory (except of course when modeling systems for which the xc-functional approximation is exact). The SI error (SIE) causes electrons to spatially delocalize, compared to the exact solution. Specifically, the derivative of the total energy with respect to a continuous occupation number is in DFT a smoothly varying, continuous function¹¹⁰, in contrast to the discontinuity implied by the discrete contributions of individual electrons to a physical wave-function.

As will be discussed in chapter 6, this delocalization error leads to unphysically small fundamental bandgaps in DFT using (semi-)local xc-functionals. The prediction of dissociation barriers, for which an accurate description of small charge differences is paramount, is another typical problem case.

4.1. Density Functional Approximations

Lacking the inherent systematicity of *ab initio* theory, the development of new DFT xc-functional approximations can at best produce models more transferable and accurate than those already in existence. Perdew et al.^{111,112} have – somewhat tongue-in-cheek – popularized this endeavor as the 'Jacob's ladder' of xc-functional approximations. The idea is, that each 'rung' of the ladder introduce a new set of possible constraints on

4.1. DENSITY FUNCTIONAL APPROXIMATIONS

some physical quantity, e.g. the charge density, its gradient, the kinetic energy density, the orbitals, non-local contributions to E_{xc} , etc. These constraints are then adapted to fulfill known physics, e.g. high- and low-density limits, restrictions on density variations, properties of model systems and so on. The actual performance and transferability of such parametrizations is in practice determined heuristically. As the scope of the following only focuses on the density functional approximations actually employed in this thesis, the reader is referred to the review by Scuseria and Staroverov¹¹³ for more detail.

The Jacob’s ladder rests on the ‘ground’ of Hartree theory ($E_{xc}[n] = 0$). The first rung is represented by the *local density approximation* (LDA)

$$E_{xc}^{\text{LDA}}[n] = \int d^3\mathbf{r} n(\mathbf{r}) \epsilon_{xc}^{\text{HEG}}(n(\mathbf{r})) \quad (4.3)$$

where $\epsilon_{xc}^{\text{HEG}}$ is the xc-energy of a homogeneous electron gas. The LDA is strictly local in space, and is exact in the limit of slowly varying densities (albeit in practice limited by the accuracy with which $\epsilon_{xc}^{\text{HEG}}$ can be determined).

The next rung is represented by the so-called *generalized gradient approximation* (GGA)

$$E_{xc}^{\text{GGA}}[n] = E_{xc}^{\text{LDA}}[n] + \int d^3\mathbf{r} \Delta\epsilon_{xc}(n, |\nabla n|) \quad (4.4)$$

where $\Delta\epsilon_{xc}(n, |\nabla n|)$ is an xc-energy gradient correction dependent on the local density n , and the local reduced density gradient ∇n . Thus, the GGA is semi-local, rather than strictly local.

The third rung is represented by *meta*-GGAs, xc-functionals dependent on the charge- and *kinetic energy* densities and -gradients. The fourth rung applies the Fock operator (cf. Eq. (3.5)) to mix non-local *exact exchange* density in a GGA or meta-GGA, resulting in so-called *hybrid* xc-functionals. Just as Hartree-Fock theory eliminates the self-interaction in the Hartree approximation, hybrid functionals eliminate a fraction of the self-interaction present in the (semi-)local approximation on which they are based, depending on the exact-exchange mixing coefficient. This is a significant advantage in many systems, in particular light organic molecules.

The specific xc-functionals used in this thesis are the LDA parametrized by Perdew and Zunger¹¹⁴ to Quantum Monte Carlo calculations of a homogeneous electron gas by Ceperley and Alder¹¹⁵, the GGA parametrized by Perdew, Burke and Ernzerhof^{116,117} (PBE), and the hybrid B3LYP and PBE0 functionals. Whereas the performance of the first is as indisputable as it is remarkable for metallic solids, LDA generally does not perform well for light molecules (e.g. for heats of formation¹¹³).

The second is the currently most popular GGA parametrization. A GGA cannot by construction simultaneously fulfill known exact constraints on electron-gas like solids and free-atom exchange interactions¹¹⁸. Still, PBE performs substantially better than the LDA for most properties of light molecules^{118–120}, and approximately as well for solid state calculations.

B3LYP has a peculiar history¹¹³: Following a proposition by Becke¹²¹ to remedy difficulties in the description of sparse matter (e.g. thermochemical reactions) with a local exchange functional Stephens et al.¹²² (in an inconspicuously titled publication) replaced an amount, determined by semi-empirical fitting to reference data for properties of organic molecules, of LDA exchange with non-local Fock exchange, in combination with the correlation functional of Lee, Yang and Parr¹²³.

The `Gaussian 03`¹²⁴ code saw the first implementation of this functional, which subsequently came to be its very definition¹¹³. Unsurprisingly, the performance of B3LYP is generally outstanding for systems similar to its defining fitting set, i.e. light molecules, and this functional initially attained considerable acclaim in the quantum chemistry community. More recent work¹²⁵ has highlighted its weaknesses, however.

In contrast, the design of PBE0^{126,127*} aims to improve upon PBE at short range while leaving its longer-range form (specifically the correlation functional), and thereby its generally favorable performance, intact. The exact-exchange mixing coefficient of 0.25 was chosen based on a non-empirical argument based on the adiabatic connection formula¹²⁸ (but is notably similar to the semi-empirically determined B3LYP value of 0.20).

4.2. Time-Dependent DFT

The generalization of DFT to time-dependent systems (TDDFT) is exploited for the calculation of UV/Vis spectra in chapter 6. This is an extremely rich topic, which again here only will be covered in the bare minimum of detail. The reader is referred to e.g. the introduction by Marques and Gross¹²⁹, or any of the several available review papers^{130–132} for greater depth.

In strict analogy to the HK theorem for a time-independent system, Runge and Gross showed¹³³, that in the case of a finite system, the properties of a time-dependent quantum system are uniquely defined by a time-dependent density $n(\mathbf{r}, t)$, in turn defined by the quantum mechanical action $A[n(\mathbf{r}, t)]$. As complicated an object as an exact, universal xc-functional $E_{xc}[n]$ must be, this action must be more esoteric still – knowledge of the true $A[n(\mathbf{r}, t)]$ implies knowledge of *all* properties of a finite quantum mechanical system, including the exact many-body interactions.

$A[n(\mathbf{r}, t)]$ defines the exchange-correlation (xc) *kernel* f_{xc} , corresponding to the functional derivative

$$f_{xc}[n](\mathbf{r}t, \mathbf{r}'t') := \frac{\delta v_{xc}[n](\mathbf{r}t)}{\delta n(\mathbf{r}t)} \quad , \quad (4.5)$$

*In some literature alternatively labeled 'PBE1PBE' or 'PBEh'.

which can be used to calculate the exact linear response function¹³⁴

$$\begin{aligned} \chi(\mathbf{r}t, \mathbf{r}'t') = & \chi_0(\mathbf{r}t, \mathbf{r}'t') + \int d^3\mathbf{x} d^3\tau d^3\mathbf{x}' d^3\tau' \chi_0(\mathbf{r}t, \mathbf{x}\tau) \\ & \cdot \left(\frac{\delta(\tau - \tau')}{|\mathbf{x} - \mathbf{x}'|} + f_{xc}[n_0](\mathbf{x}\tau, \mathbf{x}'\tau') \right) \chi(\mathbf{x}'\tau', \mathbf{r}'t') \quad , \end{aligned} \quad (4.6)$$

where χ_0 is the response function of non-interacting particles, and f_{xc} is evaluated at the ground-state charge density n_0 . In turn, the exact ground state total energy can be obtained as an integral over the exact response function¹³⁵.

In practice, just as the xc-functional in time-independent DFT, the exact xc-kernel in TDDFT is unknown, and must be approximated. A currently popular model for total energy calculations is the so-called *random phase approximation*^{136,137} (RPA), corresponding to the special case of $f_{xc}[n](\mathbf{r}t, \mathbf{r}'t') = 0$ (i.e. the Hartree density-density response).

Since the exact response function has poles ('blows up') at the exact resonant excitation energies of the system, an approximation of f_{xc} implies an approximation of all excitation energies. The Dyson-like Eq. (4.6) can be rewritten as a set of eigenvalue equations in the frequency domain, yielding predictions of the true excitation energies and corresponding oscillator strengths of the system. These can in turn be solved iteratively when reformulated as the so-called Casida's equations¹³⁸⁻¹⁴⁰.

Reminiscent of the Jacob's ladder of xc-functional approximations, TDDFT calculations of resonant excitation energies typically employ the next simplest (or 'first rung') f_{xc} -approximation after the RPA – the adiabatic LDA^{131,141} (ALDA). In the ALDA, the frequency-dependence of f_{xc} is simply ignored; the kernel has no 'memory', in contrast to the exact f_{xc} . The spatial part is treated within the standard LDA. The calculations detailed in chapter 6 approximate resonant excitation energies by means of Casida's equations and the ALDA.

5. Basis Sets

At the heart of all *ab initio* methods and Kohn-Sham DFT lies the basis set, and much of the technical detail discussed in the appendices is related to the different basis set techniques used in this thesis. Just like the ideal total energy method for a given problem, the optimal basis set in practice always represents a particular balance between accuracy, transferability and scalability: While there trivially always exists an exact and numerically optimal basis set for given wave-function – corresponding to the exact eigenstates of the system – this basis set is not transferable, and its use requires prior knowledge of the exact wave-function.

Thus, one can in general practice either i) construct a basis set as a small group of functions accurately describing typical wave-function for a given range of systems, at the cost of universal transferability, or ii) choose a universally transferable set of functions spanning all of Hilbert space, at a potentially substantial loss of numerical efficiency for certain systems. These two approaches are well represented by two of the most commonly – and also in this thesis – employed basis set forms, namely atom-centered gaussians and plane-waves, which are cursorily described below. In this as in the previous chapters, standard derivations have largely been left out in the interest of brevity. The reader is referred to the excellent introductions by Young¹⁴² and Meyer¹⁴³ for greater detail.

5.1. Gaussian Basis Sets

In general, the usefulness of a basis set is wholly determined by its systematic improvability and numerical efficiency for a given class of problems. With *analytical* basis functions in particular, necessary integrals can often be derived and rewritten on easily evaluated forms. In modern quantum chemical calculations, atomic orbitals φ are most commonly expanded in sets of gaussian functions on the form

$$\varphi = Y_{lm} \sum_i C_i \sum_j c_{ij} e^{-\zeta_{ij} r^2} \quad , \quad (5.1)$$

where the spherical harmonic Y_{lm} defines the angular momentum of the orbital, the expansion coefficients C_i are optimized with respect to the total energy, and the *contraction* coefficients c_{ij} are kept fixed. Each such contraction can contain primitive gaussians $e^{-\zeta_{ij} r^2}$, where r is the radial distance to the atomic nucleus, of a single or several exponents ζ ('zetats'). Thus, a given gaussian basis set is defined by its contraction coefficients, and can be ranked with respect to other sets in terms of the number of different zetats (i.e. degrees of variational freedom, roughly corresponding to accuracy and computational cost) it includes.

Gaussian basis sets are typically constructed to describe a range of model wave-functions based on neutral atoms and ions, with a sufficient variation in the localization of functions (i.e. 'polarized' vs. 'diffuse' functions) covering common valence wave-function shapes in between. As explained above, designing a transferable yet accurate gaussian basis set is difficult, and the quantum chemical publication record is conspicuously dominated by a mere few gaussian basis set families.

In addition to their analytical form, gaussian basis functions being referenced to atomic coordinates minimizes computational effort, since the typical spatial extent of the wave-function is matched by that of the basis set. However, precisely these circumstances can also be described as weaknesses of gaussians: Describing the rapid variation or 'hardness' of the radial cusps near the atomic nucleus in orbitals of higher angular momenta often requires very large expansions in analytical functions, reducing either computational efficiency or accuracy of the core-state description.

In quantum chemistry, molecular wave-functions are usually written as linear combinations of atomic orbitals (LCAO). This is often a very efficient choice, since a molecular wave-function often closely resembles that of the sum of its constituent atoms. However, since the atomic orbital basis is referenced to the coordinate of the nucleus of the corresponding atom, the total energy of an arbitrary fragment of a molecular wave-function depends on the basis set geometry. For example, the minimized total energy of an oxygen atom expressed in its own basis functions, is higher than that of the same atom minimized in the basis set of the oxygen molecule – the functions centered on one atom superpose on those of the other, and by the variational principle lower the contribution of either atom to the molecular total energy. This so-called basis set superposition error (BSSE) is a finite-basis artifact, and must be corrected for in e.g. molecular binding energy calculations.

5.2. Plane-waves and Pseudopotentials

A plane-wave is obviously the perfect basis function for describing a free-electron wave-function. It is also the exact eigenfunction of a homogeneous electron gas, and the standard method for periodic boundary condition (PBC) calculations of crystalline solids.

In such a calculation, three lattice vectors defining the real-space periodicity of the system are chosen. An electron moving in this crystal will experience an effective single-particle potential of the same periodicity. The Fourier series of this potential has a simple form in terms of the vectors \mathbf{G} defining the *reciprocal* lattice, i.e. the Fourier transform of the real-space lattice. Now, Bloch's theorem (see e.g. Ashcroft & Mermin¹⁴⁴ p. 133f) states, that any eigenfunction ψ of a periodic potential can be written as a plane-wave of a given wave vector \mathbf{k} , multiplied by some function u with the periodicity of the lattice, i.e.

$$\psi_{\mathbf{k}}(\mathbf{r}) = e^{i\mathbf{k}\mathbf{r}} u_{\mathbf{k}}(\mathbf{r}) \quad . \quad (5.2)$$

Therefore, under consideration of all possible \mathbf{k} 's, the full wave-function of an arbitrary and arbitrarily extended wave-function in the crystal, is wholly defined by a single period

5.2. PLANE-WAVES AND PSEUDOPOTENTIALS

of u . Put differently, if \mathbf{k} -space can be adequately sampled, it is sufficient to solve for the wave-function in the central cell only. Being periodic in the reciprocal lattice, u can in turn be expanded in plane-waves with wave-vectors of the set \mathbf{G} , yielding the final eigenfunction form of

$$\psi_{\mathbf{k}j}(\mathbf{r}) = \sum_{\mathbf{G}} C_{\mathbf{G}}^{\mathbf{k}j} e^{i(\mathbf{k}+\mathbf{G})\mathbf{r}} \quad (5.3)$$

where j is a band index and $C_{\mathbf{G}}^{\mathbf{k}j}$ are expansion coefficients (cf. C_i of Eq. (5.1)). A basis set on the form (5.3) is still infinite in two ways, namely due to the infinitely many possible wave-vectors \mathbf{k} , and the infinitely many combinations $(\mathbf{k} + \mathbf{G})$ of a given \mathbf{k} with the infinite set of \mathbf{G} vectors. The first is addressed by sampling the symmetry-irreducible wedge of \mathbf{k} -space – also known as the irreducible *Brillouin zone* – with a systematically improvable discrete grid.

Finally, a finite basis set is obtained by noting that – hand-wavingly described – the fastest spatial variation in the wave-function corresponds to a shortest necessary wave-vector $(\mathbf{k} + \mathbf{G})$. Put differently, the more spatially localized the wave-function is, the more plane-waves of different wave-vectors are necessary for its expansion (which the astute reader will recognize as an analogue of Heisenberg’s famous uncertainty relation). The reverse implication is, that a sufficiently \mathbf{k} -sampled arbitrary wave-function to arbitrary accuracy can be described by plane-waves defined by a finite set of combinations $(\mathbf{k} + \mathbf{G})$, in turn defined by maximal plane-wave kinetic energy E_{cut} :

$$\frac{1}{2} |\mathbf{k} + \mathbf{G}|^2 \leq E_{\text{cut}} \quad (5.4)$$

Plane-waves have a number of advantages over atom-centered basis sets: They are by construction orthonormal, and systematically approaching the complete basis set limit requires no ‘design’ of the basis set – simply raising E_{cut} and sampling \mathbf{k} -space with a denser grid is sufficient. Since plane-waves are referenced to the simulation cell rather than the atomic coordinates, a total energy expressed in plane-waves is BSSE free, which also greatly simplifies the evaluation of Hellmann-Feynman¹⁴⁵ forces.

However, the number of plane-waves defined by a typical cutoff and \mathbf{k} -grid is large, often an order of magnitude larger than for a comparable gaussian basis set. In particular, the problem of radial cusps in higher-angular momentum wave-functions is much more dramatic in a plane-wave basis set than in a gaussian basis set. Therefore, core-states in plane-waves are normally either a) described by an additional, strictly localized atom-centered basis set (e.g. in the all-electron FP-LAPW technique), or b) implicitly represented by a so-called pseudopotential. All plane-wave calculations of this thesis employ the latter approach.

The main justification for the use of pseudopotentials is, that molecular properties of interest usually depend strongest on the characteristics of the valence wave-function – the core-states in a molecule or solid usually differ little from those of the corresponding free atom. Thus, the wave-function near the nucleus can to good approximation be represented by a smoothly varying, soft, and consequentially by few plane-waves well-

described wave-function multiplied by a fixed projector function introducing the correct (atomic) core-state character. Practical consequences of the resulting so-called *frozen core* approximation are discussed in context in appendix B. The plane-wave expansion of a molecular wave-function in the valence region is generally relatively sparse, and can be treated without further simplification.

A number of recipes for the construction of pseudopotential projector sets from *ab initio* atomic wave-functions exists. In general, they all aim to match the all-electron and resulting pseudo wave-functions outside a given pseudization radius r_c , and as far as possible preserve the all-electron Kohn-Sham eigenvalues and general scattering properties in the pseudo-wavefunction. Additionally, the most popular potential form of a few decades ago, so-called *norm-conserving* pseudopotentials, requires the norm of the pseudo- and all-electron wave-functions integrated over r to match. This ensures a simple albeit relatively hard pseudopotential.

The pseudopotentials used in this thesis are of the so-called *ultrasoft*^{146,147} variety, in which the norm-constraint is relaxed in favor of a generalized eigenvalue formalism. The advantage to this form is a substantially softer potential requiring much smaller plane-wave basis sets. The downside is a much more complicated potential and (pseudo) total energy evaluation. In particular, eigenstates of ultrasoft pseudopotentials are only orthonormal with respect to the projector overlap matrix (much like an atom-centered basis set). This complicates operations on the wave-function such as the projections detailed in section 7.1.

Part II.

Surface-Decoupled Switches

6. Azobenzene-Functionalized Self-Assembled Monolayers

In this chapter, aliphatic self-assembled monolayers (SAMs) functionalized with azobenzene switches are studied using a variety of experimental spectroscopy techniques supported by ground state and time-dependent DFT calculations, as a collaboration within Sonderforschungsbereich (SFB) 658 of the Deutsche Forschungsgemeinschaft (DFG). The experiments and extended dipole model calculations (see section 6.5) have been carried out chiefly by Roland Schmidt and Dr. Cornelius Gahl in the research group of Prof. Dr. Martin Weinelt at the Max-Born-Institut in Berlin. The (TD)DFT calculations have been performed by ERM. Consequentially the following focuses narrowly on the contributions of theory, and their experimental context. The reader is referred to the corresponding publications^{I,II} for a more complete picture.

Aliphatic SAMs, and in particular alkanethiolate SAMs, are promising candidates for an azobenzene - substrate spacer ligand able to completely decouple the sensitive chromophore moiety from the surface electronic structure, without loss of order in the molecular over-layer. In the following, we study self-assembled monolayers of 4-trifluoromethyl-azobenzene-4'-methylenoxy-*n*-alkanethiols, i.e. azobenzene (Az) in the one para position (4, see Fig. 6.1, cf. Fig. 1.1) via an oxygen atom bound to an alkane chain of *n* methylene groups terminated by a thiol group (Az*n*), and in the other para position (4') functionalized with a CF₃ or trifluoro (TF) group (TF-Az*n*). As will be shown, evidence indicates that this compound deposited at an Au(111) surface nicely self-assembles. With the alkane chains 'standing' on the thiol group bound to the substrate, the azobenzene moieties are left ordered upright on top of the SAM, with the TF group pointing away from the surface. However, as explained in chapter 2, simpler alkanethiol / azobenzene combinations do not switch by light irradiation, which also is the case here. Understanding why is crucial for the future design of azobenzene-functionalized SAMs, and forms the main goal of this chapter.

The low to zero switching yield in these systems has already been attributed to a lack of free volume for the photo-induced motion^{83,84,86}. While this is a tempting, intuitively mechanical explanation, switching in Az6 SAMs has been successfully induced by STM-

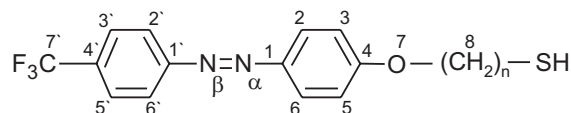


Figure 6.1.: Structural formula of the TF-Az*n* molecule, with labeled carbon and nitrogen atoms.

tip bias voltage ramping¹⁴⁸, similar to the case of pure azobenzene directly adsorbed at Au⁴⁸. This suggests that aspects of the *geometric* structure alone do not exhaustively explain the phenomenon – a more comprehensive picture, including features of the *electronic* structure, is required. In the following, it will be shown that azobenzene chromophores in a close-packed structure influence each other strongly by excitonic coupling. This leads to energetic shifts, narrowing and suppression of optical absorption lines, and delocalization of the excitation within the SAM, which is expected to strongly contribute to the suppression of the photo-isomerization reaction.

The contributions of this thesis work to the experimental collaboration have been significant in three key areas: First, the electronic structure of the azobenzene-functionalized SAMs were characterized by means of X-ray absorption spectroscopy (XAS), and near-edge X-ray absorption fine structure (NEXAFS), supported by DFT calculations. These results are presented in section 6.2.

Second, section 6.3 details the characterization of the SAM geometric structure by means of NEXAFS supported by DFT and TDDFT calculations. Finally, based on the TDDFT-predicted transition dipole moments (TDMs), the shifts observed in measured UV/Visible (UV/Vis) spectra of the SAM are modeled within an extended dipole model¹⁴⁹.

6.1. Theoretical Modeling of Pure Azobenzene

Before presenting these results however, an appropriate level of theory must be thoroughly established. In first-principles and *ab initio* simulations, this amounts to two fundamental choices, namely those of a model system of sufficient relevance for the actual system of interest (e.g. the molecule / solid), and a model chemistry (e.g. electronic structure method and basis set). Beginning with the former it is noteworthy, that for a sufficient chain length, very little to no charge transfer from opposite end-group to substrate occurs in nitrile-functionalized alkanethiolate SAMs, as shown by Feulner et al.¹⁵⁰.

Consequentially, for a TF-Azn compound of intermediate to long chain length n , the influence of the substrate electronic structure on the chromophore moiety can be expected to be small. Furthermore, while as stated intermolecular coupling plays an important role in the quenching of excited states in the SAM molecules, their geometry and general electronic structure are strongly dominated by intra-molecular interactions. Therefore, the theoretical model is here restricted to single, gas-phase molecules, neglecting effects of switch-switch and switch-substrate interactions.

Choosing a sufficient model chemistry is more involved: In addition to accurate molecular geometries and molecular distortion energies, calculations of resonant excitation energies are necessary. For the former, DFT often performs remarkably well at very modest computational cost, but for the latter, the usually most systematically accurate and transferable electronic structure methods (e.g. coupled-cluster (CC) theory) are hardly computationally tractable even for a small- to medium-sized system like the TF-Azn molecule.

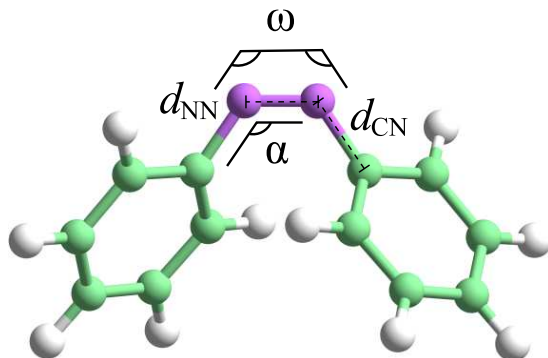


Figure 6.2.: The azobenzene cis isomer seen from the side, with the CNNC dihedral angle ω , the CNN bond angle α , and the NN and CN bond lengths d_{NN} and d_{CN} marked.

Here, the time-dependent density-functional response theory¹⁵¹ (TD-DFRT) formulation of time-dependent density-functional theory (TDDFT, see section 4.2) offers a powerful, albeit esoteric alternative: In the words of its greatest contributor, TDDFT – while in principle able to exactly calculate all excitation energies in a finite system¹³⁰ – similar to the ground-state DFT formulation,

“... has the advantage of computational speed, allowing study of larger systems than with traditional methods, and the usual disadvantage (or excitement) of being unsystematic and artful.”¹³¹

Put differently, while TD-DFRT calculations of our model molecule are computationally viable, the method is known to fail dramatically for certain systems¹⁵², and its predictive quality for the present case remains to be established. No literature on the specific TF-Azn compound exists, but given the close relationship between the electronic structures of TF-Azn chromophore moiety and pure azobenzene, the level of theory can be verified for the latter, on which a wealth of reference information is available.

All calculations described in the following were performed with the `Gaussian 03`¹²⁴ and `NWChem`¹⁵³ quantum-chemistry packages, using analysis tools of own creation. In all calculations the all-electron def-TZVP basis set¹⁵⁴ (see discussion in appendix A, section A.1) was used. Ground-state geometries are predicted by iterative minimization of Hellman-Feynman forces, with `Gaussian 03` and `NWChem` using the Broyden algorithm¹⁵⁵ and a quasi-newton algorithm with line searches, respectively.

The effects of the choice of xc-functional approximation on properties of interest remains to be established. Here, three different classes of xc-functionals are studied, namely the LDA¹¹⁴, the GGA in the PBE^{116,117} parametrization, and the B3LYP hybrid xc-functional (see section 4.1).

In Table 6.1, four characteristic geometry parameters as defined in Fig. 6.2 and optimized at all levels of theory are compared to reference theoretical and experimental data. The parameters are the CNNC dihedral angle ω , the CNN bond angle α , the NN bond length d_{NN} , and the CN bond length d_{CN} . Note that the two possible definitions of the latter three are equal by the C_2 symmetry.

		LDA	PBE	B3LYP	MP2 ¹⁵⁶	CASSCF ³⁰	Exptl. ^{12,13}
Trans	α ($^\circ$)	115	115	115	114	115	114
	ω ($^\circ$)	180	180	180	180	180	180
	d_{NN} (\AA)	1.25	1.27	1.25	1.27	1.24	1.25
	d_{CN} (\AA)	1.40	1.42	1.42	1.42	1.42	1.43
Cis	α ($^\circ$)	123	124	124	122	123	122
	ω ($^\circ$)	12	11	9	8	4	8
	d_{NN} (\AA)	1.24	1.25	1.24	1.25	1.24	1.25
	d_{CN} (\AA)	1.41	1.43	1.44	1.45	1.44	1.43

Table 6.1.: Azobenzene geometry parameters as defined in Fig. 6.2, optimized with various xc-functionals, compared to literature values of other levels of theory, and given by X-ray crystallography experiments.

The (semi-)local functionals perform well for the azobenzene geometry: Here calculated values of all studied parameters in Table 6.1 compare excellently to more accurate levels of theory and experiment, for all three functionals. Notably, the trans isomer is in all cases perfectly planar, with an ω dihedral angle of 180 degrees, in agreement with higher-level theoretical calculations⁴³.

In Table 6.2, a similar comparison of the vertical excitation energies E_i of the three lowest singlet excitations, calculated in the corresponding ground-state DFT geometry, by solving for the poles of the TD-DFRT dynamic linear response function within the adiabatic LDA^{131,141} (ALDA, see section 4.2) approximation of the exchange-correlation kernel (f_{xc}). As an additional measure of obvious importance for the gas-phase thermal distribution of isomers, the readily obtained cis-trans total energy difference, or relative isomer stability $\Delta E_{\text{C-T}}$ is compared.

In this test, the (semi-)local LDA and GGA functionals fare considerably worse: Beginning with the latter quantity one notes, that since the correlation expressions of all tested functionals are local in space, thereby largely neglecting long-range, dispersive van der Waals interactions (see initial discussion in chapter 8), the denser cis isomer should, given an xc-functional otherwise exact in the medium to short range, be under-stabilized with respect to experiment. That is, the calculated DFT $\Delta E_{\text{C-T}}$ should be larger than the experimentally measured. This is true for B3LYP, and consistent with its generally improved description of molecular properties over (semi-)local functionals. In the GGA long- and short range errors cancel, almost reproducing the experimental number. In the LDA this trend worsens, leaving the cis isomer *over*-stabilized.

The (semi-)local functionals are outperformed by the hybrid also in the calculation of resonant excitation energies. B3LYP generally shows an underestimation of a few hundred meV, comparable to or closer to the experimental value than the overestimation

6.1. MODELING OF PURE AZOBENZENE

		LDA	PBE	B3LYP	CCSD ¹⁵⁶	Exptl.
Trans	E_1	2.09	2.19	2.56	2.95	2.79 ¹⁵⁹
	E_2	3.41	3.39	3.72	4.36	3.95 ¹⁵⁹
	E_3	3.52	3.49	4.08	4.62	-
Cis	E_1	2.15	2.30	2.56	3.17	2.88 ¹⁵
	E_2	3.45	3.43	4.14	4.67	4.4 ¹⁶⁰
	E_3	3.57	3.57	4.23	4.83	-
ΔE_{C-T}		0.58	0.61	0.68	^a 0.65 ³¹	0.6 ¹⁴

Table 6.2.: Comparison between theory and experiment of the three lowest vertical singlet excitation energies in azobenzene. ^aMultistate CAS second-order perturbation theory (MSPT2). All numbers in (eV).

given by CC theory with single and double excitations (CCSD, see section 3.3). The LDA and GGA functionals underestimate excitation energies by roughly twice the error in the B3LYP calculations. The reason for this is found in the ground-state Kohn-Sham eigenvalues given by the different functionals:

Differences of virtual and occupied Kohn-Sham eigenvalues form the zeroth order approximation to the corresponding TD-DFRT resonant excitation energies¹³⁰, analogous to general extensions¹⁵⁷ of DFT to treatment of excited states. Inclusion of non-local, Fock-type exchange in a functional significantly reduces the well-known delocalization error in DFT¹¹⁰ (see chapter 4), in turn improving the fundamental band-gap¹⁵⁸ width (i.e. the difference between the ionization potential and electron affinity), which is notoriously underestimated by (semi-)local functionals.

Thus, hybrid functional HOMO - LUMO gaps are larger than those of (semi-)local functionals, and this increase carries over to other possible virtual - occupied Kohn-Sham eigenvalue differences in the system. Consequentially, TD-DFRT/B3LYP resonance energies for azobenzene are very competitive, in line with the findings of other workers^{31,87}.

However, the multi-tiered approximations implied by combining constraints of linear response and an f_{xc} local in time and space, come at the price of the possibility, that this performance is a simply an artifact due to fortuitous cancellation of errors, in which case theoretical predictions remain questionable. The fundamental approximation of linear response limits the applicability of TD-DFRT in this form to weak fields. However, since 'weak' in this context means on the scale of the atomic potential, linear response TD-DFRT is justifiable for modeling of optical excitations of all but the most powerful laser fields¹³⁰, which poses no limitation for the present work.

The form of the ALDA f_{xc} has two major consequences: First, the time-locality (or adiabaticity) implies, that the frequency-dependence of this kernel approaches the true dependence only in the low-frequency limit. Second, density-functional potentials at long

range generally* decay faster than the known exact asymptotic $1/r$ form. An f_{xc} with a spatial form derived from such an xc-functional (e.g. in ALDA) inherits this problem, and underestimates energies of the high-lying bound excited (Rydberg) states^{139,151}. Both circumstances have the consequence, that TD-DFRT/ALDA is best physically motivated for the very lowest lying resonances. Furthermore, a strongly polarized basis set like def-TZVP, while numerically efficient and accurate for ground state properties, cannot be expected to describe the with energy rapidly increasing diffuseness of higher lying virtual orbitals, which enter the response function description.

The spatial decay of f_{xc} can be corrected, e.g. by splicing on a $1/r$ potential^{151,162} with a given vertical shift, or semi-empirically¹⁶³. Tests of these methods, in combination with a more diffuse basis set, reveal no variations in the resonance energies or TDM magnitudes of interest (see appendix A section A.2). In light of the thereby well-established favorable performance of B3LYP, all further calculations described in this chapter use this functional.

On a side note, the use of TD-DFRT to calculate optical excitation energies is here restricted to the lowest lying states, in line with the above reasoning. Higher energy XAS resonances are in the following exclusively discussed and assigned in terms of ground-state Kohn-Sham orbitals and thereof derived chemical shifts, foregoing an explicit treatment of excitonic effects. However, typical X-ray field strengths being well within the realm of linear response, there is no formal reason why the TD-DFRT/ALDA formalism *couldn't* be applied also to XAS energies, with an accuracy potentially comparable to that observed for azobenzene above: The TD-DFRT/ALDA prediction of a low-energy XA transition, is subject to virtually the same deficiencies of the f_{xc} spatial form as a UV/Vis transition. The remaining hurdle to an accurately predicted, high resonance energy is the temporal non-locality of the true f_{xc} , implying an unknown frequency dependence at the relevant resonance energy, which *can*, but *must not necessarily* be strong – whether the adiabatic approximation works also at the given energy in the given system, would remain to be found out by comparison to reference data, analogous to the case of UV/Vis spectrum simulations.

6.2. Electronic Structure

In this section, the electronic structure of a pure SAM of n -methylene group alkanethiol molecules (Cn), and the switch compound with (TF- Azn) and without (Azn) the TF group, is characterized focusing on core-level chemical shifts (CLS) and deduced excitonic effects.

Core-level spectroscopy is a very powerful technique for surface adsorbed molecules¹⁶⁴, since unambiguously assigned chemical shifts of core electronic states are highly characteristic of the bonding of the corresponding atom, potentially offering a unique fingerprint of a given adsorbate, substrate and adsorption geometry.

*With the exception of functionals explicitly constructed to remedy this problem, e.g. LB94¹⁶¹, or consisting of 100% Fock exchange, e.g. the exact-exchange (EXX) or Hartree-Fock potentials.

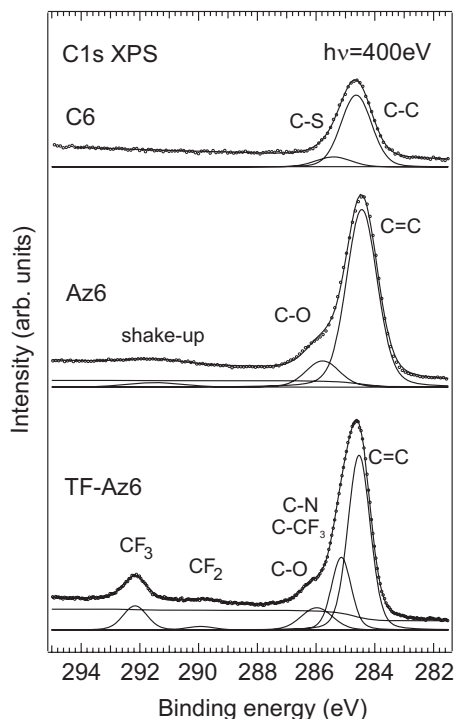


Figure 6.3.: C 1s XPS spectra of C6, Az6, and TF-Az6, with peaks deconvoluted and assigned to molecular moieties (see text).

However, as little to no geometrical information is provided by standard X-ray spectroscopy techniques *per se*, the assignment of observed shifts to given atoms, particularly when many atoms of the same element are present, can be difficult. This is where theoretical calculations are useful; within a theoretical model the geometry information is complete, and if experimentally observed shifts can be plausibly reproduced by theory, their interpretation and assignment to geometrical features is much simplified.

Core-level shifts can be described as composed of two parts: The first is a large shift of the occupied core level, predominantly due to the nearest-neighbor bonding of the core-ionized atom. By Koopmans' theorem¹⁶⁵, this so called initial-state shift is the full core-level shift described by Hartree-Fock theory^{166,167}.

The second part is due to the fact that X-ray spectroscopy, like spectroscopy techniques in general, by construction does not probe the ground state: The emitted (or resonantly excited) photo-electron 'sees' a screened 'hole' in the core level, rather than the ground state occupied level. In an exact theoretical treatment of the excited state, this final-state shift is manifested as a small positive correction to the Hartree-Fock initial state shift¹⁶⁸.

In Kohn-Sham DFT, the corresponding initial-state shifts lie *above* the exact shifts, and final-state shifts appear as small *negative* corrections¹⁶⁸. Since DFT formally is a theory for the electronic ground-state, and only with difficulty generalized to excited states¹⁵⁷, accurate DFT final-state shifts are not easily calculated. While as explained

above, TDDFT with an appropriate approximation of f_{xc} in principle could calculate XAS shifts, this idea has yet to be explored.

The heretofore most popular approach relies on the relatively small lifetime widths of the core-ionized state on the electronic energy scale¹⁶⁴: Intuitively, sufficiently metastable excited states are often well described by a ground-state functional, allowing for an approximation of the final-state shift, as the total energy difference between the ground-state and the same system with one electron of the relevant core-state removed^{168–170}.

Nevertheless, if final-state shifts are small on the scale of the separation between core-levels, the readily obtained initial-state shifts are sufficient to aid experiment^{171,172}. While orbitals of Kohn-Sham DFT lack a strict physical interpretation, they often qualitatively closely resemble the corresponding Hartree-Fock orbitals¹⁷³, and convey much of the same chemical information. Consequentially, experimental results are here compared to Kohn-Sham initial-state shifts only. All such shifts were computed in fully optimized gas-phase molecular geometries (see section 6.3).

High-resolution XPS spectra were recorded by our collaborators, focusing on S-, C- and N 1s core-levels in SAMs of the three above mentioned molecules with six methylene groups (C6, TF-Az6 and Az6), adsorbed at polycrystalline gold film on mica. As described in greater detail in our first publication^I, the results for the first in combination with the Au 4f_{7/2} signal compares well to what has been reported for highly ordered biphenyl-alkanethiol SAMs on gold¹⁷⁴, albeit with broader photo-emission peaks, indicating that while the monolayer order in the studied samples is high, it is not perfect.

Comparing to literature^{78,175,176} and aided by calculated Kohn-Sham initial-state CLSs, our collaborators comprehensively assign^I measured C- and N 1s CLSs to the various inequivalent atoms in the Az6 and TF-Az6 molecules (see Fig. 6.3). The tiny C 1s peak at 289.9 eV in the TF-Az6 spectrum is attributed to CF₂ as a consequence of X-ray induced beam damage^I. The corresponding C 1s CLSs in TF-Az6 with a CF₂ as opposed to the TF (CF₃) group have also been calculated (see Fig. 6.5). The broad C 1s peak centered at 291.5 eV in the Az6 SAMs is attributed to shake-up excitations in the π and π^* manifold accompanying the core ionization in the phenyl groups^{177–179}. Similar satellites are also found in the N 1s spectra^I.

As in pure azobenzene, the π , n and π^* orbitals of TF-Az6 correspond to the HOMO-1, HOMO, and LUMO, respectively. Calculated DFT isodensity contour plots of these as well as of the LUMO+1 and LUMO+2 π^* orbitals are shown in Fig. 6.4.

Using optical spectroscopy of the TF-Az6 molecule in ethanolic solution, our collaborators found $n - \pi^*$ and $\pi - \pi^*$ absorption bands at about 2.8 and 3.6 eV, in good agreement with the corresponding calculated TD-DFRT excitation energies of 2.57 and 3.43 eV, respectively. Angle-resolved valence-band photoemission of TF-Az6 reveals electronic binding energies of 2.8 and 4.0 eV for n and π , respectively. Based on these energies of valence Kohn-Sham orbitals and photoemission final states, the satellites found in the N 1s spectrum are assigned to $n - \pi^*$ and $\pi - \pi^*$ shakeups^I.

Energies of shakeup satellites are strongly influenced by final state effects, and transition energies include the interaction of the excited electron-hole pair with the core hole. The shake-up satellites in the Az6 C 1s XP spectrum are centered at 7.2 eV above the main line. They cannot reflect excitations to the π^* LUMO and must therefore involve

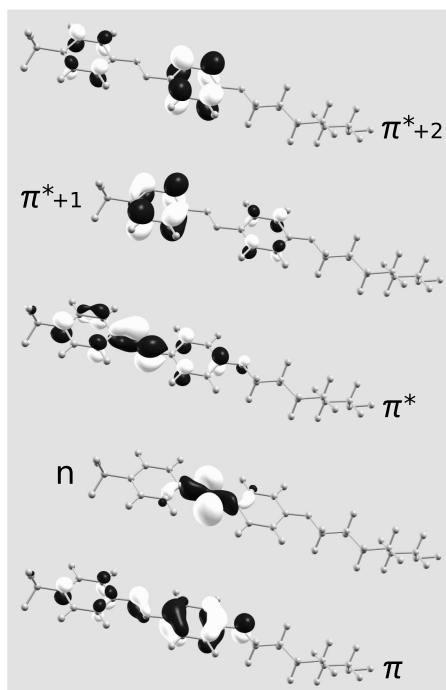


Figure 6.4.: Calculated DFT/B3LYP isodensity contours of the π , n , π^* (HOMO-1 - LUMO), LUMO+1 and LUMO+2 π^* orbitals of TF-Az6 (cf. Fig. 2.1 and 7.3). The black and white coloring of the contours represents the orbital phase.

transitions to the higher lying unoccupied π orbitals.

Inspecting the orbital contour-plots in Fig. 6.4, we see that the π^* orbital is distributed over the whole azobenzene moiety, but with the highest probability density at the nitrogen atoms. The n orbital concentrates at the azo group, while the π orbital is mainly located at the α -phenyl with some contribution also at the azo group.

The two π orbitals denoted as $\pi^* + 1$ and $\pi^* + 2$ together display a rather symmetric probability density located at the phenyl rings of the azobenzene entity. In Az6 the computed charge distribution of these two orbitals is even somewhat more symmetrically distributed among the phenyl rings, since the charge-pulling CF_3 group is replaced by a hydrogen atom. These orbitals are therefore good candidates as shake-up final states upon C 1s excitation since the probability density is mainly located at the phenyl ring.

For the free benzene molecule, the total intensity of the $\pi - \pi^*$ shake-up region amounts to about 15 % of the main line and is little affected by the hydroxyl group in the case of the phenol molecule¹⁷⁷. In the Az6 SAM the intensity of the shake-up satellites is reduced to a mere 4 %. However, the mentioned autoionization studies of nitrile-functionalized SAMs¹⁵⁰ indicate that the alkane chain decouples the azobenzene chromophore from the surface rather effectively, which on the contrary implies the expectation of a rather high intensity of the satellites. The observed weak contribution of distinct shake-up transitions to the X-ray photoemission (XP) spectrum thus suggests that intermolecular interactions in the SAM are strong and lead to a quenching of intra-molecular excitations.

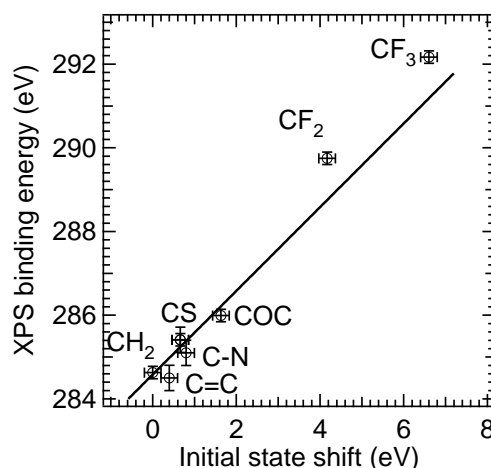


Figure 6.5.: Comparison of theoretical DFT initial-state shifts and experimental XPS core-level binding energies. The vertical error bars represent experimental resolution.

A comparison between experimentally measured and calculated Kohn-Sham initial-state CLSs is shown in Fig. 6.5. Data points related to the C6 alkane, the C-S-gold bond, the azo and the phenoxy group string together along a straight line with slope one. The CF₃ and CF₂ tail-groups show a larger binding energy, which is attributed to enhanced screening in the final state. Furthermore, the difference between the head-group which binds to the gold substrate and the tail-group which defines the SAM-vacuum interface is comparable to polymer multi-layers¹⁸⁰. In the SAMs head-group and chromophore with tail-group are separated by the alkane chain. Again, on the femtosecond time scale of core excitation and decay, charge transfer across this linker is very slow¹⁵⁰. This indicates that screening of the C 1s core holes in the azobenzene chromophore must be mediated by sizable intra- and intermolecular screening.

With experimental insights thus far on a firm footing, our collaborators carried out a series of X-ray absorption spectroscopy (XAS) and near-edge X-ray absorption fine structure spectroscopy (NEXAFS) measurements^{I,II} in order to compare the core hole to bound-state excitation in XAS and XPS core ionization, and determine structural parameters of the SAM as explained in section 6.3. Given the above sketched interpretation of the meaning of differences of Kohn-Sham eigenvalues as the zeroth approximation of the corresponding resonant excitation energy, they may be exploited for the assignment of XA resonances in precise analogy to, and motivated in the same way as, the above approach for CLSs measured by XPS. Specifically, the 1s-edge XA signals are compared to differences between the relevant calculated core-level and π^* Kohn-Sham eigenvalues.

This tool combined with the calculated spatial extension of π^* orbitals as exemplified by Fig. 6.4 allows for the consistent assignment of all experimentally observed XA resonances, as further detailed in our publications^{I,II}. Most noticeably, the relative energies E_{res} of neutral excitations and core ionization differ for nitrogen and carbon. While the N 1s XPS peak lies above the π^* -resonance at $E_{\text{res}} = -0.7$ eV, the C 1s XPS peak is

centered at about $E_{\text{res}} = 0.6$ eV below the corresponding C1 s to π^* transition. The XPS binding energies are referenced to the Au 4f line and thereby to the Fermi level of the substrate.

In other words, the XPS binding energy corresponds to the energy required to excite an electron from the core hole to the Fermi level, since the energy of one extra electron at the Fermi level is insignificant. Assuming charge transport between the gold substrate and the azobenzene chromophore, the current upon π^* -excitation would depend on the type of core hole. In the presence of a C 1s core hole charge transfer from the LUMO of the chromophore to the substrate is energetically allowed, while it is forbidden in the presence of a N 1s core hole. Here for energetic reasons electrons would flow from the substrate to the chromophore upon ionizing the 1s level.

However, there cannot be metallic screening, since in this case the XPS binding energy is expected to be lower than or equal to the XAS transition energy. Weak polarization screening of the core-excited states is more plausible. Again, this is consistent with the dependence on chain length of charge transfer in the N 1s π^* -resonance, and the above mentioned results by Feulner and coworkers¹⁵⁰: For a chain length of $n = 16$, they observed no charge transfer, and the N 1s XPS line was found at $E_{\text{res}} = -0.2$ eV, i.e., above the π^* -resonance transition. For a chain length of $n = 2$, the order of core-neutral and ionic excitation was reversed $E_{\text{res}} = +1.2$ eV, and charge transfer from the nitrile tail group to the gold surface was observed. Extrapolating the observed charge transfer time of 13 fs to a chain length of $n = 6$, the corresponding time-scale for the here studied SAMs is on the order of picoseconds.

Therefore, on the femtosecond time scale of core-hole decay, charge transfer to the substrate is negligible. However, in first autoionization experiments our collaborators observe^I non-resonant contributions in the decay of both the nitrogen and carbon core-hole. Thus charge transfer on the femtosecond time scale defined by the lifetime of the core hole must occur among the azobenzene moieties which may, however, depend on the degree of localization of the core hole.

Thus, charge transfer must be dominated not by the substrate, but by the azobenzene moieties in the SAM. This requires a densely packed SAM where the orbitals tend to form electronic bands. The interaction between the core hole and the environment will to some extent localize the charge distribution in the core-excited state. This may differ for the azo group as compared to the π -system of the phenyl rings. The push-pull system formed by the oxygen bridge and the trifluoromethyl tail-group may further modify the intermolecular interactions, since it leads to a less symmetric charge distribution already in the ground state (cf. the π orbital in Fig. 6.4). For TF-Az6, shake-up excitations upon N 1s core ionization were observed, but not in the C 1s XP spectrum, where XPS satellites appear only for the Az6 SAM. Again the different shake-up intensities for nitrogen and carbon are attributed to differences in screening of the respective core hole.

	α ($^\circ$)	ω ($^\circ$)	d_{NN} (\AA)	d_{CN} (\AA)
Trans	115	180	1.25	1.41
Cis	125	10	1.24	1.43

Table 6.3.: DFT/B3LYP optimized geometry parameters of both isomers of a single TF-Az6 molecule (cf. Table 6.1 and Fig. 6.2). Note the distinction between α as used here, and as redefined in Fig. 6.6.

6.3. Geometric Structure

The thus far established understanding of the electronic structure of TF-Az6 SAMs at gold is incomplete without comparable insight into the geometric structure, and how the two are connected, which is the topic of this and the following two sections.

The adsorbate geometry may qualitatively be discussed in terms of three components, namely the internal geometry of the molecule, the orientation of the molecule with respect to the substrate, and the structure and lateral periodicity of the molecule in the SAM.

For the first of the three, DFT/B3LYP readily predicts the gas-phase geometry of TF-Az6. While the lack of crystallographic data prevents a direct estimate of the accuracy of this result, there is no reason to expect it to be substantially worse than for the bare chromophore moiety, in particular since its structure hardly differs from that of pure azobenzene (see Table 6.3). Combined with the sheer dimensions of the various constituent moieties, these parameters provide a good idea of the lateral and vertical extension of the conformers in the SAM. The second geometrical aspect is, in addition to further addressing the question of which isomer species predominates the SAM, determined in the following.

Here, the reader is referred to our second publication^{II} for greater detail. Cursorily put, in X-ray absorption (XA), the orientation of the absorbing moiety relative to the X-ray beam can be deduced from the polarization dependence of the XA cross-section, if in turn the orientation of the XA transition dipole moment (arrows labeled “TDM” in Fig. 6.6) relative to the absorbing moiety is known. As shown above, ground-state Kohn-Sham orbitals provide approximate predictions of XA resonances in the initial-state picture. As illustrated in Fig. 6.4 and exploited in the previous section, they also hint at the extension and orientation relative to nuclear coordinates of XA final states, and consequentially, the corresponding TDMs. This allows our collaborators to unambiguously assign observed π^* and σ^* C 1s resonances to the phenyl and TF moieties, respectively.

With specific XA signals by way of the relative TDM orientation thus tied to the molecular geometry, the tilt angles α and ϑ , and the twist angle γ of the azobenzene moiety in the SAM can be deduced^{II} from the NEXAFS intensity contrast¹⁸¹ between different sample orientations (see Figures 6.6 and 6.7). Notably, the comparable values of α calculated from measurements at the C- and N 1s XA edges, clearly indicate that the

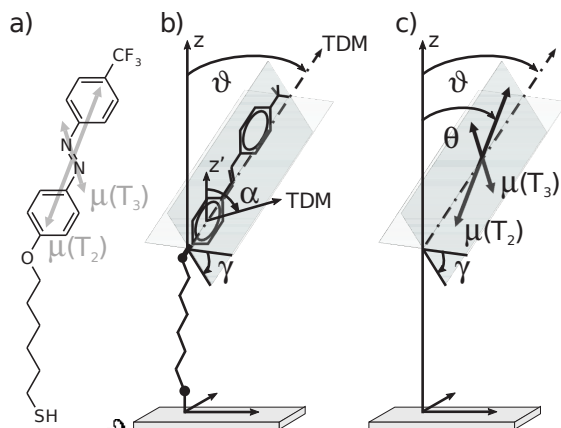


Figure 6.6.: a) Structural formula of TF-Az6, cf. Fig. 6.1. The gray double arrows represent the optical transition dipole moments (TDMs) $\mu(T_1)$ and $\mu(T_2)$ probed in UV/Vis spectroscopy, and simulated with TD-DFRT (see text). b) The definition of the angles α and ϑ used to describe the orientation of the azobenzene moiety. Note that this α is different from that of Fig. 6.2. c) Illustration of the tilt angle θ (ϑ , γ) of the optical TDMs compared to the molecular tilt and twist angle.

azobenzene moiety favors the trans isomer in the thermally equilibrated SAM – in the cis isomer, the two angles would differ considerably, due to the difference in diazo-bridge orientation (see e.g. Fig. 1.1).

However, XA as employed here only probes the average orientation of the molecules in the SAM. In order to understand possible variations from this average orientation, we again turn to DFT calculations:

The freedom of motion of the chromophore moiety in the angle γ , is coupled to its freedom of motion in the C-O-C bond angle ξ and the internal azimuthal angle χ , as defined in Fig. 6.8. This Figure shows B3LYP potential energy surface (PES) plots for an Az3 compound with a CH_3 termination of the alkane chain instead of the thiol group, and for the same molecule without the oxygen linker[†]. The PESs were obtained by incremental variation, under complete optimization of all other geometrical degrees of freedom, of ξ and χ in a dense grid for smaller values, and in a coarser grid for larger values. The plotted PES is an interpolation of the resulting irregular grid. The innermost plotted contour corresponds to 25 meV ($\sim k_B T$ at room temperature) above the minimum.

Fig. 6.8a shows that ξ is rather rigid around its equilibrium value of 120° , with the three atoms lying in the plane of the adjacent phenyl ring (for $\chi = 0^\circ$). The phenoxy group is, however, rather freely rotatable around χ in a range of $\pm 20^\circ$. As evident from Fig. 6.8b azobenzene linked directly to the alkane chain is instead almost freely rotatable around the C-phenyl bond, but with a shallow potential minimum for an orientation of the alkane chain perpendicular to the phenyl plane ($\chi = \pm 90^\circ$).

The same holds for the intensively studied biphenyl-alkanethiols (BP n). BP n are

[†]Tests revealed that the corresponding PESs for Az6 and TF-Az6 are identical.

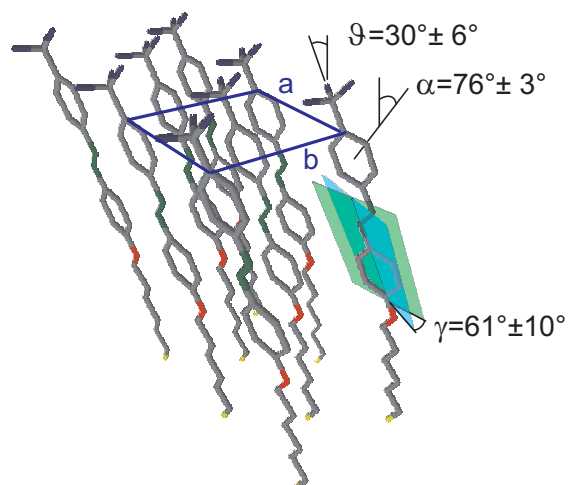


Figure 6.7.: Structural model of the SAM of the azobenzene-functionalized alkanethiols, based on the here measured molecular orientation in combination with the AFM results of Wolf and Jaschke et al.^{67,79}. The molecules are located at the corners and in the center of the rectangular unit cell with lattice vectors $a = 6.05 \text{ \AA}$ and $b = 7.80 \text{ \AA}$.

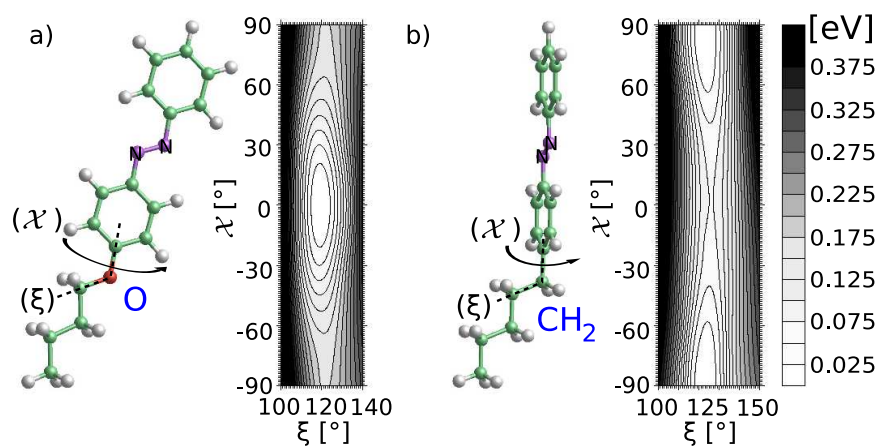


Figure 6.8.: DFT/B3LYP total energy contour plots for Az3 with the azobenzene chromophore in the trans configuration for a) an oxygen and b) a methyl alkanethiol - azobenzene linker.

known to exploit this rotational freedom to maximize the contact area of the aromatic moieties in adjacent molecules by aligning phenyl-moiety planes (so-called “ π -stacking”). The close similarity between the tilt and twist angles measured in BP n SAMs^{86,182–184} and the here obtained values of ϑ and γ in TF-Az6 SAMs is a strong indication that also the latter system undergoes π -stacking.

The third and last above defined component of the SAM structure – the periodic unit cell of the adsorbate overlayer – remains to be determined. AFM and STM measurements of Az6 on Au show that the SAM forms a well ordered nearly rectangular lattice with basis vectors $a = 6.05 \text{ \AA}$ and $b = 7.8 \text{ \AA}$ and two molecules per unit cell^{67,79}. This is the assumption of the structural model shown in Fig. 6.7.

For simplicity the model in Fig. 6.7 assumes equal orientation of the two azobenzene chromophores in the unit cell. The two angles α and ϑ fix the orientation of the chromophore with respect to the surface normal, allowing motion of the molecule on a cone. For two molecules per unit cell this would allow for a herringbone-like arrangement of the chromophores in the SAM, again congruous with previous observations for BP n SAMs¹⁸⁴.

6.4. Optical Properties

Given the proposed switching mechanism of azobenzene (see chapter 2), optical properties of the TF-Az6 SAM in the ultraviolet to visible (UV/Vis) spectrum are of obviously crucial relevance. Consequentially, this section presents UV/Vis spectroscopy performed by our collaborators^{II}, supported by TD-DFRT calculations performed by ERM. Since as explained the coupling of the substrate electronic structure to the chromophore moiety can be assumed negligible, UV/Vis spectroscopy in this system specifically probes changes in optical properties due to intermolecular interactions.

Absorption spectra in solution as well as reflection spectra from the SAM for TF-Az6 and Az6 are shown in Fig. 6.9. In ethanolic solution the spectra exhibit three main absorption features: The $n - \pi^*$ transition (denoted as T_1) at a photon energy of 2.8 eV, which is dipole forbidden in the thermally stable, inversion-symmetric trans conformation of azobenzene, the strong $\pi - \pi^*$ transition (T_2) at 3.5 eV, and a broad absorption line around 5 eV of higher $\pi - \pi^*$ transitions (T_3), where three sub-bands, marked by the vertical lines, can be discerned. The brightest TD-DFRT transition corresponding to the latter is dominated by a $\pi - \pi^* + 1$ (LUMO+1) component, distinguishing it from the in chapter 2 discussed S_3 and S_4 absorption lines, which in TF-Az6 corresponds to the HOMO-{3,4} - LUMO transitions.

Subtracting the background due to the gold substrate as calculated within a dielectric continuum-model^{II} (DCM), the SAM spectrum strongly resembles the absorption spectrum of the TF-Az6 compound in watery solution (cf. Fig. 6.9). The main difference is that the $\pi - \pi^*$ transition in the SAM is broadened and shows an additional contribution, blue-shifted by 0.6 eV relative to the T_2 absorption maximum. Note that the absolute shift is comparable for TF-Az6 and Az6. The T_3 transition at around 5 eV shows in contrast a minor red-shift of about 0.1 eV.

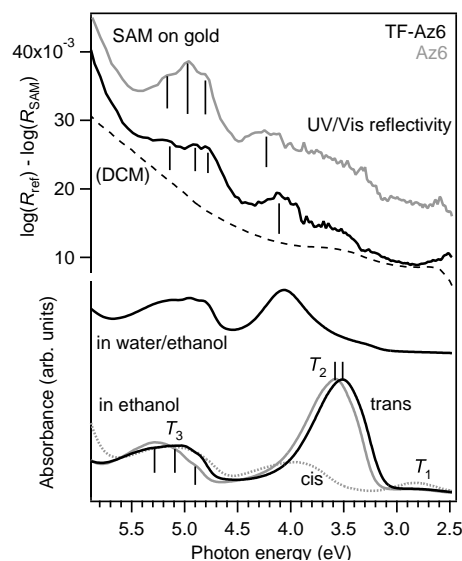


Figure 6.9.: UV/Vis absorption spectra of TF-Az6 (black lines) and Az6 (gray lines). The spectra of the SAM (upper lines) have been measured in reflection and are difference spectra of the SAM-covered and clean gold substrate. The dashed line is a dielectric continuum-model (DCM) calculation of the background of the gold substrate (see text).

6.5. Chromophore Excitonic Coupling: The Extended Dipole Model

At this point, a short recapitulation is in order. So far, previous and current results indicate that a) the molecules in the TF-Az6 SAM do not switch, b) the SAM is formed from molecules in their trans conformer, c) the chromophoric moieties are substantially screened due to inter-molecular interactions, d) like in biphenyl SAMs, these moieties exploit a degree of twist rotational freedom to maximize $\pi - \pi$ stacking, and finally e) in the SAM, the “switching” $\pi - \pi^*$ transition exhibits a considerable spectral shift. Thus, combined with the insights of previous sections, there is ample evidence for exciton band-formation¹⁸⁵ via inter-molecular coupling in the SAM. Allowing for fast quenching of molecular excited states, this would explain the low switching yield in TF-Az6 SAMs. In this section, this hypothesis is tested by a simulation of spectral shifts under the assumption of the existence of an exciton band.

Specifically, our collaborators calculate^{II} spectral shifts within the so-called extended dipole model^{149,186} (EDM). This approach is based on a very simple model Hamiltonian, which treats the interaction of an optically excited molecule with the other molecules in a crystal using a dipole approximation: The charge distribution of neutral molecules and the transition dipole moment of the excited species are approximated as point charges separated by a given distance (see Fig. 6.10a). The dipole approximation is best motivated at intermediate to small ratios of the magnitude of molecular dipoles to the separation between them, and is here justified by the size of the molecule and the SAM

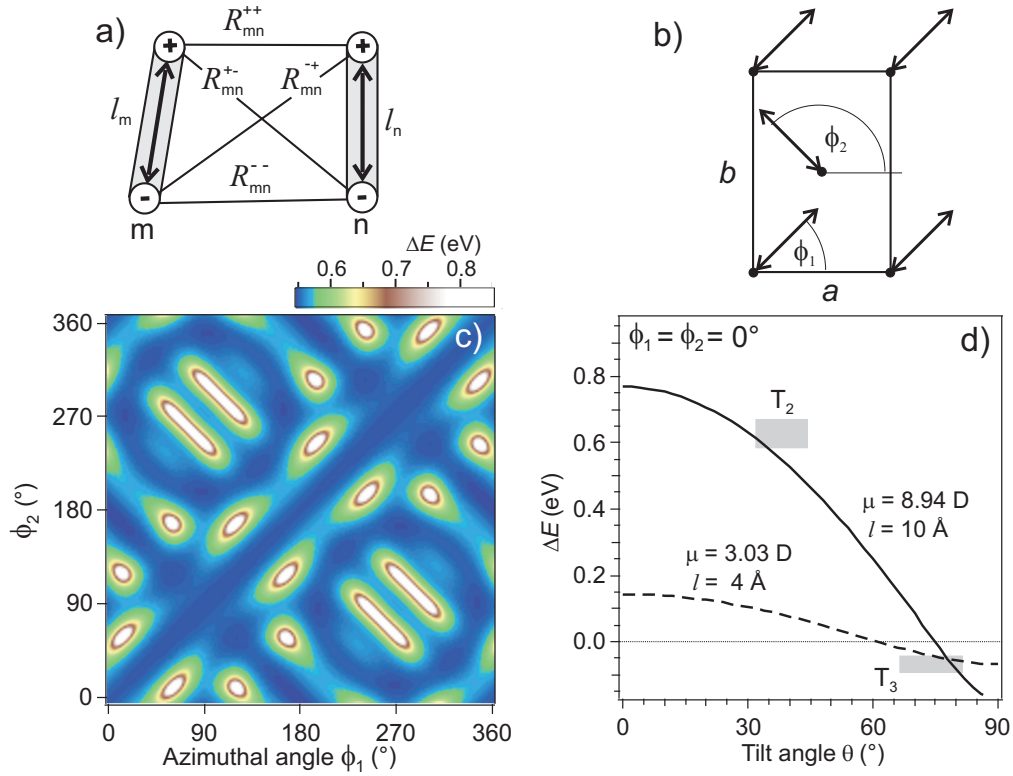


Figure 6.10.: Extended dipole model (EDM): a) Transition dipoles m and n of length l and charge separation R_{mn} . b) Top view showing the orientation of optical transition dipole moment m relative to the lattice. The angles ϕ_1 and ϕ_2 define the azimuthal orientation of the two transition dipole moments in the unit cell. c) False color plot of the calculated spectral shift of the T_2 dipole transition with respect to the azimuthal orientation ϕ_1 and ϕ_2 for fixed tilt angle $\theta = 38^\circ$. d) Calculated spectral shifts ΔE for the T_2 (solid line) and T_3 transition (dashed line) as a function of the tilt angle θ of the corresponding optical transition dipole moment. The gray horizontal bars mark the expected coordinates of the dipole moments $\mu(T_2)$ and $\mu(T_3)$: The energy shift of the transition dipole moments is taken from UV/Vis spectroscopy and the angle θ is determined by combining the orientation deduced from the NEXAFS measurements and the orientation of the optical dipole moment calculated via TD-DFRT. The extension of the bars represents the experimental errors.

unit cell.

The in the previous section determined structural model of the SAM defines the orientation and spatial distribution of dipoles. The transition dipole moments $\mu(T_2) = 8.94$ Debye and $\mu(T_3) = 3.03$ Debye of the T_2 and T_3 optical bands and their orientation with respect to the C-CF₃ axis are taken from the TD-DFRT calculations. Guided by the extent of the π -electron system along the respective directions, the lengths of the dipoles l of the T_2 and T_3 transitions are taken to be 10 Å and 4 Å, respectively. The calculations include the interaction with all neighbors in a lattice consisting of 50×50 unit cells.

The interaction between neighboring transition dipoles depends strongly on their mutual orientation. Therefore the azimuthal angles, ϕ_1 and ϕ_2 in Fig. 6.10b, of the transition dipole moment were varied independently for the two molecules. In Fig. 6.10c the angular dependence of the spectral shift is presented for the T_2 transition with a dipole length of $l = 10$ Å in a false color plot. Corresponding to $\vartheta = 30^\circ$ the tilt angle of the optical transition dipole moment is taken as $\theta = 38^\circ$.

The areas of large spectral shifts (white) correspond to angle combinations where the partial charges of the extended dipoles approach each other closely. Hence these orientations are forbidden for steric reasons. As seen from the dark diagonal stripes, all combinations of equal azimuthal orientation for both molecules in the unit cell represent configurations where the intermolecular coupling, especially the excitonic coupling, is small ($\phi_1 = \phi_2$). The same holds along the path where the molecules rotate exactly counter-clockwise ($\phi_1 = 180^\circ - \phi_2$). In these configurations the excitonic band shift for large aggregates amounts to about 0.55 eV. This is of the same order of magnitude as the experimentally observed value of 0.6 – 0.65 eV for the blue shifted absorption maximum and strongly supports that the interaction among the transition dipoles can very well describe the spectral shift of the T_2 transition in the UV/Vis spectra.

To evaluate the spectral shifts as a function of the tilt angle of the dipole moments θ with respect to the surface normal our collaborators assume a parallel configuration of the planes of the two chromophores in the unit cell as shown in Fig. 6.7, where steric hindering and repulsive dipole-dipole interactions are minimized (see Fig. 6.10c). The respective shifts of the dipole moments $\mu(T_2)$ and $\mu(T_3)$ of transitions T_2 and T_3 are depicted in Fig. 6.10d. The gray horizontal bars mark the measured energy shift of the dipole transitions T_2 and T_3 and the angular ranges for θ which are consistent with the molecular structure determined from NEXAFS, i.e. the angles α and ϑ .

Given the simplicity of the extended dipole model and the complex structure of the SAM, experimental and calculated shifts agree well. Small corrections may stem from the additional static dipole interactions resulting from a change of the charge distribution in the excited state which have been neglected here. These corrections usually result in an additional redshift¹⁸⁶. However, even the present level of the modeling unambiguously establishes that the shift of the optical transitions is a clear signature of the interaction between the transition dipoles.

6.6. Summary

We have studied SAMs of the chromophore TF-Az6, and its components C6 and Az6 adsorbed at a gold surface, using a number of complementary X-ray absorption and photoemission techniques in conjunction with hybrid-functional DFT and TDDFT. XPS in the S 1s band, aided by peak assignment via initial-state DFT core-level shifts, indicate a high degree of order in the SAM, with a single adsorbed species of the typical thiolate bond. Supported by DFT, we consistently assign C 1s and N 1s XPS signals to all constituent moieties. Observed shake-up transitions are rationalized based on the calculated probability density distribution of the frontier orbitals.

Comparing XPS binding energies and π^* -excitation energies of the azobenzene chromophore, it appears that screening of the N 1s XPS final state is weak and preferentially mediated by polarization. In contrast, the C 1s XPS final state has a lower energy than the neutral $1s^{-1}\pi^{+1}$ excitation. Therefore, the ionic state must involve sizable screening. This result is confirmed by comparing measured C 1s binding energies to simulated initial-state shifts: The latter, lacking any account of excitonic (final-state) effects, compare perfectly to the XPS signal of the methylene groups deep in the SAM, but on the same energy scale underestimate C 1s binding energies of the TF end-group. This is congruous with a sizable screening of the azobenzene moiety. As the latter cannot be due to substrate charge transfer, it must be an inter- and intra-molecular phenomenon. This strong intermolecular coupling may also lead to a rapid decay of optical excitations, offering an explanation for the low switching yield observed for azobenzene in densely packed aromatic-aliphatic SAMs on gold.

Based on NEXAFS measurements and DFT calculations the picture of the chromophore adsorption geometry is further refined. Combined with the calculated gas-phase molecular geometry, the determined NEXAFS absorption polarization dependence and reference results for the lateral periodicity provide us with a nearly complete model of the monolayer, including the chromophore extension and average orientation. The latter compares well with recent results for biphenyl SAMs, which have been shown to orient such that the phenyl π -interaction is maximized, consistent with the posited intermolecular coupling, and quenching of 'switching' excited states.

Optical properties were studied with a combination of UV/Vis spectroscopy and TDDFT. On the basis of the geometric structure and calculated UV/Vis transition dipole moments, the 0.6 – 0.65 eV redshift of the T_2 (π to π^* (LUMO)) and 0.05 eV blue-shift of the T_3 (π to π^* (LUMO+ n)) transitions are qualitatively described by an extended dipole model, demonstrating the importance of excitonic coupling among the azobenzene π systems.

This finding introduces an important new aspect in azobenzene-based surface-decoupled molecular switch design: Lest the "switching" molecular excited states be quenched, there is an upper limit to the density of functional azobenzene-based switches significantly lower than that dictated by mere molecular geometry (steric blocking). Therefore, not only must azobenzene-based switches be functionalized in such a way as to decouple the chromophoric moiety from the substrate electronic structure and transfer order from substrate to the adsorbate overlayer, their design must also provide sufficient lateral

spacing, achieved in a manner compatible with other design constraints.

Part III.

Surface Adsorbed Switches

7. Azobenzene at Coinage Metal Surfaces: The DFT-GGA Adsorption Picture

The previous chapter demonstrated how attractive intermolecular interactions between chromophore moieties can quench switching, in spite of an almost complete decoupling from the surface electronic structure. As outlined in chapter 2, a similar argument of coupling to the *substrate* electronic structure has been made to explain the generally low switching yield of azobenzene directly adsorbed at coinage metal surfaces. However, his argument is not sufficient to explain the observed substantial variations in switching behavior with ostensibly small chemical changes in substrate material and structure and switch functionalization. The understanding of these effects is vital to efficient switch design, making the investigation of the geometric and electronic structures, as well as the general bonding picture, of directly adsorbed switches a topic of utmost relevance. In this context, state of the art first-principles simulations stand to offer detailed insight unattainable by other means.

First-principles modeling of reactions and adsorption at solid surfaces is a multi-faceted research topic: Bridging the gap between traditional solid state theoretical physics and quantum chemistry, it is firmly rooted in models from both parent fields. Nevertheless, the unique characteristics of interface electronic structure generally requires further refinement of these concepts. As in depth discussed in chapter 10, given a theoretical model consistently describing electronic structure with varying system size, a meso- or macroscopic object (e.g. an extended solid surface), on the atomic scale of practically infinite (or *semi-infinite*) extension, could be simulated to within the model arbitrary accuracy by a finite system of sufficient size. However, the to a degree mutually exclusive requirements of accuracy, transferability and scalability of electronic structure methods (see chapter 3), has led to the widespread adoption of *periodic boundary condition* (PBC) techniques in theoretical surface science. In PBC, the electronic structure is inherently treated as an object of infinite extension, which allows for accurate yet tractable simulations of high-symmetry crystalline systems of small fundamental bandgaps, e.g. bulk metals.

Systems of lower symmetry or periodicity in less than three dimensions can also be treated with PBC techniques in the so-called *super-cell* approach¹⁸⁷: For example, a true solid surface resting on a macroscopic chunk of bulk material in vacuum, may to arbitrary accuracy be approximated by a slab of sufficient thickness in a super-cell of a size inversely proportional to the degree of translational symmetry of the surface, which is periodically repeated in the surface plane, i.e. in two dimensions. In three-dimensional PBC, the super-cell dimension perpendicular to the slab is extended until true vacuum conditions at the surface are achieved (see Fig. 7.1).

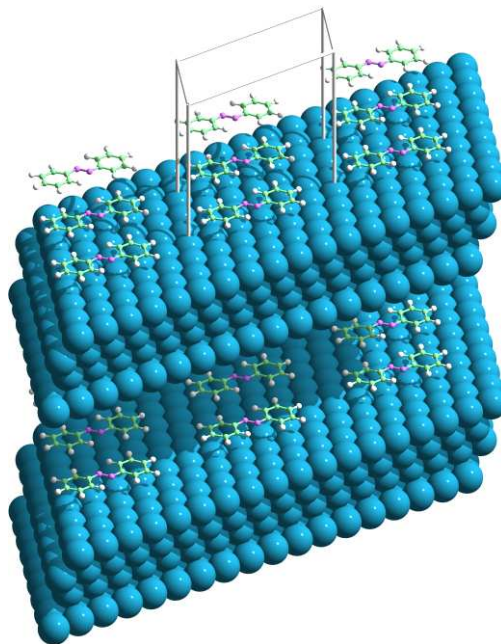


Figure 7.1.: Azobenzene in a super-cell (marked in gray) corresponding to a (6×3) unit cell of the (111) surface lattice, adsorbed at a four-layer Au(111) slab. The super-cell has been repeated once in every direction, showcasing the model adsorbate - substrate system.

Metallic surfaces pose additional difficulties: The post Hartree-Fock methods (see chapter 3.3) representing the state of the quantum chemistry art, often rely on low-order approximations of the true many-body interactions which work well for sparse matter, but not for dense matter. Some such correlation models, e.g. MP2 (see section 3.3), approach singularities in the zero-bandgap limit. Additionally, the computational scaling of typical post Hartree-Fock methods severely limit their applicability to dense matter systems, in particular when their size is dictated by a large adsorbate.

Density functional theory, tracing its ancestry to explicit models of the solid state, exhibits none of these deficiencies, and enjoys the status of method of choice for solid state calculations since over four decades. Given the relative computational simplicity and competitive performance of (semi-)local LDA- and GGA-based exchange-correlation (xc) functionals also for calculations of solid surfaces^{187,188}, it comes as no surprise that PBC DFT using in particular the latter functional family still must be considered the state of the art of first-principles simulations in surface science.

At this point the goal of this chapter can be defined as follows: We here aim to exhaustively study the bonding and meta-stable structures of azobenzene adsorbed at close-packed coinage metal (111) surfaces, using DFT-GGA. The results of this study have been published in Physical Review B^{III}. As will be demonstrated, DFT-GGA is not without deficiencies in the description of large aromatic molecules at surfaces, of which in particular two are important for the following results:

In the previous chapter, the hybrid B3LYP^{121,122} functional was chosen over LDA and

GGA functionals since the effect of the delocalization error¹¹⁰ (following self-interaction, see discussion in chapter 4) was found more influential in the latter. This problem is often equally evident in surface adsorption calculations, fundamentally affecting qualitative aspects such as the adsorption site preference of simple adsorbates^{189–192}. While recently implemented in some PBC DFT packages, the conditionally transferable, semi-empirical form of B3LYP has proven wholly inappropriate for transition metal systems¹²⁵, which is confirmed in section 10.2.

Another problem, in particular for the interaction of π -like orbitals (and consequently large aromatic molecules) with noble metals of great importance^{193–196}, is that of the underestimation or spurious description of dispersive van der Waals interactions by (semi-)local xc-functionals. This is one of the greatest contemporary challenges for first-principles theory and forms the main methodological theme of this thesis. The consequences of this issue for the current adsorption problem are discussed in depth and revisited on the level of semi-empirical correction schemes^{197–205} in chapter 8. This methodology is in turn critically reviewed in chapter 10.

Nevertheless, the bonding of azobenzene at coinage metal surfaces is complex, and we in the following carve out some governing factors in the molecule-surface interaction that appear quite robust with respect to the employed approximate xc treatment. This notably concerns a rationalization of the obtained energetic ordering of the molecular states at the surface, and an analysis of the recent tip-manipulation and photo-excitation experiments from the view point of the derived bonding mechanism.

7.1. Theory

As in the previous chapter, we choose the GGA parametrization suggested by Perdew, Burke and Ernzerhof (PBE)^{116,117}. We use a plane-wave basis-set in PBC, with the wave-function near the ionic nuclei represented by ultra-soft pseudopotentials^{146,147} (see section 5.2), as implemented in the CASTEP software package²⁰⁶. Gas phase molecular geometries and properties were determined by optimizing isolated molecules in a rectangular ($40 \times 30 \times 30$) Å³ super-cell, with Γ -point \mathbf{k} -space sampling and a plane-wave kinetic energy cutoff of 800 eV. Plane-wave calculations of isolated molecules were complemented by finite-system calculations using the NWChem package¹⁵³ and the def-TZVP¹⁵⁴ basis set, as described and motivated in the previous chapter (section 6.1).

As explained in greater detail in appendix B, sections B.1–B.3, isolated molecules adsorbed on semi-infinite (111) surfaces were modeled using the super-cell technique, with the substrate represented by a slab of metal atoms (see Fig. 7.1). The slabs were constructed from the GGA-PBE optimized lattice constants ($a_o(\text{Cu}) = 3.63$ Å, $a_o(\text{Ag}) = 4.14$ Å, $a_o(\text{Au}) = 4.19$ Å).

Depending on the registry of the trans isomer with the substrate, large (6×3) or (6×4) (111) surface unit-cells were needed to decouple the adsorbed molecule from its periodic images. No possibility for reconstruction was considered for both clean and adsorbate-covered surfaces. This enables a direct comparison of the bonding at the three coinage metal surfaces and is expected to grasp the dominant local aspect of the molecule-surface

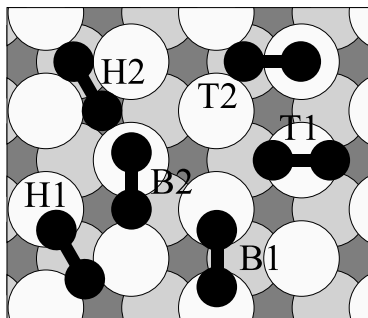


Figure 7.2.: Schematic top view indicating the initial lateral position of the two azo-bridge N atoms in the six geometry optimizations carried out to determine the most stable adsorption site at each surface (see text for nomenclature and details). N atoms, first- and second layer metal atoms are shown as black small circles, large white and large light gray circles, respectively.

interaction. On the other hand, it dismisses secondary long-range effects in the large-scale Au(111) herringbone reconstruction²⁰⁷ that have been shown to affect the ordering behavior at finite coverages⁴⁶ (see discussion in section B.2).

The most stable adsorption site was determined by full relaxation of the molecular and top layer geometrical degrees of freedom, of each of the two isomers adsorbed on one side of a three layer slab. Structure optimization relied on the BFGS algorithm²⁰⁸ as implemented in **CASTEP**, and the default convergence threshold on the maximum absolute ionic force component of 0.05 eV/Å. Determined by thorough convergence tests (section B.3), the plane-wave kinetic energy cutoff was set to 350 eV, the vacuum distance exceeded 13 Å, and reciprocal space integration was done using $(2 \times 4 \times 1)$ Monkhorst-Pack grids²⁰⁹.

In order to determine the preferred adsorption site, both azobenzene isomers were optimized in six different adsorption geometries on all three surfaces as sketched in Fig. 7.2: The molecule was centered on the bridge (B), top (T) and fcc hollow (H) surface sites, and shifted such that either the azo-bridge (-N = N-) center of mass (labeled 1) or one of the azo-bridge N atoms (labeled 2) aligned with the adsorption site. In most optimizations, the molecule relaxed towards the 1:1 metal-N atom coordinated B1 geometry (shown centered at the bottom of Fig. 7.2), which at all three surfaces and for both isomers was also the energetically most favorable among those found. Given this clear trend and the likely small differences between the fcc and hcp hollow sites, we refrained from additional explicit geometry optimizations starting from the hcp hollow sites. For the thus defined most stable geometry the absolute adsorption energy, the work function, density of states (DOS) and projected DOS (PDOS) were determined at refined computational settings and a (6×3) (111) surface unit-cell with the molecule adsorbed at a seven layer, inversion-symmetric slab (see sections B.4 and B.5).

The adsorption energy is defined as

$$E_{\text{ads}} = \frac{1}{2} [E_{\text{azo}@(\text{111})} - E_{(\text{111})}] - E_{\text{azo}(\text{gas})} \quad , \quad (7.1)$$

where $E_{\text{azo}@}(111)$ is the total energy of the relaxed azobenzene-surface system, $E_{(111)}$ the total energy of the clean slab, and $E_{\text{azo}(\text{gas})}$ the total energy of the corresponding relaxed gas-phase isomer (all three computed at the same plane-wave cutoff), and the factor $1/2$ accounts for the two adsorbates in the inversion-symmetric geometry. The adsorption energy of either cis or trans isomer at the surface is thus measured relative to its stability in the gas-phase, and a negative sign indicates that adsorption is exothermic. Using total energies of inversion-symmetric, seven layer slabs, the cis-trans relative stability $\Delta E_{\text{C-T}}$ is with the above notation defined as

$$\Delta E_{\text{C-T}} = \frac{1}{2} [E_{\text{azo}@}(111)(\text{cis}) - E_{\text{azo}@}(111)(\text{trans})] \quad . \quad (7.2)$$

Convergence tests detailed in section B.3 indicate that this central quantity is converged to within ± 30 meV at the chosen settings. Work functions have also been converged to similar accuracy (see section B.4).

The density of adsorbate-substrate system states projected on those of the isolated adsorbate has proven an invaluable resource for the characterization of adsorbate-substrate bonding^{55,210–214}, and is one of a few observables available exclusively in theoretical simulations. Many current implementations of such tools project the wave-function onto that of a sum of free atom wave-functions. The latter are readily obtained, and usually calculated anyway to establish a reference atomic total energy. For e.g. mono-atomic or some small molecular adsorbates, the true Kohn-Sham wave-function of the isolated adsorbate differs sufficiently little from that of the sum of its constituent atoms, for this approximation to be valid.

However, for adsorbates the size of azobenzene, the true isolated adsorbate wave-function is too complex for such an approximation to provide physically relevant information. We have therefore for this purpose created a tool projecting the total adsorbate system wave-function onto an actual Kohn-Sham wave-function in the same basis set. In practice, the molecular PDOS²¹⁵ $\rho_a(E)$ is defined by projections of the Kohn-Sham (KS) states of the (adsorbed) molecule-surface system $|\phi_{b,k}\rangle$ with KS Eigenvalues $\epsilon_{b,k}$ onto a certain KS orbital $|\varphi_a\rangle$ of the isolated molecule in the adsorption geometry

$$\rho_a(E) = \sum_{b,k} w_k |\langle \varphi_a | \phi_{b,k} \rangle|^2 \delta(E - \epsilon_{b,k}) \quad . \quad (7.3)$$

The summation over band indices b and \mathbf{k} -point indices k is weighted by the \mathbf{k} -point-weights w_k so that an integration of $\rho_a(E)$ over E gives $|\langle \varphi_a | \varphi_a \rangle|^2$ if sufficiently many bands of the molecule-surface system are considered: In an iterative wave-function diagonalization procedure as used here, the wave-function is expanded in a subset of the full basis set as opposed to a direct diagonalization SCF algorithm. Therefore, the projection norm depends on the size of that subspace. Furthermore, the molecular orbitals in the generalized eigenvalue formalism of ultra-soft pseudopotentials are orthonormalized with respect to the basis functions multiplied by the projectors, as opposed to the basis functions themselves. Therefore Eq. (7.3) must be evaluated considering the projector overlap matrix¹⁴⁶.

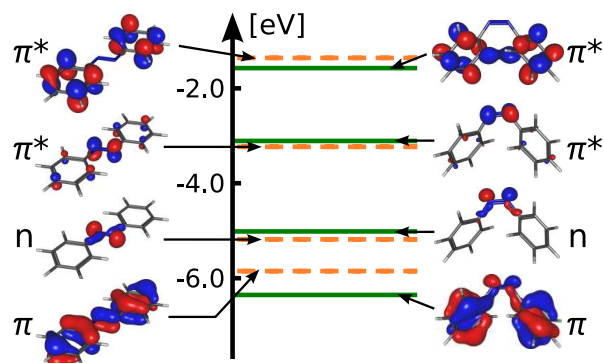


Figure 7.3.: GGA-PBE Kohn-Sham eigenvalues with respect to the vacuum level of the four frontier orbitals HOMO-1 (π), HOMO (n), LUMO (π^*) and LUMO+1 (π^*) of gas-phase trans (dashed lines) and cis (solid lines) azobenzene. Additionally shown are corresponding orbital representations superimposed on the skeleton geometric structure (left: trans, right: cis, cf. Fig. 2.1).

In order to achieve a consistent basis set, we used molecular KS orbitals $|\varphi_{a,k}\rangle$ which were calculated in the same super-cell and with the same energy cut-off and \mathbf{k} -point grid as the molecule-surface system to evaluate Eq. (7.3). We verified that the artificial dispersion of these molecular KS orbitals is indeed negligible within the desired accuracy of our computational setup, in addition to exhaustive tests of the code integrity itself, some of which are described in section B.5. In the plots below, the resulting δ -functions have finally been convoluted with a Gaussian function of 0.2 eV full width at half maximum for better visualization.

7.2. Results and Discussion

7.2.1. Gas-phase Azobenzene

We begin our analysis with the properties of gas-phase azobenzene, defined in exactly the same way as in section 6.1, at the current level of theory. Figure 7.4 illustrates these parameters in the surface adsorbed geometry (cf. Fig. 6.2). Reassuringly, the total difference of the here optimized geometry parameters and energetics and those reported for PBE/def-TZVP in Table 6.1, amounts to a mere 0.03 Å lengthening of the d_{NN} and d_{CN} bond lengths. The xc-functional being identical in both cases, this minor difference is likely due to differences in the basis set. Again, it is fair to say that with respect to the geometric structure the employed GGA functional yields results comparable to the hybrid B3LYP functional or post Hartree-Fock methods. However, the previously observed cancellation of long- and short-range errors in the relative isomer stability $\Delta E_{\text{C-T}}$ appears also here.

In line with the discussion of section 6.1, the description of the molecular frontier orbitals is more problematic. Figure 7.3 shows representations of select frontier KS orbitals that are of particular interest both with respect to the bonding mechanism

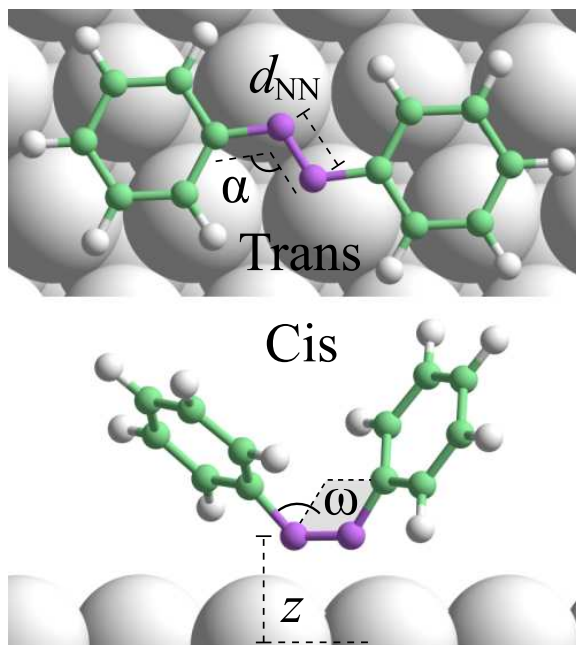


Figure 7.4.: Top panel: Top view of the azobenzene trans isomer at the preferred DFT-GGA adsorption site (i.e. the B1 geometry of Fig. 7.2). Bottom panel: Side view of the corresponding cis isomer adsorption geometry. Additionally shown in both panels are definitions of analyzed geometry parameters z , d_{NN} , ω , and α (see text; cf. Fig. 6.2).

to the surface, and with respect to possible isomerization pathways (see chapter 2, cf. 2.1). These here range from the second highest occupied molecular orbital (HOMO-1), over HOMO and lowest unoccupied molecular orbital (LUMO) to LUMO+1. Compared to the less delocalization error hampered B3LYP functional, the GGA-PBE functional yields the correct molecular character of these orbitals. The HOMO-1 and LUMO contain large contributions of the π and π^* orbital of the $-\text{N}=\text{N}-$ moiety, respectively. The HOMO consists predominantly of the N lone pairs and the LUMO+1 is centered on the π^* system of the phenyl rings. While the ordering of these frontier orbitals is identical in the hybrid and GGA functionals, the fundamental bandgap is as explained smaller in the latter (1.95 eV and 1.91 eV in PBE for trans and cis respectively, as opposed to 3.92 eV and 3.76 eV in B3LYP).

7.2.2. Adsorption Geometry and Energetics

The most favorable adsorption site obtained at all three coinage metal surfaces corresponds to the $-\text{N}=\text{N}-$ moiety bridging between two surface atoms as sketched in the B1 geometry of Fig. 7.2. While in this adsorbed state the symmetry of the gas-phase molecule is lifted, and the azo-bridge in principle could be vertically tilted with a concomitant symmetry breaking of the molecular structure as expressed by two different bond angles α of the two phenyl-rings, we find that this is not the case.

	Trans			Cis		
	z (Å)	d_{NN} (Å)	ω (°)	z (Å)	d_{NN} (Å)	ω (°)
Gas-phase	–	1.30	180	–	1.28	12
Cu(111)	1.98	1.40	141	1.93	1.35	33
Ag(111)	3.64	1.30	180	2.27	1.32	23
Au(111)	3.50	1.30	180	2.31	1.29	18

Table 7.1.: Structural parameters as defined in Fig. 7.4 for trans and cis azobenzene in the relaxed most stable adsorption geometry at the three coinage metal surfaces and compared to the optimized gas-phase structure.

At all three surfaces, the azo-bridge lies flat at a height z above the surface, and the two phenyl-rings show identical angles α , essentially unchanged from the gas-phase value, i.e. 115° and 124° for trans and cis azobenzene respectively (cf. Table 6.1). These values have therefore been left out of Table 7.1. Similarly, since d_{CN} is not further discussed here, its definition has not been included in Fig. 7.4, which illustrates the optimal adsorption geometry and the main structural parameters as discussed in the context of the gas-phase molecule.

We begin the detailed discussion with the trans isomer at Au(111) and Ag(111). The calculated geometry values listed in Table 7.1 may be summarized in that the molecule remains essentially flat, with a dihedral angle $\omega = 180^\circ$ as in the gas-phase, and sits at a rather large height > 3.5 Å above the surface. Due to some axial twisting of the phenyl-rings, the variation of z -heights exhibited by the individual atoms within the molecule nevertheless amounts to $\Delta z = 0.34$ Å and 0.37 Å on Au(111) and Ag(111), respectively. While relatively minor, this difference could play an important role in the coupling of electronic excitations with intra-molecular rotations, for which a non-planar geometry has been found a necessary prerequisite⁵⁴.

The comparatively weak bonding suggested by the large z -height is indeed confirmed by the exothermic, but small calculated adsorption energy of about -0.1 eV at both surfaces, cf. Table 7.2, and is consistent with the virtually unchanged azo-bridge bond length of 1.30 Å in the adsorption geometry, cf. Table 7.1. The correspondingly deduced weak physisorptive bonding scenario is, however, particularly prone to the prominent lack of dispersive interactions in the employed GGA-PBE functional as discussed in the introduction. Without a corresponding attractive contribution, the z -height of the molecule is exclusively governed by the steep Pauli repulsion wall encountered by the phenyl-rings, preventing a closer approach and stronger bonding of the molecule to the surface. As explained in chapter 8, this offset balance is an artifact of the lack of dispersive van der Waals interactions in the semi-local xc-functional.

Nevertheless, even at such a reduced height, the planar trans geometry fixes the azo-bridge atoms at a distance to the surface that is outside the range that would enable

	E_{ads}		$\Delta E_{\text{C-T}}$
	Trans	Cis	
Gas-phase	–	–	0.57
Cu(111)	-0.27	-1.08	-0.24
Ag(111)	-0.11	-0.42	0.26
Au(111)	-0.12	-0.27	0.42

Table 7.2.: Adsorption energies E_{ads} as defined in Eq. (7.1) for trans and cis azobenzene at the three coinage metal surfaces, and the relative energetic stability of the two adsorbed isomers $\Delta E_{\text{C-T}}$, as defined in Eq. (7.2). All values in eV.

the formation of stronger covalent bonds to the top-layer metal atoms, and is thereby the main limiting factor in the molecule-surface interaction. This problem does not exist for the cis isomer, where due to the bent molecular geometry the azo-bridge can come much closer to the surface with the phenyl-rings pointing away from the surface and thus at heights that are not yet in conflict with the repulsive wall, cf. Fig. 7.4. This picture is nicely reflected by the computed much smaller z -heights slightly in excess of 2 Å bringing the azo-bridge atoms into bond distances to the directly coordinated surface metal atoms highly reminiscent of corresponding distances in transition metal complexes²¹⁶ (see Table 7.1).

Consequently the -N=N- bond gets activated, as reflected by the slightly elongated d_{NN} bond length. In detail, the resulting optimum z -heights still seem to require some additional bending of the molecule to lift the phenyl-rings even further away from the surface as expressed by the somewhat increased dihedral angle ω for cis azobenzene at both surfaces, cf. Table 7.1. The cost for this bending partly compensates the gain from the formed azo-bridge surface bonds, but as apparent from Table 7.2, the net resulting adsorption energy for the cis isomer is still larger than in the trans case, and correspondingly, we arrive at a decrease of the relative energetic stability of the two isomers. At both Au(111) and Ag(111) the trans form is however still more stable, consistent with the conclusion from several STM studies which interpreted the measured “dumbbell” appearance of the thermally more stable adsorbed molecular configuration in terms of the trans isomer^{45,48,61}.

Continuing with the remaining Cu(111) surface, we find a much stronger interaction even at the GGA-PBE level. In contrast to the situation at Ag(111) and Au(111), both the trans and cis form of azobenzene adsorbs at a vertical z -height that brings the azo-bridge atoms to typical covalent N-Cu bond distances known from transition metal complexes²¹⁷. While due to the smaller Cu radius the Pauli repulsion for the phenyl-rings sets in at a closer distance, the low z -height of the -N=N- moiety is incompatible with a fully planar trans adsorption geometry. As shown in Table 7.1 this leads to a pronounced buckling of the molecule with a final dihedral angle ω almost equal to

that of the adsorbed cis isomer. The cost of this severe distortion of trans azobenzene again directly carries over to the final adsorption energy. As a result, whereas the d_{NN} elongation and E_{ads} are both large in the cis isomer, E_{ads} is smaller in the trans isomer despite an even greater d_{NN} elongation.

At Cu(111) this difference in the net adsorption energy finally leads to a reversal of the relative stability, i.e. we obtain the cis isomer to be more stable by -0.24 eV than the trans configuration, which as such is an intriguing find. It is again intuitively rationalized by the different preferred adsorption heights of the central azo-bridge and the closed-shell phenyl-rings, which can be much better accommodated in the three-dimensional cis form. For any strong enough azo-bridge to surface bonding this will naturally offset the higher gas-phase stability of the trans isomer, and as indicated by our calculations this seems to be the case at Cu(111). Indeed, these results are in qualitative agreement with previous work⁵⁵ on the azobenzene derivative di-meta-cyano-azobenzene (DMC) adsorbed at the Cu(100) surface.

7.2.3. Electronic Structure

Important information concerning the bonding mechanism at the surface is already provided by the electronegativity (EN) of the isolated molecule. For trans and cis azobenzene we compute the Mulliken EN^{218,219}, defined as the mean of electron affinity and ionization potential, as 4.44 eV and 4.11 eV, respectively (see Table 7.3). Again starting our discussion with the adsorption at Au(111), comparing these values to the clean surface work function $\Phi_{\text{Au}(111)} = 5.20$ eV, this suggests some charge transfer from the molecule to the metal substrate, and more specifically slightly more charge transfer in the case of the less electronegative cis isomer.

The calculated lowering of the work function for trans and cis azobenzene adsorption of -0.37 eV and -1.30 eV, respectively, is consistent with this expectation, cf. Table 7.3. Quantitatively it is important however, to realize that even without any charge transfer (or more generally charge rearrangement) upon adsorption a work function change can already result if the molecular over-layer as such exhibits a non-zero dipole moment²¹². In this respect, the two azobenzene isomers differ significantly in that the gas-phase trans configuration has no dipole moment, whereas the cis configuration exhibits a finite calculated dipole moment of 3.23 Debye.

In order to disentangle the contributions to the work function change, we therefore compute the potential change across a free-standing molecular over-layer in exactly the same geometric structure as it has in the adsorbed state. Subtracting this term we arrive at the work function change $\Delta\Phi^*$ solely due to the charge rearrangement caused by the interaction of the over-layer with the metal substrate. As shown in Table 7.3, the values for $\Delta\Phi^*_{\text{Au}(111)}$ are -0.36 eV and -0.55 eV for trans and cis azobenzene, respectively, which now fit almost too perfectly into the electronegativity picture of an only slightly larger charge transfer to the metal in case of the cis isomer.

		Trans	Cis
EA	–	1.06	0.75
IP	–	7.82	7.47
EN	–	4.44	4.11
	Φ	4.83	
Cu(111)	$\Delta\Phi$	-0.69	-0.96
	$\Delta\Phi^*$	-0.15	+0.11
	Φ	4.46	
Ag(111)	$\Delta\Phi$	-0.26	-0.77
	$\Delta\Phi^*$	-0.25	+0.03
	Φ	5.20	
Au(111)	$\Delta\Phi$	-0.37	-1.30
	$\Delta\Phi^*$	-0.36	-0.55

Table 7.3.: Electron affinity (EA), ionization potential (IP), and Mulliken electronegativity (EN) of the free trans and cis azobenzene molecule, compared to the work function of the clean surface (Φ), the change of the work function induced by the adsorbed molecule ($\Delta\Phi$), and the change of the work function after subtracting the change induced by the potential drop through the molecular over-layer ($\Delta\Phi^*$), see text. The last two values correspond to the molecular coverage as resulting from the employed surface unit cell. Nevertheless, since we use the same (6×3) unit cell for both isomers, the induced work function changes are directly comparable. All values are given in eV.

At this stage, we stress, however, the well-known limitations of the charge transfer notion at metallic surfaces¹⁸⁸. Distinguishing between an actual transfer of charge between molecule and substrate or a polarization of the molecular charge accompanied by a varying degree of charge displacement due to Pauli repulsion in the overlapping electron density tails of the bonding partners is to some degree semantics²²⁰. We make no attempt to contribute to this discussion here, and henceforth simply refer to charge transfer in quotes to emphasize its conceptual nature.

Figure 7.5 analyzes the azobenzene at Au(111) interaction in terms of the PDOS projected onto the molecular frontier orbitals. Similar to the discussion of the work function changes we aim to single out the effect of the charge rearrangement upon adsorption by also showing the level positions as they would result within a Schottky-Mott model, i.e. by simply aligning the vacuum level of the free molecule and the clean surface.

While this model in general ignores the formation of a surface dipole, we modify it for our purposes by including the above described potential change caused already by the dipole moment of the free-standing molecular over-layer. Any shift between the orbital

energy in this modified Schottky-Mott model and in the fully self-consistent calculation can this way be attributed to the charge rearrangement caused by the molecule-surface interaction.

Starting with the PDOS of trans azobenzene at Au(111) shown in the left upper panel of Fig. 7.5, we see the four projected frontier orbitals, HOMO-1, HOMO, LUMO, and LUMO+1 broadened with hardly any degree of intermixing with Au d -states. Compared to their position in the modified Schottky-Mott model all levels are roughly equally shifted by about 0.8 eV to lower energies, which is the direction one would also expect from the previously discussed “charge transfer” into the metal substrate, but which could equally well merely result from the lowering in the surface potential. Despite the down-shift, the LUMO still remains well above the Fermi-level.

Both this and the actually resulting HOMO and LUMO positions at -0.7 eV and $+1.2$ eV respectively are in reasonable agreement with scanning-tunneling spectroscopy (STS) measurements by Choi et al.⁴⁸. This suggests that the sizable self-interaction induced error in the description of the HOMO-LUMO gap of the free molecule (cf. subsection 7.2.1) is less influential here, and that the orbital energies of the surface adsorbed molecule may be rather adequately described at the GGA-PBE level.

In case of cis azobenzene adsorption at Au(111) the actual level positions are in general at lower energies, cf. Fig. 7.5. This is primarily due to the fact that because of the finite potential change caused by the free-standing molecular over-layer already the level positions in the modified Schottky-Mott model lie at lower energies. With a comparable down-shift of the self-consistently calculated frontier orbitals as for trans azobenzene (*vide infra*), this has as one consequence that the projected LUMO lies now just above the Fermi-level. As a second consequence, both the HOMO and HOMO-1 level fall right into the energy range of the Au d -band with a concomitant stronger hybridization.

The down-shift of the LUMO is with about 1.0 eV even slightly stronger than for the trans isomer, again in line with the above discussed picture of a slightly stronger “charge transfer” as inferred from electronegativity differences and work function changes, or alternatively with a stronger lowering in the surface potential due to the lower adsorption height of this isomer. The exception of the much smaller shift of the LUMO+1 level of only 0.4 eV is in this respect primarily due to the distorted adsorption geometry:

The computed LUMO+1 for a free molecule in this distorted geometry is higher in energy than in the relaxed gas-phase geometry, and taking this into account one arrives at an effective down-shift of the LUMO+1, comparable to that of the other frontier orbitals.

Moving to the azobenzene adsorption at Ag(111) we find essentially the same picture as obtained at Au(111), yet with subtle and intriguing modifications. The lower surface work function of $\Phi_{\text{Ag}(111)} = 4.46$ eV yields a considerably smaller electronegativity difference to the azobenzene molecule, and one would correspondingly expect a smaller “charge transfer”. The reduced work function change $\Delta\Phi^*$ upon trans azobenzene adsorption, i.e. after correcting for the dipole moment of the free-standing molecular over-layer, is consistently at -0.23 eV smaller than the corresponding value at Au(111), cf. Table 7.3.

The approximately uniform down-shift of the projected frontier orbitals compared to their position in the modified Schottky-Mott model shown in Fig. 7.5, is with about

7.2. RESULTS AND DISCUSSION

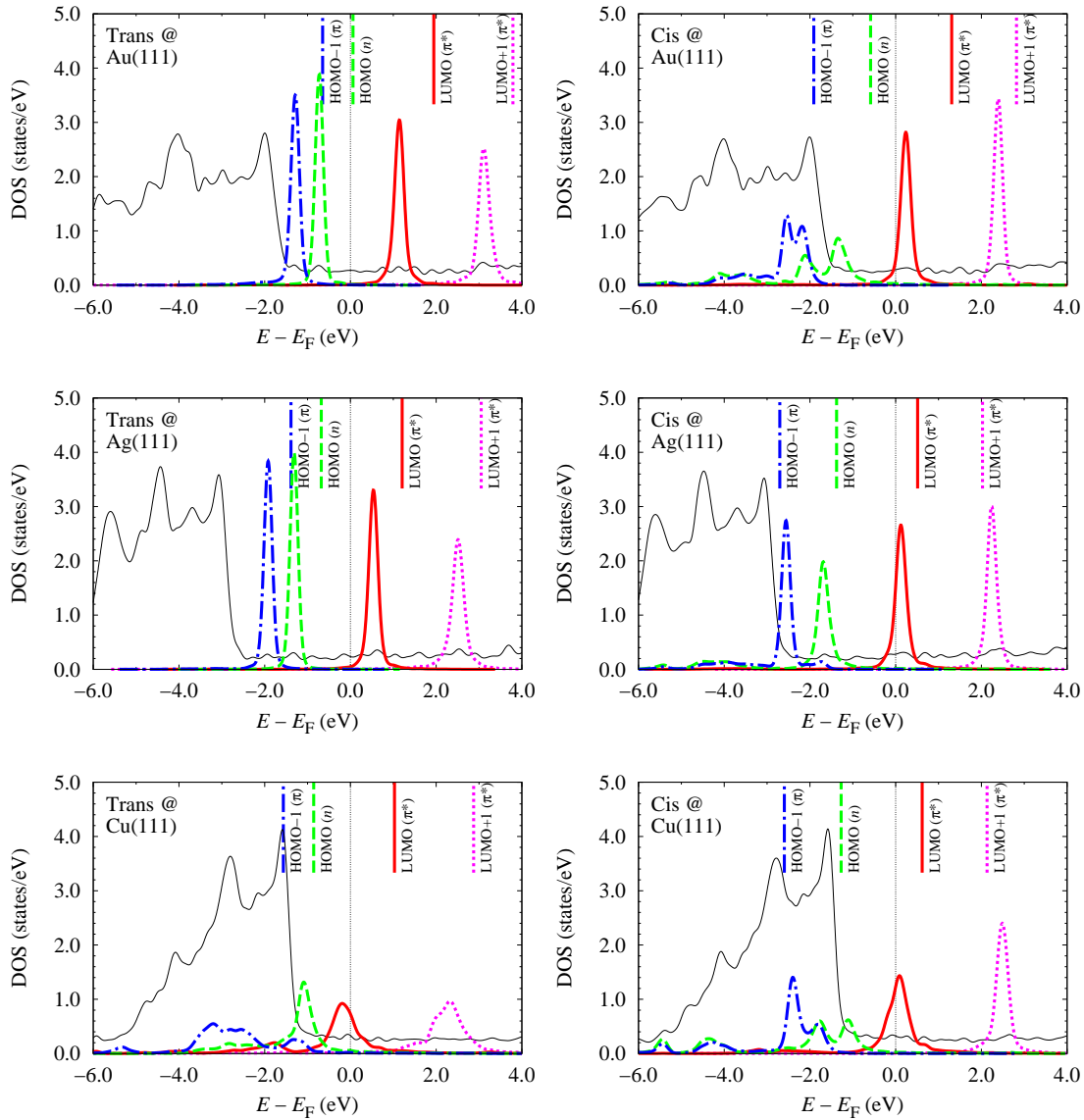


Figure 7.5.: Density of states (DOS) projected onto the frontier orbitals of gas-phase azobenzene: HOMO-1 (blue dotted line), HOMO (green dashed line), LUMO (red solid line), LUMO+1 (magenta dash-dotted line), see Fig. 7.3 for a representation of these orbitals in the free molecule. Additionally shown is the total DOS of the employed super-cell downscaled by a factor 75 (thin black line), as well as the position of the corresponding frontier orbitals (vertical sticks at the upper x -axis) in a modified Schottky-Mott picture that neglects the formation of a surface dipole through charge rearrangement upon adsorption (see text). Upper panel: Au(111). Middle panel: Ag(111), Lower panel: Cu(111). For all three surfaces adsorption of the trans isomer is shown on the left, and adsorption of the cis isomer on the right.

0.6 eV smaller than the corresponding value of 0.8 eV for trans adsorption at Au(111). Because of the much smaller Ag(111) work function the LUMO nevertheless ends up closer to the Fermi-level than was the case at Au(111), and is further lowered to just above E_F in the van der Waals corrected geometry. With the Ag d -band starting at lower energies not even the HOMO-1 has significant overlap with the metal d -states, and we find all four frontier orbitals largely retaining their molecular character, however. While all of these findings fit perfectly into the overall picture developed at Au(111), the deviations start when turning to the cis azobenzene adsorption. From the smaller electronegativity of this isomer, one would expect a slightly larger “charge transfer” than in the case of trans azobenzene, and correspondingly a somewhat larger reduced work function change $\Delta\Phi^*$ as was the case at Au(111).

However, the calculated $\Delta\Phi^*$ is essentially zero, cf. Table 7.3. We attribute this to the closeness of the LUMO to the Fermi-level already in the modified Schottky-Mott model, as apparent in Fig. 7.5. A “charge transfer” or surface potential induced down-shift of this orbital leads therefore to a significant population of this formerly unoccupied level with a concomitant charge back-donation into the molecule counteracting the work function lowering. This more complex interaction is finally also obtained for trans and cis azobenzene at Cu(111), where we now find a significant LUMO population for both isomers. That this results also for the trans case is partly already due to the strongly distorted adsorption geometries described in subsection 7.2.2 above. These distorted geometries exhibit a much increased dipole moment, which offsets the somewhat larger Cu(111) work function, cf. Table 7.2, and leads to level positions in the modified Schottky-Mott model that are as low as in the case of Ag(111).

With the higher-lying Cu d -band and the much shorter distance of the adsorbed molecule above the Cu(111) surface this enables a much stronger hybridization of the frontier orbitals than at the other two coinage metal surfaces, which is even further increased at the van der Waals corrected geometry. As a result HOMO-1, HOMO and LUMO all form broad bands with mixed metallic and molecular character and the counteracting donation and back-donation contributions result in small overall reduced work function changes $\Delta\Phi^*$ for both isomers, cf. Table 7.3.

7.3. Summary

The initially formulated goal of this chapter is to exhaustively characterize the adsorption of azobenzene at coinage metal (111) surfaces, using DFT within the GGA approximation of the xc-functional. The results may be qualitatively summarized in terms of three major contributions to the adsorption energy, namely the intra-molecular distortion energy, the Pauli repulsion between phenyl rings and substrate, and a covalent-type bonding of the azo-bridge (or -N=N- moiety) lone pair and the substrate. Whereas the second effect is weakly dependent on the adsorbate - substrate registry, the third effect prefers a 1:1 metal - N atom coordination, which due to the dimensions of the azo-bridge and the equilibrium bulk metal lattice constant is closest approximated in a geometry where the molecule centers on and aligns with the bridge site of the (111) lattice.

Important qualitative differences between substrates in the balance of these effects are observed: At Cu, the third bonding component is strong, pinning the azo-bridge at a short surface distance comparable to Cu-N bonds of transition metal complexes. In the planar trans isomer, the proximity of the phenyl rings to the surface leads to a repulsion strong enough to overcome the first bonding component, resulting in a substantial distortion of the molecular geometry compared to gas-phase. In the three-dimensional cis isomer, the phenyl rings naturally remain at a larger distance to the surface, which greatly reduces the ring repulsion, leaving the gas-phase geometry virtually unchanged. Consequentially, the cis-trans isomer relative stability at Cu(111) is reduced by nearly 1 eV from the gas-phase value, to the point of changing its sign.

At Ag(111), the overall adsorbate - substrate interaction is significantly weaker. While still strong enough to orient the adsorbate in the same geometry as at Cu(111), the third mentioned bonding component is not able to significantly distort the trans isomer. Still, the competition between azo-bridge and phenyl ring substrate interactions is weaker in the cis isomer, leaving the relative isomer stability reduced, albeit much less so than in the case of Cu, and still positive. Au(111) proves less reactive still, and exhibits a DFT-GGA bonding picture very similar to that of Ag(111), up to a less reduced relative isomer stability. These findings are intuitively rationalized in terms of the more reactive Cu *d*-band in conjunction with the smaller Cu atomic radius.

However, the severity of these predictions must be emphasized: DFT-GGA suggests, that the cis isomer is significantly more stable than the trans isomer at Cu(111), which likely would have radical consequences for the switching function at this substrate. This is however straightforward to test experimentally, and goes diametrically against current findings in similar systems^{47,55}. In fact, as will be shown in the following chapter, the strong geometrical distortion and ensuing isomer stability reversal at Cu is a mere artifact of deficiencies in the DFT-GGA description of dispersive van der Waals interactions.

Our PDOS analysis within a modified Schottky-Mott model is qualitatively unaffected by the lack of dispersive van der Waals interactions (see section B.6), and hints at possible reasons for the variety of experimentally observed switching behavior. The very strong hybridization of the adsorbate HOMO-1 to LUMO+1 with the Cu electronic structure in both isomers is a plausible explanation for the extremely low switching yield observed at Cu(111). Also at Ag and Au, hybridization and broadening of several orbitals is significant, in particular in the cis isomer, again in line with the observed failure⁶¹ of conventional light-induced isomerization of the surface mounted switch.

On the other hand, the actual degree of hybridization of the occupied orbitals just might be the key to the switch function, considering the HOMO-involving substrate-mediated charge-transfer process recently suggested in the context of the reversible photo-induced isomerization of TBA at Au(111)⁶². Another intriguing aspect is the partial occupation of the LUMO in both isomers at Cu(111) and in the cis isomer at Ag(111) with a corresponding back-donation contribution to the bonding. Only at Au(111) does the LUMO position remain distinctly above the metal Fermi-level for both isomers. This has quite some bearing on the negative ion resonance mechanism discussed in the context of tip-manipulation techniques⁸⁷ and could explain why hitherto only such isomerization of pure azobenzene has been reported for this surface⁴⁸.

8. Azobenzene at Coinage Metal Surfaces: The Role of van der Waals Interactions

In the previous chapter, a detailed and methodologically well-defined picture of the trends in azobenzene adsorption at coinage metal (111) surfaces was established at DFT-GGA level of theory. While several general features are already well described, neither the geometries nor the energetics can be presumed particularly predictive. This is predominantly due to the limitations of (semi-)local DFT exchange-correlation (xc) functionals in the description of dispersive *van der Waals* (vdW) interactions, as already briefly mentioned but yet unqualified. The characterization, evaluation and correction of these deficiencies is the goal of this chapter. The work detailed here has been published in Phys. Rev. B^{IV}.

Historically, the term “van der Waals interactions” has included *all* intermolecular interactions other than simple electrostatics. The former are traditionally divided into three major contributions: The first is the coupling of finite electric multipole moments of the isolated molecules, which is dominated by the so-called permanent dipole - permanent dipole interaction. This term is typically well described by average charge densities as given by simple mean-field theories, e.g. Hartree-Fock. The multipole coupling and electrostatic interaction changes the permanent molecular dipoles in proportion to the molecular polarizability, in a second term dominated by the the so-called induced dipole - induced dipole interaction. Finally, small fluctuations in the molecular charge density over time, corresponding to a time-dependent intermolecular field, give rise to additional, instantaneous induced dipole - induced dipole interactions. Thus, the frequency-dependence of the polarizability introduces a frequency dependence, or so-called dielectric dispersion, in the intermolecular dielectric function.

The last term is a pure correlation effect, of which only the low-frequency limit can be approximated by time-independent theory. In the limit of zero charge density overlap, i.e. at intermediate to large molecular separation, the second term is also strictly due to electronic correlation. Consequentially, neither term is generally accounted for by Hartree-Fock theory. In the following, the sum of these terms is for simplicity labeled ‘dispersive vdW interactions’.

Local or *semi-local* DFT xc-functionals face similar difficulties with non-overlapping charge densities: Consider a finite and continuous charge density n , self-consistent with a local xc-functional. At one point in space, the density $n(\mathbf{r}+\delta)$ will indirectly depend on the density $n(\mathbf{r}-\delta)$ at another, via the density $n(\mathbf{r})$ at a point in between. Thus, while the *functional* is strictly local, the charge density exhibits a finite, albeit unphysically short, correlation length. However, if \mathbf{r} is located between two well separated charge density fragments, then $n(\mathbf{r}) = 0$, and the connection is severed. Consequentially, the local

xc-functional total energy of two non-overlapping charge densities will with increasing separation much too rapidly approach the sum of the total energies of the corresponding isolated charge densities.

Of course, if the exact xc-potential is v -representable, an exact solution for the charge density could by the Hohenberg-Kohn theorem¹⁰¹ be exploited to create an exact, system- and basis set-dependent local functional of the density, which in turn would reproduce the same exact charge density and total energy, including all time-independent correlation effects. It is however obviously tremendously difficult, if even at all possible, to “build in” such non-local information in a *universally transferable* local functional, without prior knowledge of *all* exact solutions.

As a consequence, all xc-functionals with local or semi-local expressions for the correlation energy, including most of the parametrizations in the field, perform poorly for vdW-bonded systems²²¹: For example, as expected of an otherwise accurate xc approximation, GGA functionals underestimate interaction energies and equilibrium bond lengths^{220,222} (cf. previous chapter). LDA functionals do not sufficiently penalize variations in the charge density, which usually results in a comparable *overbinding*^{220,222} at short range, and a GGA-like underbinding at long range. Correspondingly, albeit more generally dependent on the approximate xc treatment, polarizabilities are grossly overestimated^{223–225} by (semi-)local xc-functionals.

An accurate description of vdW interactions is crucial for theoretical modeling of aromatic molecule adsorption and bonding in general¹⁹⁹, and because of the lack of other significant bonding contributions, for adsorption at chemically inert solid surfaces in particular^{193–195,226,227}. Even at more reactive surfaces, weak interactions can profoundly influence qualitative aspects of strong interactions¹⁹⁶. In light of the picture of azobenzene adsorption at coinage metal surfaces established in the previous chapter - of three bonding contributions in a delicate, self-consistent balance - a better treatment of weak interactions, amounting to adding a fourth component to the mix, can be expected to have significant consequences.

A phenyl moiety ($-\text{C}_6\text{H}_5$) is chemically very similar to a benzene (C_6H_6) molecule. Indeed, comparing the ~ 0.6 eV binding energy per benzene molecule adsorbed at (111) coinage metal surfaces derived from temperature programmed desorption (TPD) experiments^{34–36} to the essentially zero value obtained within DFT-GGA²¹³, suggests that the binding energy of the trans azobenzene isomer presented in the previous chapter might be underestimated by more than 1 eV.

The development of an accurate yet tractable treatment of weak correlation effects poses one of the greatest unsolved challenges in contemporary first-principles modeling, and recent years have seen a plethora of proposed solutions. These may be divided into three main categories, namely use of more accurate correlation models or higher-level theory, construction of explicitly non-local DFT correlation functionals, and development of semi-empirical dispersion correction schemes.

The first category has traditionally focused on adapting and extending well-established post Hartree-Fock methods to surface adsorption problems, e.g. in a variety of embedding techniques, in which local region of particular interest is treated with an accurate, computationally expensive level of theory, and embedded in a rest treated with a less

accurate, cheaper level of theory^{189,190,228}. This idea is applied to the adsorption of benzene in chapter 10. While this approach arguably has the best theoretical foundation of the three, it simultaneously relies on sufficient accuracy and tractability of the more expensive level of theory even for e.g. metallic systems, and locality of the important interactions, none of which must generally hold. Recent developments of the RPA (see section 4.2) as a moderately expensive alternative also fall into this category. The RPA has been successfully implemented in periodic boundary conditions^{194,222}. Still, its predictions do not perfectly match reference data¹⁹⁴, and its computational cost orders of magnitude greater than that of standard DFT.

The second category relies on the idea of treating long-range vdW interactions within a non-local xc-functional derived from an approximation of the unknown dielectric function in an arbitrary system^{229–231}, combined with a standard xc-functional for the short range. While this approach has been shown to correct DFT-GGA underbinding in some cases^{195,232}, existing implementations have proven numerically complex and more expensive than standard xc-functionals, and only moderately accurate for thermochemical benchmarks²³³. Recent work claims improvements on both counts, however^{234,235}.

While the time to solution for single total energy evaluations of several of the above methods is acceptable (on the order of weeks) even for large systems given cutting edge numerical technology and computational resources, the observed delicate interplay between geometric and electronic structure in azobenzene surface bonding requires an exhaustive exploration of adsorbate and adsorption geometries. With typical geometry optimizations for a molecule of this size requiring on the order of a hundred total energy evaluations, and energy gradient expressions not possible or yet developed for some of the above methods, we are here in practice restricted to the third category above:

In the semi-empirical dispersion correction approach, weak interactions of (semi-)local DFT are corrected by a simple analytical expression, with semi-empirically determined coefficients^{197–205}. This correction has proven remarkably accurate for a range of systems, adds zero computational cost to that of the underlying DFT, and deriving its gradient contribution is trivial. However, purporting to describe weak electronic correlation effects as a function of nuclear coordinates, this idea should of course be taken *cum grano salis*. The combination of accuracy and low cost also generally comes at the price of an uncertain transferability. In particular, the application of this methodology to metallic systems is controversial, as discussed below. Thus, in addition to a methodological improvement on the results of the previous chapter, the following aims at a critical assessment of the semi-empirical dispersion correction approach for metal surface adsorption problems. At the time this study was initiated, no accurate experimental or theoretical reference data on pure azobenzene adsorbed at coinage metal surfaces existed. Therefore, we also study the adsorption of benzene at the same substrates, as a vehicle for comparison to available TPD data.

8.1. Theory

8.1.1. Semi-Empirical Dispersion Correction Schemes

Using second-order quantum perturbation theory, Fritz London could as early as 1930^{236,237} derive the dispersion interaction between two charge neutral, spherically symmetric, non-overlapping atoms i and j as a power series in the inter-atomic distance R_{ij} . The leading term of this series is the negative sixth power of R_{ij} multiplied by an effective, system dependent dispersion (or 'C₆') coefficient. Within the second order approximation these coefficients are additive²³⁸, and the dispersion interaction of collections of atoms can be derived by summing over $C_{6,ij} \cdot R_{ij}^{-6}$ atom pair terms, or performing the corresponding volume integrals. This leads to e.g. the C_3R^{-3} vdW potential in the vicinity of a uniform, macroscopic object (a solid surface, for example).

Effective inter-atomic (or -molecular) C_6 coefficients can be calculated by integrating the corresponding frequency dependent polarizabilities $\alpha(\omega)$ over all imaginary frequencies²³⁹

$$C_{6,AB} = \frac{3}{\pi} \int_0^\infty d\omega \alpha_A(i\omega) \alpha_B(i\omega) \quad , \quad (8.1)$$

which in turn using frequency-independent quantities can be approximated²⁴⁰ as

$$C_{6,AB} \approx \frac{3}{2} \cdot \frac{\alpha_A(0) \alpha_B(0) I_A I_B}{I_A + I_B} \quad , \quad (8.2)$$

where I and $\alpha(0)$ are the atomic (molecular) ionization potential and static polarizability, respectively.

In the semi-empirical dispersion correction approach, the difference between the exact and (semi-)local DFT inter-atomic interaction is approximated by a simple isotropic potential. At long range, this potential is given by the $C_{6,ij} \cdot R_{ij}^{-6}$ term. At short range, the long-range expression is matched to the DFT potential by multiplication with a damping function $f(R_{ij}^0, R_{ij})$, which reduces the additional dispersion contribution to zero, subject to a cutoff defined by some suitably calculated combination R_{ij}^0 of the vdW radii of the atom pair, as illustrated in Fig. 8.1. The dispersion corrected xc-functional is then formed by adding the correction potential to the ordinary DFT xc-functional.

The dispersion corrected total energy E_{tot} may thus be written as

$$E_{\text{tot}} = E_{\text{DFT}} + s_6 \sum_{i=1}^N \sum_{j>i}^N f(S_R R_{ij}^0, R_{ij}) C_{6,ij} R_{ij}^{-6} \quad , \quad (8.3)$$

where E_{DFT} is the standard DFT total energy, and the sums run over all N atoms in the system. The functional dependence of the exact correction potential is accounted for by semi-empirical fitting of the parameters s_6 or S_R as detailed below.

While effortless to evaluate computationally, this general expression has obvious weaknesses, of which perhaps the most glaring is the (free-) atom-in-molecule approximation: The substantial variation of properties between effective 'atoms' of the same species in

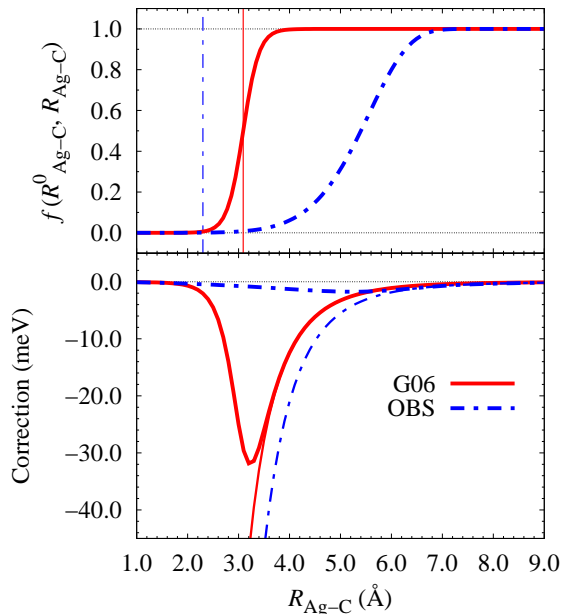


Figure 8.1.: Illustration of the dispersion correction between a Ag-C atom pair as a function of their inter-atomic distance $R_{\text{Ag-C}}$. Upper panel: The damping function $f(R_{\text{Ag-C}}^0, R_{\text{Ag-C}})$ for the OBS and G06 schemes (medium lines, see text), and the corresponding effective $R_{\text{Ag-C}}^0$ (thin lines). Lower panel: The corresponding bare $s_6 C_{6,\text{Ag-C}} R_{\text{Ag-C}}^{-6}$ potentials (medium lines) and full correction potentials after multiplication with the damping function (thick lines, cf. Eq. (8.3)). The TS correction potential is qualitatively very similar to that of G06, differing in $s_6 C_6$ and $S_R R^0$ parameters only.

the molecule, e.g. the influence of hybridization states on effective polarizability, is neglected. This may be particularly severe for the metal surface, where the lowering of the effective dielectric constant due to screening²⁴¹ should be reflected by reduced dispersion coefficients of atoms in deeper layers in the substrate.

The applicability of such semi-empirical dispersion corrections to metallic systems in general, and transition metals in particular, is therefore uncertain. In order to again focus only on trends in the obtained results robust with respect to the xc-treatment, we therefore study the variation of our results between three published, different dispersion correction schemes:

The first scheme was published by Ortmann, Bechstedt and Schmidt (OBS)²⁰⁰, and uses Eq. (8.2) and literature values for ionization potentials and static polarizabilities of varying quality to approximate dispersion coefficients. These are compiled in Table 8.1, together with those of the other two schemes. The notably shallow, long-ranged damping function in the OBS scheme illustrated in Fig. 8.1 was fitted with the GGA of Perdew and Wang (PW91)^{242,243} to reproduce the experimental c -lattice constant of graphite. This scheme was not developed for universal transferability and does not provide parameters for other xc-functionals, and is included here mainly to illustrate the influence of the damping function.

		$s_6 \cdot C_{6,ij}$ (eV·Å ⁶)			$S_R \cdot R_{ij}^0$ (Å)		
		H	C	N	H	C	N
	OBS	31.9	77.7	54.0	1.81	2.21	2.19
Au	G06	–	–	–	–	–	–
	⟨TS⟩	19.7	62.0	45.9	3.34	3.65	3.56
	OBS	35.0	86.1	59.2	1.90	2.30	2.28
Ag	G06	14.5	51.1	42.8	2.64	3.09	3.04
	⟨TS⟩	19.3	60.9	43.7	3.31	3.62	3.54
	OBS	30.6	75.0	51.6	1.75	2.15	2.13
Cu	G06	9.5	33.8	28.3	2.56	3.01	2.96
	⟨TS⟩	17.9	55.6	40.1	3.31	3.62	3.53

Table 8.1.: Calculated $C_{6,ij}$ dispersion coefficients and cutoff radii R_{ij}^0 between elements i and j . As the dispersion coefficients in the TS scheme depend slightly, $\sim \pm 5\%$ for adsorbed trans azobenzene, on the effective atomic volume we only show averaged values over all atomic constituents of each species. To allow direct comparison between the effective parameters employed by the three schemes, we show the values $s_6 C_{6,ij}$ and $S_R R_{ij}^0$, i.e. after multiplication with the xc-functional dependent scaling factors (see text). Note that the G06 scheme does not feature parameters for Au.

The second scheme is the 2006 revision²⁰¹ of a correction proposed by Grimme in 2004 (G06)²⁴⁴. It features parameters calculated from first-principles for most of the periodic table (although not including Au), a compared to OBS steeper and shorter ranged Fermi damping function, cf. Fig. 8.1, and an xc-functional dependence determined by fitting to thermochemical benchmark calculations. This popular scheme does aim for universal transferability, and has already been applied to similar surface adsorption problems^{196,226}.

However, for the present work, two design choices of G06 may prove detrimental: First, the problem of defining transferable transition element ‘atoms’, is admittedly²⁰¹ crudely solved by taking their parameters as the mean of those of the preceding noble gas atom and the following group III element. Thus, while first row G06 parameters may be more accurate than the corresponding approximate parameters in OBS, the case for the transition row in G06 is uncertain. Second, the xc-functional dependence is introduced by (effectively) scaling the dispersion coefficients with a factor $s_6 \neq 1$ (cf. Eq. (8.3)) which corrects most for the xc-functional where its influence is smallest, i.e. shifting the $C_{6,ij} \cdot R_{ij}^{-6}$ potential also at long range, where it can be expected to be most accurate.

The third scheme was recently put forth by Tkatchenko and Scheffler²⁰² (TS), and represents the state of the art. In this scheme, following the work of Johnson and

Becke²⁴⁵ and Olasz et al.²⁴⁶, the relationship between polarizability and volume²⁴⁷ is exploited to account for the relative change of 'atomic' properties in different bonding states:

Reference homonuclear dispersion coefficients derived using Eq. (8.1) from highly accurate atomic polarizabilities, calculated using self-interaction corrected TDDFT by Chu and Dalgarno²⁴⁸, are rewritten as heteronuclear coefficients²⁴⁹ and weighted with the ratio of the effective volume of each 'atom' in the molecule, to its volume in the gas phase.

The former are obtained from Hirshfeld partitioning²⁵⁰ of the self-consistent density, as further detailed below. The TS scheme uses the same Fermi damping function as the G06 scheme, but following Jurečka et al.²⁰³, instead scales the combined vdW radius by a xc-functional dependent factor $S_R \neq 1$, thereby correcting where the xc-functional influence is strongest, and leaving asymptotics intact. Atomic vdW radii are consistently obtained for each element from isodensity contours calculated from first-principles. All in all, the TS scheme has proven 2 - 4 times more accurate than other schemes in thermochemical benchmark calculations²⁰².

8.1.2. Density-Functional Theory Calculations

All azobenzene DFT calculations were performed precisely as stated in the previous chapter, with the exception that dispersion corrected geometries were optimized at four layer metal slabs. Benzene calculations were performed in the same way, in (3×3) surface unit cells (see section B.3) with the same irreducible \mathbf{k} -point density as in the azobenzene case, corresponding to a $(4 \times 4 \times 1)$ MP grid. In the benzene LDA¹¹⁴ calculations, the corresponding equilibrium lattice constant calculated in section B.1 was used to construct slab geometries.

The three above mentioned dispersion correction schemes, in addition to that of Jurečka et al.²⁰³, were implemented in real-space periodic boundary conditions (PBC) in an external FORTRAN 90 module. Compared to the Ewald-summation²⁵¹ based implementations already available in literature²⁵², a real-space implementation offers several significant advantages:

In contrast to the electrostatic potential, the dispersion correction potential converges in a crystal lattice. The energy and gradient correction for the central super-cell can therefore be calculated in shells of its periodic images, constructed to respect the symmetry of the potential. Image interactions are independent, allowing for efficient parallelization and fast evaluation, which can be necessary in applications where DFT total energy evaluations are fast (e.g. for DFT molecular dynamics of light molecules or small systems). Fourier transforms are not needed, which reduces numerical noise and eliminates the dependence on external routines.

The real-space formulation also allows for *partial* periodicity such, that a boundary condition dimensionality $0 \leq D \leq 3$ can be chosen for arbitrarily defined subsets of the super-cell atoms, and *broken* periodicity, in which the correction potential is made periodic only along the positive direction of a lattice vector, for example. For the present problem, this allows us to construct the dispersion correction potential in the precise

geometry of an isolated molecule on a 2D periodic metal slab, eliminating the need for convergence of the super-cell size with respect to unwanted lateral dispersion interactions. For systems of the size considered here, this saves tremendous amounts of computing time.

Finally, expressions for the dispersion correction contribution to the super-cell stress have been derived, enabling accurate and efficient variable super-cell calculations of e.g. molecular crystals²⁵³. Our module, including the above described functionality and more, is distributed free of charge under the Lesser GNU Public License* (LGPL), and will be interfaced to several other codes, in addition to the CASTEP²⁰⁶ implementation.

The Hirshfeld analysis is based on the (soft) pseudo charge densities for both the superposition of atomic and the self-consistent densities. Hirshfeld charges and volumes are integrated on the standard real space grid as provided by the plane-wave basis set. We compared the results of our implementation for several small organic molecules and the fcc bulk phases of Au, Ag and Cu to reference values obtained with the all-electron code FHI-AIMS²⁵⁴ which employs numerical atom centered basis functions based on radial grids. For the transition metal (pseudo-) atoms the obtained Hirshfeld volumes differ rather substantially from the reference values.

However, the ratios of the two volumes, which are the only required input for the TS scheme, are in very good agreement with the reference numbers in all cases and for all elements in this study. As a side remark, we note that this demonstrates for the first time the applicability, with very modest implementation effort, of the TS scheme to DFT calculations done with a plane wave basis set. Further details on this implementation and numerical tests will be the topic of a future publication.

Thus calculated dispersion corrections were applied as follows: Where applicable, damping function parameters (see previous section) optimized for the employed GGA-PBE functional were used, i.e. $s_6 = 0.75$ (G06)²⁰¹ and $S_R = 0.94$ (TS)²⁰² was used in Eq. (8.3). All adsorbate and gas phase molecular geometries were fully optimized with each of the three correction schemes. Since their effect on adsorption energies E_{ads} were found negligible and in light of the anticipated limitations of dispersion corrections for surface properties, intra-substrate dispersion contributions were turned off, and the substrate atoms frozen in their relaxed GGA-PBE geometry. As briefly mentioned above and further discussed below, the dispersion coefficients of deeper substrate layers should be screened by an unknown amount. In light of this, and the fact that the total effect of considering a numerically infinite number of layers amounted to an E_{ads} contribution of some 80 meV, all dispersion corrections were calculated in a four layer, asymmetric adsorbate substrate geometry.

Dispersion corrected E_{ads} and relative cis-trans isomer stabilities $\Delta E_{\text{C-T}}$, again calculated in optimized, inversion-symmetric seven layer slab geometries, were defined as in Equations (7.1) and (7.2), respectively. Since the electronic structure analysis of section is not performed for benzene, the corresponding adsorption energies were calculated in asymmetric four layer slab geometries, analogous to section B.3 and Eq. (B.3). We additionally calculated the zero-point energy correction $E_{\text{ads}}^{\text{ZPE}}$ to the benzene adsorption

*See <http://www.gnu.org/licenses/lgpl-3.0.txt>

		Trans			Cis		
		z (Å)	d_{NN} (Å)	ω (°)	z (Å)	d_{NN} (Å)	ω (°)
Gas-phase	PBE	–	1.30	180	–	1.28	12
	PBE	3.50	1.30	180	2.31	1.29	18
Au(111)	OBS	3.48	1.30	180	2.24	1.30	19
	G06	–	–	–	–	–	–
	TS	3.28	1.30	180	2.23	1.30	18
	PBE	3.64	1.30	180	2.27	1.32	23
Ag(111)	OBS	3.60	1.30	180	2.20	1.32	25
	G06	2.75	1.33	180	2.14	1.32	25
	TS	2.98	1.31	179	2.16	1.32	25
	PBE	1.98	1.40	141	1.93	1.35	33
Cu(111)	OBS	1.97	1.40	142	1.91	1.35	33
	G06	2.05	1.40	169	1.89	1.35	35
	TS	2.05	1.40	167	1.89	1.35	34

Table 8.2.: Azobenzene structural parameters as defined in Fig. 7.4 and as obtained using GGA-PBE, and GGA-PBE corrected with the OBS, G06 and TS schemes. None of these affect the gas-phase geometric parameters, which is why only the PBE values are quoted here. Note that the G06 scheme does not feature parameters for Au.

energies. Since we aim to model isolated adsorbates, the required normal modes of the benzene molecule have been obtained as Γ -point phonons. In our super-cell setup these are computed via finite displacements from equilibrium positions to obtain the nuclear Hessian by numerical differentiation of the resulting dispersion corrected forces.

8.2. Results

8.2.1. Azobenzene Gas-Phase Properties and Adsorbate Geometry

We again begin with the properties of the gas-phase molecules. Reassuringly, no dispersion correction scheme significantly alters the already very accurate GGA-PBE gas-phase geometries described in subsection 7.2.1. In line with the discussion of section 6.1, the dispersion corrected $\Delta E_{\text{C-T}}$ is reduced to 0.44 eV (OBS), 0.47 eV (G06) and 0.49 eV (TS), worsening the agreement with experiment, and confirming the cancellation of long- and short range errors in the pure GGA-PBE numbers.

Turning to adsorbed azobenzene, we first note that due to the long-range nature

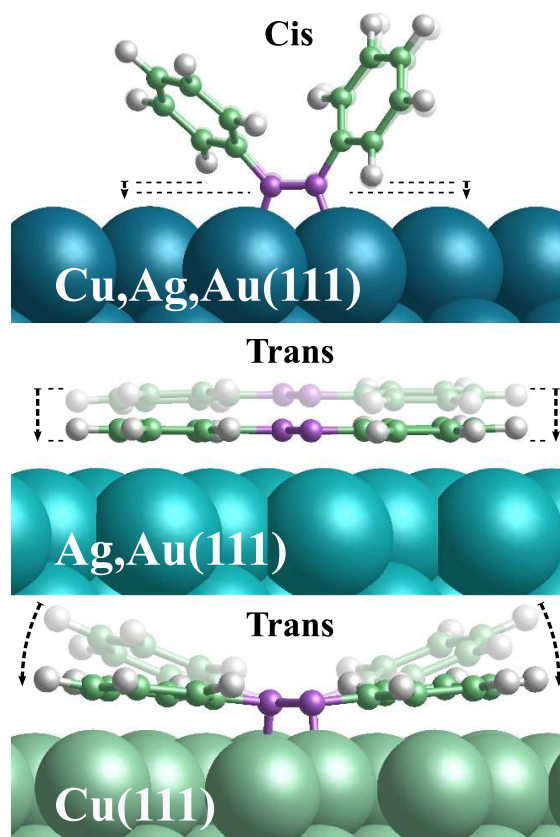


Figure 8.2.: Schematic illustration of the geometry changes induced by the G06 and TS correction schemes. Shown are side views with the GGA-PBE geometries shaded in the background as reference. The OBS scheme does not have a significant effect on the GGA-PBE geometries.

of the dispersive interactions the energetic correction provided by the semi-empirical schemes only shows a small corrugation with respect to lateral movements of the adsorbed molecule across the surface, leaving the optimal adsorption geometry largely determined by the DFT energetics. Correspondingly, full geometry optimizations of all high-symmetry adsorption geometries as defined in Fig. 7.2, at all surfaces and using all three dispersion correction schemes, again show a clear energetic preference for the B1 site.

As in our previous analysis of the in Fig. 7.4 defined vertical distance from the top surface layer to the azo-bridge plane z , the NN bond length d_{NN} , the CNNC dihedral angle ω , and the CNN bond angle α , the latter stayed unmodified from the gas-phase pure GGA-PBE value. The dispersion corrected values of the other three are listed in Table 8.2. At GGA-PBE level, gas-phase molecular geometries at Au(111) are largely unmodified by adsorption, a fact which dispersion corrections do not change:

OBS does not affect the trans isomer at all, and the geometry correction in the other cases is essentially limited to a small rigid shift of the adsorbate towards the substrate. For the trans isomer this means that the dihedral angle ω remains at its gas-phase value,

i.e. the molecule stays planar.

At Ag(111), the picture is somewhat more varied: Here, the stronger azo-bridge - surface interaction activates and elongates the NN bond in the cis isomer, a result unchanged by the dispersion corrections despite a small downward shift similar in magnitude to the changes of z observed at Au(111). For the trans isomer, correction effects range from none in the OBS scheme, to a dramatic reduction of z with concomitant elongation of d_{NN} in the G06 and TS schemes. Nevertheless, the trans isomer at Ag(111) again remains planar in all cases.

Finally, at Cu(111) the role of dispersion corrections is decidedly different from that at Au(111) and Ag(111): With GGA-PBE already yielding a strong azo-bridge to surface bond, which significantly elongates the NN bond and pins the bridge at a short vertical distance to the surface, the cis isomer z -shift induced by the dispersion schemes is smaller than at the other two substrates. Since this azo-bridge bond also determines the surface distance in the trans isomer and thereby puts the phenyl-rings well inside the range of surface Pauli repulsion, the intra-molecular distortion energy succumbs and as indicated by the large value for ω , the phenyl-rings are bent out of the molecular plane in GGA-PBE.

Again, the OBS scheme is too weak to influence this result. However, the G06 and TS schemes are not, and bend the phenyl-rings back towards the surface, yielding an ω of some 170 degrees, considerably closer to that of the gas-phase geometry (180°) than that of GGA-PBE ($\sim 140^\circ$). In fact, this restoring force, self-consistent with the ring repulsion and molecular distortion energy, is sufficient to somewhat offset the effect of the azo-bridge–surface bond, which appears as a slightly increased surface distance z .

As schematically summarized in Fig. 8.2 the OBS scheme correction is thus overall too weak to significantly modify molecular geometries. Given its shallow, long-ranged damping function, this result is readily understood: As apparent from Fig. 8.1 the less defined minimum in the correction potential turns the substrate dispersion interactions into a smooth background potential, with small gradient contributions. On the other hand, the G06 and TS schemes use similar, deeper damping functions with gradient corrections strong enough to make adsorbate geometries in principle dependent on the local substrate geometry.

However, in the cis isomers the phenyl-rings sit largely outside the large-gradient range of this G06/TS damping function. The geometry corrections are therefore small and practically identical for the two schemes. For the planar trans azobenzene this situation is different and the phenyl-rings do fall inside the large-gradient range. At Au(111) and Ag(111), where the weak azo-bridge–surface bond does not fix the molecular height, the resulting attractive dispersion interaction correspondingly pulls down the entire molecule. At Cu(111), the strong azo-bridge – surface bond prevents this, and the dispersive attraction only flattens the molecule by bringing the phenyl-rings closer to the surface.

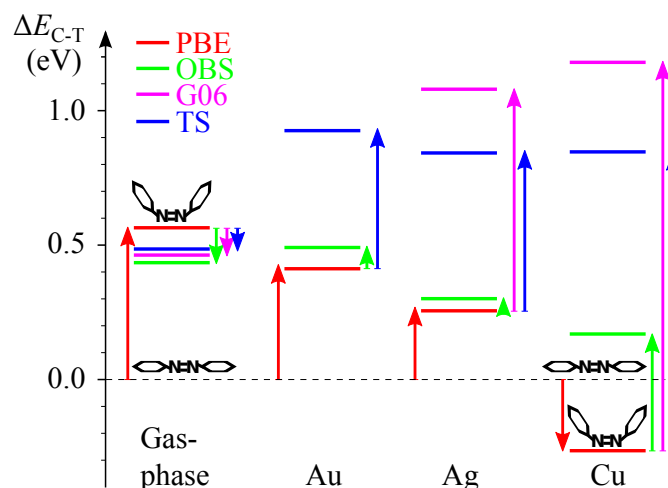


Figure 8.3.: Illustration of the effect of dispersion corrections on the cis-trans relative isomer stability ΔE_{C-T} (cf. Table 8.3), in the gas-phase, and at the three studied substrates.

8.2.2. Electronic Structure and Energetics of Adsorbed Azobenzene

Despite these partly severe changes of the molecular adsorption geometry, it is interesting to note that central electronic structure quantities like the work function Φ or projected frontier orbital positions are not much affected (see Table 8.3). Compared to the corresponding results of the previous chapter, computed work functions in dispersion corrected geometries differ e.g. between $\sim 0.1 - 0.3$ eV, and the entire qualitative rationalization in terms of hybridization and charge rearrangement remains unmodified or even more strongly supported (see section B.6).

As a side note, it is interesting to compare the difference in surface work function between isomers: In rough parity with the pure GGA-PBE results, the surface work functions are comparable for both isomers at Cu, slightly larger for trans at Ag, and larger for trans at Au by almost 1 eV. Therefore, assuming that a coverage and over-layer structure corresponding to our model could be created and switched in a real sample, the azobenzene-functionalized Au(111) surface could exhibit a strongly and possibly reversibly modifiable work function, in close resemblance to a modifiable resistor, or transistor.

This effect could probably be further enhanced with functional groups increasing the permanent dipole moment of the cis isomer. The adsorption energetics also summarized in Table 8.3 are substantially affected by the dispersion correction schemes. The general pattern of these correction effects follows that observed for the adsorption geometries:

At Au(111), the pure GGA-PBE adsorption energies are corrected by approximately 1 eV, with a comparable correction for both isomers with OBS, and the trans isomer correction some 30 % higher in the TS scheme. Consequentially, the GGA-PBE relative isomer stability ΔE_{C-T} is practically unaltered in the OBS scheme, but is doubled in the TS scheme. The Ag(111) results are qualitatively as well as quantitatively comparable to those at Au(111):

		E_{ads}		$\Delta E_{\text{C-T}}$	Φ	
		Trans	Cis		Trans	Cis
Gas-Phase	PBE	–	–	0.57	–	–
	OBS	–	–	0.44	–	–
	G06	–	–	0.47	–	–
	TS	–	–	0.49	–	–
Au(111)	PBE	-0.12	-0.27	0.42	4.82	3.89
	OBS	-1.05	-0.99	0.50	4.82	3.89
	G06	–	–	–	–	–
	TS	-1.67	-1.23	0.93	4.70	3.89
Ag(111)	PBE	-0.11	-0.42	0.26	4.20	3.68
	OBS	-1.05	-1.18	0.31	4.18	3.72
	G06	-2.20	-1.58	1.09	4.05	3.73
	TS	-1.76	-1.41	0.85	4.05	3.73
Cu(111)	PBE	-0.27	-1.08	-0.24	4.13	3.87
	OBS	-1.97	-2.25	0.16	4.12	3.86
	G06	-3.00	-2.30	1.18	3.81	3.87
	TS	-2.81	-2.46	0.85	3.81	3.88

Table 8.3.: Adsorption energies E_{ads} and work functions Φ for the azobenzene cis (C) and trans (T) isomers at the three substrates, and the relative cis-trans energetic stability $\Delta E_{\text{C-T}}$. Note that the G06 scheme does not feature parameters for Au. All numbers in eV.

Whereas OBS does not differentiate significantly between isomers, G06 and TS do, binding the trans isomer stronger and correspondingly increasing $\Delta E_{\text{C-T}}$ (see Fig. 8.3). Also at Cu(111) the dispersion corrections qualitatively resemble those at the previous two substrates, but are about 1 eV larger in magnitude.

They are therewith in all three schemes so large that they restore the energetic order of the two isomers back to that in the gas-phase, i.e. the inversion with a more stable cis isomer obtained with GGA-PBE does not prevail. Apart from dramatically increasing the adsorption energies, the overall prediction of the three semi-empirical schemes compared to the pure GGA-PBE numbers is thus a larger stabilization of the trans isomer upon adsorption. Within the G06 and TS scheme this dispersion corrected over-stabilization of the trans isomer is in fact so large, that the relative cis-trans energetic stability $\Delta E_{\text{C-T}}$ at all three substrates is larger than the corresponding gas-phase value.

Despite this qualitative agreement, the corrected energetics provided by the three

schemes shows quite pronounced quantitative differences. This holds in particular for the OBS scheme, which in the worst cases yields adsorption energies that differ by almost 1 eV from those of the G06 or TS scheme. The latter two schemes on the other hand, are sometimes even more consistent in their results than could be expected from the variation of their corresponding scaled $s_6 \cdot C_{6,ij}$ coefficients in Table 8.1.

Considering that the variation to the OBS coefficients is of similar magnitude, we conclude that the decisive factor for the large difference in the obtained energetics from OBS versus the G06 / TS schemes is less the scatter in the dispersion coefficients, but the differences in the damping function.

8.3. Discussion

Given the in the previous chapter established GGA-PBE adsorption picture, certain consequences of an additional attractive adsorbate - substrate interaction are intuitively expected: Adsorption energies should become more exothermic, somewhat more for the trans isomer, because of the shorter surface distance of its phenyl-rings. The additional interaction should pull the molecule further down, or, where this is prevented by strong covalent azo-bridge–surface bonds, should at least tend to flatten the molecular geometry by driving the Pauli-repelled phenyl-rings to smaller z -heights.

This is exactly what the studied semi-empirical corrections do (cf. Fig. 8.2), and in this respect the results appear plausible. However, the sheer magnitude predicted is much more conspicuous than the qualitative trends. This is most pronounced for the adsorption energies, which in some cases are increased by more than 2 eV. Despite the intended nature as a semi-empirical 'correction', the dispersion schemes thereby actually provide a contribution to the final adsorption energy that is up to an order of magnitude larger than the original GGA-PBE result.

Such results cannot be uncritically accepted, in particular given the uncertainty of the applicability of these correction schemes to bonding at metal surfaces. In order to assess the accuracy of the employed dispersion correction methodology, we study the related problem of benzene adsorption at the relevant substrates. In our model system, the benzene molecule is adsorbed with the molecular plane parallel to the surface, as indicated by NEXAFS measurements²⁵⁵. Since we again observe a minimal corrugation of the lateral potential energy surface, we focus only on the so-called 'HCP-B' benzene adsorption geometry²¹³, in which the molecule is centered over the hcp three-fold hollow site, and rotated such that three carbon atoms are maximally coordinated to the three-fold hollow metal atoms.

Binding energy curves as a function of the distance z between the top surface layer and the benzene center of mass are shown in Fig. 8.4, for the LDA and GGA-PBE xc-functionals, as well as for the three semi-empirical correction schemes. As ZPE corrections generally are minuscule (see Table 8.4), these curves are with the current numerical accuracy essentially equal to the corresponding desorption energy curves. In each panel, TPD desorption energies taken in the low coverage limit^{34–36} are shown as horizontal dashed gray lines. The analysis of these measurements assumes first order kinetics,

and the error bar is estimated at 0.1 eV for the Cu number³⁶.

Similar to the azobenzene case, all three correction schemes bring sizable increases of the essentially zero GGA-PBE benzene adsorption energies, reaching the magnitude of and in some cases exceeding the obtained LDA value. This similarity is if anything testament to the deficiencies of the LDA:

With an exact xc-functional, screening, i.e. the precise form of the surface dielectric function, would be accounted for and the experimental figure perfectly reproduced, given an exact ZPE correction (and an exact experimental figure). Dispersion corrections of the form (8.3) on the other hand, assume a uniform vacuum dielectric function and therefore *must* overbind in a dense matter system, even if their constituent parameters are otherwise ideal.

Compared to the dispersion corrected results, the LDA underestimation of equilibrium surface distances z (shown in Table 8.4), is comparable to the GGA-PBE overestimation. The LDA surface potentials in Fig. 8.4 decay much too fast compared to e.g. the G06 and TS curves, which have the correct C_3R^{-3} asymptotic form. The LDA also predicts a non-planar adsorption geometry at Cu(111), with the CH bonds bending 10° out of the molecular plane, in contrast to the strictly planar geometries observed in experiment²⁵⁵, and predicted by pure and dispersion corrected GGA-PBE.

In combination with the fact, that all three dispersion correction schemes despite differences in energetics and correction potential forms predict the flat-lying B1 adsorption geometry (see Fig. 7.4) to be most stable, cast doubts on the cis isomer adsorption geometry previously sug-

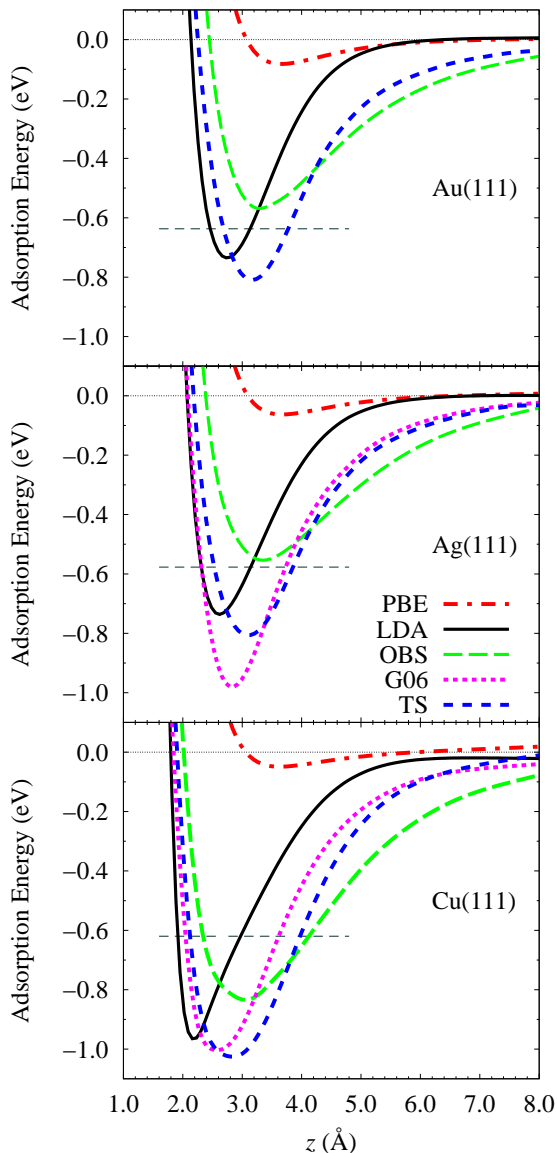


Figure 8.4.: Binding energy curves of benzene, as a function of the center-of-mass surface distance z , at all three substrates. Shown is data for LDA and GGA-PBE, and the three semi-empirical dispersion correction schemes evaluated at z -intervals of 0.25 \AA , to which curves have been fitted as a guide to the eye. For each substrate, the experimentally measured TPD desorption energy at low coverage is marked as a gray dashed horizontal line (see text).

	E_{des} (eV)		E_{ads} (eV)	$E_{\text{ads}}^{\text{ZPE}}$ (eV)	z (Å)
Au(111)	-0.64 ³⁴	PBE	-0.08	-0.03	3.77
		LDA	-0.73	-0.68	2.75
		OBS	-0.54	-0.50	3.48
		G06	—	—	—
		TS	-0.80	-0.77	3.25
Ag(111)	-0.58 ³⁵	PBE	-0.06	0.00	3.75
		LDA	-0.72	-0.67	2.66
		OBS	-0.55	-0.48	3.38
		G06	-0.97	-0.92	2.80
		TS	-0.80	-0.75	3.01
Cu(111)	-0.62 ³⁶	PBE	-0.06	-0.01	3.48
		LDA	-0.96	-0.90	2.18
		OBS	-0.82	-0.75	3.03
		G06	-1.00	-0.92	2.63
		TS	-1.05	-0.98	2.75

Table 8.4.: Results for benzene at the various substrates, including the experimentally measured desorption energy (E_{des}), the optimum molecular height (z), and the computed adsorption energy with ($E_{\text{ads}}^{\text{ZPE}}$) and without ZPE correction (E_{ads}).

gested by Choi et al.⁴⁸: Based on STM measurements supported by LDA calculations, they conclude that the cis isomer preferentially adsorbs with one phenyl ring parallel to the surface, and the azo-bridge and the other ring pointing away from the surface. Such a geometry entirely eliminates the surface - azo-bridge interaction, which obviously is the defining principle behind our results. Of course, the geometry predicted by Choi et al. could be meta-stable at higher coverages, which would explain the experimental observations.

The trends in dispersion corrected benzene adsorption energies shown in Table 8.4, are very similar to those of azobenzene. Compared to the data for the trans isomer in Table 8.3, the correspondence is almost quantitative: For instance, at Au(111) the benzene OBS and TS correction to the GGA-PBE E_{ads} is 0.46 eV and 0.72 eV respectively, and 0.47 eV and 0.78 eV per phenyl ring for azobenzene.

While all three schemes constitute improvements compared to the GGA-PBE data, the OBS numbers are highly inconsistent. Compared to experiment it underbinds, is almost in quantitative agreement and overbinds at Au, Ag and Cu, respectively. The

other two schemes as expected overbind, a tendency most pronounced at Cu(111), where the adsorption energy overestimation reaches $\sim 0.3 - 0.4$ eV. This suggests that the corresponding trans azobenzene at Cu(111) adsorption energies in Table 8.3 could contain errors of the order of $\sim 0.6 - 0.9$ eV.

The trend of increased overbinding for benzene at Au(111) to Cu(111) goes hand in hand with a systematically shorter surface distance z , cf. Table 8.2. This brings the molecule–metal atom distances entering Eq. (8.3) closer and closer to the sum of their vdW radii, and therefore into the distance range most affected by the damping function, cf. Fig. 8.1. The damping functions of all three schemes are exponential functions of the cut-off radii. Thus, while the correction energy varies linearly with errors in the better justified $C_{6,ij}$ potential, it may in- or decrease by a factor of two with a $\pm 10\%$ variation in R_{ij}^0 .

Tests dividing correction energies into contributions most and least affected by the damping functions, i.e. short- and long-ranged contributions, show that the latter 'taint' up to 25% of the total adsorption energy corrections shown here. Thus, while the longer ranged contribution is dominant, the from first-principles least motivated shorter ranged contribution is significant. Only accurate experiments or high-level theory can therefore provide the final judgment of performance of the semi-empirical correction schemes for the azobenzene at coinage metal surface problem.

8.4. Summary

The problem of azobenzene adsorption at coinage metals combines a large molecule, heavy transition metal surface chemistry and a multi-faceted bonding mechanism, in which weak vdW interactions play a crucial role. This combination forms a tremendous challenge for contemporary first-principles modeling, with DFT with (semi-)local xc-functionals still setting the standard.

In order to assess the influence of the deficient description of weak vdW interactions at this level of theory on the current adsorption problem, it has been revisited using several published semi-empirical dispersion correction schemes. Other suggested solutions to this problem are at present deemed intractable given the need for exhaustive and total energy consistent geometry optimizations, and the limitations of contemporary high-performance computing resources.

Using an efficient novel implementation of dispersion corrections in periodic boundary conditions, the changes in azobenzene adsorption energetics and geometries induced by three published dispersion correction schemes have been determined. In light of the uncertain applicability of such schemes to dense matter systems, intentionally unsuitable (OBS), better constructed and popular (G06) and comparatively highly accurate, state of the art (TS) schemes were chosen, representing the full spectrum of this methodology.

The results are qualitatively as well as quantitatively decidedly different from the pure DFT-GGA adsorption picture described in the previous chapter. Where DFT-GGA predicts vast differences between the weak physisorption at Au(111) and Ag(111) and the strong, covalent bonding and geometrical distortion at Cu(111), the ostensibly

more accurate schemes reverse the geometrical distortion at Cu, leaving geometries and relative energetics comparable across all three substrates. Geometry corrections are consistent with intuitive expectations on an attractive potential acting strongest on the phenyl rings, offsetting the Pauli repulsion effects found in the previous chapter.

The qualitative features of the electronic structure analysis of the previous chapter are either more strongly emphasized or remain unchanged with dispersion corrections, however. In particular, the considerable difference in surface work function between isomers at Au(111) remains, a feature potentially offering hitherto unknown applications of azobenzene in molecular nanotechnology.

The adsorption energy 'corrections' are generally large, approximately one order of magnitude greater than the pure DFT-GGA numbers. Since the semi-empirical correction potential relies on several drastic and conditionally transferable approximations, these adsorption energies are, while more accurate than the pure DFT-GGA values, likely not very accurate. In particular, the complete neglect of metallic screening at the surface is expected to significantly overestimate adsorption energies.

Consequentially, in order to isolate and indirectly compare the in the azobenzene adsorption dominant phenyl ring surface interaction to experimental literature, the same methodology has been applied to the problem of benzene adsorption at the relevant substrates. Calculated benzene desorption energy curves as expected reveal spurious under- and overbinding of LDA and GGA functionals. The more accurate G06 and TS schemes show a significant overbinding compared to TPD experiments, most consistent across substrates for the latter. Direct comparison to azobenzene adsorption energies suggests these to be overestimated by 0.6 - 0.9 eV, with the upper bound represented by the Cu(111) number.

Nevertheless, TPD experiments rely on various assumptions, and are in particular in the low coverage limit of limited accuracy. The absence in literature of accurate structural data also for benzene adsorbed at coinage metals leaves the comparison to experiment incomplete, at this point. Since a accurate theoretical reference is presently not an option for the adsorption of azobenzene, further experimental benchmarks are needed to assess the predictive quality of semi-empirical dispersion correction schemes for the adsorption of aromatic molecules at close-packed coinage metal surfaces. This is the topic of the following chapter.

9. An Experimental Benchmark

At this point, the verdict on the quality of the obtained theoretical adsorption picture in general, and on the performance of the semi-empirical dispersion correction methodology in particular, is still uncertain:

On the one hand, a challenging problem for which commonly employed simulation techniques fail spectacularly, have been radically redressed using state-of-the-art theory. Convincingly, the wildest, and likely wholly incorrect, predictions of chapter 7 appear nicely ironed out, and an indirect comparison to experiment suggests a reduction in energetic error from an order of magnitude to less than a factor of two.

On the other hand, the improved simulation methodology is untested, and obviously qualitatively simplistic for something as demanding as first-principles modeling of metal surface chemistry. The discussed experimental results are not strictly relevant to azobenzene adsorption, provide adsorption energy references of at best limited accuracy, and give no reference for structural parameters. While adsorption energy predictions within a factor of two are a spectacular result under the circumstances, that error is still large, and offers little bearing on precisely how far those predictions can be trusted.

Consequentially, accurate experiments on a relevant system also including measurements of structural parameters are of crucial importance to the evaluation of our theoretical methodology. Such experiments are challenging: For example, the entire range of dispersion corrected and pure DFT-GGA predictions of the azobenzene equilibrium surface distance z at any substrate (see Table 8.2) is a mere 0.66 Å. For benzene, the corresponding maximum difference between the likely underbound GGA and overbound LDA z -values is only twice that figure (see Table 8.4). Thus, in order to conclusively evaluate the dispersion-corrected DFT methodology, we require an experimental technique able to resolve inter-atomic distances perpendicular to the surface plane (or e.g. surface height profiles) at a resolution consistently and significantly better than 1.0, preferably at most 0.1 Å.

Near-incidence X-ray standing wave²⁵⁶ (NIXSW) spectroscopy is one of the few experimental techniques to fulfill all of these requirements, and has been successfully applied to similar problems²⁵⁷, providing accurate values for vertical adsorption heights and adsorption-induced molecular distortions^{257–260}. Therefore, in this chapter, dispersion corrected DFT-GGA predictions for the geometry of trans azobenzene at Ag(111) are compared to NIXSW measurements performed mainly by Giuseppe Mercurio and Dr. Sergey Subach in the group of Prof. Dr. Stefan Tautz at Forschungszentrum Jülich.

This substrate is chosen for reasons of its low reactivity and zero switching yield⁴⁹ of adsorbed azobenzene, both of which contribute to a higher prevalence of – and stronger experimental signal due to – the sought majority species. Theoretically calculated energetics are evaluated by a comparison to TPD experiments on the same system, performed

in the group of Prof. Dr. Martin Wolf at the Freie Universität Berlin.

The results of this chapter have been published in Physical Review Letters^V. As in chapter 6, in the interest of brevity, the following focuses exclusively on the experimental results and their comparison to theoretical predictions, and includes but the bare minimum of experimental technicalities.

9.1. Results and Discussion

The adsorbate geometry is here represented by two characteristic parameters: The average N atom - top surface layer distance z , as defined in Fig. 7.4, and the phenyl ring to surface plane bend, or 'tilt' angle $\tilde{\omega}$. The latter is in degrees equal to $\frac{1}{2}(180 - \omega)$, where ω is the CNNC dihedral angle defined in Fig. 7.4, assuming an azo-bridge parallel to the surface plane, and flat ($= 180^\circ$) NNCC and CCNN dihedral angles. In line with the results of sections 7.2.2 and 8.2.1 and NIXSW measurements, the theoretically calculated $\tilde{\omega}$ tilt angles differ negligibly between phenyl rings – the adsorbate geometries are nearly twofold symmetric. Nevertheless, values given in the following are averaged over the two rings.

In short, the NIXSW technique exploits the fact that adsorbate atoms located at the positions of the anti-node planes of a standing X-ray wave field induced by Bragg-reflection exhibit a maximum in the photoemission yield. Scanning the photon energy through the Bragg energy shifts the position of the anti-nodes from the lattice planes to half-way positions between them. At different photon energies the photoemission signal thus probes different vertical locations of adsorbate atoms relative to the substrate lattice planes, and can be used to extract element-specific vertical adsorption heights.

As explained in our publication^V, the diazo-bridge height is thus straightforwardly measured as $z = 3.07 \pm 0.02 \text{ \AA}$ by our collaborators. However, using conventional data analysis techniques it is difficult to differentiate between the positions of identical species with small chemical core level shifts, such as the various carbon atoms in the phenyl rings of azobenzene. Employing a novel analysis scheme^V, our collaborators are able to extract also the tilt angle $\tilde{\omega} = -1 \pm 1.5^\circ$ from the carbon-edge NIXSW data.

From the TPD experiments, our collaborators derive a desorption energy of $E_{\text{des}} = 1.00 \pm 0.1 \text{ eV}$ from the adsorbate desorption rate as a function of temperature at different coverages^V.

We now compare the experimental results to the theoretical predictions of the G06²⁰¹ and TS²⁰² dispersion correction schemes. Figure 9.1 shows binding energy curves for trans azobenzene at Ag(111), calculated exactly as the adsorption geometries detailed in section 8.2.1 (cf. Fig. 8.4). All adsorbate geometric degrees of freedom except for the azo-bridge z -coordinate were fully optimized for each point on the curves. The zero-point energy (ZPE) correction was calculated as explained in section 8.1.2, and again found so small ($\sim 20 \text{ meV}$), that the uncorrected curves of Fig. 8.4 equal the corrected desorption energy (E_{des}) curves on the scale of the plot.

At the optimized adsorption heights, both bare DFT-PBE and the two dispersion correction schemes yield an essentially planar molecule, with tilt angles of $\tilde{\omega}_{\text{PBE}} = +1^\circ$,

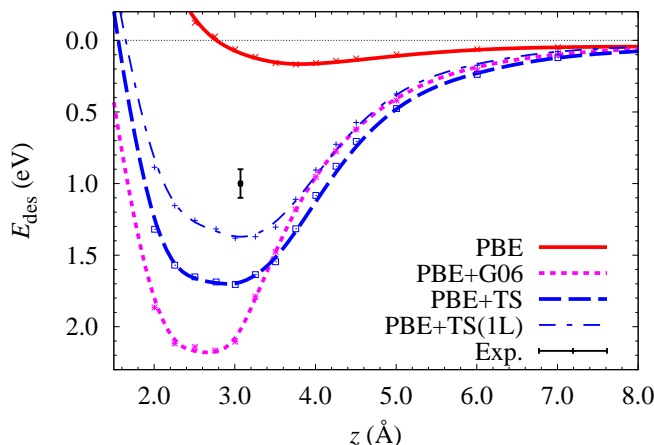


Figure 9.1.: Binding energy curves of trans azobenzene at Ag(111), computed with bare GGA-PBE and the G06 and TS dispersion correction schemes (cf. Fig. 8.4). As in Fig. 8.4, ZPE corrections are so small that the uncorrected binding energy curves equal the desorption energy curves at the current accuracy. The black data points mark the experimental values and error bars for the surface distance z , defined in Fig. 7.4, and the desorption energy E_{des} . Additionally shown is the curve computed with the TS correction reduced to the topmost layer Ag atoms (see text).

$\tilde{\omega}_{\text{PBE+G06}} = +1^\circ$, and $\tilde{\omega}_{\text{PBE+TS}} = +3^\circ$, all in similar agreement with the experimental value. This small variation indicates that, irrespective of the dispersion interaction, the differential surface interaction within the extended molecule (i.e. the difference between the surface interactions of the various parts of the molecule) is too weak to overcome the molecular distortion cost.

In contrast, the adsorption height z is a very sensitive indicator of the strength of vdW interactions. As determined in the previous chapter and illustrated by Fig. 9.1, the equilibrium surface distances are 3.64 Å, 2.75 Å and 2.98 Å for pure GGA-PBE, G06 and TS, respectively (see Table 8.2). Thus, on the scale of the GGA-PBE difference to experiment, G06 overbinds by 56 %. The TS scheme overbinds by a mere 16 %, corresponding to an absolute difference near the limits of numerical resolution, given the established accuracy of the current computational model and the rather flat minimum of the TS curve (see Fig. 9.1).

Unfortunately, the improved structure goes hand in hand with a notable overbinding. In fact, in absolute numbers, the popular G06 scheme ($E_{\text{des}} = 2.16$ eV) overbinds more than bare GGA-PBE underbinds. The refined TS scheme performs somewhat better ($E_{\text{des}} = 1.71$ eV). If the steepness of the Fermi-type damping function is varied in large bounds, the results of both dispersion correction schemes change negligibly, in line with the results of the previous chapter. This makes it unlikely that the *functional form* of the damping function itself is responsible for the overbinding.

As discussed in section 8.3, the Fermi damping function as used in both dispersion correction schemes is an exponential function of the effective vdW radii R_{ij}^0 , making the

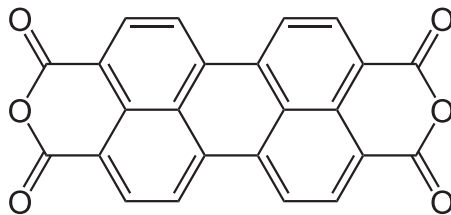


Figure 9.2.: Structural formula of the PTCDA molecule. The image source is public domain courtesy of Wikipedia (see <http://de.wikipedia.org/wiki/PTCDA>).

dispersion correction energy near the equilibrium sensitive to variations to errors in R^0 parameters. For example, increasing constituent R^0 parameters reduces the predicted adsorption energy. However, such variations also lead to corresponding changes in the equilibrium surface distance, which for the TS scheme substantially worsens the quality of the predicted geometry, if the desorption energy is 'corrected' in this way. The comparison to experiment therefore allows us to exclude R^0 parameters, i.e. the *onset* of the damping function as a main error source. A similar relation between bond strength and adsorption height will also hold for changes of the short-range potential. Consequentially, deficiencies in the exchange-correlation approximation of the PBE functional are also an unlikely cause of the overbinding.

As again in section 8.3 observed for the benzene calculations, the lack of screening in the dispersion correction potential is a more plausible culprit. According to News²⁶¹, the screening length l at a jellium surface is well approximated according to

$$l \approx \lambda^{-1} + \frac{\pi}{4k_F} \quad (9.1)$$

where λ is the Fermi wavelength in the Thomas-Fermi jellium model, and k_F is the Fermi wavelength in the surface system. Liebsch²⁶² reaches similar conclusions. Replacing k_F in (9.1) by λ , scaled by the ratio between the Ag clean surface and bulk Fermi vectors calculated with GGA-PBE, and using the reference¹⁴⁴ Ag $\lambda = 1.20 \text{ \AA}$ yields an approximate l of some 1.63 \AA . While an imprecise measure, this indicates that the true surface screening length very likely is substantially shorter than one Ag(111) slab inter-layer spacing (2.39 \AA , see sections B.1 and B.2).

Thus, we may mimic the effects of a dielectric function equal to that of vacuum out to the Ag jellium surface screening length, and zero beyond, by simply excluding all but the top slab layer in the dispersion correction calculation. Again, while a crude approximation of little or no *quantitative* predictive quality, this illustrates the *qualitative* effects of screening on the dispersion correction.

Consequentially, the TS binding curve is in Fig. 9.1 also plotted with a dispersion correction only including the top layer metal atoms. As shown, the overbinding is in this curve indeed substantially reduced, without a significant effect on the geometry – the screening error corresponds to a rather uniform background potential contributing little to the energy gradient. Thus, while absolute energetics of the TS scheme are inaccurate, its prediction of the geometry appears accurate for the right reason. The same effect

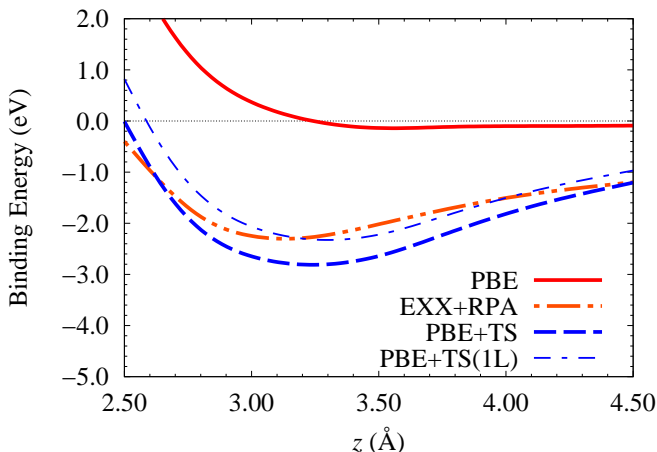


Figure 9.3.: PBE+TS binding energy curves of PTCDA (see Fig. 9.2) adsorbed at a Ag(111) slab, with four (blue dashed line) and one (blue dot-dashed line) substrate layers included in the correction potential, compared to GGA-PBE (red solid line) and EXX+RPA (orange double dot - dashed line) curves obtained by Rohlfling and Bredow¹⁹⁴ (cf. Fig. 9.1, note the difference in scale).

occurs for the single-layer G06 curve (which is not shown in Fig. 9.1 for clarity).

However, with a conditionally transferable method the possibility still remains, that this is but a fortuitous, system-dependent fluke. We therefore also verify the dependence of the TS surface potential on slab thickness for the case of the perylene-3,4,9,10-tetracarboxylic dianhydride (PTCDA) molecule (see Fig. 9.2) adsorbed at Ag(111). In Fig. 9.3, binding curves obtained by Rohlfling and Bredow¹⁹⁴ using GGA-PBE and the RPA (see section 4.2) on an exact-exchange (EXX) ground-state are compared to four- and single layer TS scheme curves. The surface distance z is in this case defined as the vertical distance between the top surface layer and the plane of the flat-lying molecule. The TS PTCDA curves were obtained by calculating the dispersion correction for the molecule in its fully optimized gas-phase geometry at various z -distances, and adding these numbers to the PBE curve published by Rohlfling and Bredow.

While the single-layer TS curve notably reproduces the high-level and prohibitively expensive RPA binding energy prediction, it must again be emphasized that this approach is much too crude for a quantitative prediction. Here as in the azobenzene example, it is the qualitative fact that the PTCDA at Ag(111) equilibrium surface distance predicted by the TS scheme does not change significantly with approximate screening (reduction of substrate layers included in the correction potential) that is important (see Fig. 9.3). It also deserves to be noted, that the RPA and TS predictions of the equilibrium z are remarkably similar, 3.1 and 3.2 Å, respectively.

9.2. Summary

In this chapter, an accurate experimental benchmark for the theoretical predictions for trans azobenzene adsorbed at Ag(111) has been established, using TPD and state of the art NIXSW methods combined with novel analysis techniques. In short, both the G06 and TS dispersion correction schemes substantially overestimate the desorption energy, albeit the latter less so than the former, in congruence with the benzene calculations of section 8.3. Correspondingly, the G06 scheme yields a significantly shorter equilibrium surface distance than the TS scheme, with the prediction of the latter in remarkable agreement with experiments.

Our analysis of this discrepancy in predictions conclusively shows, that the lack of metallic screening inherent in the semi-empirical dispersion correction approach is predominantly to blame for the error in the calculated desorption energy. However, appearing as a uniform background potential, the screening error contributes very little to the energy gradient, and therefore hardly affects the geometry prediction. This is observed for both schemes, in the system of interest as well as for a PTCDA molecule adsorbed at Ag(111). In this test, the refined TS scheme notably reproduces the equilibrium distance given by high-level RPA calculations.

On the one hand, this affirms that the semi-empirical dispersion correction approach is insufficient for a comprehensive description of the role of vdW interactions in adsorption at metal surfaces. On the other hand, the insight that the adsorption geometries are less sensitive to the neglect of screening is intriguing. It suggests, that these schemes may provide significantly improved structural data at zero additional computational cost. As discussed in chapter 8, it is less the cost of a single calculation than that of the hundreds needed in an exhaustive structure search that makes higher-level theory presently intractable for modeling of adsorption of organic molecules, in particular for one as complex as azobenzene. Therefore, judging by the results of this chapter, the TS dispersion correction scheme holds tremendous promise as a 'structure exploration tool', reducing the need for computationally expensive calculations to select, accurate geometries.

Still, in particular the comparison to TPD energetics is not entirely unambiguous. A thorough and stringent test using a well-defined, more accurate level of theory is considerably more satisfying to a theorist. This is the topic of the following chapter.

Part IV.

Outlook

10. The Exchange-Correlation Correction Method: Benzene at Cu(111)

The previous chapter ended with a somewhat mixed message: As shown, the TS semi-empirical correction to van der Waals (vdW) interactions in DFT-GGA is remarkably accurate for adsorbate geometry of for azobenzene at Ag(111).

Inherently neglecting metallic screening of vdW interactions at the surface, this approximation is less of an improvement over DFT-GGA for adsorption energetics, however. Thus, a natural next step investigates the possible routes to correcting also this deficiency, beginning with an appropriate benchmark for the TS-corrected DFT-GGA energetics.

Precise experimental measurements of adsorption energies are difficult to obtain. TPD as compared to in chapters 8 and 9, measures desorption rather than adsorption energies. While the latter can be derived from the former, this is generally not possible without assumptions concerning the desorption kinetics. The accuracy of TPD for these systems is also rather limited³⁴⁻³⁸. Microcalorimetry, exemplifying a technique able to measure adsorption energies directly is exacting in general, and at desirable accuracy in particular.

Furthermore, a mere quantitative measure of the accuracy of the calculated energetics is not very informative: The main difficulty in first-principles modeling of aromatic molecules at metal surfaces is really nothing other than the balance between computational scalability, accuracy and transferability discussed in chapter 3.

Since an accurate, transferable (e.g. post Hartree-Fock) method is intractable for systems of this size and complexity, we are forced to use a semi-empirical solution, sacrificing transferability for computational tractability and accuracy.

Even an exact experimental measurement cannot answer the remaining question of how limited the applicability of this methodology is, making a well-defined theoretical benchmark by far the most rewarding.

Thus, the topic of this first outlook chapter may be formulated in terms of two questions, namely whether i) a strictly non-empirical, *ab initio* benchmark is presently at all possible for this class of systems, and ii) if yes, what the performance and limitations of such a benchmark for the adsorption of aromatic molecules at metal surfaces are. In the following, these questions are addressed in the context of an application of the so-called exchange-correlation (xc) correction method^{189,228,263} to the adsorption of benzene at Cu(111). Intended as a proof-of-concept, the discussion is kept at a conceptual level, with finer detail of the calculations relegated to appendix C.

10.1. Theory

The xc-correction method relies on a simple central concept: Suppose we want to calculate an arbitrary energetic property E_B^∞ in an infinitely extended system, using a given level of theory B . The property E_B^∞ can be approximated by the same property in the corresponding *finite* system (cluster) of N constituent atoms. The accuracy of this approximation goes to infinity with N . By simple addition and subtraction, E_B^∞ can be written as the same property calculated at another level of theory A , added to the difference of the property between the two levels of theory calculated in the finite system:

$$E_B^\infty = E_A^\infty + [E_B^\infty - E_A^\infty] \approx E_A^\infty + [E_B(N) - E_A(N)] = E_A^\infty + E_{xc-c}(N) \quad (10.1)$$

Here, the xc-correction energy as a function of cluster size $E_{xc-c}(N)$ is identified in the last step. This equation has a few important properties:

First, since properties of an infinite system can be described by a converged periodic boundary condition (PBC) model (e.g. DFT-GGA, see e.g. chapters 7 through 9), it offers a connection from such a model to an *arbitrary* other level of theory defined in a finite system. Second, the accuracy of the approximation can be *systematically* and *arbitrarily* improved by converging $E_{xc-c}(N)$ with respect to N .

Third, if the property E is local, as for instance the interaction energy of a finite adsorbate with an extended substrate, $E_{xc-c}(N)$ is monotonically convergent²⁶⁴. Fourth, if both levels of theory are properly size consistent and -extensive, $E_{xc-c}(N)$ will at each N consist of only those higher order xc energy terms described by B , but not by the less accurate level of theory A . Such higher order terms may be even more short-ranged than the total localized interaction itself, implying a convergence of $E_{xc-c}(N)$ for a finite, and *small* N .

One might thus summarize the xc-correction approach as offering a route to *minimal* computational effort at an *arbitrary* given accuracy of the xc treatment – or put differently, a simple theoretical framework offering an arbitrary choice of balance of scalability, accuracy and transferability. Notably, this is achieved entirely without the need for embedding environments, or non-standard numerical implementations – the two last terms of Eq. (10.1) are entirely independent, and are in appendix C as in previous chapters calculated using the CASTEP²⁰⁶ plane-wave DFT and NWChem¹⁵³ quantum chemistry packages, respectively.

10.2. Results

In previous chapters, DFT results have been discussed from the perspective of two major limitations of standard present-day xc-functionals, namely self-interaction, and weak, long-range interactions. These are representative of many challenges faced by current first-principles modeling. Thus, in order to illustrate the application of the xc-correction methodology to a general problem, we here follow a hierarchical progression of popular quantum chemistry methods: As further explained in section 4.1, the exact exchange

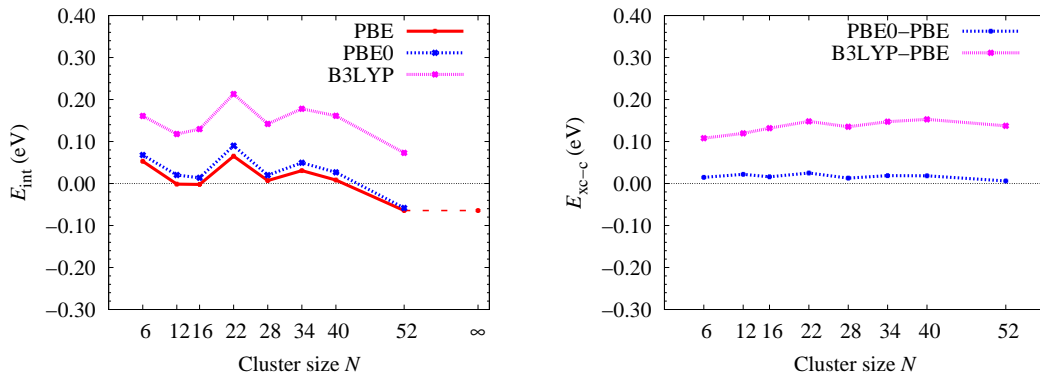


Figure 10.1.: Hybrid functional xc-correction calculations. Left: The interaction energy E_{int} as a function of cluster size, at PBE (red solid line), PBE0 (blue dotted line) and B3LYP (magenta dotted line) level of theory. Note the added PBC model E_{ads} value (labeled ' ∞ '). Right: The resulting PBE0-PBE and B3LYP-PBE xc-corrections $E_{\text{xc-c}}$.

density included in hybrid DFT xc-functionals cancels a fraction of the self-interaction error, improving the description of the short-ranged potential. Consequentially, hybrid DFT forms a natural first level at which to explore xc-corrections to DFT-GGA. However, since it by now is well established that the main difficulty in the modeling of this class of problems are long-ranged interactions, we further proceed to calculate xc-corrections at the 'lowest' available level of explicitly correlated post Hartree-Fock techniques - MP2 (see section 3.3).

Specifically, the PBE0^{126,127} and B3LYP^{121,122} hybrid xc-functional parametrizations are studied here. This choice is not accidental: As discussed in section 4.1, PBE0 is but for the exact-exchange component identical to PBE^{116,117}. Therefore, the xc-correction of PBE0 on PBE provides a precise measure of the role of exchange interactions in the adsorption of benzene at Cu(111). As further explained in section 6.1, the B3LYP functional includes a comparable amount of Fock exchange, in combination with various LDA and GGA components semi-empirically determined via fits to a benchmark training set of light organic molecule properties. The comparison of the B3LYP correction on PBE – in a system fundamentally different from that training set – to that of PBE0, thereby highlights the effects of semi-empiricity on the transferability of hybrid xc-functionals.

$E_{\text{xc-c}}$ is calculated for various carefully chosen cluster geometries of $N = 6$ to $N = 52$ Cu atoms, with a single benzene molecule (see section C.1 and Fig. C.1). Since the geometry of neither adsorbate nor substrate changes significantly upon adsorption, the adsorbate-substrate system essentially equals the sum of the clean surface and gas-phase molecule, in turn leaving the adsorption energy E_{ads} for all intents and purposes equal to the benzene at Cu(111) interaction energy E_{int} . The left side of Fig. 10.1 shows the PBE^{116,117}, PBE0 and B3LYP E_{int} as a function of cluster size. This plot nicely illustrates the difficulties in the application of finite-system theory to an extended, metallic system – the interaction energy does not converge over the entire size range for *any* level of theory.

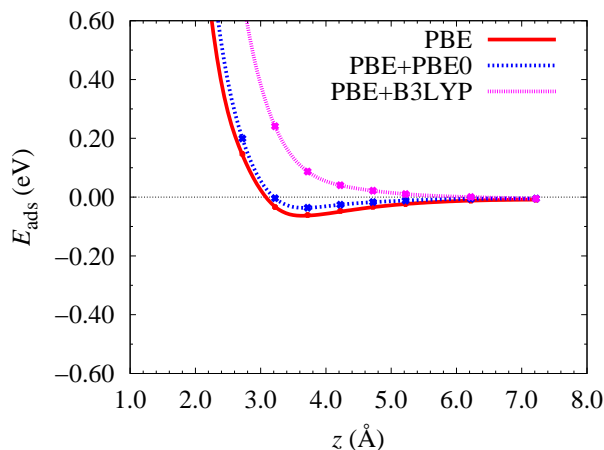


Figure 10.2.: Binding curves of benzene at Cu(111) xc-corrected at PBE0 (blue dotted line) and B3LYP (magenta dotted line) level. The xc-corrections were calculated in the 22 Cu cluster geometry of Fig. C.1, and added to the PBE E_{ads} curve (red solid line) of Fig. 8.4. Interaction energy xc-corrections were evaluated at z -increments of 0.50 Å.

However, the *variation* of E_{int} with cluster size is very similar at all three levels of theory. Therefore, the differences between the curves, or corresponding $E_{\text{xc-c}}$ plotted on the right of Fig. 10.1, rapidly converge to *constant* values: By Eq. (10.1), we can therefore obtain the PBE0 and B3LYP adsorption energy curves by simply adding the corresponding xc-corrections to the PBC PBE curve of Fig. 8.4. The result of this addition is shown in Fig. 10.2. A few qualitative features of these curves stand out:

PBE0 exchange is more repulsive than PBE exchange. It is therefore not surprising that the former binds less than the latter. The difference is however very small at intermediate to large distances. PBE0 therefore a) underestimates the benzene at Cu(111) E_{ads} to a degree comparable to the PBE number of Table 8.4, and b) does not significantly modify the prediction of the equilibrium surface distance z . The B3LYP curve is endothermic everywhere, consequentially predicting no equilibrium adsorbate - substrate distance at all. This rather vivid failure of B3LYP is in line with its previously observed performance for transition metal systems¹²⁵.

In summary, hybrid functional calculations do not provide much of an improved theoretical benchmark for the dispersion corrected GGA calculations of the previous chapters, much as expected. Instead, we proceed to study the MP2 xc-corrections. In Fig. 10.3, the PBE and MP2 E_{int} and the resulting $E_{\text{xc-c}}$ up to and including the 40 Cu cluster is plotted. Comparing to the right of Fig. 10.1, it is clearly evident that the MP2 xc-correction is not constant over the cluster range. This is readily explained in terms of the long-ranged vdW interaction per cluster volume contained in the MP2, but not in the PBE E_{int} , leading to a difference divergent with N .

Consequentially, the quantity to correct must be reformulated. MP2 by construction only includes correlation effects to second order. Since this premise is identical to that of the London series (see section 8.1.1) we make the Ansatz, that the MP2 $E_{\text{xc-c}}$ can be

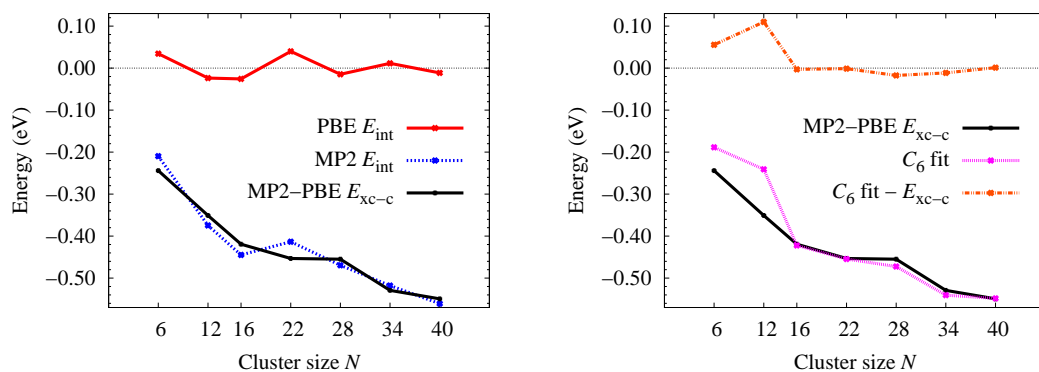


Figure 10.3.: Left: The MP2-PBE xc-correction (black solid line) derived from the PBE (red solid line) and MP2 (blue dotted line) E_{int} as functions of the cluster size. Right: The MP2 xc-correction expression extrapolated on the form of Eq. C.5 (magenta dotted line), the MP2 E_{xc-c} as at left, and the difference of the calculated and fitted quantities (orange dot-dashed line).

extrapolated as a C_6 -type expression, as further explained in section C.2. In the right of Fig. 10.3, the resulting extrapolation is compared to the calculated E_{xc-c} .

As illustrated by the dash-dotted orange line in the right of Fig. 10.3, the accuracy of this Ansatz is remarkable. Given a perfect fit, this line – representing the difference between the fitted and calculated MP2 xc-correction – would have been zero everywhere. Here, the fitted Eq. (C.5) matches the MP2 xc-correction up to a mean error and sample variation amount to a mere -6 and 8 meV, respectively. Additionally, the 16 Cu E_{xc-c} , which is not included in the fit statistic, is reproduced to very high accuracy.

This is a vivid illustration of the power of the xc-correction scheme: A tremendously simple concept, it in this formulation does not require any methodological development at all. Still, in combination with the most basic of physical understanding, it here provides the – judging by the publication record – first ever successful numerical description of an oft-attempted problem^{227,265,266}. The generalization to more sophisticated methods than MP2, or indeed to xc-corrections upon xc-corrections, follows naturally from these results.

However, as explained in section C.2, whereas the effect of an appropriately accounted for screening would amount to effectively lowered surface dispersion coefficients, the MP2 xc-correction extrapolated to a truly semi-infinite surface correspond to *larger* dispersion coefficients, implying an adsorption energy on the same scale of the obviously over-estimated corresponding TS²⁰² scheme energetics. Thus, while we *can* benchmark the dispersion correction schemes at higher levels of theory, the specific choice of MP2 does not offer any improvement either.

10.3. Summary

In light of the perceived need for a non-empirical theoretical benchmark for the interaction of a phenyl moiety with close-packed coinage metal surfaces, this chapter presents higher-level calculations on the adsorption of benzene at Cu(111), within the so-called exchange-correlation correction scheme.

As shown, neither commonly used hybrid xc-functionals nor MP2 are able to provide a theoretical benchmark more accurate than the previously studied semi-empirical dispersion correction schemes. Put differently, neither state-of-the-art formulations of the short-range interactions in organic compounds, nor a self-interaction free, non-empirical treatment of the long-range interactions inadequately described by (semi-)local DFT functionals, is able to improve on the adsorption picture provided by the semi-empirical approximations employed in the previous chapters.

In a sense, this makes it abundantly clear just how demanding this problem is: Even within the xc-correction scheme, and as explained in section C.1 fully exploiting the reduction in computational prefactor offered by the so-called resolution of identity (RI) approximation to MP2, a fully *ab initio* treatment of second-order correlation effects in the adsorption of benzene at Cu(111) is enormously demanding at relevant cluster sizes. Still, this technique neither quantitatively nor qualitatively outperforms the highly approximate second-order effects introduced by the dispersion correction approach.

These results therefore suggest, that quantitative *ab initio* predictions of chemical accuracy for this problem require terms beyond the strict second-order approximation of MP2, i.e. starting with the so-called disconnected higher excitations found in e.g. CCSD⁹⁶ (see section 3.3). With its N^6 scaling negating most of the hypothetical performance gain of the RI approximation, CCSD could most likely not be applied to the range of clusters here studied with MP2, given the capacity of currently available high-performance computing resources. However, as already mentioned, higher order terms are not seldom very short-ranged – therefore, a simple rote application of the above approach to the CCSD xc-correction on MP2 is potentially rapidly convergent and well behaved.

The RPA offers another possible step forward: While it still must be considered unclear whether the RPA *per se* would yield a Cu(111) surface potential more accurate for the right reason, it is as explained in section 4.2 but a special case of a formally exact expression – the higher order terms of this problem missing in MP2 constitute an interesting benchmark for a reasonably formulated, non-zero exchange-correlation kernel.

Lastly, a step back to a broader perspective is in order: The challenge for first-principles theory posed by this class of problems needs no further emphasis. Still, the results of the previous and current chapters make the plausible case, that the problem of scanning a large chemical space of adsorption geometries of aromatic molecules at metal surfaces, in addition to making accurate *ab initio* predictions for the chemically most relevant of those structures, may be reduced to the application of well-established better approximations of electronic correlation. Under the circumstances, this can only be characterized as a tremendous step forward.

11. Future Steps

Scientific work is often best understood in its contemporary context. In closing of this thesis, I will therefore try to connect the dots of the immediate past leading up to the project, via its contributions and connections to recent and current developments in the field, to likely future avenues of exploration.

As the miniaturization of microelectronic components progresses towards fully exploiting the plentiful room at the bottom promised by Feynman, controlling objects of molecular size becomes necessary, making simply substituting components for controllable molecules a natural step. Of these, a simple on / off switch is the arguably simplest example with obvious applications.

As an emergent fruit-fly of the molecular switches class, the bi-stably and reversibly isomerizable azobenzene molecule has been the topic of an exponentially increasing number of scientific publications over the past two decades. In particular, the experimental route towards a technical implementation of *individually* switchable molecules, dominated by studies of switch adsorption at solid interfaces within the only slightly older field of surface science, has produced a rich variety of still largely unexplained phenomena. Of these, the switch - surface interaction and coupling is a paramount issue.

Following the limits of high-performance computing, theoretical simulations from first-principles provide a unique and increasingly detailed perspective on chemistry and condensed matter theory in general, and where they overlap – in surface science – in particular. However, simulations predictive of the complex electronic excitations in azobenzene have only in recent years become routinely possible. Predictive simulations of physisorption of aromatic molecules at surfaces are still far from routine.

This thesis begins with the ostensibly simplest route to switch adsorption at surfaces; that of decoupling switch moieties from the substrate electronic structure using large ligands. Combined with spectroscopy techniques probing the full electronic spectrum of the switch compound, theoretical modeling of its ground- as well as excited state properties provides a consistent picture of the self-assembled adsorption geometry and the switching mechanism. The results are somewhat surprising: While literature on this well characterized molecule largely attributes its low switching efficiency to – and focuses on minimizing – presumed effects of the environment and functional groups, we identify interactions among the switch moieties *themselves* as the likely culprit. Thus indicating that loss of function is *intrinsic* to the switch moiety above a critical component density, this profoundly affects the viability of azobenzene as a component in e.g. storage media.

The methodological theme of this thesis begins with an investigation of two questions of utmost importance for the theoretical description of the opposite limit of switch - surface decoupling, namely whether the effect on the switch of the substrate electronic structure is sufficient to warrant its explicit inclusion in the model, and if yes, whether the current

state of the art technique for this class of systems, density-functional theory (DFT) using (semi-)local exchange-correlation (xc) functionals, yields qualitatively correct results.

The answers are yes, and – because of the inadequate description of weak *van der Waals* (vdW) interactions in (semi-)local xc-functionals – no, respectively. This puts the problem at somewhat of an impasse, since the need for a consistent geometric and electronic structure is particularly strong in this system, and current methods known to accurately predict geometries *and* weak electronic correlation effects cannot feasibly handle the surface electronic structure, and vice versa.

Consequentially, the thesis proceeds by evaluating current developments in the field of semi-empirical corrections to vdW interactions in DFT. While an ostensibly substantial qualitative improvement over pure DFT, this technique is too crude for accurate quantitative predictions for this class of systems. In the following step, the theoretically predicted geometries and energetics are therefore compared to results of accurate and innovative experimental techniques.

The outcome is mixed: Whereas semi-empirical corrections as expected substantially overestimate adsorption energies, in particular the most sophisticated scheme yields a highly accurate geometry. This again is a result of great significance, since it indicates a potential for exhaustive and accurate structural searches for this class of problems, from which the most chemically relevant geometries can be selected for an improved treatment of energetics. Finally, a non-empirical and arbitrarily improvable possible solution for such focused high-level simulations is presented, along with the results of proof-of-concept calculations.

Given this summarily described insight into the bonding of azobenzene at solid surfaces, the hitherto considerable gap between theory and experiment in this field can slowly be bridged: While the goal of precise predictions of experimentally observed energetics remains elusive, the observed error in the semi-empirical dispersion correction technique – approximately corresponding to a constant shift of the potential energy surface seen by the adsorbate at the substrate – is a minor limitation. For instance, given accurate geometries, comparably accurate charge densities can often be easily obtained even with simpler xc-functionals, and with them a wealth of information on adsorbate bonding, as exemplified by the electronic structure analysis of subsection 7.2.3.

Furthermore, if predictive geometries can be calculated at the computational cost of a DFT calculation – i.e. at sub N^3 scaling – then not only can considerably larger systems than pure azobenzene now be feasibly treated, but the computational limitations on system size grow almost linearly with time, given the exponential increase in computing power. Therefore, the most rewarding future route turns from investigating the basic aspects of the adsorption itself, to systems of greater technical relevance and potential:

While the adsorption of DMC⁵⁵ (see chapter 2) has already been studied using standard DFT, our refined methodology could in greater detail describe the role of the dicyano functional groups in the switch adsorption, and correspondingly, provide a more accurate measure of their influence on the general electronic structure of the adsorbed switch, allowing for a more informed analysis of the observed switching behavior. Preparatory calculations of DMC at Cu(111) have already been completed.

Dispersion corrected DFT calculations of the adsorption of the TBA molecule (see Fig.

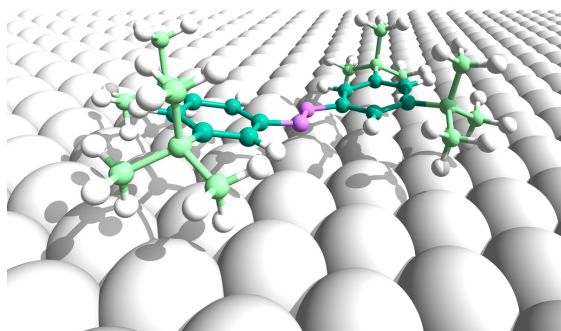


Figure 11.1.: The geometry of the trans TBA (see chapter 2) molecule at an Au(111) surface, optimized using GGA-PBE corrected with the TS²⁰² scheme (see chapter 8).

11.1) at noble metal surfaces, perhaps the most promising subcategory of azobenzene adsorption studies, are also well underway. Apart from allowing for a qualitative comparison to published TPD and two-photon photoemission spectra⁴⁹ (2PPE), e.g. within an initial-state approximation similar to that discussed in section 6.1, the readily obtainable dispersion corrected harmonic vibrational spectra would make direct comparison to recorded HREELS data⁶⁵ possible.

While the direct contribution of weak correlation interactions to the vibrational modes is likely small, the indirect contribution via the predicted adsorbate geometry, is as likely substantial. Such a comparison could provide precise information about the local adsorption geometry, which purely experimental approaches so far have been unable to – and standard theoretical techniques couldn't – produce.

Given reasonable consistency of predictions and observations at this point, the answer to another exciting question could be within reach: Hagen et al.⁶² rationalize the observed increase of switching yield of TBA at Au(111) with temperature, in terms of substrate - adsorbate charge transfer due to thermally excited hot carriers in the substrate. While highly plausible, this explanation omits the possible role of a likewise thermally excited adsorbate in the process, which may amount to an effectively increased adsorbate - substrate coupling upon excitation of certain vibrational modes. Again, theory could here provide essential and otherwise unattainable information.

Finally, a still more tantalizing goal, is the study of M-TBA (see chapter 2). Should the theoretical results for the TBA adsorbate - substrate wave-function hybridization hold up to closer scrutiny, an explanation for the odd site-dependent switching efficiency of M-TBA⁵¹ is within the realm of possibility.

Acknowledgments

“Stand on the shoulders of giants.”

This old adage is the motto of Google Scholar*, a search engine for scientific literature I have often made use of in the course of this thesis work. It has a particular meaning to me: Since my childhood, I have felt a sense of awe reading works of and about the great historical scientific minds, on whose intellectual feats the very foundation of our modern society rests. The opportunity to be a part of the scientific process, and the remote possibility of perhaps contributing something of my own, was and is a primary driving force behind my choice to study science, and ultimately, this thesis.

However, science is not built on the shoulders of past intellectual giants alone – in my opinion, the success of a strive to excel hinges on the confidence only unconditional love and support from loved ones, family and friends can provide.

I therefore want to take this rare opportunity to thank

Min Älskade Katrin, for doubling my joys and halving my burdens. You have given me much, and will give me so much more still. For that, I am eternally grateful.

My parents and closest family Eva, John, Klas and Gustav, for giving me all possible means to pursue my goals, and supporting me at every turn.

My late grandfather, to whom this work is dedicated, for walking tall through life, and setting an example I am proud to follow.

You are *my* giants.

If anything, my years at the Fritz-Haber-Institut have shown me the importance of a free and open discourse for scientific work, and the strength in sheer numbers of colleagues with which to discourse – rarely have I wanted for expert guidance when, as was and is often the case, my curiosity has outweighed my ability. To that end, I have been particularly fortuitous to be funded by an International Max-Planck Research School (IMPRS[†]) scholarship, and project C3 of Sonderforschungsbereich (SFB) 658[‡], providing an invaluable extension to my scientific and social contexts.

*See scholar.google.com

[†]See www.imprs-cs.mpg.de

[‡]See userpage.physik.fu-berlin.de/~sfb658

ACKNOWLEDGMENTS

Credit is therefore also due to

My FHI supervisor Karsten Reuter, for despite my best unwitting efforts to the contrary unfailingly keeping my mind on track, and being an outstanding boss and teacher.

My FU / MBI supervisor Martin Weinelt, for a very rewarding collaboration.

My good friend and colleague Jörg Meyer, for fruitful collaboration on chapters 7 through 9, and his keen intellect and steadfast helpfulness.

Our collaborators Roland Schmidt and Cornelius Gahl, and the group of Stefan Tautz, for very worthwhile work on chapters 6 and 9, respectively.

My FHI and FU coworkers Matthias Scheffler, Volker Blum, Patrick Rinke, Xinguo Ren, Hong Jiang, Martin Fuchs, Alexandre Tkatchenko, Johan Carlsson, Martin Wolf, Stefan Kurth, and Eberhard 'Hardy' Gross for particularly helpful discussions.

My friends and coworkers at the FHI Theory Department and in the Junior Research Group in general, but in particular Hakim Meskine, Andrea Sanfilippo, Yongsheng Zhang, Mariana Rossi, Matteo Cavalleri, Ralf Gehrke, Adnan Sarfraz, Julia Stähler, and Felix Hanke, for brightening my days during and after work.

Our excellent theory department secretaries headed by Gaby Tysper, along with the other non-scientific staff at the FHI, for diligently keeping our workplace running smooth.

Modern science is also strongly dependent on technical resources. Computing time awarded in one grant from the DEISA[§] Consortium (co-funded by the EU, FP6 projects 508830/031513), and three grants from the Leibniz Rechenzentrum (LRZ[¶]) is gratefully acknowledged.

Last but not least I wish to point out, that this thesis work has been carried out almost exclusively using free and open source software (F/OSS): Apart from two of the electronic structure packages employed, every single program, from desktop operating systems to code development tools, script interpreters, algebraic solvers, data analysis tools, statistical tools, plotters, crystal and chemical visualizers, image illustration and processing software, desktop publishing, office and typesetting software etc., is freely downloadable by anyone, anywhere, anytime. Where software needs have not been met by existing code, new code has been developed, all of which in turn will be distributed free of charge under some version of the GNU Public License (GPL^{||}), in the hope of at least marginally repaying the hard-working, and largely unrewarded, F/OSS community.

Thank you all.

[§]See www.deisa.org

[¶]See www.lrz-muenchen.de

^{||}See www.gnu.org/licenses/gpl.html

Part V.

Appendices

A. Surface-Decoupled Switches

A.1. Basis Set Tests

This section details basis set tests for the ground state properties of pure azobenzene, in line with the methodological discussion of section 6.1. The test aims to find the optimal balance between computational cost and accuracy in the relevant properties, namely the ground state geometry and electronic structure, in particular the 1s Kohn-Sham eigenvalues used for the assignment of measured XPS binding energies. Basis sets of four cardinal numbers (ζ) have been tested: The first is a single ζ , Slater-type orbital (STO) basis set, 'STO-3G'^{267,268}. The second is the double- ζ LANL2DZ set, which for the relevant elements is equal to the D95V²⁶⁹ set. The third is the first revision of the Karlsruhe triple- ζ (TZ), valence (V, limited to one contraction for the core states) basis set with one set of polarization functions (P), or 'def-TZVP'¹⁵⁴. The fourth and last is the Dunning correlation-consistent (cc), quadruple- ζ (QZ) set augmented (aug-) with one set of diffuse functions, or aug-cc-pvQZ^{270,271}.

The first set is of very limited accuracy. The second is inaccurate by modern standards, the third represents the quality routinely found in literature, and the fourth is near the complete basis set limit of DFT. As is often the case, molec-

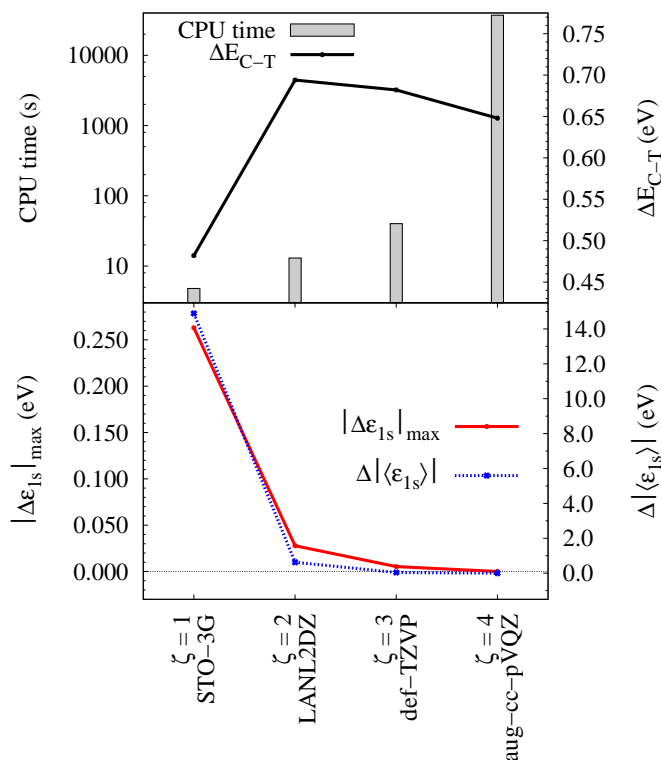


Figure A.1.: Basis set test on pure trans-azobenzene at single, double, triple and augmented quadruple ζ -level. Top left scale: The CPU time needed for one single-point calculation. Note the logarithmic scale. Top right scale: The cis-trans isomer relative stability ΔE_{C-T} . Bottom left scale: The maximum absolute change of any C 1s Kohn-Sham eigenvalue with respect to the quadruple ζ -value. Bottom right scale: The change in absolute average C 1s Kohn-Sham eigenvalues with respect to the quadruple ζ -value.

	def-TZVP ¹⁵⁴		IGLO-III ²⁷²	
	B3LYP	+ZND ¹⁶³	B3LYP	+ZND ¹⁶³
E_1 (eV)	2.56	2.48	2.56	2.48
μ_1 (D)	0.00	0.00	0.00	0.00
E_2 (eV)	3.72	3.73	3.68	3.70
μ_2 (D)	7.33	7.31	7.37	7.36
E_3 (eV)	4.08	4.10	4.05	4.07
μ_3 (D)	1.88	1.83	1.84	1.79

Table A.1.: The three lowest excitation energies (in electronvolt) and absolute transition dipole moments (in Debye) of trans-azobenzene, with the def-TZVP and IGLO-III basis sets, both tested for the ZND (see text) correction of the exchange-correlation kernel spatial decay.

ular geometries were found to be very robust with respect to the basis set, and relevant geometry parameters hardly varied, even between the double- and quadruple ζ -value. Thus, the outcome is decided by cost versus electronic structure accuracy. This is represented by four numbers, in Fig. A.1 plotted for a single trans-azobenzene molecule with the B3LYP functional (from left to right, top to bottom): The CPU time needed for one single-point calculation on a 16 CPU IBM Power5+ server with the given basis set, the cis-trans isomer relative stability ΔE_{C-T} , the maximum absolute change of any C 1s Kohn-Sham (KS) eigenvalue with respect to the quadruple ζ -value, and the change in absolute average C 1s KS eigenvalues with respect to the quadruple ζ -value (the latter two being defined as zero at the most accurate level of theory).

First, the CPU time ranges from negligible (seconds) at single-, to easily manageable (minutes) at triple-, to intractable for all intents and purposes (approximately twelve hours) at quadruple ζ -level. Second, the relative isomer stability quickly converges to within an acceptable 50 meV already at double ζ -level. Third and fourth, both maximal individual and collective, average changes in the C 1s KS levels are converged to within a negligible few meV of the largest basis set, at triple ζ -level. In summary, the sought optimal balance is represented by the def-TZVP triple ζ basis set.

A.2. TDDFT: ALDA / Basis Set Tests

This section aims to verify, that the unphysically fast spatial decay of the B3LYP / ALDA exchange-correlation kernel, and the lack of diffuse functions in the (for the ground state well-converged, see previous section) def-TZVP basis set do not affect the resonant excitation energies of interest. This is in practice done by comparing the three lowest singlet excitation energies E_n , and, since they enter the extended dipole model of section 6.5, the transition dipole moment magnitudes μ_n , for all combinations of the

A.2. TDDFT: ALDA / BASIS SET TESTS

standard, polarized def-TZVP basis set, the considerably more diffuse, triple ζ IGLO-III basis set²⁷², and with and without the semi-empirically determined potential correction of Zhan, Nichols and Dixon (ZND)¹⁶³ adapted for the B3LYP ALDA kernel.

The results for a single trans-azobenzene molecule at TDDFT / B3LYP level of theory are presented in Table A.1. In short, results vary less than acceptable 50 meV / 60 milli Debye. Thus, the good performance of TDDFT / ALDA / B3LYP for azobenzene can safely be considered more than an artifact of the basis set or failures in the TDDFT treatment of Rydberg states.

B. Surface Adsorbed Switches

This chapter provides information supplementary to that given in the main text, on the modeling of pure azobenzene adsorbed at coinage metal (111) surfaces. In addition to testing and verification of our PDOS code (section B.5), and a study of the effects of dispersion corrections on our PDOS findings (section B.6), the purpose of the following is twofold: On the one hand the computational model must be chosen such, that the error in relevant quantities compared to the fully computationally converged limit is acceptable. On the other, these calculations, as opposed to those of the preceding chapter, employ ultra-soft pseudopotentials¹⁴⁶ with non-local core corrections²⁷³ to represent the electron wave-function near the ionic nuclei. This is an additional approximation, the effects of which must be determined and minimized.

The advantages of pseudopotentials are significant: Only valence electrons are treated explicitly, which dramatically reduces the total number of electrons and thereby the size of the computational problem, in particular for heavier elements. Since the pseudopotential easily can be constructed to reproduce the valence electronic structure of a fully relativistic atom, computationally expensive and complicated relativistic corrections crucial to all-electron calculations of e.g. gold chemistry²⁷⁴ can be avoided.

However, these simplifications, like most other in first-principles modeling, come at a price: The optimal form of the pseudopotential core wave-function projector set (see section 5.2) depends on a multitude of choices. For example, if the core pseudization radius r_c is chosen too large, the pseudo and all-electron wave-functions will no longer agree in a chemically relevant spatial region, and one risks projectors overlapping between potentials, creating an unphysical, spurious wave-function in the interstitial region. This is a particularly important consideration for ultra-soft pseudopotentials, which use larger r_c . If one chooses r_c too small, the pseudo wave-function will approach the true all-electron wave-function, but described by a pure plane-wave basis set, without the support of the atom-centered functions in the mixed basis sets typically used in all-electron plane-wave calculations (e.g. using the full potential - linearized augmented plane wave or FP-LAPW technique). Thus, the pseudopotential calculation quickly becomes *less* efficient than a standard all-electron calculation for too small r_c .

Furthermore, the projector set (as in the closely related²⁷⁵ projector augmented wave or PAW technique) remains fixed, regardless of the form of the valence pseudo wave-function. This *frozen core* approximation influences e.g. core-polarization effects, introducing another element of uncertainty in the pseudopotential calculation. While it is technically possible to self-consistently optimize the projectors with respect to the pseudo valence wave function, this would again correspond to an extremely inefficient all-electron calculation, negating the justification for the pseudopotential. Additionally, even a perfectly constructed pseudopotential by construction shifts the true total DFT

potential by an unphysical constant. Therefore, differences of pseudo total energies or their variation with physical variables correspond to physical quantities, but the pseudo total energy itself does not.

These circumstances all beg the question how to ensure that approximations inherent in the pseudopotential approximation do not invalidate the results. The answer is simply, by thorough heuristic testing of a carefully chosen (or indeed, for the specific problem constructed) set of potentials, comparing characteristic quantities relevant for the problem of interest to the corresponding all-electron results. This, along with establishing converged settings for other numerical approximations employed, is the main goals of sections B.1 and B.2.

With the thereby established minimal acceptable computational model, section B.3 proceeds to establish a suitable model of surface adsorbed azobenzene. Section B.4 details further refinements necessary for maximum accuracy in the surface work function calculations. Finally, section B.6 shows results of DOS and PDOS calculations obtained with semi-empirically dispersion corrected (see chapter 8) DFT-GGA.

B.1. Convergence Tests: Bulk Metal Properties

As explained in subsection 7.2.1, the geometry of single azobenzene molecules optimized in large super-cells using the library pseudopotentials distributed with CASTEP, agree with the all-electron geometries and energetics presented in section 6.1 up to a 0.03 Å lengthening of the two studied bond lengths (d_{NN} and d_{CN}). The high plane-wave kinetic energy (E_{kin}) cutoff of 800 eV was needed because of the rapid variation (or 'hardness') of the aromatic wave-function of the molecule, which is common for such systems. Consequentially, the H, C and N pseudopotentials are deemed sufficient for the description of gas-phase molecular properties.

Modeling the metallic surfaces is more involved. Small bandgap systems are particularly prone to inefficiencies in \mathbf{k} -space sampling due to the discontinuity of the zero-temperature density of states at the Fermi level E_{F} . A popular remedy for this, is to fractionally redistribute the occupation of bands just below to bands just above E_{F} .

If the Fermi-Dirac distribution function is chosen, this corresponds to a physical thermal broadening at a given temperature related to the distribution width. Thus, this procedure adds a *generalized entropy* to the DFT total energy²⁷⁶. The SCF ground state is found by minimizing the *free energy* of the resulting so-called Mermin functional.

However, a system of zero-temperature ions and high-temperature electrons is rarely what is intended in DFT calculations – the entropy term enters as a mere numerical artifact, which when large can have detrimental effects on in particular the energy gradient^{277,278} (nuclear forces). Extensive testing revealed, that a simple gaussian smearing function resulted in a low entropy per smearing function width, and an overall stable SCF convergence. All calculated free energies have been corrected by subtracting half the entropy term, which for gaussian smearing has been shown to agree with the exact entropy correction to third order²⁷⁶.

B.1. BULK METAL PROPERTIES

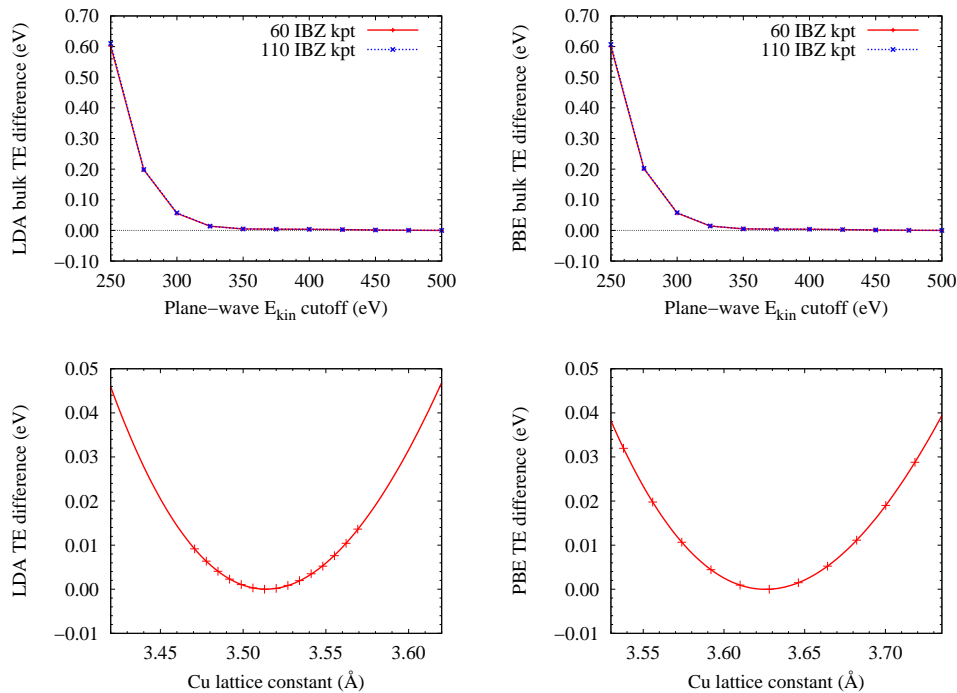


Figure B.1.: The dependence of bulk Cu fcc crystal total energy per atom on plane-wave kinetic energy cutoff E_{kin} (top) and lattice constant at fixed $E_{\text{kin}} = 350$ eV (bottom). Left: The LDA functional. Right: The PBE functional.

The first step in creating the surface model is to establish the corresponding bulk properties. Since chapter 8 includes a comparison of the LDA and GGA adsorption pictures for benzene, the following tests are all carried out for both functionals. In the top panel of Fig. B.1, the total energy per atom in a bulk Cu fcc crystal at the experimental lattice constant of 3.61 Å as a function of plane-wave kinetic energy E_{kin} cutoff has been plotted for an intermediate (60 points in the irreducible Brillouin zone) and dense (110 irreducible points) Monkhorst-Pack²⁰⁹ (MP) \mathbf{k} -space sampling grid.

Identical results have been obtained for very low (50 meV) to intermediate (250 meV) smearing widths. The plots show the crystal energy per atom converging to high precision at $E_{\text{kin}} = 350$ eV already at the intermediate \mathbf{k} -point grid, for both functionals. As identical results have been obtained for Ag and Au, only the Cu plots are shown.

With this converged E_{kin} cutoff and \mathbf{k} -point grid and a conservative smearing width of 150 meV, the variation of the bulk total energy per atom with the crystal lattice constant (shown at the bottom of Fig. B.1) is fitted to the Murnaghan equation of state²⁷⁹. The fit produces values for the lattice constant a_0 , the bulk modulus B_0 and the bulk total energy per atom E_0 of the crystal equilibrium. The former two are in Table B.1, unless otherwise stated, compared to all-electron calculations using the same functional parametrizations, for all three substrate materials and both levels of theory. The agreement between the here calculated a_0 and reference values is excellent. The somewhat more sensitive B_0 shows greater but acceptable differences.

B.2. Convergence Tests: Clean (111) Surface Properties

In this section the clean surface model is constructed, following the same procedure as in the previous section. The clean (111) surfaces are modeled by rotating the fcc primitive cell into a coordinate system with the x - and y -vectors in, and the z -vector perpendicular to the (111) plane. Viewed along this z -vector, the bulk-truncated (111) surface consists of atoms on a trigonal lattice of lattice constant $\frac{a_0}{\sqrt{2}}$, forming layers spaced $\frac{a_0}{\sqrt{3}}$ apart. Layers $n+1$, $n+2$ and $n+3$ ($n = 1, 2, 3 \dots$) are offset to the top layer by the xy -translations to the centers of the two inequivalent triangles formed by the top layer lattice and zero, respectively (see Fig. 7.2 and 7.4). The (111) surface is thus ABC stacked. An $(m \times n)$ surface unit cell is modeled by a super-cell (see Fig. 7.1) spanned by two vectors in the surface plane at an angle of 120° and lengths of $m \cdot \frac{a_0}{\sqrt{2}}$ and $n \cdot \frac{a_0}{\sqrt{2}}$, respectively.

Were this system not periodic also in the third direction, the quality of the super-cell surface model would be determined by the slab thickness alone - separated by an increasing number of sufficiently bulk like layers, the electronic structure at either side of the slab would approach that of a true surface resting on an infinitely thick bulk material. Specifically, the amount of energy required to create the surface from the bulk crystal, or *surface energy* σ would converge towards the exact value at the relevant level of theory.

However, as the system is $3D$ periodic, the slabs interact electrostatically also in the third direction. The properties of the model must consequentially also be converged for the vacuum separation of the slabs. In the multipole expansion of the slab interaction the dipole coupling decays slowest. Because of their inversion symmetry, clean bulk-truncated (111) slabs are dipole neutral, however²⁸⁰.

Since cleaving a crystal effectively breaks bonds formed by the surface atoms, introducing an asymmetry in the charge density surrounding them, the structure of surfaces generally does not remain that of truncated bulk^{187,188}. Instead, surfaces often *relax*, changing the inter-layer spacing of the top layer(s) and / or *reconstruct* in lateral atomic displacements lowering the surface strain. Of the latter, the complicated “herringbone” reconstruction of Au(111) with a $(22 \pm 1 \times \sqrt{3})$ surface unit cell²⁰⁷ is the quintessential example.

On the one hand, this reconstruction is relevant to the present work. On the other, its long range has two consequences: First, the individual displacements of each surface atom from the bulk truncated lateral positions are small. Second, the tremendously large resulting super-cells, with small surface energy gains per atom due to reconstruction, imply a computational involvement and accuracy beyond the aim of the present work - here, the focus is on *adsorption* at the Au(111) surface, rather than the surface itself.

In the following, the Au surfaces have therefore not been allowed to reconstruct. Cu(111) and Ag(111) do not reconstruct. Assuming the force on the top layer(s) is converged within the computational model, surface relaxation can be accounted for by optimizing an increasing number of top inter-layer distances in a slab of increasing thickness, until the deepest optimized layer doesn't relax.

B.2. SURFACE PROPERTIES

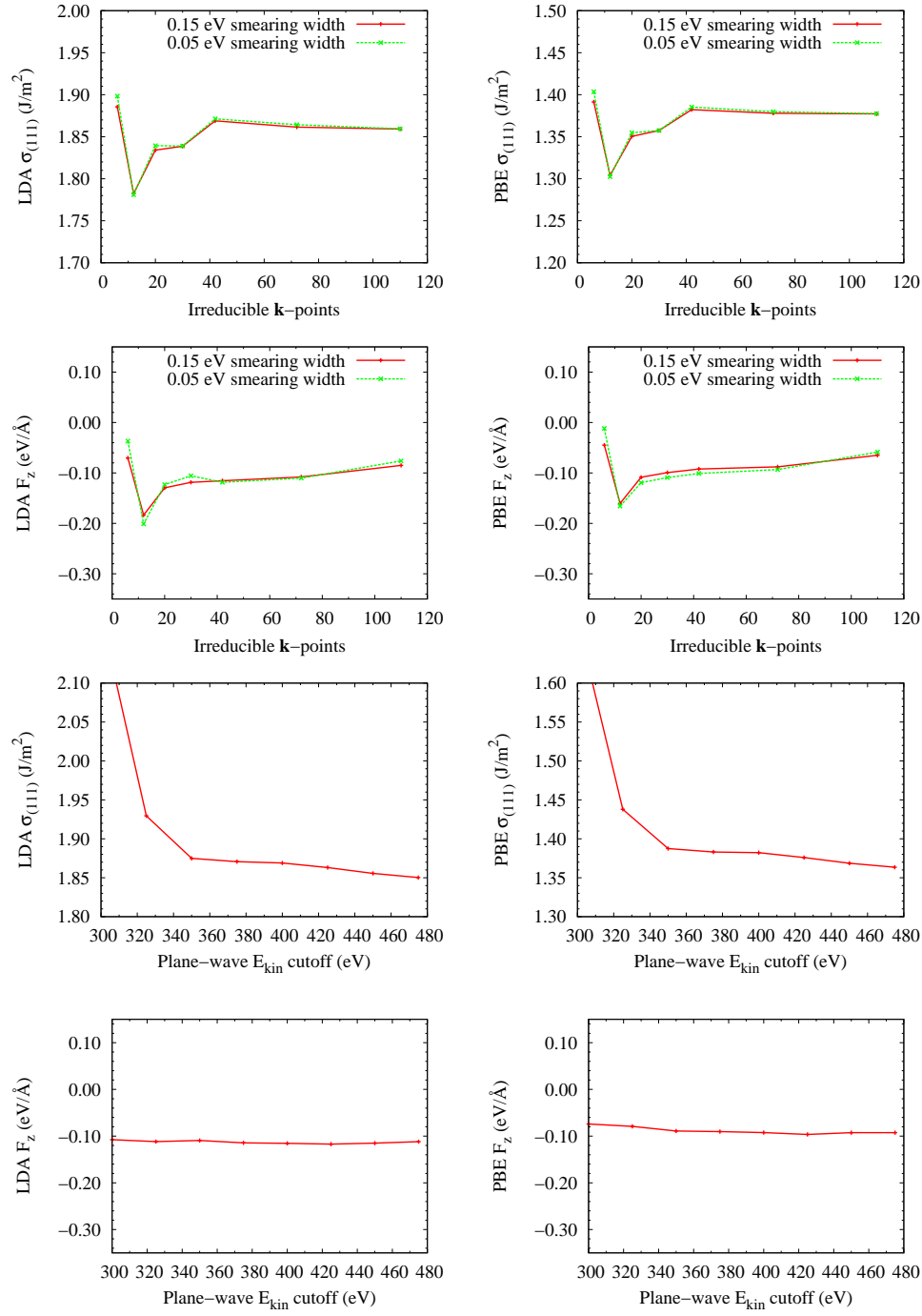


Figure B.2.: Convergence tests of the Cu surface energy ($\sigma_{(111)}$) and z-component of the force on the top layer (F_z). At right and left, results for the LDA and GGA functionals, respectively. Top two panels: Convergence with \mathbf{k} -points in the irreducible Brillouin zone. Bottom two panels: Convergence with plane-wave E_{kin} cutoff. Identical results have been obtained for Ag and Au.

APPENDIX B. SURFACE ADSORBED SWITCHES

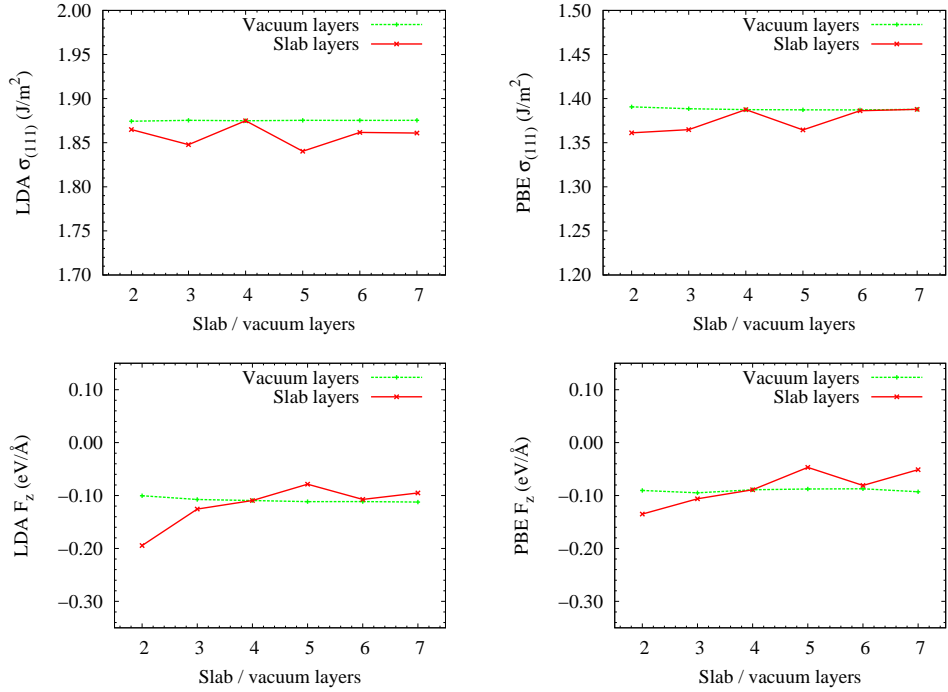


Figure B.3.: Clean Cu $\sigma_{(111)}$ and F_z convergence with respect to slab thickness and vacuum distance. Top panel: Convergence with \mathbf{k} -points in the irreducible Brillouin zone. Bottom two panels: Convergence with plane-wave E_{kin} cutoff. Identical results have been obtained for Ag and Au.

		a_0 (\AA)		B_0 (Mbar)		$\sigma_{(111)}$ (J/m^2)	
Au	LDA	4.08	^a 4.08 ²⁸¹	2.03	^a 1.82 ²⁸¹	1.16	^c 1.25 ²⁸²
	PBE	4.19	4.19 ²⁸¹	1.43	1.34 ²⁸¹	0.78	^d 0.70 ²⁸³
Ag	LDA	4.00	^a 4.00 ²⁸¹	1.49	^a 1.40 ²⁸¹	1.24	1.21 ²⁸⁴
	PBE	4.14	4.14 ²⁸¹	0.98	0.94 ²⁸¹	0.81	0.81 ²⁸⁵
Cu	LDA	3.51	^b 3.52 ²⁷⁸	1.90	^b 1.92 ²⁷⁸	1.87	^b 1.92 ²⁷⁸
	PBE	3.63	3.63 ²⁷⁸	1.45	1.42 ²⁷⁸	1.38	1.41 ²⁷⁸

Table B.1.: Comparison of bulk and surface properties obtained in this work to values found in literature. The latter have been obtained via all-electron calculations using the same xc-functionals, with exceptions where numbers have been calculated with ^athe VWN5 LDA parametrization²⁸⁶, ^bthe PW92 LDA parametrization²⁸⁷, ^cnorm-conserving pseudopotentials, and ^dthe PAW method.

B.2. SURFACE PROPERTIES

Consequentially, this section focuses on converging the (111) surface energy $\sigma_{(111)}$ and the z -component of the force on the top surface layer, with respect to four parameters: The E_{kin} cutoff and \mathbf{k} -point grid as in the previous section, and the slab thickness and vacuum distance. In a super-cell consisting of a (1×1) surface unit cell with k single-atom layers, the (111) surface energy is calculated according to

$$\sigma_{(111)} = \frac{1}{2} \cdot \frac{4(E - k \cdot E_0)}{a_0^2 \sqrt{3}} \quad (\text{B.1})$$

where E is the slab total energy, E_0 and a_0 are the equilibrium bulk total energy per atom and lattice constant, respectively, and the prefactor accounts for the fact that the slab has two surfaces. As no physical reason for wave-function dispersion in the direction perpendicular to the surface exists, \mathbf{k} -space is only sampled in the Γ -point in the super-cell z -direction.

The results of the convergence tests in this section are shown in Fig. B.2 and Fig. B.3. Unless otherwise stated, these calculations were performed for a four layer slab of a (1×1) surface unit cell lateral extension, with a plane-wave E_{kin} cutoff of 350 eV and a $(12 \times 12 \times 1)$ MP grid. As identical results have been obtained for Ag and Au, only plots for Cu are shown.

Results for the first two independent variables are shown in Fig. B.2. In line with the reasoning of the previous section, convergence with respect to irreducible \mathbf{k} -points is plotted for small (50 meV) and intermediate (150 meV) smearing widths. The plots show both properties of interest converging to an acceptable precision at 42 irreducible \mathbf{k} -points, corresponding to a $(12 \times 12 \times 1)$ MP grid, for both xc-functionals. Since no significant differences between the small and numerically more efficient intermediate smearing widths are observed, all further calculations use the latter.

In the lower panel of Fig. B.2, the convergence of the two properties with respect to the plane-wave E_{kin} cutoff is shown. The surface energy converges to hundredths of a Joule per square meter at $E_{\text{kin}} = 350$ eV. The top layer force quickly converges to almost arbitrary accuracy with the E_{kin} cutoff. Again, the convergence behavior for the two xc-functionals is identical.

Convergence tests for the latter two independent variables are shown in Fig. B.3. Given the dipole neutrality of the slab geometries, the relevant properties unsurprisingly converge rapidly with vacuum “layers”, defined as the vacuum distance resulting from a slab layer removal. As for the slab thickness, the convergence of relevant properties is more erratic, consistent with the quantum size effects arising in slabs of this dimension²⁸⁸. While the converged surface energy value is well approximated by that obtained with a four layer slab, the top layer force component converges slightly slower.

Therefore, the relaxed surface geometry has been calculated in slabs of up to 13 layers. The relative changes in inter-layer spacings Δd_{ij} have been calculated according to

$$\Delta d_{ij} = \frac{d_{ij} - d_0}{d_0} \quad (\text{B.2})$$

where d_{ij} is the relaxed distance between layers i and j counting from the top, and

	LDA		GGA-PBE	
	(%)	Ref. ²⁷⁸	(%)	Ref. ²⁷⁸
Δd_{12}	-0.75	-1.58	-0.69	-1.19
Δd_{23}	0.27	-0.73	-0.12	-0.65
Δd_{34}	0.00	-0.43	0.00	-0.24

Table B.2.: Changes in the top inter-layer spacings of relaxed clean Cu (111) as defined in Eq. B.2, compared to reference all-electron values. Reference LDA values were obtained using the PW92 LDA parametrization²⁸⁷.

$d_0 = \frac{a_0}{\sqrt{3}}$ is the bulk inter-layer spacing. The results for clean Cu(111) are listed in Table B.2. While the here calculated relative changes in top inter-layer spacing are generally notably smaller than the reference numbers, it is important to remember, that the *absolute* differences to literature still remain minuscule - for example, with the calculated Cu lattice constant, the in Table B.2 typical difference of half a percent corresponds to approximately one picometer in absolute terms, which is well within the limits of the required accuracy. The negligible relaxation of Cu(111) surfaces is well established in DFT^{278,289} as well as in experiments²⁹⁰.

The results of the bulk and surface convergence tests have been compiled and compared to literature in Table B.1. Where possible, literature values obtained with all-electron calculations using the same xc-functional parametrization as in the current work have been chosen. Values for which no all-electron result using the LDA parametrization¹¹⁴ of the current work has been found, have been compared to literature values calculated with comparably accurate LDA parametrizations^{286,287} to the same free electron-gas data¹¹⁵. Values for which no all-electron calculation have been found, are compared to literature values calculated with norm-conserving pseudopotentials and the projector-augmented wave (PAW) method.

Despite these minor variations, the overall agreement between bulk and surface properties obtained in this and high quality previous work is generally very good. The question of whether the employed approximation of an ultra-soft pseudopotential in a plane-wave basis set is sufficient to provide an accurate surface model, can therefore be answered positively.

B.3. Adsorbed Azobenzene Convergence Tests

In this section, the by now familiar convergence test procedures are repeated in order to establish a computationally efficient yet accurate model for the relevant aspects of azobenzene adsorption at all three substrates. In contrast to the previous section, only the adsorption of azobenzene within the GGA-PBE^{116,117} approximation to the xc-functional is of interest.

As our study aims to characterize the bonding of a single molecule with an in principle

B.3. ADSORBED AZOBENZENE CONVERGENCE TESTS

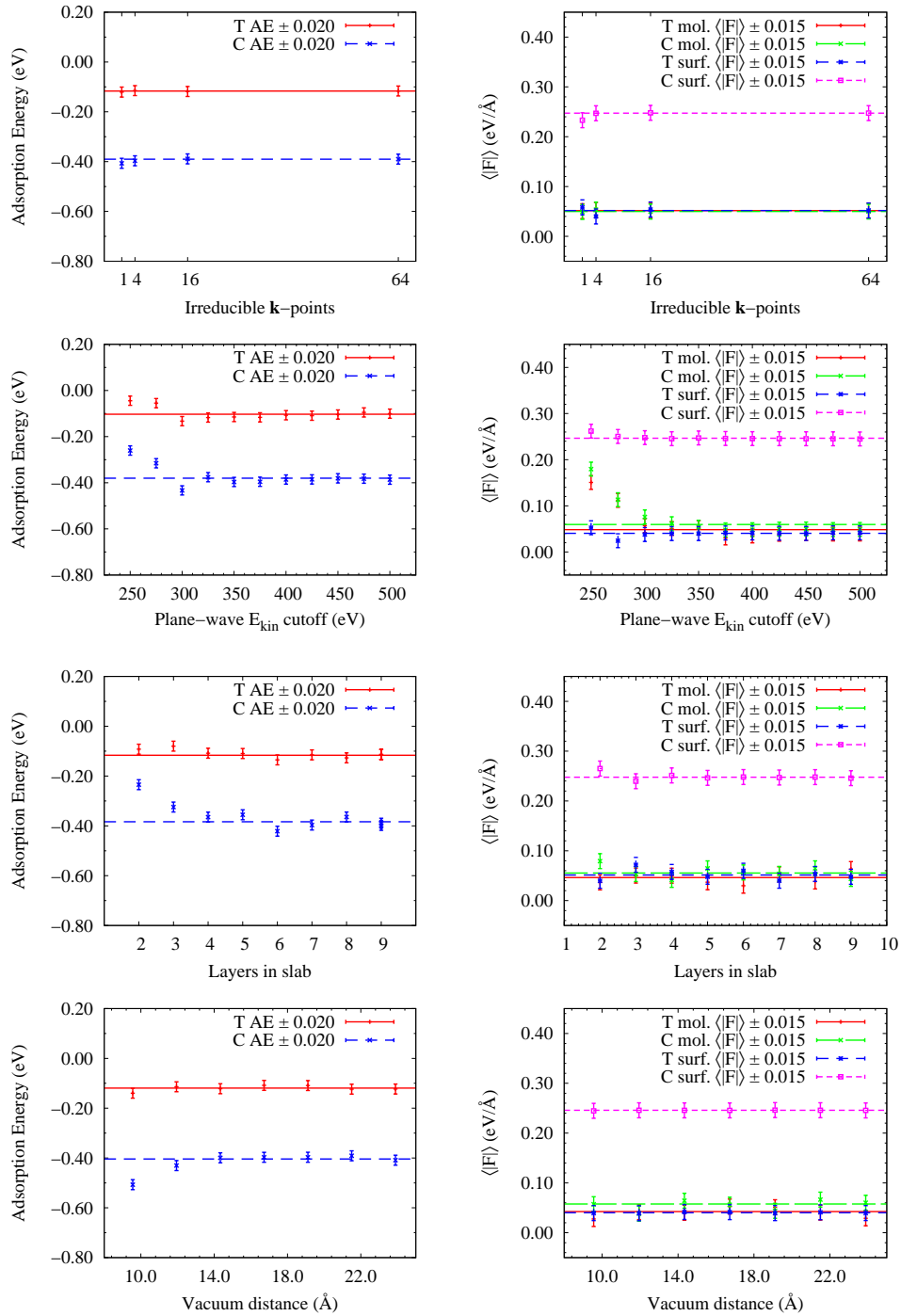


Figure B.4.: GGA-PBE convergence tests of azobenzene adsorbed at Ag(111), from top to bottom with respect to number of irreducible k -points, plane-wave E_{kin} cutoff, metal layers in slab, and vacuum distance between slabs. Left: Trans (T) and cis (C) adsorption energies. Right: Average force on the molecule (mol.), and on the adsorption site surface atoms (surf.). Each data series is shown with a given error bar, and the linearly weighted average of the series as a guide to the eye. All calculations were performed in the B1 adsorption geometry and a (6×3) surface unit super-cell (see text).

infinitely extended surface, a natural first step is to determine the lateral extension of the super-cell necessary to minimize the adsorbate - adsorbate interaction (see Fig. 7.1). Since the lateral extension of the trans isomer is greater than that of the cis isomer (see Fig. 1.1 and 7.4), it is sufficient to do so for the former.

The phenyl rings give trans azobenzene the dimension of a benzene molecule along its short axis in the molecular plane. The smallest surface unit cell able to accommodate a flat lying single benzene molecule is (3×3) , at all three surfaces. A simple calculation of the binding energy of the center molecule in a large sheet of benzene molecules in the Cu (3×3) periodicity, approximately corresponding to one adsorbed monolayer (ML) revealed, that the GGA-PBE direct intermolecular interactions in this system amount to circa 7 meV per molecule. For an azobenzene molecule in the same lateral periodicity along the short axis one could expect this number to roughly double, given the two phenyl moieties. Still, this number is sufficiently small on the scale of the numerical accuracy of interest here. Since as we shall see the adsorbate - substrate interaction is generally weak for adsorbates of this size, substrate mediated lateral interactions are expected to be small.

The azobenzene trans isomer is shorter than twice the sum of its width and one intermolecular distance along the short dimension. However, it is too long for a (5×3) cell in the B1 adsorption geometry (see Fig. 7.2), which here is chosen as the test system. Thus, a (6×3) cell, with a still weaker adsorbate - adsorbate interaction along the long dimension than the short, is chosen for the convergence tests of this section.

Our study requires an accurate computational model for the geometric as well as the electronic structure of the adsorbate - substrate system. Correspondingly, tests in this section are performed on the molecular adsorption energy E_{ads} , the average force on the molecule, and the average force on the substrate, here represented by the adsorption site metal atoms. The adsorption energy must be defined with respect to a relevant reference energy. Here, similar to section 7.1, the adsorption energy is calculated as

$$E_{\text{ads}} = E_{\text{azo}@ (111)} - E_{(111)} - E_{\text{azo}(\text{gas})} \quad (\text{B.3})$$

where $E_{\text{azo}@ (111)}$ is the total energy of the adsorbate - substrate system, $E_{(111)}$ is the total energy of a clean, bulk-truncated slab in a (6×3) super-cell, and $E_{\text{azo}(\text{gas})}$ is the total energy of the isolated adsorbate, fully optimized in a rectangular $(40 \times 30 \times 30) \text{ \AA}^3$ super-cell with Γ -point \mathbf{k} -space sampling. For simplicity, the bulk-truncated geometry is chosen for the clean slab reference, which is justified due to the negligible surface relaxation found in the previous section. The gas-phase molecular reference is of course fully converged for super-cell lateral extension.

Since similar to the preceding sections the test results are identical for all three surfaces, only the results for Ag(111) are shown in Fig. B.4. Based on the results of previous sections, these calculations were unless otherwise stated performed with a four layer slab geometry, a vacuum separation of 15 \AA , a plane-wave E_{kin} cutoff of 350 eV and an MP \mathbf{k} -point grid of $(2 \times 4 \times 1)$. Because of the geometrical relation between real and \mathbf{k} -space (i.e. reciprocal space, see section 5.2), the latter grid in a (6×3) super-cell yields the same density of irreducible points as the $(12 \times 12 \times 1)$ grid in a (1×1) cell.

	Φ	Ref.
Au(111)	5.24	5.15 ²⁹¹
Ag(111)	4.46	4.45 ²¹⁰
Cu(111)	4.85	4.78 ²⁷⁸

Table B.3.: Work functions Φ of clean coinage metal (111) surfaces, cf. Table 7.3. Reference numbers for Au, Ag and Cu have been obtained using GGA-PBE and ultra-soft pseudopotential, norm-conserving pseudopotential and all-electron techniques, respectively. All numbers in eV.

Figure B.4 shows, that the adsorption energy and force components both are converged to very high accuracy already at the coarsest \mathbf{k} -point grid of 4 irreducible points. The results for the four times more dense ($4 \times 8 \times 1$) MP grid of 16 irreducible points are indistinguishable from those of the sixteen times denser ($8 \times 16 \times 1$) MP grid of 64 irreducible points, on the scale of the plots. The E_{kin} cutoff test yields similar results, in that the adsorption energy and force averages of both isomers already at the default of $E_{\text{kin}} = 350$ eV are converged to within ± 20 meV and ± 15 meV / (\AA), respectively.

The results of the slab thickness test are, as with the surface energies, influenced by quantum size effects in the slab. In particular for the cis isomer, the variation of the adsorption energy after three layers is just barely within the plotted error bar of ± 20 meV. On the other hand, all four force components studied are well converged already at three slab layers. This slab thickness is therefore used in the geometry optimizations detailed in chapter 7, albeit not for calculating the corresponding binding energies (see discussion at the end of the following section).

Finally, the convergence of the relevant properties with vacuum distance is smoother. Unsurprisingly, the adsorption energy of the taller cis isomer converges after that of the trans isomer, at a slab - slab separation of the default 15 \AA . The converged vacuum distance is comparable at Au, and somewhat shorter (13 \AA) at Cu.

B.4. Work Functions

In chapter 7, the projected density of states of adsorbed azobenzene is analyzed within a modified Schottky-Mott model. Since projection is done on an isolated molecule, the PDOS must be shifted by the surface work function Φ for its energy scale to be comparable to that of the adsorbed system DOS.

The work function is defined as the difference between the chemical potential μ and the potential at infinite separation from the system, i.e. the vacuum potential V_{vac} . At zero temperature, the former is equal to the Fermi energy E_{F} . In a finite system the latter is trivially defined, but in periodic boundary conditions this is more complicated. In principle, given a super-cell with sufficient vacuum separation between periodic images of the system, the potential in the center of the vacuum equals V_{vac} . Establishing a proper vacuum reference is thus subject to convergence of the model, much like the

APPENDIX B. SURFACE ADSORBED SWITCHES

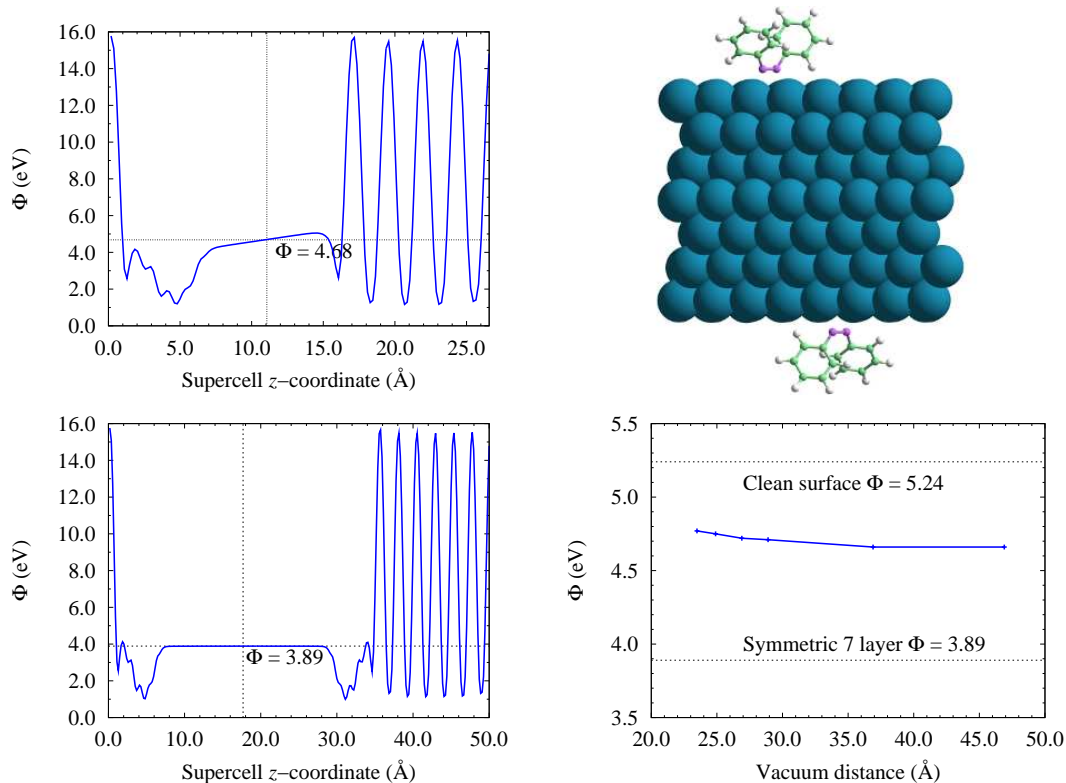


Figure B.5.: Work functions Φ of the azobenzene cis isomer at the Au(111) surface. Top left: Φ of the molecule adsorbed on one side of a 5 layer slab, as a function of super-cell z -coordinate. Top right: The geometry of the asymmetric slab, inverted in the fourth layer to form an inversion symmetric 7 layer slab, with adsorption on both sides. Bottom left: Φ as a function of super-cell z -coordinate for the inversion symmetric slab. Bottom right: Convergence of the asymmetric slab Φ as a function of vacuum distance in the super-cell, compared to Φ for inversion symmetric and clean slabs. Qualitatively identical results have been obtained for Ag and Cu.

properties discussed in the previous two sections.

In practice, the electronic potential in the super-cell is mapped onto a regular, three-dimensional grid. Grid points are then averaged in x and y , resulting in a one-dimensional potential as a function of the z -coordinate in the super-cell. The work function is given by the value of the electronic potential in the center of the vacuum, minus the Fermi energy of the system.

For the dipole neutral, clean surfaces this approach works well without modification: Even for a moderate vacuum separation the electronic potential rapidly decays to a constant vacuum value, and the resulting work functions are in excellent agreement with literature values (see Table B.3). Nevertheless, work functions are substantially more sensitive to fine computational detail than total energies.

This is illustrated by the fact, that the density of the grid on which the charge density is represented had to be increased, with the grid point spacing in reciprocal space increased from the $1.8 \mathbf{k}_{\text{cut}}$ otherwise used, to the maximum of $2.0 \mathbf{k}_{\text{cut}}$, to ensure full

Φ convergence. Additionally, the SCF convergence energy threshold was lowered from otherwise 10^{-7} eV / atom to $5 \cdot 10^{-9}$ eV / atom.

The surface work functions of the adsorbed molecules pose additional challenges, however: In Fig. B.5, the work function of a cis isomer fully geometry optimized at one side of a four layer slab, with an additional bulk layer added, is shown at top left. Note, that the electronic potential spiking above the vacuum value (shown as tall peaks at right) at the ionic nuclei is an unphysical artifact of the pseudopotential approximation of no consequence for the properties of interest, namely the Fermi energy and vacuum electronic potential.

In this system, the potential between the adsorbate and the periodic image of the substrate never entirely flattens out. Taking the potential at the center of the vacuum as the best approximation of V_{vac} , we obtain a Φ of 4.68 eV, relatively close to that of the clean slab (5.24 eV). However, this value is likely tainted by the finite dipole moment of the asymmetric slab coupling to its periodic images, and must be thoroughly converged with respect to vacuum distance.

Such a test is shown in the bottom right of Fig. B.5, where the asymmetric Φ is compared to that of the clean surface, and an inversion symmetric seven layer geometry (shown in the same figure at top right). The latter has been obtained by inverting the (as described in chapter 7) fully geometry optimized, four layer adsorbate-substrate system in the bottom layer, forming a strictly inversion symmetric seven layer slab with a molecule adsorbed at both sides.

The substantially reduced dipole moment of this geometry not only couples less to periodic images, as indicated by the rapid decay of the electronic potential towards V_{vac} as shown in the bottom left of Fig. B.5, but also by the Kleinman proof²⁸⁰ zeroes the *internal* dipole moment in the slab, providing a far better approximation of the electronic structure of an actual surface atop a semi-infinite bulk system.

As shown in the bottom right of Fig. B.5, the latter contribution is considerably more important than that of the dipole coupling between periodic images: The asymmetric Φ converges slowly with vacuum distance towards a lower value than that of the clean surface, but will not reach the inversion symmetric Φ of 3.89 eV.

While as shown in the previous section energetics and forces are well converged in the computationally much cheaper asymmetric four layer system, making it ideal for e.g. geometry optimizations, the corresponding inversion symmetrized slabs represent a still better converged surface model. Therefore, adsorption energy, relative isomer stability and PDOS calculations in chapter 7 are performed in these systems.

B.5. (P)DOS Convergence Tests

As explained in chapter 7, the current work requires the development and implementation of an analysis tool capable of projections of adsorbate-substrate system wave-functions onto isolated molecular wave-functions. The integrity and accuracy of this tool has been thoroughly tested with respect to projection sum rules, and compared to less advanced implementations in other software packages for a range of simple projections (e.g. on

APPENDIX B. SURFACE ADSORBED SWITCHES

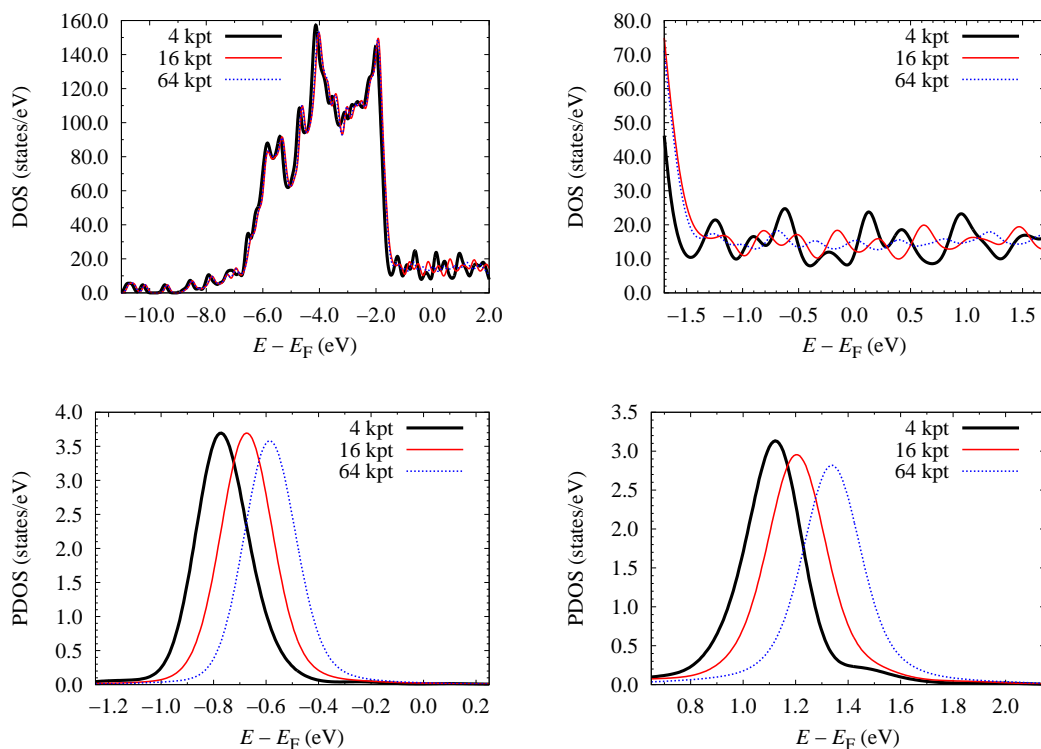


Figure B.6.: Convergence of DOS and PDOS of the trans isomer at an asymmetric 5 layer Au slab, with irreducible \mathbf{k} -points (labeled 'kpt' in plots). Top left: The adsorbed system DOS. Top right: Detail of the DOS, showing variations in the surface states. Bottom panel: The adsorbed system DOS projected on the isolated molecule HOMO and LUMO at left and right, respectively. Again, qualitatively identical results have been obtained for Ag and Cu.

either atom of a diatomic molecule).

However, as mentioned in the previous section, the precise electronic structure, i.e. the Kohn-Sham orbitals of a given system, are often more sensitive to subtle computational details than the total energy (and thereof derived properties). Consequentially, the DOS and PDOS must also be converged for aspects of the computational model. Variations in the plane-wave E_{kin} cutoff produced no changes in the DOS and PDOS, which were also found similarly insensitive to changes in the pseudopotentials. Slab thickness and vacuum distance are as explained in the previous section already set very high on the scale of necessary accuracy.

The DOS and PDOS convergence with irreducible \mathbf{k} -points of a test system consisting of a trans azobenzene molecule adsorbed at an asymmetric 5 layer slab, is shown in Fig. B.6. The general DOS shows small qualitative differences between the 4 irreducible \mathbf{k} -points of the minimal ($2 \times 4 \times 1$) MP grid and the denser ($4 \times 8 \times 1$) and ($8 \times 16 \times 1$) grids, which in turn are comparatively very similar.

Unsurprisingly, this difference becomes more obvious when focusing only on the surface

B.6. DISPERSION CORRECTED (P)DOS

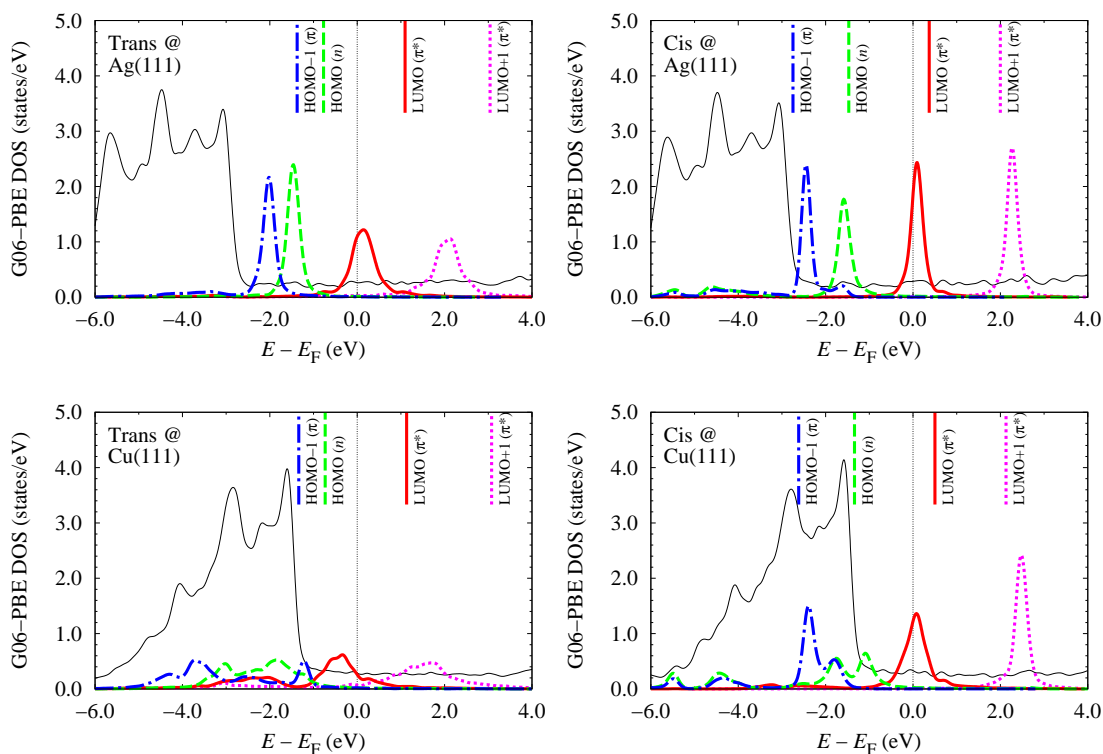


Figure B.7.: DOS and PDOS, obtained in the same way as that of Fig. 7.5, of adsorbate geometries calculated with the PBE xc-functional and the G06²⁰¹ dispersion correction scheme. Trans and cis isomer plots at Ag and Cu are shown at left and right and from top to bottom, respectively. The DOS, shown as a thin black line in the background of each plot, has been scaled with a factor 75 to bring it on the same scale as the PDOS. The PDOS of the four relevant orbitals, and the corresponding Kohn-Sham eigenvalues of the isolated gas-phase molecule, are shown as colored peaks and identically colored lines drawn from the upper plot border, respectively. Note that the G06 scheme offers no parameters for Au.

states, as shown in the top right of Fig. B.6. For the HOMO PDOS shown in the bottom left of Fig. B.6 all grids are qualitatively similar, and the quantitative differences are limited to a positive energetic shift of the centroid of the projection with increasing \mathbf{k} -point density. The LUMO PDOS of the sparsest grid shows a small but distinct tail at higher energy, which does not appear with the denser grids. In short, the of the three intermediately dense ($4 \times 8 \times 1$) MP grid is deemed optimal for the DOS / PDOS calculations.

B.6. Dispersion Corrected DOS and PDOS

Chapter 7 focuses on those properties of the DFT-GGA bonding of azobenzene at coinage metal (111) surfaces, that remain unchanged with application of dispersion corrections

as described in chapter 8. Among these, the qualitative features of the DOS and PDOS are mentioned. For completeness, the results of the same PDOS analysis as described in chapter 7 for the dispersion corrected geometries are presented in this section.

The OBS scheme does not significantly modify any of the GGA-PBE optimized geometries. Consequentially, its DOS / PDOS is for all three surfaces indistinguishable from the results presented in Fig. 7.5, and has been left out here. The G06 scheme on the other hand strongly modifies the GGA-PBE adsorbate geometries. However, the isolated adsorbate projected PDOS, shown in Fig. B.7 only for Cu and Ag since the G06 scheme lacks parameters for Au, shares and in some cases even more vividly exhibits the features identified in the GGA-PBE analysis:

At Ag(111), while the hybridization of frontier orbitals is small compared to the Cu case, the LUMO in both isomers hybridizes significantly with the substrate electronic structure, notably in the cis isomer being pinned at the Fermi level. At Cu, the entire spectrum of projected frontier orbitals hybridizes very strongly with the substrate, in particular in the trans isomer. This effect is much stronger in the dispersion corrected geometries.

In the TS scheme (see Fig. B.8), the situation at Cu and Ag is similar to that of the G06 scheme. Interestingly however, the strong hybridization of the LUMO observed at Cu and Ag is not seen in the TS-corrected geometry at Au - instead, the LUMO remains largely unaffected, and clearly above the Fermi level in both isomers.

While the here calculated DOS is severely limited by the functional approximation, for example the Ag *d*-band appears some one eV higher in Fig. B.7 and B.8 than in experimental measurements, this hints at a possible explanation for the considerably greater switching yield at Au compared to Ag and Cu.

B.6. DISPERSION CORRECTED (P)DOS

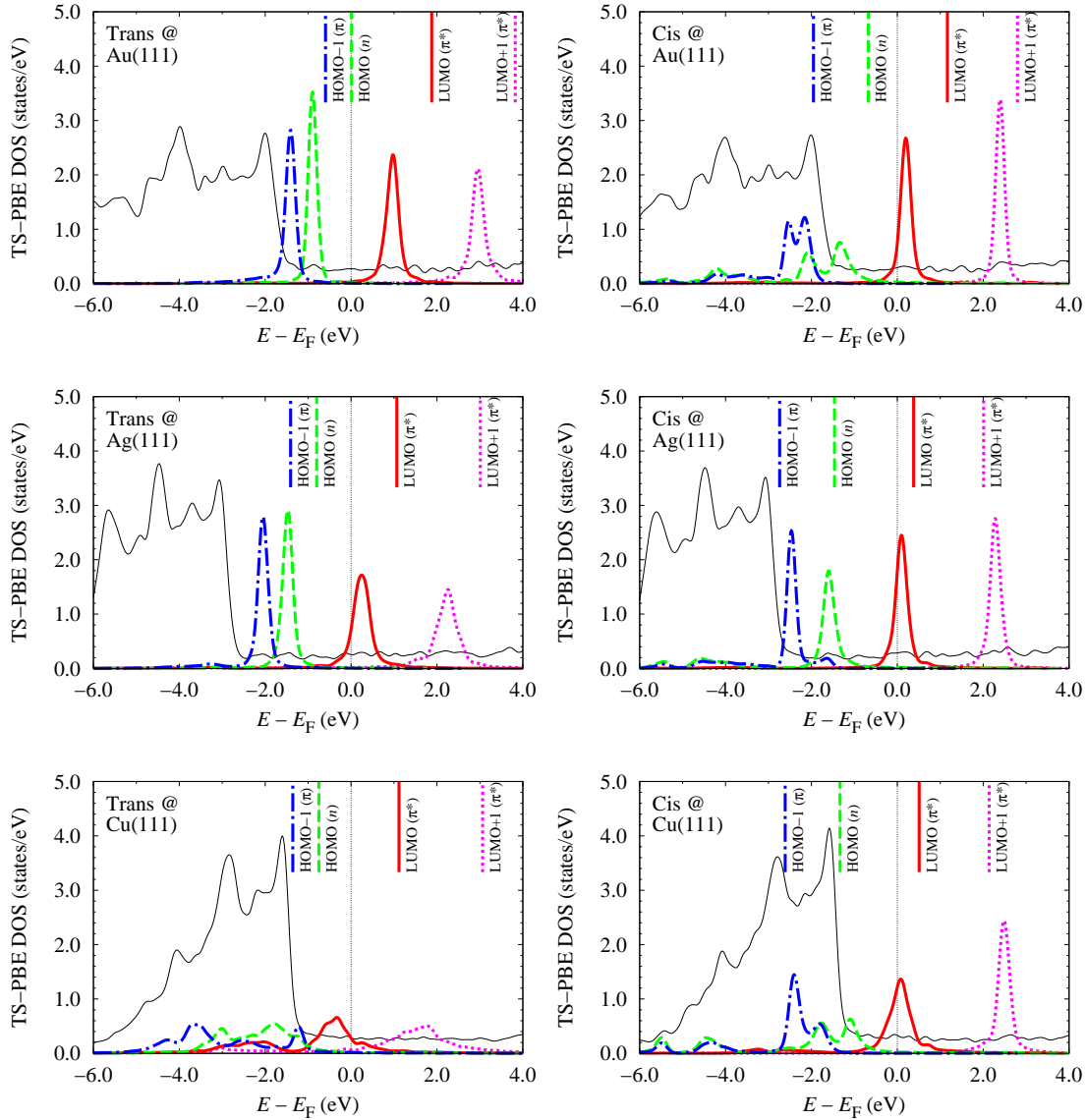


Figure B.8.: DOS and PDOS, obtained in the same way as that of Fig. 7.5, of adsorbate geometries calculated with the PBE xc-functional and the TS²⁰² dispersion correction scheme. Trans and cis isomer plots at Au, Ag and Cu are found at left and right and from top to bottom, respectively. The DOS, shown as a thin black line in the background of each plot, has been scaled with a factor 75 to bring it on the same scale as the PDOS. The PDOS of the four relevant orbitals, and the corresponding Kohn-Sham eigenvalues of the isolated gas-phase molecule, are shown as colored peaks and identically colored lines drawn from the upper plot border, respectively.

C. The Exchange-Correlation Correction Method

In this chapter, the technical detail of the exchange-correlation (xc) correction calculations discussed in chapter 10 is presented. Specifically, section C.1 reports on the rationale of the chosen cluster geometries, in addition to systematic basis set convergence tests and a discussion of the employed RI-MP2 approximation (see below). Section C.2 gives the detail of the MP2 adsorption energy extrapolation.

C.1. Cluster Geometries and Basis Sets

With the general methodology defined in section 10.1, we here establish an appropriate model chemistry and -system. The target system is a benzene molecule adsorbed at a Cu(111) surface in the 'HCP-B' geometry²¹³, as described in section 8.3. The periodic model has threefold rotational symmetry in the surface plane, and is treated as non-magnetic (i.e., non spin-polarized). As established in sections B.2 and B.3, a three layer slab represents the bare minimum in terms of an acceptable PBC surface model for the clean surface as well as for azobenzene adsorption. The same holds for adsorption of the weaker interacting benzene molecule. Consequentially, a series of cluster geometries for the calculation of $E_{xc-c}(N)$ have been defined as follows:

A large sheet of a three-layer slab with a single adsorbate was formed from the adsorbate geometry optimized as described in subsection 8.1.2 at PBC GGA-PBE^{116,117} level of theory and a surface distance z (see section 8.3) of 3.75 Å. Out of this system, clusters with even numbers of metal atoms, corresponding to half-spheres centered on the z -coordinate of the top layer and the xy -coordinates of the adsorbate center of mass were cut, resulting in the 22 and 52 Cu clusters shown in Fig. C.1. Removing even numbers of metal atoms consistent with the C_3 symmetry from these, in turn produces the other six geometries shown.

The smallest cluster in the range contains 6 top layer atoms of the first adsorbate coordination shell. The next larger geometry adds another 6 atoms in the second layer. The 16 Cu cluster includes the second coordination shell of the top layer, and four atoms in the second layer. The larger clusters all have three layers and increasing adsorbate coordination up to parts of the third coordination shell in the 52 Cu cluster. In addition to the C_3 symmetry, all but the 16 Cu cluster are C_s (mirror) symmetric in planes spanned by vectors between opposing hydrogen atoms and the cluster surface normal (see Fig. C.1).

While large compared to the semi-empirically corrected equilibrium distances of Table 8.4, the chosen adsorbate - substrate distance offers a simplification: In this geometry, the

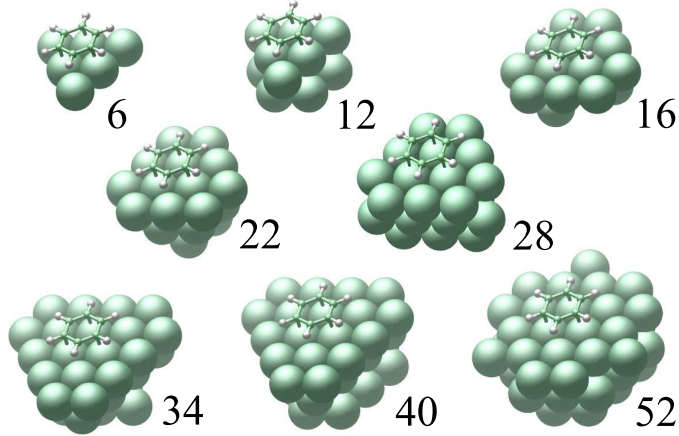


Figure C.1.: The Cu cluster geometries used in the xc-correction calculation, shown with the adsorbed benzene molecule, and labeled by their constituent number of Cu atoms. All clusters have C_3 symmetry, and all but the 16 Cu cluster are C_s (mirror) symmetric. Clusters 22 through 52 are cut out of a three layer slab.

optimal GGA-PBE adsorbate and substrate geometries differ not at all and negligibly to those of the gas-phase molecule and the truncated bulk surface, respectively. Therefore, we can here define the xc-correction E_{xc-c} at B level of theory to the benzene adsorption energy, as the correction on the adsorbate - cluster *interaction* energy E_{int}^X , without affecting the molecular and clean surface reference for the adsorption energy:

$$E_{xc-c}(N) \simeq E_{int}^B(N) - E_{int}^{PBE}(N) \quad , \quad (C.1)$$

where

$$E_{int}^X(N) = E_{mol@cl}^X(N) - [E_{cl}^X(N) - E_{mol}^X(N)] \quad , \quad (C.2)$$

and $E_{mol@cl}^X$, E_{cl}^X , and E_{mol}^X are the total energies of the molecule adsorbed at the Cu cluster, the clean cluster and the isolated molecule, respectively. This correction is then added to the PBC GGA-PBE adsorption energy of section 8.1.2, to form the xc-corrected adsorption energy E_{ads}^{xc-c} .

The cluster total energies are here calculated using atom-centered basis sets, and therefore include the basis set superposition error energy (BSSE, see section 5.1), which by way of $E_{int}^X(N)$ taints E_{ads}^{xc-c} . In the following, this is approximately remedied using the so-called counterpoise BSSE correction²⁹², which amounts to evaluating the three fragments of Eq. (C.2) in the exact same atomic orbital basis set (and integration grid, where applicable). Thus, E_{mol}^X is indirectly N -dependent via the basis functions of the metal cluster. Finally, the wave-functions in all calculations of $E_{int}(N)$ are treated as all-electron, closed shell (spin-compensated) and non-relativistic, as mentioned above.

The MP2 correlation energy is formulated in terms of four-index electron repulsion integrals (ERIs). The cost of evaluating these is proportional to the product of the squares of the numbers of occupied and virtual orbitals. In metal clusters, large num-

bers of electrons per atom naturally lead to large occupied orbital spaces, already for small clusters. The sensitive dependence of the MP2 correlation energy on the shape of virtual orbitals imply a requirement of many basis functions per atom in order to obtain physically meaningful results, which in turn leads to large virtual orbital spaces.

This combination makes standard MP2 for all intents and purposes intractable for all but the smallest clusters shown in Fig. C.1. Consequentially, all MP2 results presented here have been obtained using the so-called resolution of identity (RI) approximation^{293,294} to MP2. In this technique, four-index ERIs (4-ERIs) are approximated by linear combinations of products of three-index ERIs (3-ERIs), with auxiliary atom-centered basis functions P, Q as

$$(ia | jb) \approx (ia | Q)V_{PQ}^{-1}(P | jb) \quad , \quad (\text{C.3})$$

using the integral notation convention (3.7), and where

$$V_{PQ} = (P | Q) \quad (\text{C.4})$$

The advantages of this approximation for the present work can hardly be overstated: Approximate 4-ERIs are created 'on the fly', using fast linear algebra routines optimized for the computer architecture, decisively outperforming regular 4-ERI integral routines. Even if the auxiliary basis set equals the atomic basis set, making Eq. (C.3) exact to integral numerical precision, the total number of 3-ERIs is far, far smaller than the number of 4-ERIs.

Thus, the information necessary to construct all approximate 4-ERIs can often be cached in Random Access Memory (RAM), and accessed with a memory bandwidth many orders of magnitude greater than for disk storage. RAM caching is generally not an option for standard MP2 in any but the very smallest systems. If the RAM is insufficient also for the 3-ERIs, they can be stored on disk and accessed with bandwidth limitations on RI-MP2 performance correspondingly smaller compared to MP2. Additionally, the auxiliary basis set can be optimized^{295,296} for a given atomic orbital basis set and maximum RI error (difference between RI-MP2 and MP2 total energies), which further significantly reduces storage requirements and increases performance.

While the RI approximation does not reduce the number of necessary approximate 4-ERIs, and therefore does not affect the scaling of MP2, the general reduction of the computational *prefactor* is in literature²⁹⁶ conservatively estimated at one order of magnitude. In the calculations presented here, that performance gain is closer to two orders of magnitude (e.g. reducing times-to-solution of an estimated 4 - 6 weeks to ~ 6 hours), for the price of RI errors in MP2 interaction energies of ~ 10 meV, as determined by exhaustive tests.

Appropriate atomic orbital basis sets for all levels of theory remain to be established in a consistent fashion. The dual requirements of accurate RI-MP2 energies and systematic basis set convergence are satisfied by the use of the family of basis sets developed for use with the TURBOMOLE* package, of which the previously employed def-TZVP¹⁵⁴ set is a

*See www.turbomole.com

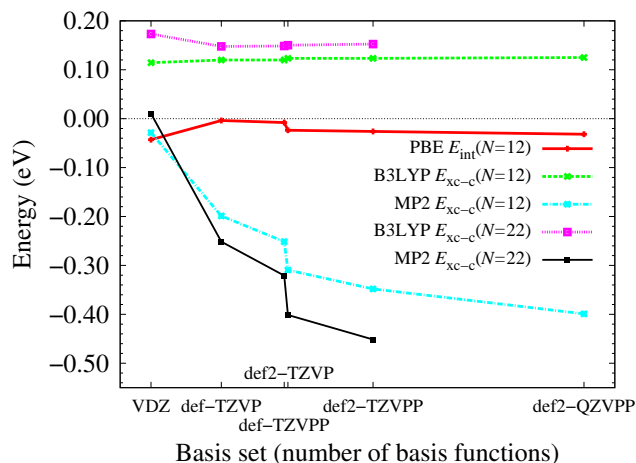


Figure C.2.: The B3LYP and MP2 xc-corrections in the 12 and 22 Cu clusters (cf. Fig. C.1), and the PBE E_{int} in the 12 Cu cluster, as a function of the number of functions in the basis set. Note the nearly identical number of basis functions in the def-TZVPP and def2-TZVP basis sets.

member, and for which highly optimized yet accurate RI-auxiliaries^{295,297} already exist.

Figure C.2 shows MP2 and hybrid functional (represented by B3LYP) xc-convergence tests using the valence double- ζ (VDZ) basis set, the def-TZVP set with (def-TZVPP¹⁵⁴) and without a second set of polarization functions, the second, more accurate revision (def2-²⁹⁸) of the triple- ζ sets, and the second revision of a doubly polarized, quadruple- ζ set (def2-QZVPP²⁹⁹).

Notably, the def2-TZVP set includes extra functions on the Cu atom in contrast to the similarly sized def-TZVPP set, resulting in a substantially increased accuracy per basis function of the former. This appears as a nearly discontinuous step in the curves of Fig. C.2. All calculations have been performed in the 12 Cu cluster geometry, and are supplemented by the corresponding numbers calculated in the 22 Cu geometry up to def2-TZVPP level, in order to show the qualitatively similar basis set convergence over the cluster size range.

In short, the hybrid functional xc-corrections converge rapidly with basis set size. While the B3LYP (not shown) and PBE E_{int} both converge separately at def2-TZVP level, the corresponding $E_{\text{xc-c}}$ are converged to high accuracy already at def-TZVP level, i.e. at approximately a 28 % reduction in necessary basis set size. This illustrates another benefit of the xc-correction scheme: Contributions of the B level of theory to $E_{\text{xc-c}}$, are not necessarily as basis set dependent as E_B itself. Therefore, if the basis set dependence of the A level of theory is congruent with that of B , $E_{\text{xc-c}}$ converges correspondingly faster with basis set size – the final, xc-corrected energy is calculated with an *optimal* basis set.

However, MP2 is as explained much more basis set dependent than, and its convergence with basis set size incongruent with that of, DFT. Correspondingly, the xc-correction energy does not converge in the basis set size range studied in Fig. C.2. Additionally, emphasizing the impact of the RI approximation on the present work, while evaluation

of the RI-MP2 correlation energy in the 22 Cu cluster with the def2-QZVPP basis set would be feasible with readily available computing resources, calculating the corresponding Hartree-Fock ground state is not, nor would it be in the larger cluster geometries. Therefore, a complete basis set (CBS) limit extrapolation³⁰⁰ of any merit cannot be performed. Instead, the RI-MP2 numbers are calculated with the def2-TZVPP set, which judging by Fig. C.2 appears to yield qualitatively, albeit not quantitatively, converged results. The MP2 E_{xc-c} is calculated with respect to def2-TZVP PBE numbers.

C.2. The MP2 XC-Correction

In Fig. 10.3, the PBE E_{int} calculated with the def2-TZVP basis set, the (RI-)MP2 E_{int} calculated with the def2-TZVPP basis set and the resulting E_{xc-c} is plotted. E_{xc-c} is extrapolated based on the Ansatz, that the MP2 correction on the benzene at Cu(111) PBE E_{int} can be written as the sum of a constant κ , analogous to the hybrid functional E_{xc-c} convergent with N , and C_6 -type inter-atomic interactions of some effective coefficients.

This amounts to fitting three unknowns, namely κ , and effective Cu - C and Cu - H dispersion coefficients $C_{6,\text{Cu-C}}$ and $C_{6,\text{Cu-H}}$ to the MP2 E_{xc-c} observable. Unfortunately, the position vectors of the carbon and hydrogen atoms are practically linearly dependent by the symmetry of the benzene molecule. Combined with the likely non-uniqueness of the optimal parameters for the long-range interaction, this leaves the results of such a fit ambiguous.

Instead, we rely on the fact that the TS²⁰² dispersion correction scheme as used in the previous two chapters is known to produce highly accurate dispersion coefficients for light molecules. If the ratio of the unknown MP2 dispersion coefficients is fixed to the corresponding average ratio $\Lambda_{\text{TS}} = \left\langle \frac{C_{6,\text{Cu-H}}^{\text{TS}}}{C_{6,\text{Cu-C}}^{\text{TS}}} \right\rangle = 0.30$ in the corresponding PBC model geometry of section 8.3, the long-range term in the fit is reduced to one variable $C_{6,\text{Cu-C}}$ (or equivalently, $C_{6,\text{Cu-H}}$ with an inverted Λ_{TS}). Since this variable describes a heteronuclear interaction, the difference to the corresponding TS value can be viewed as a uniform scaling of either the Cu *or* the C and H homonuclear coefficients (see subsection 8.1.1).

In short, the MP2 xc-correction is reformulated as

$$E_{xc-c}(N) = \kappa - C_{6,\text{Cu-C}} \left[\sum_{i=1}^N \sum_{j=1}^6 R_{ij,\text{Cu-C}}^{-6} + \Lambda_{\text{TS}} \cdot R_{ij,\text{Cu-H}}^{-6} \right] \quad (\text{C.5})$$

where $R_{ij,\text{Cu-C}}$ ($R_{ij,\text{Cu-H}}$) is the inter-atomic distance between Cu atom i and C (H) atom j . Since we wish to extrapolate the interaction with the most surface-like clusters in the range, only xc-corrections in three-layer cluster geometries have been included in the observable sample.

The fitted $\kappa = 0.34$ eV has a simple physical interpretation, as the sum of the Hartree-Fock - PBE xc-correction and those second-order correlation contributions poorly de-

scribed by the free-atom-in-molecule approximation (see section 8.1.1), e.g. due to the adsorbate image dipole. The fact that κ for fixed $C_{6,\text{Cu-C}}$ goes to the exact *Hartree-Fock* $E_{\text{xc-c}}$ with increasing z in a test geometry confirms this view. The value fitted for the dispersion coefficient $C_{6,\text{Cu-C}}$ is 78.6 ($\text{eV}\cdot\text{\AA}^6$), some 46 % higher than the corresponding TS value of 53.9 (in turn somewhat lower than the azobenzene value of Table 8.1).

With this information, the MP2/def2-TZVPP benzene adsorption energy at an extended, three-layer Cu(111) surface can be calculated. The relatively large adsorbate - substrate distance z in the cluster geometries again offers a simplification: In the corresponding TS-corrected PBC PBE geometry, the TS damping function contribution to the dispersion correction energy is negligible (< 1 meV). Therefore, the MP2 E_{ads} by Eq. (10.1) equals the PBC PBE E_{ads} of the corresponding geometry, added to κ , and the corresponding TS correction energy scaled by the ratio of the MP2 and TS $C_{6,\text{Cu-C}}$ coefficients, for a total of -0.67 eV.

This is not a prediction of the converged MP2 adsorption energy in the true equilibrium structure. However, the calculated MP2/def2-TZVPP number is similar to the TS E_{ads} of -0.71 eV in the corresponding geometry (cf. Fig. 8.4). In Fig. C.2, the MP2 interaction energy of the 12 Cu geometry increases by 16 % from the triple- to the quadruple- ζ basis set. This figure can in turn be expected to increase in the CBS limit. Scaling the MP2 E_{int} of Fig. 10.3 by this factor, in turn increases the extrapolated E_{ads} by a comparable factor. While a crude estimate, this suggests that the CBS MP2 E_{ads} exceeds that of TS in the current geometry.

Furthermore, the equilibrium properties of a dispersion-bonded system are determined by the balance between exchange repulsion and correlation attraction. Therefore, two possibilities exist for the true equilibrium MP2 properties of the current system: The equilibrium z could be large, comparable to or greater than that of the cluster geometries. As explained, this implies a slightly overestimated (~ 0.1 eV, cf. Table 8.4) equilibrium E_{ads} compared to experiment, but, given the similarity between the benzene and azobenzene geometries predicted by TS and the azobenzene geometry measured by NIXSW in chapters 8 and 9, also probably corresponds to a substantial overestimation of the true equilibrium z . Alternatively, at a smaller MP2 equilibrium z , the MP2 overestimation of the equilibrium E_{ads} would likely be comparable to or greater than that of TS. Results of a small number of test calculations in the 22 Cu geometry at shorter z , are consistent with the latter case.

Zusammenfassung

Eine der wissenschaftlichen Visionen der Nanotechnologie ist die Herstellung und gezielte Manipulation von mechanischen und elektronischen Bauteilen auf der Nanometerskala. Ein Weg zu solcher Kontrolle auf molekularer Ebene sind einzeln adressierbare Moleküle. Von diesen sind Moleküle, die durch äußere Einflüsse bi-stabil und reversibel modifizierbar sind – sogenannte molekulare Schalter – ein einfaches Beispiel mit offensichtlichem Anwendungspotential. Das Azobenzol-Molekül sticht hierbei durch seine besonders effiziente und stabile cis-trans Photoisomerisierung in Lösung hervor. Direkte Adressierbarkeit einzelner oder weniger Schaltereinheiten erfordert jedoch offensichtlich eine Lokalisierung und Ordnung der Schalter, so wie sie z.B. durch Adsorption auf Festkörperoberflächen erreicht werden kann.

Bisherige Versuche adsorbiertes Azobenzol zu Schalten waren jedoch nicht erfolgreich. Der Einsatz von Liganden zur gezielten Modifizierung der Schalter-Substrat Wechselwirkung erscheint vielversprechend, führte aber in der überwiegenden Zahl der bislang getesteten Fälle ebenfalls zum Verlust der Schaltfunktion. Diese Arbeit untersucht Azobenzol auf Festkörperoberflächen in den zwei Modellfällen der direkten Adsorption oder einer kompletten Entkopplung durch Liganden. Mit der Zielsetzung einer quantitativen Modellierung mit Vorhersagecharakter werden hierzu eine breite Palette von sogenannten first-principles oder ab initio Methoden der Elektronenstrukturtheorie und der theoretischen Oberflächenphysik eingesetzt. Da gerade die Natur der Wechselwirkung organischer Moleküle mit Metalloberflächen eine enorme Herausforderung für diese Methoden darstellt, ist neben den materialwissenschaftlichen Aspekten ein zweites Hauptthema methodologischer Natur. Dies betrifft insbesondere die Beschreibung dispersiver Wechselwirkungen bei gleichzeitiger Behandlung der ausgedehnten Festkörperoberfläche.

In Kombination mit Röntgen- und UV/Vis-Spektroskopie Experimenten werden in dieser Arbeit Azobenzol-funktionalisierte selbstorganisierte Monoschichten (self-assembled monolayers, SAMs) als Beispiel für Liganden entkoppelte Adsorption untersucht. Als Hauptgrund für den Verlust der Schaltfunktion wird hierbei exzitonische Kopplung innerhalb des Schalterensembles identifiziert. Neben bisher diskutierten sterischen Limitierungen bedeutet dies einen zweiten fundamentalen Aspekt, der überhalb einer kritischen Komponentendichte intrinsisch zum Verlust der Schaltfunktion führt und entsprechend beim Design zukünftiger Oberflächen-entkoppelter Schalterarrays berücksichtigt werden muss.

Die direkte Adsorption wird anhand dichtgepackter Münzmetalloberflächen (Cu, Ag und Au) untersucht. Die zur korrekten Beschreibung der metallischen Bandstruktur notwendig explizite Berücksichtigung der ausgedehnten Oberfläche führt hierbei zu großen Simulationzellen. Es wird gezeigt, dass die momentane Standard-Methode für solche Probleme – die Dichtefunktionaltheorie (DFT) mit (semi-)lokalen Austausch-Korrelations-

funktionalen – zu qualitativ falschen Ergebnissen führt, insbesondere aufgrund der ungenügenden Beschreibung der langreichweitigen van der Waals Wechselwirkungen. Da entsprechende Systemgrößen aktuell nicht mit genaueren ab initio Methoden handhabbar sind, wird das Problem im Rahmen semi-empirischer Dispersionskorrekturen zur DFT (DFT-D) analysiert bzw. deren Verlässlichkeit im Detail überprüft. Im Vergleich zu experimentellen state-of-the-art Beugungsdaten ist die DFT-D Vorhersage der Adsorptionsgeometrie auffallend genau. Die unzureichende energetische Beschreibung wird hingegen auf die Vernachlässigung elektronischer Abschirmeffekte an der metallischen Oberfläche zurückgeführt. Mit diesem Verständnis wird somit nicht nur ein Weg zur Verbesserung aktueller DFT-D Ansätze geliefert, sondern auch bereits bestehende DFT-D Ansätze als Mittel zur genauen Stukturbestimmung z. B. für weiterführende höhere ab-initio Rechnungen erarbeitet. Ein möglicher Zugang zu solchen ab initio Rechnungen für die hier diskutierten Systeme wird zuletzt im Ausblick diskutiert.

Lebenslauf

Aus Gründen des Datenschutzes ist der Lebenslauf
in der Online-Version nicht enthalten

Publications

- [I] R. Schmidt, E. McNellis, W. Freyer, D. Brete, T. Gießel, C. Gahl, K. Reuter, and M. Weinelt, "Azobenzene-Functionalized Alkanethiols in Self-Assembled Monolayers on Gold", *Appl. Phys. A* **93**, 267 (2008).
- [II] C. Gahl, R. Schmidt, D. Brete, E. R. McNellis, W. Freyer, R. Carley, K. Reuter, and M. Weinelt, "Structure and Excitonic Coupling in Self-Assembled Monolayers of Azobenzene-Functionalized Alkanethiols", *J. Am. Chem. Soc.* **132**, 1831 (2010).
- [III] E. McNellis, J. Meyer, A. Dehghan Baghi, and K. Reuter, "Stabilizing a Molecular Switch at Solid Surfaces: A Density Functional Theory Study of Azobenzene on Cu(111), Ag(111), and Au(111)", *Phys. Rev. B* **80**, 035414 (2009).
- [IV] E. R. McNellis, J. Meyer, and K. Reuter, "Azobenzene at Coinage Metal Surfaces: The Role of Dispersive van der Waals Interactions", *Phys. Rev. B* **80**, 205414 (2009).
- [V] G. Mercurio, E. R. McNellis, I. Martin, S. Hagen, F. Leyssner, S. Soubatch, J. Meyer, M. Wolf, P. Tegeder, F.S. Tautz, and K. Reuter, "Structure and Energetics of Azobenzene at Ag(111): Benchmarking Semi-Empirical Dispersion Correction Approaches", *Phys. Rev. Lett.* **104**, 036102 (2010).

Bibliography

- [1] W. Gärtner, "The Light Shall Show the Way - Or: The Conformational Changes of the Retinal Chromophore in Rhodopsin Upon Light Activation", *Angew. Chem. Int. Ed.* **40**, 2977 (2001).
- [2] Z. F. Liu, K. Hashimoto, and A. Fujishima, "Photoelectrochemical Information Storage Using an Azobenzene Derivative", *Nature* **347**, 658 (1990).
- [3] T. Ikeda and O. Tsutsumi, "Optical Switching and Image Storage by Means of Azobenzene Liquid-Crystal Films", *Science* **268**, 1873 (1995).
- [4] M. Del Valle, R. Gutiérrez, C. Tejedor, and G. Cuniberti, "Tuning the Conductance of a Molecular Switch", *Nat. Nanotechnol.* **2**, 176 (2007).
- [5] Y. Yu, M. Nakano, and T. Ikeda, "Photomechanics: Directed Bending of a Polymer Film by Light", *Nature* **425**, 145 (2003).
- [6] A. Teitel, "Über Eine Besondere Mechanische Wirkung des Polarisierten Lichts", *Naturwissenschaften* **44**, 370 (1957).
- [7] B. S. Neporent and O. V. Stolbova, "The Orientation Photodichroism of Viscous Solutions", *Opt. Spectrosc.* **10**, 146 (1961).
- [8] B. S. Neporent and O. V. Stolbova, "Reversible Orientation Photodichroism in Viscous Solutions of Complex Organic Substances", *Opt. Spectrosc.* **14**, 331 (1963).
- [9] A. M. Makushenko, B. S. Neporent, and O. V. Stolbova, "Reversible Orientational Photodichroism and Photoisomerization of Aromatic Azo Compounds I: Model of the System", *Opt. Spectrosc.* **31**, 295 (1971).
- [10] A. M. Makushenko, B. S. Neporent, and O. V. Stolbova, "Reversible Orientational Photodichroism and Photoisomerization of Complex Organic Compounds in Viscous Solutions. II: Azobenzene and Substituted Azobenzene Derivatives", *Opt. Spectrosc.* **31**, 397 (1971).
- [11] T. Todorov, L. Nikolova, and N. Tomova, "Polarization Holography. 1: A New High-Efficiency Organic Material With Reversible Photoinduced Birefringence", *Appl. Opt.* **23**, 4309 (1984).
- [12] A. Mostad and C. Rømming, "A Refinement of the Crystal Structure of *Cis*-Azobenzene", *Acta Chem. Scand.* **25**, 3561 (1971).

BIBLIOGRAPHY

- [13] J. A. Bouwstra, A. Schouten, and J. Kroon, "Structural Studies of the System *Trans*-Azobenzene/*Trans*-Stilbene. I. A Reinvestigation of the Disorder in the Crystal Structure of *Trans*-Azobenzene, $C_{12}H_{10}N_2$ ", *Acta Crystallogr. Sect. C* **39**, 1121 (1983).
- [14] H. K. Schulze, H. J. Petrick, H. K. Cammenga, and H. Klinge, "Thermodynamic Properties of the Structural Analogues Benzo[*c*]cinnoline, *Trans*-Azobenzene, and *Cis*-Azobenzene", *Z. Phys. Chem. Neue Fol.* **107**, 1 (1977).
- [15] G. S. Kumar and D. C. Neckers, "Photochemistry of Azobenzene-Containing Polymers", *Chem. Rev.* **89**, 1915 (1989).
- [16] T. Schultz, J. Quenneville, B. Levine, A. Toniolo, T. J. Martinez, S. Lochbrunner, M. Schmitt, J. P. Schaffer, *et al.*, "Mechanism and Dynamics of Azobenzene Photoisomerization", *J. Am. Chem. Soc.* **125**, 8098 (2003).
- [17] T. Nägele, R. Hoche, W. Zinth, and J. Wachtveitl, "Femtosecond Photoisomerization of *Cis*-Azobenzene", *Chem. Phys. Lett.* **272**, 489 (1997).
- [18] T. Fujino, S. Y. Arzhantsev, and T. Tahara, "Femtosecond Time-Resolved Fluorescence Study of Photoisomerization of *Trans*-Azobenzene", *J. Phys. Chem. A* **105**, 8123 (2001).
- [19] Z. F. Liu, K. Morigaki, T. Enomoto, K. Hashimoto, and A. Fujishima, "Kinetic Studies on the Thermal *Cis*-*Trans* Isomerization of an Azo Compound in the Assembled Monolayer Film", *J. Phys. Chem.* **96**, 1875 (1992).
- [20] G. Zimmerman, L.-Y. Chow, and U.-J. Paik, "The Photochemical Isomerization of Azobenzene", *J. Am. Chem. Soc.* **80**, 3528 (1958).
- [21] E. R. Talaty and J. C. Fargo, "Thermal *Cis*-*Trans*-Isomerization of Substituted Azobenzenes: A Correction of the Literature", *Chem. Commun. (London)* **2**, 65 (1967).
- [22] P. D. Wildes, J. G. Pacifici, G. Irick Jr., and D. G. Whitten, "Solvent and Substituent on the Thermal Isomerization of Substituted Azobenzenes. Flash Spectroscopic Study", *J. Am. Chem. Soc.* **93**, 2004 (1971).
- [23] H. Rau and E. Lüddecke, "On the Rotation-Inversion Controversy on Photoisomerization of Azobenzenes. Experimental Proof of Inversion", *J. Am. Chem. Soc.* **104**, 1616 (1982).
- [24] H. Rau, "Further Evidence for Rotation in the π, π^* and Inversion in the n, π^* Photoisomerization of Azobenzenes", *J. Photochem.* **26**, 221 (1984).
- [25] S. Monti, G. Orlandi, and P. Palmieri, "Features of the Photochemically Active State Surfaces of Azobenzene", *Chem. Phys.* **71**, 87 (1982).

- [26] I. K. Lednev, T.-Q. Ye, R. E. Hester, and J. N. Moore, "Femtosecond Time-Resolved UV-Visible Absorption Spectroscopy of Trans-Azobenzene in Solution", *J. Phys. Chem.* **100**, 13338 (1996).
- [27] I. K. Lednev, T.-Q. Ye, P. Matousek, M. Towrie, P. Foggi, F. V. R. Neuwahl, S. Umapathy, R. E. Hester, *et al.*, "Femtosecond Time-Resolved UV-Visible Absorption Spectroscopy of Trans-Azobenzene: Dependence on Excitation Wavelength", *Chem. Phys. Lett.* **290**, 68 (1998).
- [28] P. Cattaneo and M. Persico, "An *ab initio* Study of the Photochemistry of Azobenzene", *Phys. Chem. Chem. Phys.* **1**, 4739 (1999).
- [29] T. Ishikawa, T. Noro, and T. Shoda, "Theoretical Study on the Photoisomerization of Azobenzene", *J. Chem. Phys.* **115**, 7503 (2001).
- [30] A. Cembran, F. Bernardi, M. Garavelli, and L. Gagliardi, "On the Mechanism of the Cis-Trans Isomerization in the Lowest Electronic States of Azobenzene: S_0 , S_1 and T_1 ", *J. Am. Chem. Soc.* **126**, 3234 (2004).
- [31] L. Gagliardi, G. Orlandi, F. Bernardi, A. Cembran, and M. Garavelli, "A Theoretical Study of the Lowest Electronic States of Azobenzene: The Role of Torsion Coordinate in the Cis-Trans Photoisomerization", *Theor. Chem. Acc.* **111**, 363 (2004).
- [32] M. L. Tiago, S. Ismail-Beigi, and S. G. Louie, "Photoisomerization of Azobenzene from First-Principles Constrained Density-Functional Calculations", *J. Chem. Phys.* **122**, 094311 (2005).
- [33] E. W.-G. Diau, "A New Trans-to-Cis Photoisomerization Mechanism of Azobenzene on the $S_1(n,\pi^*)$ Surface", *J. Phys. Chem. A* **108**, 950 (2004).
- [34] D. Syomin, J. Kim, B. E. Koel, and G. B. Ellison, "Identification of Adsorbed Phenyl (C_6H_5) Groups on Metal Surfaces: Electron-Induced Dissociation of Benzene on Au(111)", *J. Phys. Chem. B* **105**, 8387 (2001).
- [35] X. L. Zhou, M. E. Castro, and J. M. White, "Interactions of UV Photons and Low Energy Electrons With Chemisorbed Benzene on Ag (111)", *Surf. Sci.* **238**, 215 (1990).
- [36] M. Xi, M. X. Yang, S. K. Jo, B. E. Bent, and P. Stevens, "Benzene Adsorption on Cu (111): Formation of a Stable Bilayer", *J. Chem. Phys.* **101**, 9122 (1994).
- [37] D. Syomin and B. E. Koel, "Probing the Reactivity of C_6 -Hydrocarbons on Au Surfaces: Cyclohexane, Cyclohexyl and Cyclohexene on Au (111)", *Surf. Sci.* **498**, 61 (2002).
- [38] X. L. Zhou, A. L. Schwaner, and J. M. White, "Syntheses and Reactions of Vinyl and Phenyl Fragments on Silver (111)", *J. Am. Chem. Soc.* **115**, 4309 (1993).

- [39] D. Dulić, S. J. van der Molen, T. Kudernac, H. T. Jonkman, J. J. D. de Jong, T. N. Bowden, J. van Esch, B. L. Feringa, *et al.*, "One-Way Optoelectronic Switching of Photochromic Molecules on Gold", *Phys. Rev. Lett.* **91**, 207402 (2003).
- [40] N. Katsonis, M. Lubomska, M. Pollard, B. L. Feringa, and P. Rudolf, "Synthetic Light-Activated Molecular Switches and Motors on Surfaces", *Progr. Surf. Sci.* **82**, 407 (2007).
- [41] A. Natansohn and P. Rochon, "Photoinduced Motions in Azo-Containing Polymers", *Chem. Rev.* **102**, 4139 (2002).
- [42] A. F. Grimes, S. E. Call, D. A. Vicente, D. S. English, and E. J. Harbron, "Toward Efficient Photomodulation of Conjugated Polymer Emission: Optimizing Differential Energy Transfer in Azobenzene-Substituted PPV Derivatives", *J. Phys. Chem. B* **110**, 319183 (2006).
- [43] L. Briquet, D. P. Vercauteren, E. A. Perpète, and D. Jacquemin, "Is Solvated Trans-Azobenzene Twisted or Planar?", *Chem. Phys. Lett.* **417**, 190 (2006).
- [44] L. Briquet, D. P. Vercauteren, J. Andre, E. A. Perpète, and D. Jacquemin, "On the Geometries and UV/Vis Spectra of Substituted Trans-Azobenzenes", *Chem. Phys. Lett.* **435**, 257 (2007).
- [45] M. J. Comstock, J. Cho, A. Kirakosian, and M. F. Crommie, "Manipulation of Azobenzene Molecules on Au (111) Using Scanning Tunneling Microscopy", *Phys. Rev. B* **72**, 153414 (2005).
- [46] A. Kirakosian, M. J. Comstock, J. Cho, and M. F. Crommie, "Molecular Commensurability With a Surface Reconstruction: STM Study of Azobenzene on Au(111)", *Phys. Rev. B* **71**, 113409 (2005).
- [47] J. A. Miwa, S. Weigelt, H. Gersen, F. Besenbacher, F. Rosei, and T. R. Linderoth, "Azobenzene on Cu (110): Adsorption Site-Dependent Diffusion", *J. Am. Chem. Soc.* **128**, 3164 (2006).
- [48] B.-Y. Choi, S.-J. Kahng, S. Kim, H. Kim, H. W. Kim, Y. J. Song, J. Ihm, and Y. Kuk, "Conformational Molecular Switch of the Azobenzene Molecule: A Scanning Tunneling Microscopy Study", *Phys. Rev. Lett.* **96**, 156106 (2006).
- [49] P. Tegeder, S. Hagen, F. Leyssner, M. V. Peters, S. Hecht, T. Klamroth, P. Saalfrank, and M. Wolf, "Electronic Structure of the Molecular Switch Tetra-Tert-Butyl-Azobenzene Adsorbed on Ag(111)", *Appl. Phys. A* **88**, 465 (2007).
- [50] Y. Wang, X. Ge, G. Schull, R. Berndt, C. Bornholdt, F. Koehler, and R. Herges, "Azo Supramolecules on Au(111) With Controlled Size and Shape", *J. Am. Chem. Soc.* **130**, 4218 (2008).
- [51] C. Dri, M. V. Peters, J. Schwarz, S. Hecht, and L. Grill, "Spatial Periodicity in Molecular Switching", *Nat. Nanotechnol.* **3**, 649 (2008).

- [52] J. Henzl, T. Bredow, and K. Morgenstern, "Irreversible Isomerization of the Azobenzene Derivate Methyl Orange on Au (111)", Chem. Phys. Lett. **435**, 278 (2007).
- [53] J. Henzl, M. Mehlhorn, and K. Morgenstern, "Amino-Nitro-Azobenzene Dimers as a Prototype for a Molecular-Level Machine", Nanotechnology **18**, 495502 (2007).
- [54] N. Henningsen, K. J. Franke, I. Fernández-Torrente, G. Schulze, B. Priewisch, K. Rück-Braun, J. Dokić, T. Klamroth, *et al.*, "Inducing the Rotation of a Single Phenyl Ring With Tunneling Electrons", J. Phys. Chem. C **111**, 14843 (2007).
- [55] N. Henningsen, R. Rurali, K. J. Franke, I. Fernández-Torrente, and J. I. Pascual, "Trans to Cis Isomerization of an Azobenzene Derivative on a Cu (100) Surface", Appl. Phys. A **93**, 241 (2008).
- [56] N. Henningsen, K. J. Franke, G. Schulze, I. Fernández-Torrente, B. Priewisch, K. Rück-Braun, and J. I. Pascual, "Active Intramolecular Conformational Dynamics Controlling the Assembly of Azobenzene Derivatives at Surfaces", ChemPhysChem **9**, 71 (2008).
- [57] K. Morgenstern, "Isomerization Reactions on Single Adsorbed Molecules", Acc. Chem. Res. **42**, 213 (2009).
- [58] J. Henzl, M. Mehlhorn, H. Gawronski, K.-H. Rieder, and K. Morgenstern, "Reversible Cis-Trans Isomerization of a Single Azobenzene Molecule", Angew. Chem. Int. Ed. **45**, 603 (2006).
- [59] M. Alemani, M. V. Peters, S. Hecht, K.-H. Rieder, F. Moresco, and L. Grill, "Electric Field-Induced Isomerization of Azobenzene by STM", J. Am. Chem. Soc. **128**, 14446 (2006).
- [60] L. Óvári, M. Wolf, and P. Tegeder, "Reversible Changes in the Vibrational Structure of Tetra-Tert-Butylazobenzene on a Au(111) Surface Induced by Light and Thermal Activation", J. Phys. Chem. C **111**, 15370 (2007).
- [61] M. J. Comstock, N. Levy, A. Kirakosian, J. Cho, F. Lauterwasser, J. H. Harvey, D. A. Strubbe, J. M. J. Fréchet, *et al.*, "Reversible Photomechanical Switching of Individual Engineered Molecules at a Metallic Surface", Phys. Rev. Lett. **99**, 038301 (2007).
- [62] S. Hagen, F. Leyssner, D. Nandi, M. Wolf, and P. Tegeder, "Reversible Switching of Tetra-Tert-Butyl-Azobenzene on a Au(111) Surface Induced by Light and Thermal Activation", Chem. Phys. Lett. **444**, 85 (2007).
- [63] M. J. Comstock, N. Levy, J. Cho, L. Berbil-Bautista, M. F. Crommie, D. A. Poulsen, and J. M. J. Fréchet, "Measuring Reversible Photomechanical Switching Rates for a Molecule at a Surface", Appl. Phys. Lett. **92**, 123107 (2008).

- [64] M. Alemani, S. Selvanathan, F. Ample, M. V. Peters, K.-H. Rieder, F. Moresco, C. Joachim, S. Hecht, *et al.*, "Adsorption and Switching Properties of Azobenzene Derivatives on Different Noble Metal Surfaces: Au(111), Cu(111), and Au(100)", *J. Phys. Chem. C* **112**, 10509 (2008).
- [65] M. Wolf and P. Tegeder, "Reversible Molecular Switching at a Metal Surface: A Case Study of Tetra-Tert-Butyl-Azobenzene on Au(111)", *Surf. Sci.* **603**, 1506 (2009).
- [66] G. Jiang, K. M. Park, J. Y. Park, H. Shin, and R. Advincula, "Electro-Nanopatterning of Surface Relief Gratings on Azobenzene Layer-by-Layer Ultrathin Films by Current-Sensing Atomic Force Microscopy", *J. Phys. Chem. B* **110**, 17309 (2006).
- [67] M. Jaschke, H. Schönherr, H. Wolf, H.-J. Butt, E. Bamberg, M. K. Besocke, and H. Ringsdorf, "Structure of Alkyl and Perfluoroalkyl Disulfide and Azobenzenethiol Monolayers on Gold(111) Revealed by Atomic Force Microscopy", *J. Phys. Chem.* **100**, 2290 (1996).
- [68] S. Kucharski, R. Janik, H. Motschmann, and C. Radüge, "Trans-Cis Isomerisation of Azobenzene Amphiphiles Containing a Sulfonyl Group", *New J. Chem.* **23**, 765 (1999).
- [69] P. S. Weiss, "Functional Molecules and Assemblies in Controlled Environments: Formation and Measurements", *Acc. Chem. Res.* **41**, 1772 (2008).
- [70] M. Zharnikov and M. Grunze, "Thiol-Derived Self-Assembling Monolayers", *J. Phys.: Condens. Matter* **13**, 11333 (2001).
- [71] S. F. Bent, "Heads or Tails: Which Is More Important in Molecular Self-Assembly?", *ACS Nano* **1**, 10 (2007).
- [72] G. Pace, V. Ferri, C. Grave, M. Elbing, C. von Hänisch, M. Zharnikov, M. Mayor, M. A. Rampi, *et al.*, "Cooperative Light-Induced Molecular Movements of Highly Ordered Azobenzene Self-Assembled Monolayers", *Proc. Nat. Acad. Sci.* **104**, 9937 (2007).
- [73] L. Dubois and R. G. Nuzzo, "Synthesis, Structure, and Properties of Model Organic Surfaces", *Annu. Rev. Phys. Chem.* **43**, 437 (1992).
- [74] A. Ulman, "Formation and Structure of Self-Assembled Monolayers", *Chem. Rev.* **96**, 1533 (1996).
- [75] G. E. Poirier, "Characterization of Organosulfur Molecular Monolayers on Au(111) Using Scanning Tunneling Microscopy", *Chem. Rev.* **97**, 1117 (1997).
- [76] P. Cyganik, M. Buck, W. Azzam, and C. Wöll, "Self-Assembled Monolayers of ω -Biphenylalkanethiols on Au(111): Influence of Spacer Chain on Molecular Packing", *J. Phys. Chem. B* **108**, 4989 (2004).

- [77] P. Cyganik, M. Buck, J. D. E. T. Wilton-Ely, and C. Wöll, "Stress in Self-Assembled Monolayers: ω -Biphenyl Alkane Thiols on Au(111)", *J. Phys. Chem. B* **109**, 10902 (2005).
- [78] P. Cyganik, M. Buck, T. Strunskus, A. Shaporenko, J. D. E. T. Wilton-Ely, M. Zharnikov, and C. Wöll, "Competition as a Design Concept: Polymorphism in Self-Assembled Monolayers of Biphenyl-Based Thiols", *J. Am. Chem. Soc.* **128**, 13868 (2006).
- [79] H. Wolf, H. Ringsdorf, E. Delamarche, T. Takami, H. Kang, B. Michel, C. Gerber, M. Jaschke, *et al.*, "End-Group-Dominated Molecular Order in Self-Assembled Monolayers", *J. Phys. Chem.* **99**, 7102 (1995).
- [80] H. Kondoh, C. Kodama, H. Sumida, and H. Nozoye, "Molecular Processes of Adsorption and Desorption of Alkanethiol Monolayers on Au (111)", *J. Chem. Phys.* **111**, 1175 (1999).
- [81] L. M. Molina and B. Hammer, "Theoretical Study of Thiol-Induced Reconstructions on the Au (111) Surface", *Chem. Phys. Lett.* **360**, 264 (2002).
- [82] Y. Yourdshahyan and A. M. Rappe, "Structure and Energetics of Alkanethiol Adsorption on the Au(111) Surface", *J. Chem. Phys.* **117**, 825 (2002).
- [83] W. B. Caldwell, D. J. Campbell, K. Chen, B. R. Herr, C. A. Mirkin, A. Malik, M. K. Durbin, P. Dutta, *et al.*, "A Highly Ordered Self-Assembled Monolayer Film of an Azobenzenealkane thiol on Au(111): Electrochemical Properties and Structural Characterization by Synchrotron In-Plane X-Ray Diffraction, Atomic Force Microscopy, and Surface-Enhanced Raman Spectroscopy", *J. Am. Chem. Soc.* **117**, 6071 (1995).
- [84] Z. Wang, A.-M. Nygård, M. J. Cook, and D. A. Russell, "An Evanescent-Field-Driven Self-Assembled Molecular Photoswitch for Macrocyclic Coordination and Release", *Langmuir* **20**, 5850 (2004).
- [85] M. Ito, T. X. Wei, P.-L. Chen, H. Akiyama, M. Matsumoto, K. Tamada, and Y. Yamamoto, "A Novel Method for Creation of Free Volume in a One-Component Self-Assembled Monolayer. Dramatic Size Effect of Para-Carborane", *J. Mater. Chem.* **15**, 478 (2005).
- [86] M. Elbing, A. Błaszczuk, C. von Hänisch, M. Mayor, V. Ferri, C. Grave, M. A. Rampi, G. Pace, *et al.*, "Single Component Self-Assembled Monolayers of Aromatic Azo-Biphenyl: Influence of the Packing Tightness on the SAM Structure and Light-Induced Molecular Movements", *Adv. Funct. Mater.* **18**, 2972 (2008).
- [87] G. Fuchsel, T. Klamroth, J. Dokić, and P. Saalfrank, "On the Electronic Structure of Neutral and Ionic Azobenzenes and Their Possible Role as Surface Mounted Molecular Switches", *J. Phys. Chem. B* **110**, 16337 (2006).

BIBLIOGRAPHY

- [88] B. Das and S. Abe, "Molecular Switch on a Metal Surface", J. Phys. Chem. B **110**, 4247 (2006).
- [89] P. A. M. Dirac, "Quantum Mechanics of Many-Electron Systems", Proc. R. Soc. Lond. A **123**, 714 (1929).
- [90] A. Szabo and N. S. Ostlund, "Modern Quantum Chemistry" (Dover Publications, New York, 1996).
- [91] M. Born and R. Oppenheimer, "Zur Quantentheorie der Molekeln", Ann. Phys. **389**, 457 (1927).
- [92] W. Pauli, "Über den Zusammenhang des Abschlusses der Elektronengruppen im Atom Mit der Komplexstruktur der Spektren", Z. Phys. **31**, 765 (1925).
- [93] W. Pauli, "The Connection Between Spin and Statistics", Phys. Rev. **58**, 716 (1940).
- [94] D. R. Hartree, "The Wave Mechanics of an Atom With a Non-Coulomb Central Field", Proc. Cam. Phil. Soc. **24**, 89 (1928).
- [95] V. Fock, "Näherungsmethode zur Lösung des Quantenmechanischen Mehrkörperproblems", Z. Phys. **61**, 126 (1930).
- [96] T. H. Dunning Jr., "A Road Map for the Calculation of Molecular Binding Energies", J. Phys. Chem. A **104**, 9062 (2000).
- [97] C. Møller and M. S. Plesset, "Note on an Approximation Treatment for Many-Electron Systems", Phys. Rev. **46**, 618 (1934).
- [98] M. O. Sinnokrot, E. F. Valeev, and C. D. Sherrill, "Estimates of the *ab initio* Limit for $\pi-\pi$ Interactions: The Benzene Dimer", J. Am. Chem. Soc. **124**, 10887 (2002).
- [99] S. Tsuzuki, K. Honda, and R. Azumi, "Model Chemistry Calculations of Thiophene Dimer Interactions: Origin of π -Stacking", J. Am. Chem. Soc. **124**, 12200 (2002).
- [100] R. M. Dreizler and E. K. U. Gross, "Density Functional Theory: An Approach to the Quantum Many-Body Problem" (Springer, Berlin Heidelberg, 1990).
- [101] P. Hohenberg and W. Kohn, "Inhomogeneous Electron Gas", Phys. Rev. **136**, 864 (1964).
- [102] M. Levy, "Universal Variational Functionals of Electron Densities, First-Order Density Matrices, and Natural Spin-Orbitals and Solution of the *v*-Representability Problem", Proc. Nat. Acad. Sci. **76**, 6062 (1979).
- [103] G. Vignale and M. Rasolt, "Density-Functional Theory in Strong Magnetic Fields", Phys. Rev. Lett. **59**, 2360 (1987).

-
- [104] D. C. Langreth, "New Theoretical Support for Density-Functional Theory as Commonly Applied", Phys. Rev. Lett. **52**, 2317 (1984).
- [105] A. Görling, "Density-Functional Theory Beyond the Hohenberg-Kohn Theorem", Phys. Rev. A **59**, 3359 (1999).
- [106] J. T. Chayes, L. Chayes, and M. B. Ruskai, "Density Functional Approach to Quantum Lattice Systems", J. Stat. Phys. **38**, 497 (1985).
- [107] W. Kohn and L. J. Sham, "Self-Consistent Equations Including Exchange and Correlation Effects", Phys. Rev. **140**, 1133 (1965).
- [108] U. von Barth, "Basic Density-Functional Theory - Overview", Physica Scripta **T109**, 9 (2004).
- [109] A. Ghosh, "Just How Good Is DFT?", J. Biol. Inorg. Chem. **11**, 671 (2006).
- [110] A. J. Cohen, P. Mori-Sanchez, and W. Yang, "Insights Into Current Limitations of Density Functional Theory", Science **321**, 792 (2008).
- [111] J. Tao, J. P. Perdew, V. N. Staroverov, and G. E. Scuseria, "Climbing the Density Functional Ladder: Nonempirical Meta-Generalized Gradient Approximation Designed for Molecules and Solids", Phys. Rev. Lett. **91**, 146401 (2003).
- [112] J. P. Perdew, A. Ruzsinszky, J. Tao, V. N. Staroverov, G. E. Scuseria, and G. I. Csonka, "Prescription for the Design and Selection of Density Functional Approximations: More Constraint Satisfaction With Fewer Fits", J. Chem. Phys. **123**, 062201 (2005).
- [113] G. E. Scuseria and V. N. Staroverov, "Theory and Applications of Computational Chemistry: The First 40 Years (A Volume of Technical and Historical Perspectives)" (Elsevier, Amsterdam, 2005), pp. 669–724.
- [114] J. P. Perdew and A. Zunger, "Self-Interaction Correction to Density-Functional Approximations for Many-Electron Systems", Phys. Rev. B **23**, 5048 (1981).
- [115] D. M. Ceperley and B. J. Alder, "Ground State of the Electron Gas by a Stochastic Method", Phys. Rev. Lett. **45**, 566 (1980).
- [116] J. P. Perdew, K. Burke, and M. Ernzerhof, "Generalized Gradient Approximation Made Simple", Phys. Rev. Lett. **77**, 3865 (1996).
- [117] J. P. Perdew, K. Burke, and M. Ernzerhof, "ERRATA: Generalized Gradient Approximation Made Simple [Phys. Rev. Lett. 77, 3865 (1996)]", Phys. Rev. Lett. **78**, 1396 (1997).
- [118] J. P. Perdew, A. Ruzsinszky, G. I. Csonka, O. A. Vydrov, G. E. Scuseria, L. A. Constantin, X. Zhou, and K. Burke, "Restoring the Density-Gradient Expansion for Exchange in Solids and Surfaces", Phys. Rev. Lett. **100**, 136406 (2008).

BIBLIOGRAPHY

- [119] M. Ernzerhof and G. E. Scuseria, "Assessment of the Perdew–Burke–Ernzerhof Exchange–Correlation Functional", *J. Chem. Phys.* **110**, 5029 (1999).
- [120] J. Paier, R. Hirschl, M. Marsman, and G. Kresse, "The Perdew–Burke–Ernzerhof Exchange–Correlation Functional Applied to the G2-1 Test Set Using a Plane-Wave Basis Set", *J. Chem. Phys.* **122**, 234102 (2005).
- [121] A. D. Becke, "Density-Functional Thermochemistry. III. The Role of Exact Exchange", *J. Chem. Phys.* **98**, 5648 (1993).
- [122] P. J. Stephens, F. J. Devlin, C. F. Chabalowski, and M. J. Frisch, "Ab initio Calculation of Vibrational Absorption and Circular Dichroism Spectra Using Density Functional Force Fields", *J. Phys. Chem.* **98**, 11623 (1994).
- [123] C. Lee, W. Yang, and R. G. Parr, "Development of the Colle-Salvetti Correlation-Energy Formula Into a Functional of the Electron Density", *Phys. Rev. B* **37**, 785 (1988).
- [124] M. J. Frisch, G. W. Trucks, H. B. Schlegel, G. E. Scuseria, M. A. Robb, J. R. Cheeseman, J. A. Montgomery Jr., T. Vreven, *et al.*, "Gaussian 03, Revision B 05" (Gaussian, Inc, Pittsburgh PA, 2003).
- [125] Y. Zhao and D. G. Truhlar, "Density Functionals With Broad Applicability in Chemistry", *Acc. Chem. Res.* **41**, 157 (2008).
- [126] C. Adamo and V. Barone, "Toward Chemical Accuracy in the Computation of NMR Shieldings: The PBE0 Model", *Chem. Phys. Lett.* **298**, 113 (1998).
- [127] C. Adamo and V. Barone, "Toward Reliable Density Functional Methods Without Adjustable Parameters: The PBE0 Model", *J. Chem. Phys.* **110**, 6158 (1999).
- [128] O. Gunnarsson and B. I. Lundqvist, "Exchange and Correlation in Atoms, Molecules, and Solids by the Spin-Density-Functional Formalism", *Phys. Rev. B* **13**, 4274 (1976).
- [129] M. A. L. Marques and E. K. U. Gross, "A Primer in Density Functional Theory" (Springer, Berlin Heidelberg, 2003), pp. 144–184.
- [130] H. Appel, E. K. U. Gross, and K. Burke, "Excitations in Time-Dependent Density-Functional Theory", *Phys. Rev. Lett.* **90**, 043005 (2003).
- [131] K. Burke, J. Werschnik, and E. K. U. Gross, "Time-Dependent Density Functional Theory: Past, Present, and Future", *J. Chem. Phys.* **123**, 062206 (2005).
- [132] P. Elliott, F. Furche, and K. Burke, "Excited States from Time-Dependent Density Functional Theory", *Rev. Comp. Chem.* **26**, 91 (2009).
- [133] E. Runge and E. K. U. Gross, "Density-Functional Theory for Time-Dependent Systems", *Phys. Rev. Lett.* **52**, 997 (1984).

-
- [134] M. Petersilka, U. J. Gossmann, and E. K. U. Gross, "Excitation Energies from Time-Dependent Density-Functional Theory", *Phys. Rev. Lett.* **76**, 1212 (1996).
- [135] J. F. Dobson, "Time-Dependent Density Functional Theory" (Springer, Berlin Heidelberg, 2006).
- [136] F. Furche, "Molecular Tests of the Random Phase Approximation to the Exchange-Correlation Energy Functional", *Phys. Rev. B* **64**, 195120 (2001).
- [137] F. Furche, "Developing the Random Phase Approximation Into a Practical Post-Kohn-Sham Correlation Model", *J. Chem. Phys.* **129**, 114105 (2008).
- [138] M. E. Casida, "Recent Advances in Density Functional Methods, Part I" (World Scientific, Singapore, 1995), p. 155.
- [139] C. Jamorski, M. Casida, and D. R. Salahub, "Dynamic Polarizabilities and Excitation Spectra from a Molecular Implementation of Time-Dependent Density-Functional Response Theory: N_2 as a Case Study", *J. Chem. Phys.* **104**, 5134 (1996).
- [140] R. E. Stratmann, G. E. Scuseria, and M. J. Frisch, "An Efficient Implementation of Time-Dependent Density-Functional Theory for the Calculation of Excitation Energies of Large Molecules", *J. Chem. Phys.* **109**, 8218 (1998).
- [141] R. Bauernschmitt and R. Ahlrichs, "Treatment of Electronic Excitations Within the Adiabatic Approximation of Time Dependent Density Functional Theory", *Chem. Phys. Lett.* **256**, 454 (1996).
- [142] D. C. Young, "Computational Chemistry: A Practical Guide for Applying Techniques to Real-World Problems" (Wiley, New York, 2001).
- [143] B. Meyer, "Computational Nanoscience: Do it Yourself!", vol. 31 (John von Neumann Institute for Computing, Jülich, 2006), pp. 71–83.
- [144] N. W. Ashcroft and N. D. Mermin, "Solid State Physics" (Thomson Learning, London, 1976).
- [145] R. P. Feynman, "Forces in Molecules", *Phys. Rev.* **56**, 340 (1939).
- [146] D. Vanderbilt, "Soft Self-Consistent Pseudopotentials in a Generalized Eigenvalue Formalism", *Phys. Rev. B* **41**, 7892 (1990).
- [147] K. Laasonen, A. Pasquarello, R. Car, C. Lee, and D. Vanderbilt, "Car-Parrinello Molecular Dynamics With Vanderbilt Ultrasoft Pseudopotentials", *Phys. Rev. B* **47**, 10142 (1993).
- [148] R. Micheletto, M. Yokokawa, M. Schroeder, D. Hobarra, Y. Ding, and T. Kakiuchi, "Real Time Observation of Trans-Cis Isomerization on Azobenzene SAM Induced by Optical Near Field Enhancement", *Appl. Surf. Sci.* **228**, 265 (2004).

BIBLIOGRAPHY

- [149] H. Kuhn and C. Kuhn, *"J-Aggregates"* (World Scientific, 1996), pp. 1–40.
- [150] S. Neppl, U. Bauer, D. Menzel, P. Feulner, A. Shaporenko, M. Zharnikov, P. Kao, and D. L. Allara, *"Charge Transfer Dynamics in Self-Assembled Monomolecular Films"*, Chem. Phys. Lett. **447**, 227 (2007).
- [151] M. E. Casida, C. Jamorski, K. C. Casida, and D. R. Salahub, *"Molecular Excitation Energies to High-Lying Bound States from Time-Dependent Density-Functional Response Theory: Characterization and Correction of the Time-Dependent Local Density Approximation Ionization Threshold"*, J. Chem. Phys. **108**, 4439 (1998).
- [152] Z. L. Cai, K. Sendt, and J. R. Reimers, *"Failure of Density-Functional Theory and Time-Dependent Density-Functional Theory for Large Extended π Systems"*, J. Chem. Phys. **117**, 5543 (2002).
- [153] E. J. Bylaska, W. A. de Jong, N. Govind, K. Kowalski, T. P. Straatsma, M. Valiev, D. Wang, E. Apra, *et al.*, *"NWChem, a Computational Chemistry Package for Parallel Computers, Version 5.1"* (Pacific Northwest National Laboratory, Richland, Washington 99352-0999, USA, 2007).
- [154] A. Schäfer, C. Huber, and R. Ahlrichs, *"Fully Optimized Contracted Gaussian Basis Sets of Triple Zeta Valence Quality for Atoms Li to Kr"*, J. Chem. Phys. **100**, 5829 (1994).
- [155] C. Peng, P. Y. Ayala, H. B. Schlegel, and M. J. Frisch, *"Using Redundant Internal Coordinates to Optimize Equilibrium Geometries and Transition States"*, J. Comput. Chem. **17**, 49 (1996).
- [156] H. Fliegl, A. Köhn, C. Hättig, and R. Ahlrichs, *"Ab initio Calculation of the Vibrational and Electronic Spectra of Trans- and Cis-Azobenzene"*, J. Am. Chem. Soc **125**, 9821 (2003).
- [157] A. Görling, *"Density-Functional Theory for Excited States"*, Phys. Rev. A **54**, 3912 (1996).
- [158] M. Grüning, A. Marini, and A. Rubio, *"Effect of Spatial Nonlocality on the Density Functional Band Gap"*, Phys. Rev. B **74**, 161103 (2006).
- [159] H. Rau, *"Photochemistry and Photophysics"*, vol. 2 (CRC Publishing: Boca Raton, FL, 1990), p. 119.
- [160] H. H. Jaffé, S.-J. Yeh, and R. W. Gardner, *"The Electronic Spectra of Azobenzene Derivatives and Their Conjugate Acids"*, J. Mol. Spectrosc. **2**, 120 (1958).
- [161] R. van Leeuwen and E. J. Baerends, *"Exchange-Correlation Potential With Correct Asymptotic Behavior"*, Phys. Rev. A **49**, 2421 (1994).

-
- [162] D. J. Tozer and N. C. Handy, "Improving Virtual Kohn–Sham Orbitals and Eigenvalues: Application to Excitation Energies and Static Polarizabilities", *J. Chem. Phys.* **109**, 10180 (1998).
- [163] C.-G. Zhan, J. A. Nichols, and D. A. Dixon, "Ionization Potential, Electron Affinity, Electronegativity, Hardness, and Electron Excitation Energy: Molecular Properties from Density Functional Theory Orbital Energies", *J. Phys. Chem. A* **107**, 4184 (2003).
- [164] J. N. Andersen and C.-O. Almbladh, "High Resolution Core Level Photoemission of Clean and Adsorbate Covered Metal Surfaces", *J. Phys.: Condens. Matter* **13**, 11267 (2001).
- [165] T. Koopmans, "Über Die Zuordnung Von Wellenfunktionen Und Eigenwerten zu den Einzelnen Elektronen Eines Atoms", *Physica* **1**, 104 (1934).
- [166] L. Hedin and A. Johansson, "Polarization Corrections to Core Levels", *J. Phys. B* **2**, 1336 (1969).
- [167] R. Manne and T. Åberg, "Koopmans' Theorem for Inner-Shell Ionization", *Chem. Phys. Lett.* **7**, 282 (1970).
- [168] M. Borg, M. Birgersson, M. Smedh, A. Mikkelsen, and D. L. Adams, "Experimental and Theoretical Surface Core-Level Shifts of Aluminum (100) and (111)", *Phys. Rev. B* **69**, 235418 (2004).
- [169] M. Birgersson, C.-O. Almbladh, M. Borg, and J. N. Andersen, "Density-Functional Theory Applied to Rh(111) and CO/Rh(111) Systems: Geometries, Energies, and Chemical Shifts", *Phys. Rev. B* **67**, 045402 (2003).
- [170] L. Triguero, L. G. M. Pettersson, and H. Ågren, "Calculations of Near-Edge X-Ray-Absorption Spectra of Gas-Phase and Chemisorbed Molecules by Means of Density-Functional and Transition-Potential Theory", *Phys. Rev. B* **58**, 8097 (1998).
- [171] M. Methfessel, D. Hennig, and M. Scheffler, "Enhanced Screening of Core Holes at Transition-Metal Surfaces", *Surface Review and Letters* **2**, 197 (1995).
- [172] S. Lizzit, A. Baraldi, A. Groso, K. Reuter, M. V. Ganduglia-Pirovano, C. Stampfl, M. Scheffler, M. Stichler, *et al.*, "Surface Core-Level Shifts of Clean and Oxygen-Covered Ru(0001)", *Phys. Rev. B* **63**, 205419 (2001).
- [173] R. Stowasser and R. Hoffmann, "What Do the Kohn-Sham Orbitals and Eigenvalues Mean?", *J. Am. Chem. Soc.* **121**, 3414 (1999).
- [174] K. Heister, H.-T. Rong, M. Buck, M. Zharnikov, M. Grunze, and L. S. O. Johansson, "Odd-Even Effects at the S-Metal Interface and in the Aromatic Matrix of Biphenyl-Substituted Alkanethiol Self-Assembled Monolayers", *J. Phys. Chem. B* **105**, 6888 (2001).

- [175] H. A. Biebuyck, C. D. Bain, and G. M. Whitesides, "Comparison of Organic Monolayers on Polycrystalline Gold Spontaneously Assembled from Solutions Containing Dialkyl Disulfides or Alkanethiols", *Langmuir* **10**, 1825 (1994).
- [176] A. Shaporenko, A. Terfort, M. Grunze, and M. Zharnikov, "A Detailed Analysis of the Photoemission Spectra of Basic Thioaromatic Monolayers on Noble Metal Substrates", *J. Electron Spectrosc. Relat. Phenom.* **151**, 45 (2006).
- [177] D. Nordfors, A. Nilsson, N. Martensson, S. Svensson, U. Gelius, and S. Lunell, "Experimental and INDO/CI Calculated Gas Phase C1s Shake-Up Spectra of C₆H₆, C₆H₅OH, and C₆H₅CH₂OH", *J. Chem. Phys.* **88**, 2630 (1988).
- [178] D. Clark, D. L. Adams, A. Dilks, J. Peeling, and H. Thomas, "Some Aspects of Shake-Up Phenomena in Some Simple Polymer Systems", *J. Electron Spectrosc. Relat. Phenom.* **8**, 51 (1976).
- [179] M. Weinelt, N. Wassdahl, T. Wiell, O. Karis, J. Hasselström, P. Bennich, A. Nilsson, J. Stöhr, *et al.*, "Electronic Structure of Benzene on Ni(100) and Cu(110): An X-Ray-Spectroscopy Study", *Phys. Rev. B* **58**, 7351 (1998).
- [180] J. Fulghum, "Recent Developments in High Energy and Spatial Resolution Analysis of Polymers by XPS", *J. Electron Spectrosc. Relat. Phenom.* **100**, 331 (1999).
- [181] J. Stöhr and D. A. Outka, "Determination of Molecular Orientations on Surfaces from the Angular Dependence of Near-Edge X-Ray-Absorption Fine-Structure Spectra", *Phys. Rev. B* **36**, 7891 (1987).
- [182] J. F. Kang, A. Ulman, S. Liao, R. Jordan, G. Yang, and G.-Y. Liu, "Self-Assembled Rigid Monolayers of 4'-Substituted-4-Mercaptobiphenyls on Gold and Silver Surfaces", *Langmuir* **17**, 95 (2001).
- [183] N. Ballav, B. Schüpbach, O. Dethloff, P. Feulner, A. Terfort, and M. Zharnikov, "Direct Probing Molecular Twist and Tilt in Aromatic Self-Assembled Monolayers", *J. Am. Chem. Soc.* **129**, 15416 (2007).
- [184] H.-T. Rong, S. Frey, Y.-J. Yang, M. Zharnikov, M. Buck, M. Wühn, C. Wöll, and G. Helmchen, "On the Importance of the Headgroup Substrate Bond in Thiol Monolayers: A Study of Biphenyl-Based Thiols on Gold and Silver", *Langmuir* **17**, 1582 (2001).
- [185] A. S. Davydov, "Theory of Molecular Excitons" (McGraw-Hill, New York, 1962).
- [186] N. Kato, K. Yuasa, T. Araki, I. Hirose, M. Sato, N. Ikeda, K.-I. Iimura, and Y. Uesu, "Determination of a Merocyanine J-Aggregate Structure and the Significant Contribution of the Electric Dipole Interaction to the Exciton Band Wave-length", *Phys. Rev. Lett.* **94**, 136404 (2005).
- [187] A. Michaelides and M. Scheffler, "Textbook of Surface and Interface Science", vol. I (Wiley-VCH, 2010).

-
- [188] M. Scheffler and C. Stampfl, *"Handbook of Surface Science: Electronic Structure"*, vol. 2 (Elsevier, Amsterdam, 2000).
- [189] Q.-M. Hu, K. Reuter, and M. Scheffler, *"Towards an Exact Treatment of Exchange and Correlation in Materials: Application to the "CO Adsorption Puzzle" and Other Systems"*, Phys. Rev. Lett. **98**, 176103 (2007).
- [190] S. Sharifzadeh, P. Huang, and E. Carter, *"Embedded Configuration Interaction Description of CO on Cu (111): Resolution of the Site Preference Conundrum"*, J. Phys. Chem. C **112**, 4649 (2008).
- [191] G. Kresse, A. Gil, and P. Sautet, *"Significance of Single-Electron Energies for the Description of CO on Pt(111)"*, Phys. Rev. B **68**, 073401 (2003).
- [192] A. Stroppa and G. Kresse, *"The Shortcomings of Semi-Local and Hybrid Functionals: What We Can Learn from Surface Science Studies"*, New J. Phys. **10**, 063020 (2008).
- [193] P. S. Bagus, V. Staemmler, and C. Wöll, *"Exchangelike Effects for Closed-Shell Adsorbates: Interface Dipole and Work Function"*, Phys. Rev. Lett. **89**, 096104 (2002).
- [194] M. Rohlfing and T. Bredow, *"Binding Energy of Adsorbates on a Noble Metal Surface: Exchange and Correlation Effects"*, Phys. Rev. Lett. **101**, 266106 (2008).
- [195] P. Sony, P. Puschnig, D. Nabok, and C. Ambrosch-Draxl, *"Importance of van der Waals Interaction for Organic Molecule-Metal Junctions: Adsorption of Thiophene on Cu(110) as a Prototype"*, Phys. Rev. Lett. **99**, 176401 (2007).
- [196] N. Atodiresei, V. Caciuc, P. Lazić, and S. Blügel, *"Chemical Versus van der Waals Interaction: The Role of the Heteroatom in the Flat Absorption of Aromatic Molecules C₆H₆, C₅NH₅, and C₄N₂H₄ on the Cu(110) Surface"*, Phys. Rev. Lett. **102**, 136809 (2009).
- [197] X. Wu, M. C. Vargas, S. Nayak, V. Lotrich, and G. Scoles, *"Towards Extending the Applicability of Density Functional Theory to Weakly Bound Systems"*, J. Chem. Phys. **115**, 8748 (2001).
- [198] Q. Wu and W. Yang, *"Empirical Correction to Density Functional Theory for van der Waals Interactions"*, J. Chem. Phys. **116**, 515 (2002).
- [199] F. Ortmann, W. G. Schmidt, and F. Bechstedt, *"Attracted by Long-Range Electron Correlation: Adenine on Graphite"*, Phys. Rev. Lett. **95**, 186101 (2005).
- [200] F. Ortmann, F. Bechstedt, and W. G. Schmidt, *"Semiempirical van der Waals Correction to the Density Functional Description of Solids and Molecular Structures"*, Phys. Rev. B **73**, 205101 (2006).

BIBLIOGRAPHY

- [201] S. Grimme, "Semiempirical GGA-Type Density Functional Constructed With a Long-Range Dispersion Correction", *J. Comput. Chem.* **27**, 1787 (2006).
- [202] A. Tkatchenko and M. Scheffler, "Accurate Molecular van der Waals Interactions from Ground-State Electron Density and Free-Atom Reference Data", *Phys. Rev. Lett.* **102**, 073005 (2009).
- [203] P. Jurečka, J. Černý, P. Hobza, and D. R. Salahub, "Density Functional Theory Augmented With an Empirical Dispersion Term. Interaction Energies and Geometries of 80 Noncovalent Complexes Compared With *ab initio* Quantum Mechanics Calculations", *J. Comput. Chem.* **28**, 555 (2006).
- [204] P. L. Silvestrelli, "Van der Waals Interactions in DFT Made Easy by Wannier Functions", *Phys. Rev. Lett.* **100**, 053002 (2008).
- [205] P. L. Silvestrelli, K. Benyahia, S. Grubisić, F. Ancilotto, and F. Togo, "Van der Waals Interactions at Surfaces by Density Functional Theory Using Wannier Functions", *J. Chem. Phys.* **130**, 074702 (2009).
- [206] S. J. Clark, M. D. Segall, C. J. Pickard, P. J. Hasnip, M. I. J. Probert, K. Refson, and M. C. Payne, "First Principles Methods Using CASTEP", *Z. Kristallogr.* **220**, 567 (2005).
- [207] N. Takeuchi, C. T. Chan, and K. M. Ho, "Au (111): A Theoretical Study of the Surface Reconstruction and the Surface Electronic Structure", *Phys. Rev. B* **43**, 13899 (1991).
- [208] B. G. Pfrommer, M. Côté, S. G. Louie, and M. L. Cohen, "Relaxation of Crystals With the Quasi-Newton Method", *J. Comp. Phys.* **131**, 233 (1997).
- [209] H. J. Monkhorst and J. D. Pack, "Special Points for Brillouin-Zone Integrations", *Phys. Rev. B* **13**, 5188 (1976).
- [210] W.-X. Li, C. Stampfl, and M. Scheffler, "Oxygen Adsorption on Ag(111): A Density-Functional Theory Investigation", *Phys. Rev. B* **65**, 075407 (2002).
- [211] N. Lorente, M. F. G. Hedouin, R. E. Palmer, and M. Persson, "Chemisorption of Benzene and STM Dehydrogenation Products on Cu(100)", *Phys. Rev. B* **68**, 155401 (2003).
- [212] V. De Renzi, R. Rousseau, D. Marchetto, R. Biagi, S. Scandolo, and U. del Pennino, "Metal Work-Function Changes Induced by Organic Adsorbates: A Combined Experimental and Theoretical Study", *Phys. Rev. Lett.* **95**, 046804 (2005).
- [213] A. Bilić, J. R. Reimers, N. S. Hush, R. C. Hoft, and M. J. Ford, "Adsorption of Benzene on Copper, Silver, and Gold Surfaces", *J. Chem. Theory Comput.* **2**, 1093 (2006).

-
- [214] A. Ferretti, C. Baldacchini, A. Calzolari, R. Di Felice, A. Ruini, E. Molinari, and M. G. Betti, "Mixing of Electronic States in Pentacene Adsorption on Copper", *Phys. Rev. Lett.* **99**, 46802 (2007).
- [215] N. Lorente and M. Persson, "Theoretical Aspects of Tunneling-Current-Induced Bond Excitation and Breaking at Surfaces", *Faraday Discuss.* **117**, 277 (2000).
- [216] S. Paramonov, N. Kuzmina, and S. Troyanov, "Synthesis and Crystal Structure of Silver(I) Carboxylate Complexes, $\text{Ag}(\text{P}^n\text{Bu}_3)[\text{C}(\text{CH}_3)_3\text{COO}]$ and $\text{Ag}(\text{Phen})_2[\text{CF}_3\text{COO}] \cdot \text{H}_2\text{O}$ ", *Polyhedron* **22**, 837 (2003).
- [217] D. J. Szalda, T. J. Kistenmacher, and L. G. Marzilli, "Observation of a Direct Interaction Between the Carbonyl Oxygen, O(6), of a N(7)-Bonded 6-Oxopurine and a Metal Center. Preparation and Crystal and Molecular Structure of (N-3,4-Benzosalicylidene-N',N'-Dimethylethylenediamine)(theophyllinato)copper(II) Monohydrate", *J. Am. Chem. Soc.* **98**, 8371 (1976).
- [218] R. S. Mulliken, "A New Electroaffinity Scale; Together With Data on Valence States and on Valence Ionization Potentials and Electron Affinities", *J. Chem. Phys.* **2**, 782 (1934).
- [219] R. S. Mulliken, "Electronic Structures of Molecules XI. Electroaffinity, Molecular Orbitals and Dipole Moments", *J. Chem. Phys.* **3**, 573 (1935).
- [220] J. L. F. Da Silva, C. Stampfl, and M. Scheffler, "Adsorption of Xe Atoms on Metal Surfaces: New Insights from First-Principles Calculations", *Phys. Rev. Lett.* **90**, 066104 (2003).
- [221] S. Kristyán and P. Pulay, "Can (semi)local Density Functional Theory Account for the London Dispersion Forces?", *Chem. Phys. Lett.* **229**, 175 (1994).
- [222] J. Harl and G. Kresse, "Cohesive Energy Curves for Noble Gas Solids Calculated by Adiabatic Connection Fluctuation-Dissipation Theory", *Phys. Rev. B* **77**, 045136 (2008).
- [223] S. A. C. McDowell, R. D. Amos, and N. C. Handy, "Molecular Polarisabilities - a Comparison of Density Functional Theory With Standard *ab initio* Methods", *Chem. Phys. Lett.* **235**, 1 (1995).
- [224] S. J. A. van Gisbergen, P. R. T. Schipper, O. V. Gritsenko, E. J. Baerends, J. G. Snijders, B. Champagne, and B. Kirtman, "Electric Field Dependence of the Exchange-Correlation Potential in Molecular Chains", *Phys. Rev. Lett.* **83**, 694 (1999).
- [225] B. Champagne, E. A. Perpète, D. Jacquemin, and S. J. A. van Gisbergen, "Assessment of Conventional Density Functional Schemes for Computing the Dipole Moment and (Hyper)Polarizabilities of Push-Pull π -Conjugated Systems", *J. Phys. Chem. A* **104**, 4755 (2000).

BIBLIOGRAPHY

- [226] N. Atodiresei, V. Caciuc, J.-H. Franke, and S. Blügel, "Role of the van der Waals Interactions on the Bonding Mechanism of Pyridine on Cu(110) and Ag(110) Surface: First-Principles Study", *Phys. Rev. B* **78**, 045411 (2008).
- [227] P. S. Bagus, K. Hermann, and C. Wöll, "The Interaction of C_6H_6 and C_6H_{12} With Noble Metal Surfaces: Electronic Level Alignment and the Origin of the Interface Dipole", *J. Chem. Phys.* **123**, 184109 (2005).
- [228] C. Tuma and J. Sauer, "A Hybrid MP2/Planewave-DFT Scheme for Large Chemical Systems: Proton Jumps in Zeolites", *Chem. Phys. Lett.* **387**, 388 (2004).
- [229] Y. Andersson, D. C. Langreth, and B. I. Lundqvist, "Van der Waals Interactions in Density-Functional Theory", *Phys. Rev. Lett.* **76**, 102 (1996).
- [230] H. Rydberg, M. Dion, N. Jacobson, E. Schröder, P. Hyldgaard, S. I. Simak, D. C. Langreth, and B. I. Lundqvist, "Van der Waals Density Functional for Layered Structures", *Phys. Rev. Lett.* **91**, 126402 (2003).
- [231] M. Dion, H. Rydberg, E. Schröder, and D. C. Langreth, "Van der Waals Density Functional for General Geometries", *Phys. Rev. Lett.* **92**, 246401 (2004).
- [232] S. D. Chakarova-Käck, E. Schröder, B. I. Lundqvist, and D. C. Langreth, "Application of van der Waals Density Functional to an Extended System: Adsorption of Benzene and Naphthalene on Graphite", *Phys. Rev. Lett.* **96**, 146107 (2006).
- [233] O. A. Vydrov and T. Van Voorhis, "Improving the Accuracy of the Nonlocal van der Waals Density Functional With Minimal Empiricism", *J. Chem. Phys.* **130**, 104105 (2009).
- [234] A. Gulans, M. J. Puska, and R. M. Nieminen, "Linear-Scaling Self-Consistent Implementation of the van der Waals Density Functional", *Phys. Rev. B* **79**, 201105 (2009).
- [235] O. A. Vydrov and T. Van Voorhis, "Nonlocal van der Waals Density Functional Made Simple", *Phys. Rev. Lett.* **103**, 063004 (2009).
- [236] R. Eisenschitz and F. London, "Über Das Verhältnis der van der Waalsschen Kräfte zu den Homöopolaren Bindungskräften", *Z. Phys.* **60**, 491 (1930).
- [237] F. London, "Zur Theorie Und Systematik der Molekularkräfte", *Z. Phys.* **63**, 245 (1930).
- [238] A. J. Stone, "The Theory of Intermolecular Forces" (Oxford University Press, New York, 1996).
- [239] H. B. G. Casimir and D. Polder, "The Influence of Retardation on the London-van der Waals Forces", *Phys. Rev.* **73**, 360 (1948).

-
- [240] J. A. Yoffe and G. M. Maggiora, "The London Approximation and the Calculation of Dispersion Interactions as a Sum of Atom-Atom Terms", *Theor. Chem. Acc.* **56**, 191 (1980).
- [241] J. J. Rehr, E. Zaremba, and W. Kohn, "Van der Waals Forces in the Noble Metals", *Phys. Rev. B* **12**, 2062 (1975).
- [242] Y. Wang and J. P. Perdew, "Spin Scaling of the Electron-Gas Correlation Energy in the High-Density Limit", *Phys. Rev. B* **43**, 8911 (1991).
- [243] J. P. Perdew, J. A. Chevary, S. H. Vosko, K. A. Jackson, M. R. Pederson, D. J. Singh, and C. Fiolhais, "Atoms, Molecules, Solids, and Surfaces: Applications of the Generalized Gradient Approximation for Exchange and Correlation", *Phys. Rev. B* **46**, 6671 (1992).
- [244] S. Grimme, "Accurate Description of van der Waals Complexes by Density Functional Theory Including Empirical Corrections", *J. Comput. Chem.* **25**, 1463 (2004).
- [245] E. R. Johnson and A. D. Becke, "A Post-Hartree-Fock Model of Intermolecular Interactions", *J. Chem. Phys.* **123**, 024101 (2005).
- [246] A. Olsz, K. Vanommeslaeghe, A. Krishtal, T. Veszprémi, C. Van Alsenoy, and P. Geerlings, "The Use of Atomic Intrinsic Polarizabilities in the Evaluation of the Dispersion Energy", *J. Chem. Phys.* **127**, 224105 (2007).
- [247] T. Brinck, J. S. Murray, and P. Politzer, "Polarizability and Volume", *J. Chem. Phys.* **98**, 4305 (1993).
- [248] X. Chu and A. Dalgarno, "Linear Response Time-Dependent Density Functional Theory for van der Waals Coefficients", *J. Chem. Phys.* **121**, 4083 (2004).
- [249] K. T. Tang, "Dynamic Polarizabilities and van der Waals Coefficients", *Phys. Rev.* **177**, 108 (1969).
- [250] F. L. Hirshfeld, "Bonded-Atom Fragments for Describing Molecular Charge Densities", *Theoret. Chim. Acta (Berl.)* **44**, 129 (1977).
- [251] P. P. Ewald, "Die Berechnung Optischer Und Elektrostatischer Gitterpotentiale", *Ann. Phys.* **369**, 253 (1921).
- [252] T. Kerber, M. Sierka, and J. Sauer, "Application of Semiempirical Long-Range Dispersion Corrections to Periodic Systems in Density Functional Theory", *J. Comput. Chem.* **29**, 2088 (2008).
- [253] M. A. Neumann and M.-A. Perrin, "Energy Ranking of Molecular Crystals Using Density Functional Theory Calculations and an Empirical van der Waals Correction", *J. Phys. Chem. B* **109**, 15531 (2005).

- [254] V. Blum, R. Gehrke, F. Hanke, P. Havu, V. Havu, X. Ren, K. Reuter, and M. Scheffler, "Ab initio Molecular Simulations With Numeric Atom-Centered Orbitals", *Comput. Phys. Comm.* **180**, 2175 (2009).
- [255] K. Weiss, S. Gebert, M. Wühn, H. Wadepohl, and C. Wöll, "Near Edge X-Ray Absorption Fine Structure Study of Benzene Adsorbed on Metal Surfaces: Comparison to Benzene Cluster Complexes", *J. Vac. Sci. Technol. A* **16**, 1017 (1998).
- [256] D. P. Woodruff, "Surface Structure Determination Using X-Ray Standing Waves", *Rep. Prog. Phys.* **68**, 743 (2005).
- [257] A. Hauschild, K. Karki, B. C. C. Cowie, M. Rohlfing, F. S. Tautz, and M. Sokolowski, "Molecular Distortions and Chemical Bonding of a Large π -Conjugated Molecule on a Metal Surface", *Phys. Rev. Lett.* **94**, 36106 (2005).
- [258] C. Stadler, S. Hansen, F. Pollinger, C. Kumpf, E. Umbach, T.-L. Lee, and J. Zegehnagen, "Structural Investigation of the Adsorption of SnPc on Ag(111) Using Normal-Incidence X-Ray Standing Waves", *Phys. Rev. B* **74**, 035404 (2006).
- [259] A. Gerlach, S. Sellner, F. Schreiber, N. Koch, and J. Zegehnagen, "Substrate-Dependent Bonding Distances of PTCDA: A Comparative X-Ray Standing-Wave Study on Cu(111) and Ag(111)", *Phys. Rev. B* **75**, 045401 (2007).
- [260] L. Kilian, A. Hauschild, R. Temirov, S. Soubatch, A. Scholl, A. Bendounan, F. Reinert, T.-L. Lee, *et al.*, "Role of Intermolecular Interactions on the Electronic and Geometric Structure of a Large Pi-Conjugated Molecule Adsorbed on a Metal Surface", *Phys. Rev. Lett.* **100**, 136103 (2008).
- [261] D. M. Newns, "Dielectric Response of a Semi-Infinite Degenerate Electron Gas", *Phys. Rev. B* **1**, 3304 (1970).
- [262] A. Liebsch, "Electronic Screening at Metal Surfaces and the Connection With Physical Phenomena", *Physica Scripta* **35**, 354 (1987).
- [263] C. Filippi, S. B. Healy, P. Kratzer, E. Pehlke, and M. Scheffler, "Quantum Monte Carlo Calculations of H_2 Dissociation on Si(001)", *Phys. Rev. Lett.* **89**, 166102 (2002).
- [264] W. Kohn, "Density Functional and Density Matrix Method Scaling Linearly With the Number of Atoms", *Phys. Rev. Lett.* **76**, 3168 (1996).
- [265] G. Witte, S. Lukas, P. S. Bagus, and C. Wöll, "Vacuum Level Alignment at Organic/Metal Junctions: "Cushion" Effect and the Interface Dipole", *Appl. Phys. Lett.* **87**, 263502 (2005).
- [266] K. A. Fossler, R. G. Nuzzo, P. S. Bagus, and C. Wöll, "The Adsorption of Cyclopropane and Cyclohexane on Cu(111): An Experimental and Theoretical Investigation on the Nature of the CH-Metal Interaction", *Angew. Chem. Int. Ed.* **41**, 1735 (2002).

- [267] W. J. Hehre, R. F. Stewart, and J. A. Pople, "Self-Consistent Molecular-Orbital Methods. I. Use of Gaussian Expansions of Slater-Type Atomic Orbitals", *J. Chem. Phys.* **51**, 2657 (1969).
- [268] J. B. Collins, P. von Ragué Schleyer, J. S. Binkley, and J. A. Pople, "Self-Consistent Molecular Orbital Methods. XVII. Geometries and Binding Energies of Second-Row Molecules. A Comparison of Three Basis Sets", *J. Chem. Phys.* **64**, 5142 (1976).
- [269] T. H. Dunning Jr and P. J. Hay, "Modern Theoretical Chemistry", vol. 3 (Plenum, New York, 1976), pp. 1–28.
- [270] R. A. Kendall, T. H. Dunning Jr., and R. J. Harrison, "Electron Affinities of the First-Row Atoms Revisited. Systematic Basis Sets and Wave Functions", *J. Chem. Phys.* **96**, 6796 (1992).
- [271] D. E. Woon and T. H. Dunning Jr., "Gaussian Basis Sets for Use in Correlated Molecular Calculations. V. Core-Valence Basis Sets for Boron Through Neon", *J. Chem. Phys.* **103**, 4572 (1995).
- [272] W. Kutzelnigg, U. Fleischer, and M. Schindler, "NMR—Basic Principles and Progress", vol. 23 (Springer, Heidelberg, 1990), p. 165.
- [273] S. G. Louie, S. Froyen, and M. L. Cohen, "Nonlinear Ionic Pseudopotentials in Spin-Density-Functional Calculations", *Phys. Rev. B* **26**, 1738 (1982).
- [274] B. A. Heß, ed., "Relativistic Effects in Heavy-Element Chemistry and Physics" (Wiley, Chichester, 2003).
- [275] G. Kresse and D. Joubert, "From Ultrasoft Pseudopotentials to the Projector Augmented-Wave Method", *Phys. Rev. B* **59**, 1758 (1999).
- [276] N. Marzari, "Ab-Initio Molecular Dynamics for Metallic Systems" (Ph.D. Dissertation, University of Cambridge, 1996).
- [277] F. Wagner, T. Laloyaux, and M. Scheffler, "Errors in Hellmann-Feynman Forces Due to Occupation-Number Broadening and How They Can be Corrected", *Phys. Rev. B* **57**, 2102 (1998).
- [278] J. L. F. Da Silva, C. Stampfl, and M. Scheffler, "Converged Properties of Clean Metal Surfaces by All-Electron First-Principles Calculations", *Surf. Sci.* **600**, 703 (2006).
- [279] F. D. Murnaghan, "The Compressibility of Media Under Extreme Pressures", *Proc. Nat. Acad. Sci.* **30**, 244 (1944).
- [280] L. Kleinman, "Bulk Charge Neutrality in (111) Semiconductor Slabs", *Phys. Rev. B* **11**, 3900 (1975).

BIBLIOGRAPHY

- [281] J. E. Peralta, J. Uddin, and G. E. Scuseria, "Scalar Relativistic All-Electron Density Functional Calculations on Periodic Systems", *J. Chem. Phys.* **122**, 084108 (2005).
- [282] R. J. Needs and M. Mansfield, "Calculations of the Surface Stress Tensor and Surface Energy of the (111) Surfaces of Iridium, Platinum and Gold", *J. Phys.: Condens. Matter* **1**, 7555 (1989).
- [283] Y. J. Feng, K. P. Bohnen, and C. T. Chan, "First-Principles Studies of Au(100)-Hex Reconstruction in an Electrochemical Environment", *Phys. Rev. B* **72**, 125401 (2005).
- [284] M. Methfessel, D. Hennig, and M. Scheffler, "Calculated Surface Energies of the 4d Transition Metals: A Study of Bond-Cutting Models", *Appl. Phys. A* **55**, 442 (1992).
- [285] O. M. Løvvik and R. A. Olsen, "Density Functional Calculations of Hydrogen Adsorption on Palladium–Silver Alloy Surfaces", *J. Chem. Phys.* **118**, 3268 (2003).
- [286] S. H. Vosko, L. Wilk, and M. Nusair, "Accurate Spin-Dependent Electron Liquid Correlation Energies for Local Spin Density Calculations: A Critical Analysis", *Can. J. Phys.* **58**, 1200 (1980).
- [287] J. P. Perdew and Y. Wang, "Accurate and Simple Analytic Representation of the Electron-Gas Correlation Energy", *Phys. Rev. B* **45**, 13244 (1992).
- [288] P. J. Feibelman and D. R. Hamann, "Quantum-Size Effects in Work Functions of Free-Standing and Adsorbed Thin Metal Films", *Phys. Rev. B* **29**, 6463 (1984).
- [289] T. Rodach, K. P. Bohnen, and K. M. Ho, "First Principles Calculations of Lattice Relaxation at Low Index Surfaces of Cu", *Surf. Sci.* pp. 66–72 (1993).
- [290] S. Å. Lindgren, L. Walldén, J. Rundgren, and P. Westrin, "Low-Energy Electron Diffraction from Cu(111): Subthreshold Effect and Energy-Dependent Inner Potential; Surface Relaxation and Metric Distances Between Spectra", *Phys. Rev. B* **29**, 576 (1984).
- [291] N. E. Singh-Miller and N. Marzari, "First-Principles Study of the Surface Energies, Work Functions, and Surface Relaxations of Low Index Metallic Surfaces", Arxiv preprint arXiv:0801.1077 (2008).
- [292] S. F. Boys and F. Bernardi, "The Calculation of Small Molecular Interactions by the Differences of Separate Total Energies. Some Procedures With Reduced Errors", *Mol. Phys.* **19**, 553 (1970).
- [293] J. L. Whitten, "Coulombic Potential Energy Integrals and Approximations", *J. Chem. Phys.* **58**, 4496 (1973).
- [294] O. Vahtras, J. Almlöf, and M. W. Feyereisen, "Integral Approximations for LCAO-SCF Calculations", *Chem. Phys. Lett.* **213**, 514 (1993).

- [295] F. Weigend, M. Häser, H. Patzelt, and R. Ahlrichs, "RI-MP2: Optimized Auxiliary Basis Sets and Demonstration of Efficiency", *Chem. Phys. Lett.* **294**, 143 (1998).
- [296] C. Hättig, "Optimization of Auxiliary Basis Sets for RI-MP2 and RI-CC2 Calculations: Core-Valence and Quintuple-Zeta Basis Sets for H to Ar and QZVPP Basis Sets for Li to Kr", *Phys. Chem. Chem. Phys.* **7**, 59 (2005).
- [297] A. Hellweg, C. Hättig, S. Höfener, and W. Klopper, "Optimized Accurate Auxiliary Basis Sets for RI-MP2 and RI-CC2 Calculations for the Atoms Rb to Rn", *Theor. Chem. Acc.* **117**, 587 (2007).
- [298] F. Weigend and R. Ahlrichs, "Balanced Basis Sets of Split Valence, Triple Zeta Valence and Quadruple Zeta Valence Quality for H to Rn: Design and Assessment of Accuracy", *Phys. Chem. Chem. Phys.* **7**, 3297 (2005).
- [299] F. Weigend, F. Furche, and R. Ahlrichs, "Gaussian Basis Sets of Quadruple Zeta Valence Quality for Atoms H-Kr", *J. Chem. Phys.* **119**, 12753 (2003).
- [300] K. A. Peterson and T. H. Dunning Jr., "Intrinsic Errors in Several *ab initio* Methods: The Dissociation Energy of N₂", *J. Phys. Chem.* **99**, 3898 (1995).